A principal component approach to space-based gravitational wave astronomy

Michele Dawn Leighton

Submitted in partial fulfillment of the requirements for the
Degree of Doctor of Philosophy

School of Physics and Astronomy
College of Science and Engineering
University of Glasgow

October 2016

Abstract

The current approach to data analysis for the Laser Interferometry Space Antenna (LISA) depends on the time delay interferometry observables (TDI) which have to be generated before any weak signal detection can be performed. These are linear combinations of the raw data with appropriate time shifts that lead to the cancellation of the laser frequency noises. This is possible because of the multiple occurrences of the same noises in the different raw data. Originally, these observables were manually generated starting with LISA as a simple stationary array and then adjusted to incorporate the antenna's motions. However, none of the observables survived the flexing of the arms in that they did not lead to cancellation with the same structure.

The principal component approach is another way of handling these noises that was presented by Romano and Woan which simplified the data analysis by removing the need to create them before the analysis. This method also depends on the multiple occurrences of the same noises but, instead of using them for cancellation, it takes advantage of the correlations that they produce between the different readings. These correlations can be expressed in a noise (data) covariance matrix which occurs in the Bayesian likelihood function when the noises are assumed be Gaussian. Romano and Woan showed that performing an eigendecomposition of this matrix produced two distinct sets of eigenvalues that can be distinguished by the absence of laser frequency noise from one set. The transformation of the raw data using the corresponding eigenvectors also produced data that was free from the laser frequency noises. This result led to the idea that the principal components may actually be time delay interferometry observables since they produced the same outcome, that is, data that are free from laser frequency noise. The aims here were (i) to investigate the connection between the principal components and these observables, (ii) to prove that the data analysis using them is equivalent to that using the traditional observables and (ii) to determine how this method adapts to real LISA especially the flexing of the antenna.

For testing the connection between the principal components and the TDI observables a 10×10 covariance matrix containing integer values was used in order to obtain an algebraic solution for the eigendecomposition. The matrix was generated using fixed unequal arm lengths and stationary noises with equal variances for each noise type.

Results confirm that all four Sagnac observables can be generated from the eigenvectors of the principal components. The observables obtained from this method however, are tied to the length of the data and are not general expressions like the traditional observables, for example, the Sagnac observables for two different time stamps were generated from different sets of eigenvectors. It was also possible to generate the frequency domain optimal AET observables from the principal components obtained from the power spectral density matrix. These results indicate that this method is another way of producing the observables therefore analysis using principal components should give the same results as that using the traditional observables. This was proven by fact that the same relative likelihoods (within 0.3%) were obtained from the Bayesian estimates of the signal amplitude of a simple sinusoidal gravitational wave using the principal components and the optimal AET observables.

This method fails if the eigenvalues that are free from laser frequency noises are not generated. These are obtained from the covariance matrix and the properties of LISA that are required for its computation are the phase-locking, arm lengths and noise variances. Preliminary results of the effects of these properties on the principal components indicate that only the absence of phase-locking prevented their production. The flexing of the antenna results in time varying arm lengths which will appear in the covariance matrix and, from our toy model investigations, this did not prevent the occurrence of the principal components. The difficulty with flexing, and also non-stationary noises, is that the Toeplitz structure of the matrix will be destroyed which will affect any computation methods that take advantage of this structure. In terms of separating the two sets of data for the analysis, this was not necessary because the laser frequency noises are very large compared to the photodetector noises which resulted in a significant reduction in the data containing them after the matrix inversion. In the frequency domain the power spectral density matrices were block diagonals which simplified the computation of the eigenvalues by allowing them to be done separately for each block. The results in general showed a lack of principal components in the absence of phase-locking except for the zero bin. The major difference with the power spectral density matrix is that the time varying arm lengths and non-stationarity do not show up because of the summation in the Fourier transform.

Declaration

The work described in this thesis was carried out by the Author with help from her supervisor Prof. Graham Woan. Information obtained from other sources have been clearly cited.

Chapter 1 provides the background and the scope for the research in this thesis which uses information from other sources that have been appropriately cited. It begins with an overview of gravitational waves including its detection, sources and waveforms. The focus of the thesis is on data analysis for space-based gravitational wave detectors and is based on the original ESA-NASA Laser Interferometer Space Antenna therefore an overview of its design, current status and main data analysis issues is given. It briefly shows how the current approach for LISA was driven by the need to prove its viability because of the large number of sources and the overwhelming laser frequency noises occurring in its data which led to each problem being independently tackled. The target here is the laser frequency noises for which the current approach to the problem is the time delay interferometry observables which have to be previously generated before any data an can be performed. An overview of the laser noise cancellation using these observables is given. The thesis is based on the work done by Romano and Woan where the use of principal components as another approach to producing the data required for doing LISA science was introduced. An overview of this technique is provided.

The traditional time delay interferometry observables such as the Sagnac and the Michelson were manually generated using instinct and are just listed in the literature. Chapter 2 is the Author's interpretation and illustration of the laser frequency noises cancellation in the time delay interferometry observables. It includes examples for the Sagnac ζ and the Michelson X observables showing how they are affected by the phase-locking of the lasers and the rotational motion of the antenna. It also illustrates why the Sagnac do not survive the motions of LISA.

In Chapter 3 the Author generates the covariance and power spectral density functions for the LISA raw data and the optimal AET time delay observables required for creating the matrices which are the sources of the principal components. The sample matrices were produced from a computer program written by the Author using MATLAB. This chapter uses background information for deriving the functions and

generating the matrices which have been cited.

Chapter 4 produces the results of the Author's investigation into the connection between the principal components and the time delay observables. The matrices generated in this chapter were also produced from the Author's computer program using MATLAB. This chapter uses background information to explain eigenvalues and eigenvectors and to show how they are generated which have been clearly cited.

Chapter 5 presents the results of the Author's application of the principal component analysis to the raw LISA data and the comparison with the conventional approach using of the time delay interferometry observables. This is illustrated by estimation of the amplitude of a continuous gravitational wave buried in a toy model of LISA data. The matrices, simulated data and the likelihood plots were all produced from the computer program created by the Author using MATLAB.

Chapter 6 presents the results of the Author's investigations of how the principal components approach handles the effects of more realistic LISA data. These components are obtained from the covariance and the power spectral density matrices therefore, this investigation was approached by testing the how they were affected by different properties of LISA. Matrices were generated to reflect these effects and the principal components obtained from them were tested for the required eigenvalues. All the matrices generated in these were produce from the Author's computer program using MATLAB.

Chapter 7 gives the summary of the results, Author's conclusions and thoughts for future work. Any references to other literature have been appropriately cited.

Acknowledgements

Firstly, I would like to thank my primary supervisor Graham Woan for his encouragement, guidance and technical support without which I would not have been successful in completing my research. I would also like to thank my second supervisor Lyndsay Fletcher for her constructive comments and encouragement in the final stages when I was struggling with writing the thesis.

I would like to thank Sheila Rowan and Craig Buttar for the help and practical advice they gave me that got me through my first year. I would also like to thank Sheila for letting me know about that quiet place for working which was used often.

I would like to thank my adviser of studies Heather Lambie for her help in getting me through the last and most stressful stage of my degree. Without her help I would not have succeeded in submitting my thesis. I would also like to thank the people in the counseling services for their help with stress management especially Sandy, Fiona, Katie and Sabhia.

Finally, I am very lucky to have family and friends who stood by me when things did not go the way they should have. A very special thanks to my mother Pauline Thompson, siblings Jacqueline, Eddison, Natasha, Dena and Bobette, and friends John and Isabelle especially for the financial assistance they provided even when it was difficult for them. Without this help I could not have completed my degree. Also, thank you John and Suzy for getting me up in the mornings and keeping me focused on reaching the end.

Contents

List of Figures

List of Tables

Chapter 1

Introduction

1.1 Gravity

Gravity, for both Newton and Einstein, is a property of matter/energy relating to its mass that causes objects to move closer to one another but they differ in how this motion is produced. In the classical view, as defined by Newton's Law of Universal Gravitation, this motion is due to an attractive force that is created by the objects mass. This force is gravity and it is transmitted through gravitational fields that are set up by matter/energy in the surrounding space. In General Relativity on the other hand, this motion is due to the deformation of the space surrounding matter that produces a positive curvature towards its centre of mass. This curved space results in the deflection of the path of other objects creating motion that mimics an attractive force. This motion in the curved space is gravity and the gravitational field is the curvature of space [17].

In Einstein's view of gravity, this curvature is not only caused by matter nor does it only affect space. The Special Theory of Relativity coupled space with time and matter with energy [14, 27]. In this theory matter and energy are equivalent as shown by Einstein's the energy-momentum equation ($E^2 = m_0^2c^4 + p^2c^2$) so that spacetime/space can be also distorted by energy [14]. Time and space exist as a 4-dimensional continuum called a Minkowski spacetime which means that both could be distorted.

Newton's gravity involves motion under the influence of forces while for Einstein it is about motion in curved space therefore, it is dependent on the geometry of space; it is a geometric theory [17]. The curvature of space/spacetime is defined by Einstein's field equation relating the curvature tensor $\mathbf{G}$ to the source of distortion, the stress-energy-momentum tensor $\mathbf{T}$ which can be written as

$$\mathbf{G} = \frac{8\pi G}{c^4}\mathbf{T} \tag{1.1}$$

where G is the universal gravitational constant and c is the speed of light [13]. In curved spacetime the shortest straightest path is along a geodesic and motion along these paths

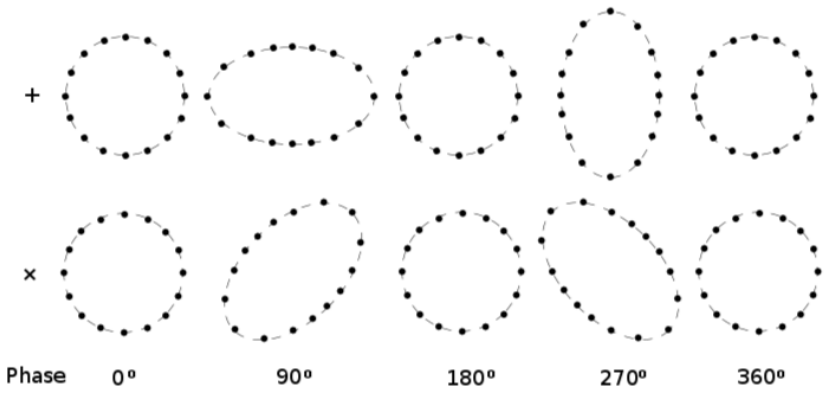

Figure 1.1: The effects of the cross and plus polarisations of a gravitational wave on a ring of free particles

is described by the geodesic equations [17]. Significant curvature is produced from very dense sources which are very large masses packed in small volumes [13]. This can be easily seen from the differential form of Gauss's law where the field strength/intensity is defined as the gravitational flux through a surface which is

$$\nabla \cdot \mathbf{g} = -4\pi G\rho \tag{1.2}$$

where ρ is the mass density and G is the gravitational constant [55]. So that the more densely packed objects will have stronger fields or, for Einstein, greater curving power.

1.2 Gravitational waves

The prediction of gravitational waves by Einstein came from the weak field approximation of the field equations, nearly flat spacetime, for which the solution is a wave equation. They travel at the speed of light and transport energy as gravitational radiation. The properties according to General Relativity are that they are transverse and have two independent polarizations. Their transverse nature is manifested in how spacetime is distorted which is in a plane perpendicular to the direction of their propagation. They are also area preserving in the transverse plane in that the stretching of spacetime in one direction will cause a corresponding squeezing in a direction perpendicular to the other producing two types of polarizations, h_+ and $h_\times$, that are 45° to each other. The effects of the different polarisations on a ring of particles is shown in Figure 1.1.

The first evidence for their existence was indirectly obtained from measurements of changes in the orbits of pulsars in binary systems which, according to general relativity,

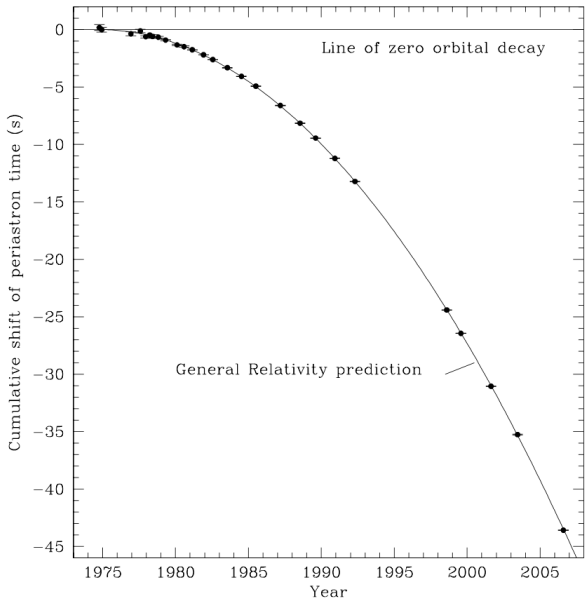

Figure 1.2: The orbital decay of the binary pulsar PSR B1913+16 comparing the observations (points) and theoretical values (line) based on General Relativity. Weisberg, Nice and Taylor [80]

decreases because of gravitational damping with energy being lost through gravitational radiation. This was first observed by Taylor and Weisberg [64] from observations of PSR B1913+16 a binary system containing a pulsar discovered by Hulse and Taylor [35]. Figure 1.2 shows the results of over thirty years of observations of this binary presented by Weisberg, Nice and Taylor [80]. The theoretical model used to determine the decay rate was based on General Theory of Relativity which produced a 0.997 ± 0.002 agreement with the observed decay rate supporting this theory of gravity.

The actual observation of gravitational waves was made by the two LIGO detectors at Livingston and Hanford of the coalescence of a binary system consisting of two black holes on September 14, 2015 [3, 1]. The plots of the waveforms are given in Figure 1.3 showing the system's inspiral, merger and final ring-down into a single black hole. From just this observation came proof of gravitational waves, the existence of black holes and, the fact that the waveforms match that predicted by General Theory of Relativity, support for this theory of gravitation. Confirmation came from the observation of another binary black hole coalescence on December 26, 2015 by these detectors [2].

1.2.1 Sources of gravitational waves

Gravitational waves are the propagating oscillations of the gravitational fields [57]. The gravitational field is determined by the distribution of the mass-energy of the source

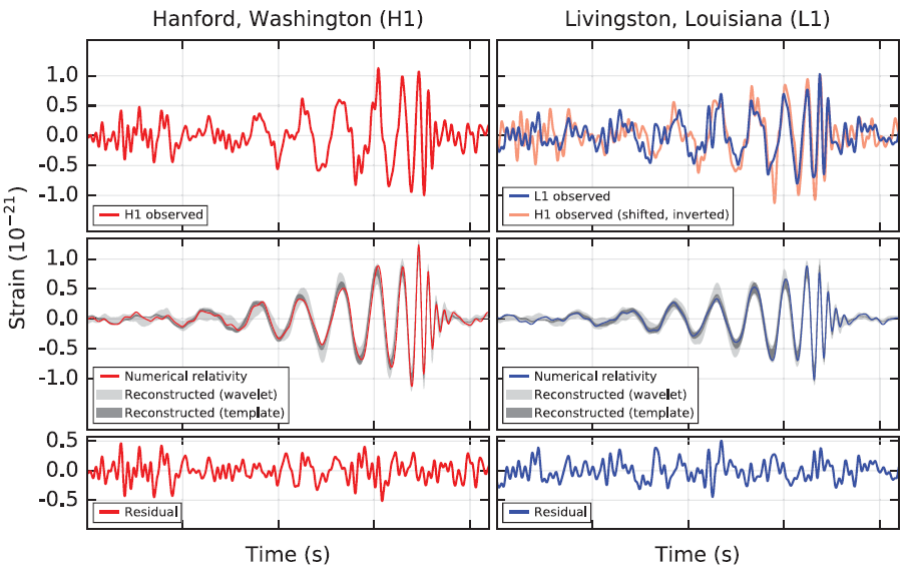

Figure 1.3: The gravitational waves produced from the merger of a pair of black holes GW150914 observed by two LIGO detectors. Abbott et. al. [3]

and its strength will only change if there is a change in this distribution through a loss/gain or from accelerated motion. For single sources this can be achieved through asymmetric spinning or from symmetric spinning with structural asymmetry. Examples of this type are spinning neutron stars which will produce continuous gravitational wave (Figure 1.4a). Single sources can also produce gravitational waves from non-spherical collapses or explosions such as core collapse of white dwarfs or the supernovae [52] with sample waveform as shown in Figure 1.4c. Continuous and burst waveforms are also produced by binary systems with the former being obtained when these systems are in stable orbits [52]. Bursts from binaries can be produced by those with extreme mass ratios, such as a super-massive black holes with a compact object, that are in highly eccentric orbits [12]. Inspirals, like the one shown in Figure 1.4b, can be obtained from the coalescence and merger of compact binaries such as two black holes or two neutron stars. There will also be stochastic gravitational waves (Figure 1.4d) produced for the superposition of incoherent sources from distant merges of neutron stars or supermassive black holes or from the cosmological background [52].

1.3 Space-based gravitational wave detectors

Blair et. al. [13] indicated that the minimum length for a detector baseline to achieve optimum sensitivity is half the wavelength of the gravitational signal being observed.

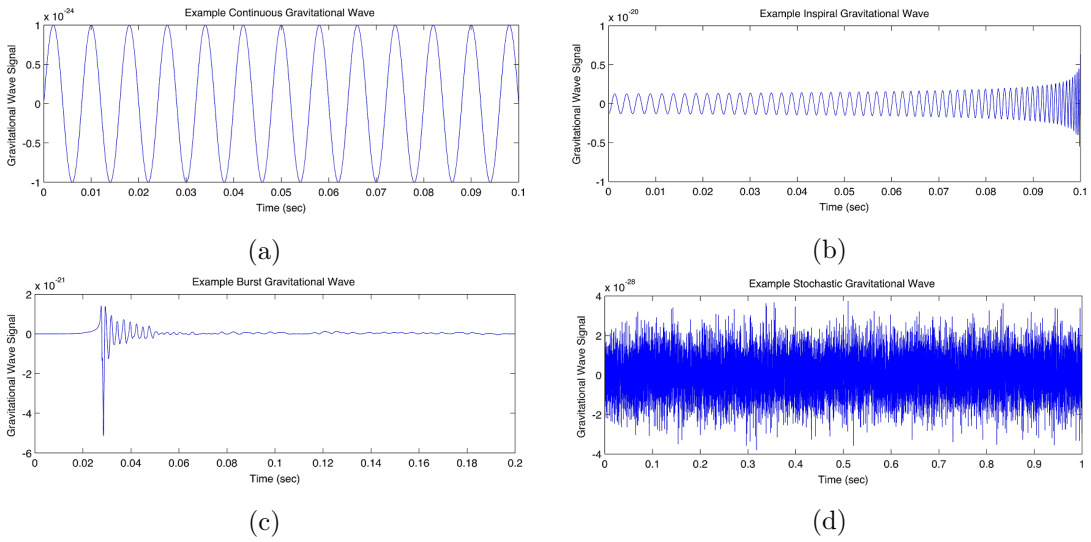

Figure 1.4: Examples of the types of waveforms expected from some of the gravitational waves sources. (LIGO Science Collaboration [40])

For the frequency ranges in gravitational wave spectrum shown in Figure 1.5 this gives lengths of approximately 15×10^{20} km to 15 km. Currently, the longest detector is LIGO which is a Michelson-type laser interferometer with physical lengths of 4 km which is less than a third the lowest wavelength. The restriction on the arm length is largely due to physical limitations caused by the curvature of the Earth but also includes building and operational costs, vacuum system maintenance and the alignment of the interferometer [13, 25]. The other main problem affecting ground-based detectors are seismic noises due to vibrations and fluctuations in the gravity-gradient in the Earth's surface [50]. Isolators can compensate for the vibrations but gravity-gradient noises, which are due to random gravitational forces associated with the changes in the mass density in the detectors surroundings, cannot be shielded and is the limiting noise source below 10 Hz [58]. Reducing the effects from these noises is accomplished by locating the detectors in seismically quieter sites which can increase sensitivities to 1 Hz [50]. The underground location for KAGRA detector takes advantage of the decrease in the seismic waves with depth. Even with these limitations, the first observations of gravitational waves was produced by the LIGO ground-based observatories at Livingston and Hanford. There is a suggestion for a 40 km ground-based interferometers from Dwyer et. al. [25] using the natural depressions in areas that are bowls, such as the Carson Sink, to compensate for the Earth's curvature and to help reduce the amount of excavation. However, for really long baselines and observations below 1 Hz the only option is space which also

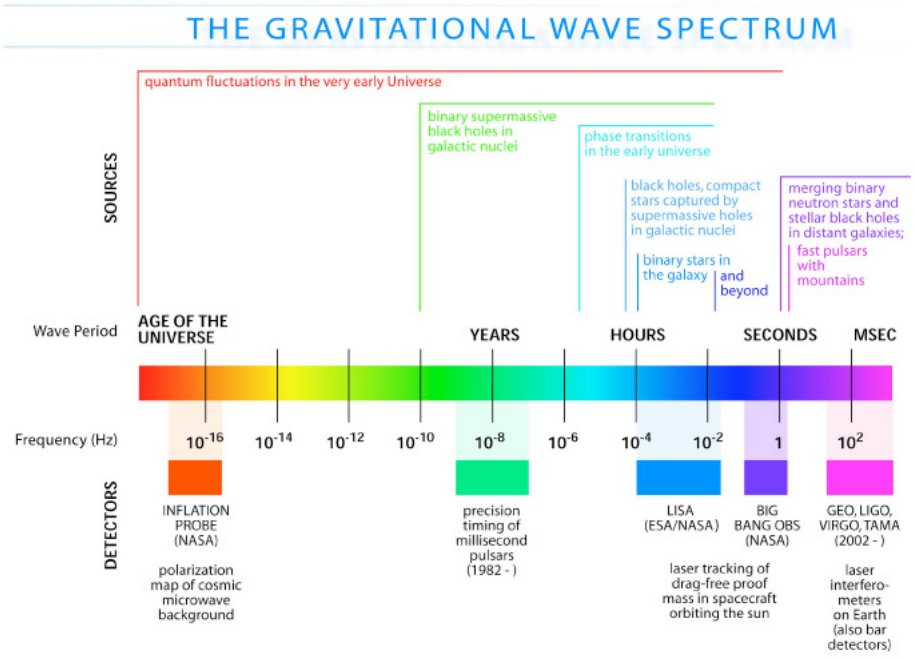

Figure 1.5: The gravitational wave spectrum and detectors. (From LIGO Science Collaboration: http://www.ligo.org/science/faq.php)

has the advantage of operating in a natural vacuum. The baselines can be formed either between Earth and a space-based test mass or entirely between space-based test masses. For the Earth-space combination the space test mass can either be spacecraft or pulsars. The former involves Doppler tracking using microwave signals to monitor changes in the separation between the Earth and the spacecraft for the passage of a gravitational wave and the frequency band for this type is 10^{-4} Hz to 1 Hz [65, 57]. For the Earth-pulsar combination the arrival times of the pulses are monitored for changes which could be caused by the passage of a gravitational wave crossing their path. This method is limited by the fact that the pulsar periods are not constant and only give stable values after being averaged over a long period of time. The most stable of these systems are the millisecond pulsars [57]. An example of the baseline for this combination is 1.7×10^{15} km for the millisecond pulsar PSR J0437–4715. The frequency range for this type of observation is about 10^{-7} Hz to 10^{-9} Hz which is the middle of the spectrum given in Figure 1.5 [65]. The space-based option involves using satellites that track each other using lasers. The passage of a gravitational wave will change the separations between them which will be monitored by the satellites using laser interferometry. Their operating frequency band is 10^{-4} Hz to 10^{-1} Hz [57]. The first detector of this type is the

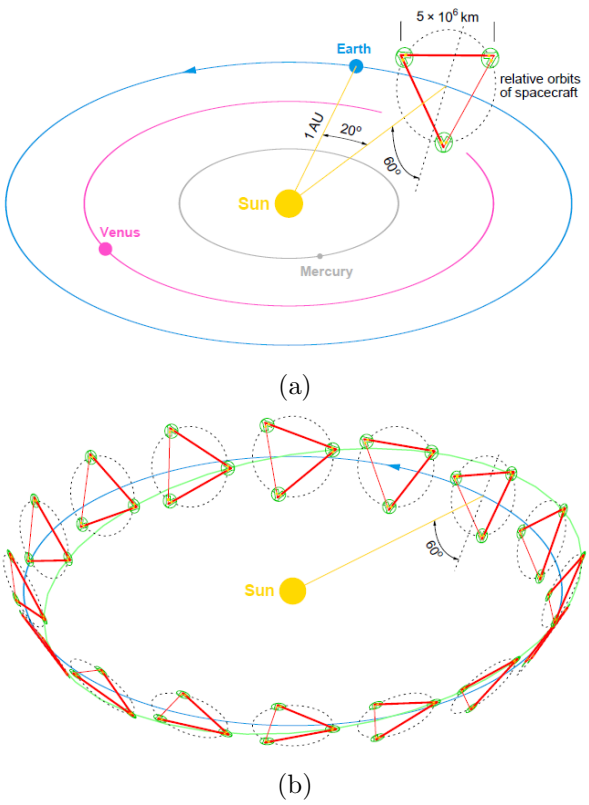

Figure 1.6: Schematic diagram showing the location and orbit of LISA (a) and its annual motion (b) (European space agency. Pre-Phase A Report [10]

Laser Interferometer Space Antenna (LISA) which was a joint project between NASA and ESA. Our investigations will be based on this detector which will be discussed in the next section.

1.4 Laser Interferometer Space Antenna - LISA

The first detailed design and mission plan for LISA was laid out in the early Pre-Phase A reports [10, 29, 21, 11]. In this design the antenna consists of three satellites in their own free fall orbit around the Sun with inclinations and eccentricities that keep the spacecraft in a triangular formation that trials the Earth by 20°. The separation between each spacecraft is 5×10^9m. The yearly motion of the antenna causes its plane to rotate about the centre of mass which is on located on the ecliptic and tilted at 60° [10]. Schematic diagrams showing its location relative to the Sun and the Earth and its rotational motion are given in Figure 1.6. The three spacecraft are identical in design containing two optical benches arranged in a Y-shape as shown in Figure 1.7a. Within each bench is a proof mass, a laser, beam splitters, photodetectors, a reference

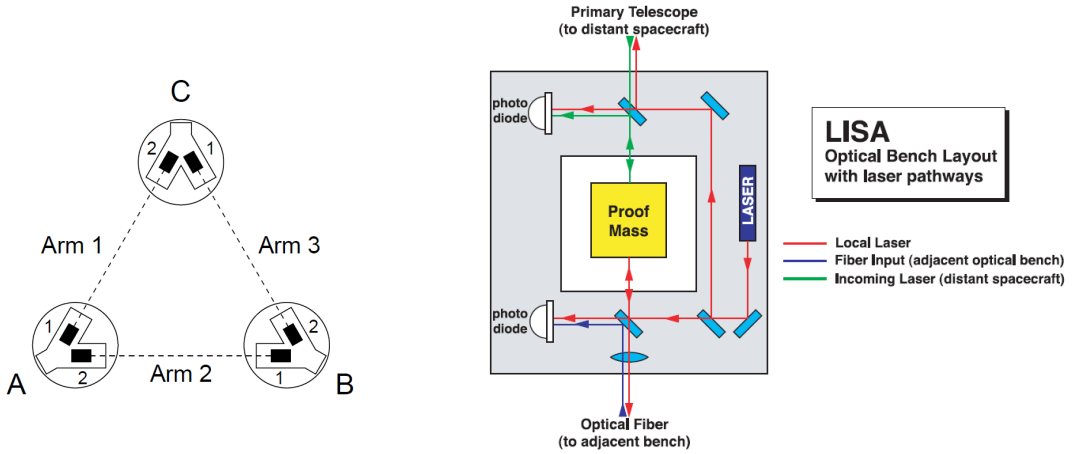

(a) (b)

Figure 1.7: Schematic diagrams of LISA showing (a) the positioning and orientation of the optical benches in each satellite (Pre-Phase A Report [10]) and (b) the original design of LISA's optical bench (Larson [39]).

cavity for stabilising the laser, a phase modulator for conveying clock information and for data exchange between the spacecraft, and a telescope. A schematic of this is given in Figure 1.7b. The proof masses are in their own drag-free orbits. LISA is a nearly omni-directional detector and its configuration allows it to act as a multidetector where it can function as three independent interferometers which can be used to detect the different polarisations of a gravitational wave [10].

1.4.1 Design changes - the split configuration

In LISA the changes in each arm are measured by the two spacecraft located at the each end. The end of the arms are defined by the proof masses (mirrors) but how these measurements are obtained differ from the conventional Michelson interferometer. In the Pre-phase A design of LISA this measurement is between a proof mass at one end and optical bench at the other. This is illustrated in Figure 1.7b where the beam being transmitted to the distant spacecraft (red) is not reflected off the proof mass but the incoming beam (green) is reflected off the proof mass before it goes to the photodetector. There are also measurements taken between the two optical benches on each spacecraft where the opposite occurs. The beam going to the other bench (red) is first reflected off the local proof mass before being transmitted and the beam being received from the other bench (green) goes directly to the photodetector. The distance measurement is therefore split into a long-arm measurement from optical bench of the transmitting

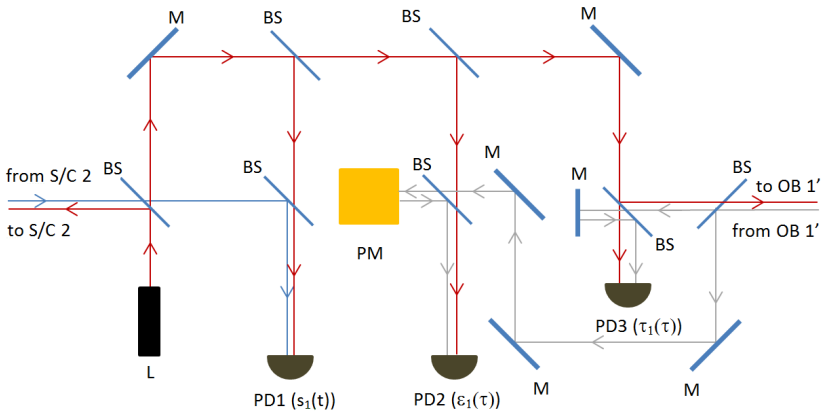

Figure 1.8: A schematic of the split configuration showing the three different measurements $s_1(t)$, $\epsilon_1(t)$ and $\tau_1(t)$. In the diagram L, M, BS and PM represent the laser, mirrors, beam splitters and proof masses, respectively. Also, PD, S/C and OB indicate the photodetectors, spacecraft and optical benches, respectively. Based on diagram from Otto, Heinzel and Danzmann [46].

spacecraft to the proof mass on the receiving spacecraft plus the short-arm measurement on the transmitting spacecraft between the optical bench and its local proof mass.

In the final design before LISA became an ESA-only project the measurements were divided into three sections consisting of one long-arm and two short-arm measurements. The laser beam in the long-arm measurement no longer interacts with either of the proof masses. This design change is illustrated in Figure 1.8 showing the new configuration which is the baseline from 2006 [46]. As illustrated in Figure 1.8 there are three sets of optical bench readings that are needed for the science data. These readings are:

Spacecraft to spacecraft measurements $s_i(t)$: These are the readings between the spacecraft at the end of each arm which are called the inter-spacecraft or long arm measurements. They are the result of the incoming light from the distant spacecraft being interfered with the local light on the receiving optical bench which is recorded at photodetector PD1 in Figure 1.8.

Proof mass to proof mass measurements $\epsilon_i(t)$: These are the internal measurements between the two proof masses of the optical benches on each spacecraft which called the intra-spacecraft readings. There are due to the local light on one optical bench being interfered with the light from the other optical bench. They monitor the test mass motion and are recorded at photodetector PD2 in Figure 1.8.

Laser with laser $\tau_i(t)$: These are the reference interferometer measurements obtained

from the interference of the lasers on the two optical benches on each spacecraft and recorded at photodetector PD3 in Figure 1.8.

1.4.2 Current status

The transfer of the LISA mission to ESA in 2011 resulted in changes in the name, design and mission. The name change reflected the different design of the two options namely, evolved LISA (eLISA) which was a smaller scale of the original LISA and the New Gravitational Wave Observer (NGO). NGO is a reduced version of LISA with the same number of spacecraft but with only two arms and with reduced lengths of 1×10^9 m. The final name is eLISA with the design specifications of NGO which is shown in Figure 1.9. The predicted launch date is in 2034.

1.4.3 LISA Pathfinder - LPF

Before launching LISA some of its technology are being tested by the LISA Pathfinder (LPF) which was launched on December 3, 2015. This is a scaled down version of LISA with only one spacecraft with two test masses each suspended in their vacuum container and are separated by 38 cm [41]. The mission objectives obtained from ESA LISA Pathfinder fact sheet web page are to:

- Demonstrate drag-free and attitude control in a spacecraft with two free test masses.
- Test feasibility of laser interferometry with picometre resolution at low frequency – approaching $10^{-12}\mathrm{m}/\sqrt{\mathrm{Hz}}$ in the frequency band 1-30 mHz.
- Test the endurance of the different instruments and hardware in the space environment

LISA pathfinder arrived at its location at the first Sun-Earth Lagrangian point L1 on January 23, 2016 and the test masses were released into their own free fall orbits on February 13 and 17 and started its science phase on March 1, 2016 [28].

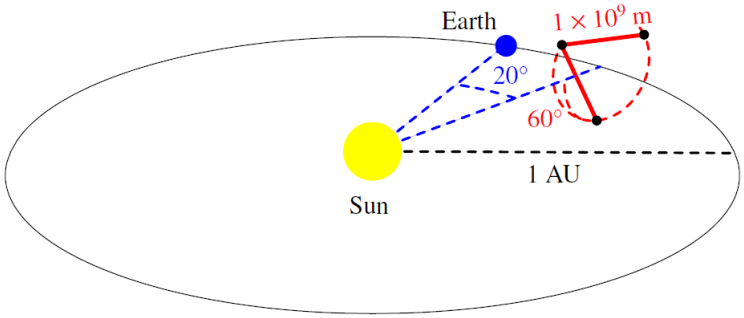

Figure 1.9: Schematic of eLISA orbit showing the reduction in the number of arms and their lengths. Amaro-Seoane et. al. [49]

1.5 LISA data analysis: current approach

The two issues affecting LISA that are critical to its success in producing science are the overwhelming laser frequency noises and the large number of sources that will occur in its data. Interestingly, these are associated with the same properties of LISA that give it the advantages over the ground-based detectors. Being in space allows it to have long arms for observing in the low frequency band which is implemented using free-falling spacecraft in orbit around the Sun. However, the long arms introduce significant travel times between the spacecraft which, combined with its orbital motion and the perturbations from planets, causes unequal time varying arm lengths that create problems with the laser frequency noise cancellation. The level of this noise is expected to be about 10^7 greater than that of large proportion of its signals. The low frequency bandwidth in which it operates is densely populated by a large number of sources consisting of approximately 2×10^8 binaries of which several million will occur in its bandwidth in the 0.1 mHz to 3 mHz region [18, 75, 30].

The current approach to resolving these problems resulted from the need to show that the LISA project was viable in that it could still produce useful information. This led to the development of a kind of divide and conquer approach in which problems were tackled separately with the Mock LISA Data Challenges for handling the source problem and the development of the time delay interferometry observables for laser frequency noise cancellation.

1.5.1 Source confusion

Of the millions of sources occurring in LISA's bandwidth only about 10^4 will be resolvable [8, 30]. This presents two major challenges referred to as source confusion and source confusion noise. The former is related to the overlapping of the sources caused by cross-correlations of their signals occurring strongly below 2 mHz [22]. The confusion noise is related to the unresolved sources which will produce a background noise. The challenge is to untangle the signals and determine the confusion noise level in order to distinguish it from the instrumental noises.

The Mock LISA Data Challenges (MLDC) have different levels and goals. The levels presented an approach to the analysis problem that was similar to the laser noise cancellation in that they started with simple models of LISA data and gradually introduced more of the complexities the data. For example, the first challenge data sets had a single signal or small set of overlapping ones embedded in Gaussian noise with no confusion noise with the main goal of developing the data analysis tools. The main site for the challenges is AstroGravS a service provided by NASA [32] containing all the challenges and links to papers. Overviews are provided by Arnaud et. al. [8, 9].

One outcome in terms of the signal extraction was the realisation that correlations between the signals meant that a global solution was required where all the signals were fitted using a filter bank consisting of models of every type of source occurring in the data [19]. The framework for this was shown to be Bayesian presented by Umstätter et. al. [75, 76] where they were able to also define a confusion noise limit and determine the number of signals which was also an unknown.

1.5.2 Laser frequency noise

The ability of a laser to maintain the same frequency over a specified time period determines its frequency stability and the random fluctuation of its stability is called frequency or phase noise [38]. In LISA the problem occurs because these frequency fluctuations occur at levels of $1.0 \times 10^{-13}/\sqrt{\text{Hz}}$ in the millihertz band while its goal is to observe signals at levels of $10^{-20}/\sqrt{\text{Hz}}$) or lower [69]. The simple illustration of the problem is given in Figure 1.10 using examples of the two levels of noises and a single sinusoidal signal. The effects of the individual noises on the signal are shown in plots

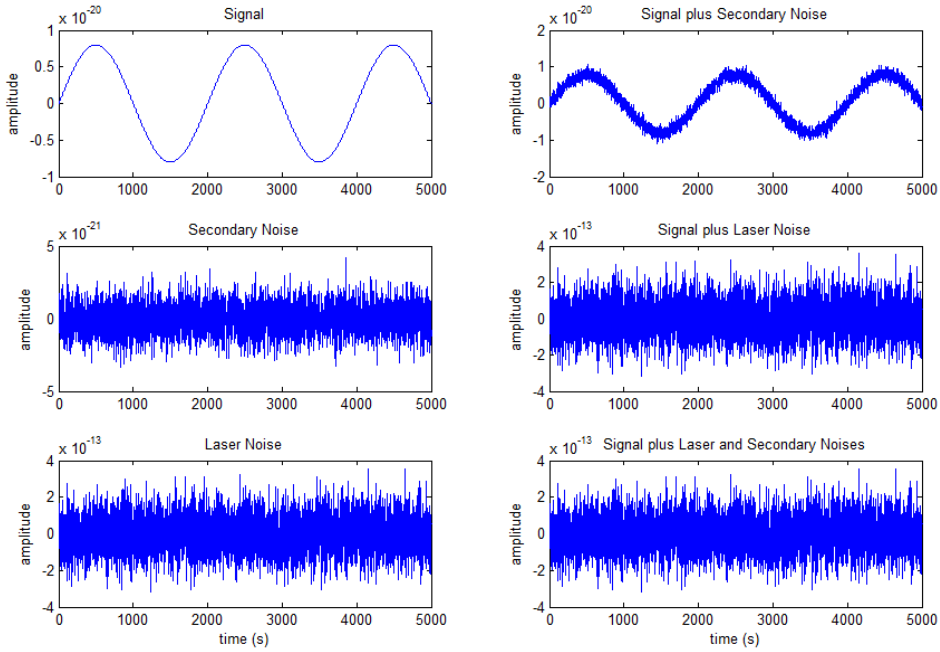

Figure 1.10: Sample plots to show the effects of the primary (middle left) and secondary (bottom left) noises on a simple sinusoidal signal (top left). The combinations of the individual noises with the signal are given in the top and middle panels on the right. The bottom right plot is the combination of both noises and the signal.

on the right where only in the top plot, which is a combination of the signal with the secondary noise, is the signal is still visible. The laser noise totally overwhelms both the signal and the secondary noises in the middle and bottom plots. The goal was to find a way to cancel the laser frequency noises or reduce them to the level of the secondary noises. This noise is also present in ground-based laser interferometer detectors but the symmetry (fixed with equal lengths) and shortness of their arms ($\approx 10^{-5}$ s for 4 km arms) allows cancellation by directly differencing the readings because the delays, and hence noise, are the same in each arm. The very long arms of LISA (5×10^9 m) result in significant light travel times of about 16.7s between the space craft and the variations in their lengths cause differences of up to 1% (5×10^7 m) [36] which rules out this method of noise cancellation for LISA.

1.5.3 Time delay interferometry

Time delay interferometry (TDI) is a post processing technique that was introduced by Armstrong, Estabrook and Tinto [6, 26, 69, 7, 70, 68] for canceling the laser frequency noise which was based on earlier works for noise cancellation in an unequal-arm Michelson interferometer [31, 66, 67]. The process involves using linear combinations

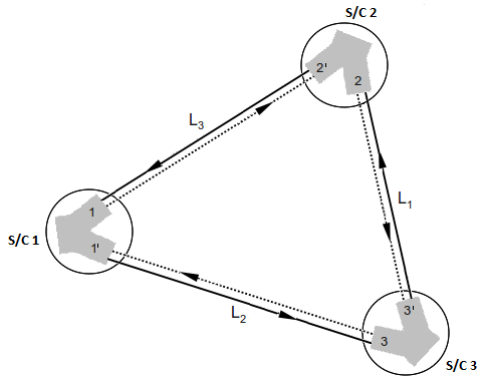

Figure 1.11: Schematic of LISA showing the labeling of the spacecraft (S/C i), optical benches and arms (L_i). The optical benches are labeled with primed i' and unprimed (i) integers.

of the individual data streams with appropriate time shifts to cancel the laser noises and relies on multiple occurrences of the same noise in the readings from the different optical benches. Each spacecraft has two optical benches giving six inter-spacecraft measurements of fractional frequencies $y_i(t)$, obtained from beating the laser from a distant spacecraft with the local laser on the receiving spacecraft, and six intra-spacecraft readings $z_i(t)$, from beating the two lasers on each spacecraft [6]. These are illustrated in Figure 1.12. For a simple drag-free model of LISA with static arms and no orbital or rotational motion, the inter-spacecraft (y_i) and intra-spacecraft (z_i) readings for the laser frequency noises can be written as

$$\begin{aligned} y_i^{laser}(t) &= C_{j'}(t - D_k) - C_i(t), \\ z_i^{laser}(t) &= C_{i'}(t) - C_i(t), \end{aligned} \tag{1.3}$$

where C_i and $C_{j'}$ are the laser frequency noises in the receiving and transmitting space craft, respectively [6]. D_k is the light travel time in the arm between the spacecraft which is equal to L_k/c where L_k is the arm length and c is the speed of light. Using the readings for the photodetectors at the ends of arm L_3 in Figure 1.11 which are $y_1(t)$ and $y_{2'}(t)$ with laser noise contributions $[C_{2'}(t - D_3) - C_1(t)]$ and $[C_1(t - D_3) - C_{2'}(t)]$, respectively, the equations for these noises are

$$\begin{aligned} y_1^{laser}(t) &= C_{2'}(t - D_3) - C_1(t), \\ y_{2'}^{laser}(t) &= C_1(t - D_3) - C_{2'}(t), \end{aligned} \tag{1.4}$$

which show the same noises occurring in the two readings but at different times of $(t - D_3)$ and t. These noises also occur in the internal readings for the same two optical

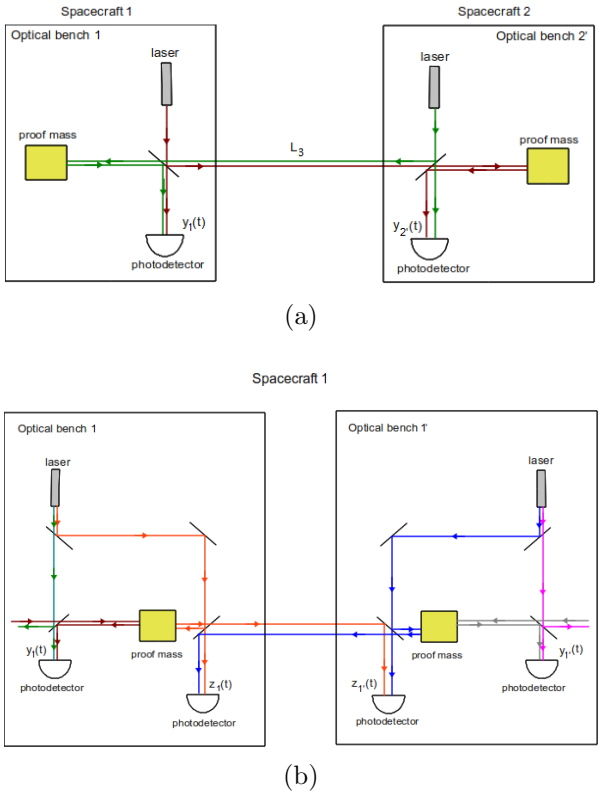

Figure 1.12: Schematic diagram illustrating the Pre-phase A optical bench measurements using spacecraft 1 and 2 showing (a) the inter-spacecraft readings between spacecraft 1 and 2 (red and green lines) and (b) and the intra-spacecraft readings between optical benches 1 and $1'$ on spacecraft 1 (orange and blue lines).

benches $z_1(t)$ and $z_{2'}(t)$ which are

$$\begin{aligned} z_1^{laser}(t) &= C_{1'}(t) - C_1(t), \\ z_{2'}^{laser}(t) &= C_2(t) - C_{2'}(t), \end{aligned} \tag{1.5}$$

where the noises all occur at the same times t [26].

How these multiple occurrences are used to cancel laser phase noises can be shown using the laser frequency noises C_1 and $C_{2'}$ in the previous equations. Laser frequency noise C_1 occurs at time t in $y_{2'}$ and z_1 in Equations 1.4 and 1.5. Subtracting $z_1^{laser}(t)$ from $y_1^{laser}(t)$ gives

$$\begin{aligned} y_1^{laser}(t) - z_1^{laser}(t) &= [C_{2'}(t - D_3) - C_1(t)] - [C_{1'}(t) - C_1(t)] \\ &= C_{2'}(t - D_3) - C_{1'}(t), \end{aligned} \tag{1.6}$$

where this noise is canceled leaving two other noises $C_{2'}(t - D_3)$ and $C_{1'}(t)$. Laser frequency noise $C_{2'}$ also occurs in the internal readings $z_{2'}^{laser}$ of spacecraft 2 but at a

different time. Shifting this reading by D_3 to match that in Equation 1.6 gives

$$z_{2'}^{laser}(t - D_3) = C_2(t - D_3) - C_{2'}(t - D_3), \tag{1.7}$$

which when added to Equation 1.6 gives the required cancellation which is

$$\begin{aligned} y_1^{laser}(t) - z_1^{laser}(t) + z_{2'}^{laser}(t - D_3) &= C_{2'}(t - D_3) - C_{1'}(t) + C_2(t - D_3) - C_{2'}(t - D_3) \\ &= C_2(t - D_3) - C_{1'}(t). \end{aligned} \tag{1.8}$$

The cancellation of $C_{2'}$ could have been done by shifting $y_{2'}^{laser}(t)$ by D_3 instead giving

$$\begin{aligned} y_{2'}^{laser}(t - D_3) &= C_1(t - D_3 - D_3) - C_{2'}(t - D_3) \\ &= C_1(t - 2D_3) - C_{2'}(t - D_3), \end{aligned} \tag{1.9}$$

and then adding this to Equation 1.6 to obtain

$$\begin{aligned} y_1^{laser}(t) - z_1^{laser}(t) + y_{2'}^{laser}(t - D_3) &= C_{2'}(t - D_3) - C_{1'}(t) + C_1(t - 2D_3) - C_{2'}(t - D_3) \\ &= C_1(t - 2D_3) - C_{1'}(t). \end{aligned} \tag{1.10}$$

This process is repeated until all the laser frequency noises are canceled and the data that are obtained are the time delay interferometry combinations or observables. For the conventional time delay observables this was done manually using trial and error.

The various possibilities for combining the raw data for canceling the noises resulted in combinations with different structures some resembling certain types of interferometers and were named accordingly, for example, the Michelson and the Sagnac combinations. In a Michelson interferometer a single beam is split between two perpendicular arms and reflected off mirrors at the ends of the arms back to the splitter where they are recombined with the final phase measurements being the difference of the readings in the two arms. In a Sagnac the mirrors are arranged so that the optical path is a closed ring. Two beams obtained from splitting a single laser are directed along clockwise and counter-clockwise paths and then recombined at the splitter. In the Michelson and Sagnac time delay interferometry observables the individual terms occur in a pattern matching these differences. This is illustrated in Figure 1.13 with a few other combinations. The arrows indicate the direction of the measurements in the combinations with the recording optical benches located at the arrowhead.

The first set of time delay interferometry combinations were based on a simple model of LISA which are the first (1^{st}) generation TDIs. Those that include the rotational

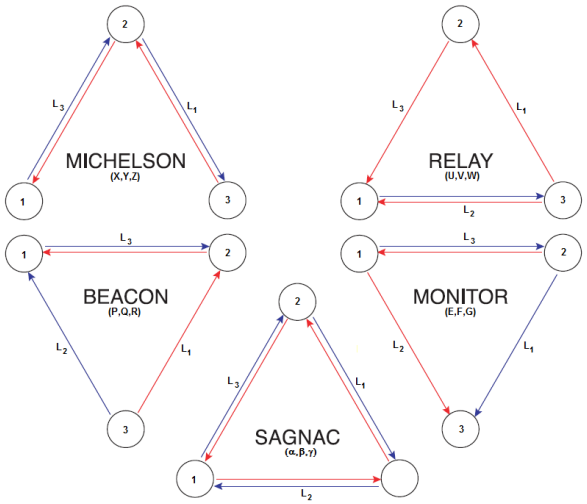

Figure 1.13: Diagrams illustrating some of the time delay interferometry combinations including the Michelson and Sagnac. The readings used for each combination and the direction of their measurements are indicated by the arrows. Reproduced from Larson [39] with labels added to show the arms and spacecraft.

motion of the antenna but not the flexing of the arms are the modified TDIs or TDI 1.5 [59, 20, 70]. The 2^{nd} generation TDIs incorporate all the motions of LISA [60, 20, 70]. Some of the combinations retain the structure of their inter-spacecraft readings when the orbital motion effects are taken into account. For those that do not, a new set of generalised combinations with similar names were obtained but not all resulted in the cancellation of the noises [60].

1.5.3.1 The effects of LISA's motions on time delay interferometry

Recall that the problem with the laser frequency noises is that the inequality of LISA's arm lengths rules out the possibility of cancellation by the direct differencing of the readings from the different arms as used in ground-based interferometer detectors. Any behaviour of LISA that directly changes the arm lengths will affect the laser frequency noise cancellation which will in turn affect the time delay interferometry combinations. In the Pre-phase A model of the optical bench [10], the ends of the arms, and their lengths, are determined from the positions of the proof masses and optical benches. The inter-spacecraft reading $y_i(t)$ is made between the receiving (local) optical bench and the proof mass of the transmitting spacecraft which will be affected by the non-inertial motions of the proof masses and optical benches. Recall that the first generation inter-spacecraft and intra-spacecraft readings for the laser frequency noises have simple

structures which are

$$y_i^{laser}(t) = C_{j'}(t - D_k) - C_i(t),$$
$$z_i^{laser}(t) = C_{i'}(t) - C_i(t).$$

With the optical bench and proof mass noises these become

$$y_i^{laser}(t) = C_{j'}(t - D_k) - C_i(t) - \hat{n}_k \cdot \vec{V}_{j'}(t - D_k) + 2\hat{n}_k \cdot \vec{v}_i(t) - \hat{n}_k \cdot \vec{V}_i(t),$$
$$z_i^{laser}(t) = C_{i'}(t) - C_i(t) - 2\hat{n}_j \cdot [\vec{v}_{i'}(t) - \vec{V}_{i'}(t)], \tag{1.11}$$

where $\hat{n}_i$ is a unit vector along arm i measured in the counter-clockwise direction and, $\vec{v}_i(t)$ and $\vec{V}_i(t)$ are the random velocities associated with proof mass i and optical bench i, respectively [26]. The effects of the rotational motion of LISA is to cause the light travel times in each arm to be dependent on the direction of measurement that is, $D_{k'} \neq D_k$ where k' and k indicates the clockwise and counter-clockwise directions in arm k, respectively.

The offsets in the inter-spacecraft readings now have to account for this difference, for example, the optical benches at the end of arm k will contain the same laser frequency noises but with offsets measured in the opposite directions. If $y_i(t)$ and $y_{j'}(t)$ represent these readings then their directionally dependent versions, excluding the acceleration noises, will be

$$y_i^{laser}(t) = C_{j'}(t - D_k) - C_i(t),$$
$$y_{j'}^{laser}(t) = C_i(t - D_{k'}) - C_{j'}(t). \tag{1.12}$$

The flexing or breathing of the arms caused by perturbations from nearby objects makes the arm lengths time dependent which will occur as $D_k(t)$, for example, for $y_i(t)$ with flexing becomes

$$y_i^{laser}(t) = C_{j'}[t - D_k(t)] - C_i(t). \tag{1.13}$$

Note that the time dependent version will cover the rotational effects. The two were separated to illustrate the different motions associated with the different generations of the time delay interferometry observables. For the second generation observables the order that the offsets occur is important. An alternate way of writing the equations for the observables uses a compact notation where the time shifts are subscripts, for example, $y_i(t - D_k)$ is replaced with $y_{i,k}$. For the second generation equations both the

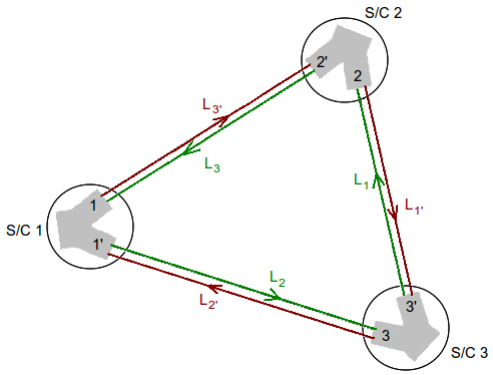

Figure 1.14: Schematic of LISA showing the directional dependence of the arm lengths with the clockwise and counter-clockwise directions labeled $L_{i'}$ and L_i, respectively. The spacecraft are indicated by S/C i with their corresponding optical benches by i and i'.

comma and semicolon are used as separators [60, 70] with the following meaning

$$\begin{aligned} y_{,i} &= y[t - D_i(t)], \\ y_{;ij} &= y\big\{t - D_j(t) - D_i\big[t - D_j(t)\big]\big\}, \\ y_{;ijk} &= y\big(t - D_k(t) - D_j\big[t - D_k(t)\big] - D_i\big\{t - D_k(t) - D_j[t - D_k(t)]\big\}\big). \end{aligned} \tag{1.14}$$

In the following sections brief overviews of the Sagnac and the Michelson combinations illustrating how their structure changes with the motions of LISA are given. No explanation will given for why this occurs as this will be done in Chapter 2. The aim here is to introduce the current approach to handling the laser frequency noises for understanding where the possibilities are for improvements in the data analysis. The compact notation will be used in the next section.

1.5.3.2 The Sagnac combinations

The Sagnac observables consists of two kinds which are the six-pulse (α, β, γ) and the fully symmetric (ζ) combinations. The simplest forms of these combinations for stationary static model of LISA, not motion effects, using α and ζ combinations are

$$\begin{aligned} \alpha(t) = &\big[y_{1'}(t) + y_{3'}(t - D_2) + y_{2'}(t - D_1 - D_2)\big] \\ &- \big[y_1(t) + y_2(t - D_3) + y_3(t - D_1 - D_3)\big], \\ \zeta(t) = &\big[y_{1'}(t - D_1) + y_{3'}(t - D_3) + y_{2'}(t - D_2)\big] \\ &- \big[y_1(t - D_1) + y_2(t - D_2) + y_3(t - D_3)\big], \end{aligned} \tag{1.15}$$

where the terms within them are grouped to show the differencing of readings in different directions. For synthesizing the Sagnac structure, the α, β and γ combinations are obtained by using spacecraft 1, 2 and 3 as beam splitters, respectively. Six-pulse refers to the fact that the gravitational wave signal will have a six-pulse response in these combinations corresponding to the six different times occurring in them [6]. These combinations have three time patterns occurring in them which are t, $(t - D_i)$ and $(t - D_i - D_j)$ which distinguishes them from the fully symmetric Sagnac ζ where all the readings have been shifted by one offset, $(t - D_i)$. Also, the ζ Sagnac has no central spacecraft (beam-splitter) and has a very low response to gravitational wave signals. With the compact notation these can be written as

$$\begin{aligned}\alpha &= [y_{1'} + y_{3',2} + y_{2',12}] - [y_1 + y_{2,3} + y_{3,13}],\\ \zeta &= [y_{1',1} + y_{3',3} + y_{2',2}] - [y_{1,1} + y_{2,2} + y_{3,3}].\end{aligned}$$

Accounting for the accelerations of the proof masses and optical benches requires the intra-spacecraft readings for the laser frequency noise cancellation. From Estabrook et. al. [26], including the acceleration noise changes α and ζ in Equation 1.15 to

$$\begin{aligned}\alpha = [y_{1'} + y_{3',2} + y_{2',12}] - [y_1 + y_{2,3} + y_{3,13}]\\ + \frac{1}{2}\big\{[z_1 - z_{1'}] + [z_1 - z_{1'}]_{,123} + [z_2 - z_{2'}]_{,3} + [z_2 - z_{2'}]_{,12}\\ + [z_3 - z_{3'}]_{,2} + [z_3 - z_{3'}]_{,13}\big\},\end{aligned} \tag{1.16}$$

and

$$\begin{aligned}\zeta = [y_{1',1} + y_{3',3} + y_{2',2}] - [y_{1,1} + y_{2,2} + y_{3,3}]\\ + \frac{1}{2}\big\{[z_1 - z_{1'}]_{,1} + [z_1 - z_{1'}]_{,23} + [z_2 - z_{2'}]_{,2} + [z_2 - z_{2'}]_{,13}\\ + [z_3 - z_{3'}]_{,3} + [z_3 - z_{3'}]_{,12}\big\},\end{aligned} \tag{1.17}$$

where the structure of the inter-spacecraft readings do not change. However, including the effects of the rotational motion which causes the directional dependence of the arm lengths breaks the symmetry of the Sagnac in that there are no combinations that will retain the same structure with respect to the inter-spacecraft readings [20, 26]. However, there are other generalised or modified Sagnac combinations α_i and ζ_i [26, 60, 59] with three combinations for each with roughly similar structure but with twice the number

of terms. Examples of these generalised combinations from Shaddock [59] are

$$\begin{aligned}\alpha_1 = {} & [y_{1'} + y_{3',2'} + y_{2',1'2'}] - [y_1 + y_{2,1} + y_{3,31}] \\ & - [y_{1'} + y_{3',2'} + y_{2',1'2'}]_{,231} + [y_1 + y_{2,1} + y_{3,31}]_{,2'3'1'} \\ & - \frac{1}{2}\big\{[z_{1'} - z_1] - [z_{1'} - z_1]_{,2'313'1'2} + [z_{2'} - z_2]_{,1} + [z_{2'} - z_2]_{,1'2} \\ & \quad + [z_{2'} - z_2]_{,12'3'1'} - [z_{2'} - z_2]_{,1'2'231} + [z_{3'} - z_3]_{,2'} + [z_{3'} - z_3]_{,31} \\ & \quad - [z_{3'} - z_3]_{,2'231} - [z_{3'} - z_3]_{,312'3'1'}\big\},\end{aligned}$$

$$\begin{aligned}\zeta_1 = {} & [y_{1,11'} + y_{2,2'1'} + y_{3,31}] - [y_{1',11'} + y_{3',31} + y_{2',2'1'}] \\ & + [y_{1',123} + y_{3',33'2'} + y_{2',2'23}] - [y_{1,1'3'2'} + y_{2,2'23} + y_{3,33'2'}] \\ & - \frac{1}{2}\big\{[z_{3'} - z_3]_{,31} + [z_{3'} - z_3]_{,1'2'1} - [z_{3'} - z_3]_{,3'32'} - [z_{3'} - z_3]_{,232'1} \\ & \quad + [z_{2'} - z_2]_{,1'1} + [z_{2'} - z_2]_{,1'2'} - [z_{2'} - z_2]_{,232'} + [z_{2'} - z_2]_{,31'1} \\ & \quad - [z_{2'} - z_2]_{,3'232'} - [z_{2'} - z_2]_{,3'31'2'}\big\}\end{aligned} \tag{1.18}$$

with the terms grouped to show a Sagnac-type arrangement. The second generation combination includes the flexing of the antenna which for the generalised α_1 is

$$\begin{aligned}\alpha_1(t) = {} & [y_{1'} + y_{3';2'} + y_{2';1'2'}] - [y_1 + y_{2;3} + y_{3;13}] \\ & - \big[y_1 + y_{2;3} + y_{3;13}\big]_{;3'1'2'} + [y_{1'} + y_{3';2'} + y_{2';1'2'}]_{;213} \\ & - \frac{1}{2}\big\{[z_{1'} - z_1] + [z_{1'} - z_1]_{;2133'1'2'} - [z_{2'} - z_2]_{;3} - [z_{2'} - z_2]_{;1'2'} \\ & \quad + [z_{2'} - z_2]_{;33'1'2'} + [z_{2'} - z_2]_{;1'2'213} - [z_3 - z_3]_{;2'} - [z_{3'} - z_3]_{;13} \\ & \quad + [z_{3'} - z_3]_{;2'213} + [z_{3'} - z_3]_{;133'1'2'}\big\},\end{aligned} \tag{1.19}$$

where the order of the offsets are important [20, 77]. Shaddock [59] indicates that this combination does not lead to perfect cancellation of the laser frequency noises which is also true of the generalised ζ_1 combination [70]. The level of the residual noises remains to a first order in the systematic velocities [60].

1.5.3.3 The Michelson combinations

The unequal arm Michelson observables consists of the three combinations X, Y and Z centred on spacecraft 1,2 and 3, respectively. The simple form of the X combination

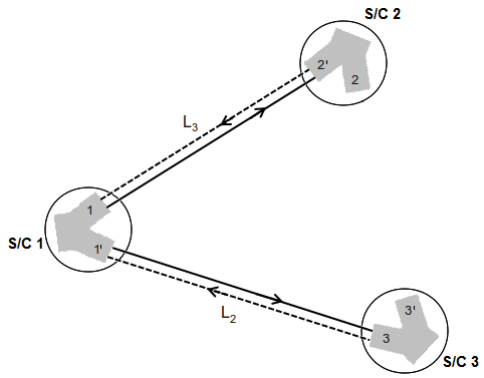

Figure 1.15: Schematic of LISA showing the spacecraft, optical benches and arms that are used in the Michelson X observable.

for static arms and no antenna motion, can be written as

$$\begin{aligned} X(t) = &\left\{\left[y_{1'}(t) + y_3(t - D_2)\right] - \left[y_1(t) + y_{2'}(t - D_3)\right]\right\} \\ &+ \left\{\left[y_1(t - 2D_2) + y_{2'}(t - D_3 - 2D_2)\right]\right. \\ &\left. - \left[y_{1'}(t - 2D_3) + y_3(t - D_2 - 2D_3)\right]\right\}, \end{aligned} \tag{1.20}$$

and the compact form is

$$X = \left\{\left[y_{1'} + y_{3,2}\right] - \left[y_1 + y_{2',3}\right]\right\} + \left\{\left[y_{1,22} + y_{2',322}\right] - \left[y_{1',33} + y_{3233}\right]\right\}.$$

The are four groups of readings consisting of sums of the contributions from the optical benches at the ends of the arms adjacent to the spacecraft 1 which can be seen in Figure 1.15. The sum in each group simulates reflection at the end of the arm. For example, the first term of the equation is the sum of the readings at the end of arm L_2 which are $y_{1'}$ of spacecraft 1 and y_3 of spacecraft 3. These can be interpreted as the transmission of a beam from optical bench $1'$ from an earlier time $(t - D_2)$ to optical bench 3 and then back to optical bench $1'$ arriving at time t. Similarly, the second term is a sum of the readings along arm L_3 so that the first line in the equation is the subtraction of the left readings from the right. This also occurs in the second line but for earlier times and with right subtracted from left. One advantage of these combinations is that they require only the four optical benches while the Sagnac combinations use all six optical bench readings. This would allow LISA to operate if some of the benches are not functional. Like the Sagnac, accounting for the spacecraft motions effects, the drag-free case, the

combination gains contributions from the intra-spacecraft readings becoming

$$X = \big\{[y_{1'} + y_{3,2}] - [y_1 + y_{2',3}]\big\} + \big\{[y_1 + y_{2',3}]_{,22} - [y_{1'} + y_{3,2}]_{,33}\big\} + \frac{1}{2}\big\{[z_1 - z_{1'}] - [z_1 - z_{1'}]_{,22} - [z_1 - z_{1'}]_{,33} + [z_1 - z_{1'}]_{,2233}\big\}, \quad (1.21)$$

where the structure of the inter-spacecraft readings remain the same. With rotation Equation 1.21 becomes

$$X = \big\{[y_{1'} + y_{3,2'}] - [y_1 + y_{2',3}]\big\} + \big\{[y_1 + y_{2',3}]_{,22'} - [y_{1'} + y_{3,2'}]_{,3'3}\big\} + \frac{1}{2}\big\{[z_1 - z_{1'}] - [z_1 - z_{1'}]_{,22'} - [z_1 - z_{1'}]_{,3'3} + [z_1 - z_{1'}]_{,22'3'3}\big\}, \quad (1.22)$$

where the only difference is that there are now primed and unprimed offsets to indicate the directional dependence of their measurement. However, like the Sagnac, the flexing of the arms does change the structure of the Michelson combinations requiring more terms with more complex offsets due to their dependence on time. The generalised X_i combinations have twice the number of terms for example, the X_1 given by Shaddock et. al. [60] is

$$\begin{aligned} X_1 = {} & \big\{[y_{1'} + y_{3;2}] - [y_1 + y_{2';3'}]\big\} + \big\{[y_1 + y_{2';3}]_{;22'} - [y_{1'} + y_{3;2'}]_{;3'3}\big\} \\ & + \big\{[y_1 + y_{2';3}]_{;3'322'} - [y_{1'} + y_{3;2'}]_{;22'3'3}\big\} + \big\{[y_{1'} + y_{3;2'}]_{;3'33;322'} - [y_1 + y_{2';3}]_{;22'22'3'3}\big\} \\ & + \frac{1}{2}\big\{[z_1 - z_{1'}] - [z_1 - z_{1'}]_{;22'} - [z_1 - z_{1'}]_{;3'3} + [z_1 - z_{1'}]_{;22'22'3'3} \\ & + [z_1 - z_{1'}]_{;3'33'322'} - [z_1 - z_{1'}]_{;22'3'33'322'}\big\}. \end{aligned} \quad (1.23)$$

The difference with the generalised Michelson combination compared with the generalised Sagnac is that it cancels laser frequency noise several orders of degrees below the secondary noises [60].

1.5.4 Time delay interferometry combinations for different signal responses

In the previous section we saw that it was possible to synthesize two different types of interferometers, the Michelson and Sagnac, illustrating how LISA can operate as these two different types of detectors simultaneously. Also, each configuration has different options depending on which spacecraft acted as the beam splitter which increases the number of detectors it can synthesize simultaneously. This offered the possibility of improving the responses to gravitational waves from combinations of the different

"detectors" that would improve the signal to noise ratio.

1.5.4.1 Improving LISA's sensitivity

Prince. et. al. [51] used this approach to produce combinations that provided optimal sensitivity which are the A, E and T. These are based on the Sagnacs and generated in the frequency domain. The equations for these are

$$\begin{aligned}
\widetilde{A}(f) &= \frac{1}{\sqrt{2}}\big[\widetilde{\gamma}(f) - \widetilde{\alpha}(f)\big], \\
\widetilde{E}(f) &= \frac{1}{\sqrt{6}}\big[\widetilde{\alpha}(f) - 2\widetilde{\beta}(f) + \widetilde{\gamma}(f)\big], \\
\widetilde{T}(f) &= \frac{1}{\sqrt{3}}\big[\widetilde{\alpha}(f) + \widetilde{\beta}(f) + \widetilde{\gamma}(f)\big],
\end{aligned} \tag{1.24}$$

where $\sim$ represents the Fourier transform and for $\tilde{A}$ this is

$$\widetilde{A}(f) = \mathcal{F}[A(t)] = \int_{-\infty}^{\infty} A(t) e^{-2\pi i f t} dt. \tag{1.25}$$

In the previous section the antenna motions destroyed the Sagnacs and their generalised counterparts contain residual laser frequency noises. This means that the AET which are linear combinations of the first generation Sagnac will also be affected by the orbital motion. Also shown was that the Michelson combinations even though their structure also changed with the flexing leading to their generalised counterparts they were still able to eliminate the laser frequency noises. This led to AET being recreated in terms of these with one set of these as used by Adams and Cornish [4] being

$$\begin{aligned}
\widetilde{A}(f) &= \frac{1}{3}\big[2\widetilde{X}(f) - \widetilde{Y}(f) - \widetilde{Z}(f)\big], \\
\widetilde{E}(f) &= \frac{1}{\sqrt{3}}\big[\widetilde{Z}(f) - \widetilde{Y}(f)\big], \\
\widetilde{T}(f) &= \frac{1}{3}\big[\widetilde{X}(f) + \widetilde{Y}(f) + \widetilde{Z}(f)\big],
\end{aligned} \tag{1.26}$$

where they have similar structure with some rearrangement in $\widetilde{A}$ and $\widetilde{E}$ except for $\widetilde{T}$ which is the sum of all three. Nayak et. al. [42] used the same approach to produce another set of observables that increased the sensitivity of LISA. These were generated in the frequency domain and also based on the Sagnac α, β and γ observables. The

combination they produced were

$$
\begin{aligned}
Y^{(1)} &= \frac{1}{6}\big[\alpha + \beta - 2\gamma\big], \\
Y^{(2)} &= \frac{1}{\sqrt{2}}\big[\beta - \alpha\big], \\
Y^{(3)} &= \frac{1}{3}\big[\alpha + \beta + \gamma\big],
\end{aligned} \tag{1.27}
$$

showing slight differences from those in Equation 1.24.

1.5.4.2 Zero signal solution

The approach was also used to produce combinations with null responses to gravitational waves which would be useful in isolating the instrumental noises and would also be helpful in separating it from the source confusion noise. The first generation ζ combination whihc has a low response offered this opportunity but does not survive LISA's orbital motion. Cornish and Hellings [20] produced a $\Delta\zeta$ combination that had the same properties when accounting for the rotational motion but it did not survive the flexing of the antenna.

One combination that achieves this is the zero-signal solution η with the ability to identify a signal's location using only two of its parameters which is independent of assumptions about the signal waveform. It is an improvement on the ζ combination in terms of its ability to discriminate gravitational wave background noise from instrumental noise [72, 71]. This combination was also generated in the frequency domain using the first generation Sagnac and is given by

$$
\begin{aligned}
\widetilde{\eta}(f) \equiv & \big[\beta_+(f,\theta,\phi)\gamma_\times(f,\theta,\phi) - \beta_\times(f,\theta,\phi)\gamma_+(f,\theta,\phi)\big]\widetilde{\alpha}(f), \\
& + \big[\gamma_+(f,\theta,\phi)\alpha_\times(f,\theta,\phi) - \gamma_\times(f,\theta,\phi)\alpha_+(f,\theta,\phi)\big]\widetilde{\beta}(f), \\
& + \big[\alpha_+(f,\theta,\phi)\beta_\times(f,\theta,\phi) - \alpha_\times(f,\theta,\phi)\beta_+(f,\theta,\phi)\big]\widetilde{\gamma}(f),
\end{aligned} \tag{1.28}
$$

where θ and ϕ are the two parameters describing the sources location. The $+$ and $\times$ terms in the brackets represent the antenna pattern functions of α, β and γ for the plus and cross polarisations, respectively. Being formulated using the Sagnac they will be sensitive to the orbital motions but this could possibly be handled in the same way as the optimal TDIs by using the Michelson-type combinations.

1.5.5 Computational approaches for time delay interferometry

Manually generating the time delay interferometry combinations is slow and inefficient giving only a small set of possible combinations. The next obvious step is a computer-based generation of these observables and two methods were presented for this which are the algebraic approach introduced by Dhurandhar, Nayak and Vinet [24] and the geometric approach by Vallisneri [77]. An overview of their methods and how they adapt to the motions of LISA is presented this section.

1.5.5.1 Algebraic time delay interferometry

The algebraic approach is based on computational commutative algebra and provides a mathematical foundation for the time delay interferometry [24, 43, 44, 68]. Starting with the first generation assumption of a stationary static LISA array where all motion effects are ignored, recall that the laser frequency noises contributions to the inter-spacecraft measurements can be written as

$$y_i(t) = C_j(t - D_k) - C_i(t), \tag{1.29}$$

where $D_k = L_i/c$ represent the light travel time, offset, in arm k with length L_k. c is the speed of light. Their approach was to focus on the delays in the three arms of the antenna and form a polynomial with them. This is done by first replacing the shifted time $(t - D_k)$ with a shift operator E_k given by

$$E_k f(t) = f(t - D_k). \tag{1.30}$$

Using this notation and ignoring the time component Equation 1.29 becomes

$$y_i = E_k C_j - C_i. \tag{1.31}$$

They grouped the six optical bench readings into two sets of readings of U^i and V^i that represent those in each arm for the clockwise and counter-clockwise directions, respectively. Here i represents the number of the recording optical bench. For example, for spacecraft 1, the optical bench readings and corresponding U and V representations are

$$\begin{aligned} y_1 &= E_3 C_2 - C_1, \qquad & V^1 &= C_1 - E_3 C_2, \\ y_{1'} &= E_2 C_3 - C_1, \qquad & U^1 &= E_2 C_3 - C_1, \end{aligned} \tag{1.32}$$

where the counter-clockwise reading is the negative of the y_1 that is, $V^1 = -y_1$. The other four combinations are

$$\begin{aligned} U^2 &= E_3C_1 - C_2, \qquad U^3 = E_1C_2 - C_3, \\ V^2 &= C_2 - E_1C_3, \qquad V^3 = C_3 - E_2C_1. \end{aligned} \tag{1.33}$$

Their aim was to find linear combinations of these with appropriate offsets applied to each U^i and V^i that will lead to cancellation of the laser noise. The total delay, the number of offsets to apply to t, would be a linear combination of the offsets D_i which they expressed as $k_1D_1 + k_2D_2 + k_3D_3$ where k_i is an integer applied to the corresponding offset D_i. Using their shift notation this is $E_1^{k_1}E_2^{k_2}E_3^{k_3}$ which, for the static arms assumption, is a polynomial in the three variables (E_1, E_2, E_3). Using p_i and q_i to represent the polynomials associated with V^i and U^i, respectively, they rephrased the problem of laser frequency noise cancellation as finding linear combinations of these that will sum to zero which they gave as

$$\sum_{i=1}^{3} \Big[p_iV^i + q_iU^i \Big] = 0. \tag{1.34}$$

This provided a mathematical formulation of the laser frequency noise cancellation problem. In order to obtain a complete set of solutions they avoided those that would lead to higher order polynomials and aimed for a simpler set that formed what they termed "the first module of syzygies". They also pointed out that to satisfy Equation 1.34 all the coefficients of the laser frequency noises must cancel independently resulting in a set of only three equations to be solved which they gave as

$$\begin{aligned} p_1 - q_1 + E_{12}q_2 - E_{13}p_3 &= 0, \\ p_2 - q_2 + E_{23}q_3 - E_{21}p_1 &= 0, \\ p_3 - q_3 + E_{31}q_1 - E_{32}p_2 &= 0. \end{aligned} \tag{1.35}$$

They obtained a set of six independent generators d^I which are those in the second column of Table 1.1 [43] that can produce a complete set of solutions to Equation 1.34. The elements for the noise canceling combinations or modules are linear combinations of these set of generators [43, 44] which can be obtained from

$$X = \sum_{I=1}^{6} \alpha_{(I)} d^I, \tag{1.36}$$

where $\alpha_{(I)}$ are polynomial coefficients in E_i. These generators provide the coefficients

Table 1.1: The generators for the TDI variables (noise canceling modules) using the algebraic approach. The coefficients p and q are associated with the long arm data stream which include laser phase noise and signal. E_i is a delay operator representing time offset in the arm i [43].

Generator	Coefficients	
	$p_1, p_2, p_3, q_1, q_2, q_3$	r_1, r_2, r_3
d^1	$E_3(1-E_{3'}E_2)$, $(E_1E_3-E_{3'})$, $(1-E_{3'}E_2)$, 0, 0, $(1-E_1E_3E_2)$	$E_3(E_{3'}E_2-1)$, $E_1E_3(E_{3'}E_2-1)$, $(E_{3'}E_2-1)$
d^2	$E_{3'}(1-E_3E_{1'})$, 0, $(E_1-E_{1'}E_{3'})$, $(E_{3'}-E_1E_3)$, 0, $E_1(1-E_3E_{1'})$	$E_{3'}(E_3E_{1'}-1)$, $E_1E_{3'}(E_3E_{1'}-1)$, $E_1(E_3E_{1'}-1)$
d^3	0, $(1-E_{1'}E_3)$, $(E_2-E_{2'}E_{1'})$, $(E_{2'}-E_3E_2)$, $(1-E_3E_{1'})$, 0	$E_{2'}(E_3E_{1'}-1)$, $(E_3E_{1'}-1)$, $E_2(E_3E_{1'}-1)$
d^4	$(E_{2'}-E_3E_2)$, $(E_{2'}E_1-1)$, $E_2(E_1E_{2'}-1)$, 0, $(E_1E_3E_2-1)$, 0	$E_3E_2E_1(1-E_{2'}E_1)$, $(1-E_{2'}E_1)$ $E_2(1-E_{2'}E_1$
d^5	$(E_{3'}E_2-1)$, $(E_{1'}E_{3'}-E_1)$, 0, $(E_{3'}E_2-1)$, 0, $(E_1E_2-E_{1'})$	$(1-E_{3'}E_2)$, $E_1(1-E_{3'}E_2)$, $E_{1'}(1-E_{3'}E_2)$
d^6	$(E_3-E_{2'}E_{3'})$, 0, $(1-E_{2'}E_1)$, 0, $(E_{3'}-E_1E_3)$, $(1-E_{2'}E_1)$	$E_3(E_{2'}E_1-1)$, $E_{3'}(E_{2'}E_1-1)$, $(E_{2'}E_1-1)$

for p_i and q_i in Equation 1.34. Using this method the coefficients needed to obtain the Sagnac α, ζ and Michelson Z combinations with no motion effects given in their first paper [24] are

$$\begin{aligned}
\alpha &= X^3 = (1,\ E_3,\ E_1E_3,\ 1,\ E_1E_2,\ E_2),\\
\zeta &= X^2 = (E_1,\ E_2,\ E_3,\ E_1,\ E_2,\ E_3),\\
Z &= X^1 = (E_1E_3 - E_2,\ 0,\ E_3^2 - 1,\ 0,\ E_1E_2 - E_1,\ E_3^2 - 1).
\end{aligned} \tag{1.37}$$

These are the offsets to apply to the U^i and V^i terms in Equation 1.34. Using the Sagnac ζ as an example, to derive the traditional expression insert the corresponding coefficients from Equation 1.37 into Equation 1.34 which gives

$$\zeta = E_1V^1 + E_2V^2 + E_3V^3 + E_1U^1 + E_2U^2 + E_3U^3. \tag{1.38}$$

Next the U^i and V^i terms are replaced with their corresponding optical bench readings $y_i(t)$ giving

$$\zeta = -E_1y_1(t) - E_2y_2(t) - E_3y_3(t) + E_1y_{1'}(t) + E_2y_{2'}(t) + E_3y_{3'}(t). \tag{1.39}$$

The shift operator E_i is expanded to give

$$\begin{aligned}
\zeta = &[y_{1'}(t-D_1) + y_{3'}(t-D_3) + y_{2'}(t-D_2)]\\
&- [y_1(t-D_1) + y_2(t-D_2) + y_3(t-D_3)],
\end{aligned} \tag{1.40}$$

which is the equation for the Sagnac ζ combination.

The algebraic approach survived the optical bench and orbital motion effects. Like the conventional Michelson the directional dependence of the arm lengths that occurs with the orbital motion is incorporated into the shift operator E_i. They used the double notation ij for this but here this is replaced with the prime notation i' to indicate the

counterclockwise direction. They introduced three more offsets to account for this which increased the size of the polynomial to six variables $(E_1, E_{1'}, E_2, E_{2'}, E_3, E_{3'})$. They adjusted the expressions for U and V to include the motion and added an extra term Z^i for the internal readings z between the optical benches on a spacecraft which were needed to the noise cancellation. This gave a new set of nine equations which are

$$\begin{aligned} U^1 &= E_{2'}\widetilde{C}_3 - \widetilde{C}_{1'}, \qquad U^2 = E_{3'}\widetilde{C}_1 - \widetilde{C}_{2'}, \qquad U^3 = E_{1'}\widetilde{C}_2 - \widetilde{C}_{3'}, \\ V^1 &= \widetilde{C}_1 - E_3\widetilde{C}_2, \qquad V^2 = \widetilde{C}_2 - E_1\widetilde{C}_3, \qquad V^3 = \widetilde{C}_3 - E_2\widetilde{C}_1, \\ Z^1 &\equiv \widetilde{C}_1 - \widetilde{C}_{1'}, \qquad Z^2 \equiv \widetilde{C}_2 - \widetilde{C}_{2'}, \qquad Z^3 \equiv \widetilde{C}_3 - \widetilde{C}_{3'}, \end{aligned} \tag{1.41}$$

where $\widetilde{C}_i$ is the combination of the optical bench motions Δ_i and the laser noises. For example, for the noises in spacecraft 1 this is

$$\widetilde{C}_1 = C_1 - \vec{\Delta}_1, \qquad \widetilde{C}_{1'} = C_{1'} + \vec{\Delta}_{1'}. \tag{1.42}$$

The intra-spacecraft readings and corresponding Z_i for spacecraft 1 are

$$z_1 = C_1 - C_{1'} + \eta_1 - 2\vec{\Delta}_1, \qquad z_{1'} = C_{1'} - C_1 + \eta_1 + 2\vec{\Delta}_{1'}, \tag{1.43}$$

where Z is given by

$$Z^1 = \frac{1}{2}(z_1 - z_{1'}) \equiv \widetilde{C}_1 - \widetilde{C}_{1'}. \tag{1.44}$$

The new equation to solved for obtaining laser frequency noise cancellation was

$$\sum_{i=1}^{3} \Big[p_i V^i + q_i U^i + r_i Z^i \Big] = 0, \tag{1.45}$$

where r_i is the polynomial associated with Z_i. The conditions for the noise cancellation now involves six equations which are

$$\begin{aligned} p_1 + E_{12}q_2 + r_1 &= 0, \qquad E_{13}p_3 + q_1 + r_1 = 0, \\ p_2 + E_{23}q_3 + r_2 &= 0, \qquad E_{21}p_1 + q_2 + r_2 = 0, \\ p_3 + E_{31}q_1 + r_3 &= 0, \qquad E_{32}p_2 + q_3 + r_3 = 0,. \end{aligned} \tag{1.46}$$

The number of generators was the same but the number of coefficients now included extra terms for r given in column three of Table 1.2 and the set of generators became $d^I(p_i, q_i, r_i)$. The noise canceling combinations are obtained by using Equation 1.36 as shown previously.

This method depends on forming polynomials with the offsets in each arm and with

Table 1.2: The coefficients for the Sagnac α and ζ and Michelson X adjusted for optical bench and orbital motions [43].

TDI	Coefficients $[p_1, p_2, p_3, q_1, q_2, q_3, r_1, r_2, r_3]$
α_1	$[(1 - E_{3'}E_{2'}E_{1'}),\ E_3(1 - E_{3'}E_{2'}E_{1'}),\ E_3(E_1(1 - E_{3'}E_{2'}E_{1'}),\ (1 - E_3E_2E_1),\ E_{2'}E_{1'}(1 - E_3E_2E_1),\ E_{2'}(1 - E_3E_2E_1),$ $E_{3'}E_3E_2E_{2'}E_{1'}E_1 - 1,\ E_3(E_{3'}E_{2'}E_{1'} - 1) + E_{2'}E_{1'}(E_3E_2E_1 - 1),\ E_{2'}(E_3E_2E_1 - 1) + E_3E_1(E_{3'}E_{2'}E_{1'} - 1)]$
ζ_1	$[E_{1'}(E_{3'}E_{2'} - E_1),\ E_{2'}(E_3E_2 - E_{1'}),\ E_3(E_{3'}E_{2'} - E_1),\ E_{1'}(E_3E_2 - E_{1'}),\ E_{2'}(E_3E_2 - E_{1'}),\ E_3(E_{3'}E_{2'} - E_1),$ $(E_{1'}E_1 - E_{3'}E_3E_2E_{2'}),\ E_{2'}(E_{1'} - E_3E_2) + E_3E_{1'}(E_1 - E_{3'}E_{2'}),\ E_3(E_1 - E_{3'}E_{2'}) + E_{2'}E_1(E_{1'} - E_3E_2)]$
X	$[(1 - E_3E_{1'}),\ 0,\ E_{1'}(E_{2'}E_1 - 1),\ (1 - E_{2'}E_1),\ E_1(E_3E_{1'} - 1),\ 0,\ (E_2E_{2'} - 1)(1 - E_{3'}E_2),\ 0,\ 0]$

the simple static array this results in three values and with rotation this requires six. The flexing introduces a time dependency and hence the possible values for these offsets are no longer a fixed number. So forming polynomials of these is no longer a simple matter and hence it does not easily adapt to that case [77, 68].

1.5.5.2 Geometric time delay interferometry

This method was presented by Vallisneri [77] and is based on a physical interpretation of the time delay interferometry observables as synthesized interferometric measurements. He arranged the laser noise cancellation at a bench for a particular time t into four basic groups based on the beams arrival and departure at the optical benches. He gave three possible types of combinations for the two beams consisting of both simultaneously arriving at a bench, both simultaneously departing from a bench, and one arriving and one departing simultaneously as illustrated in Figure 1.16a. He indicated the direction of the measurements using arrows with the arrowhead terminating where they are taken. At points where the same parts of the arrows met, that is, two tails or two heads, the measurements are subtracted and for a combination of a head and a tail the measurements are added. According to Vallisneri, laser frequency noise cancellation is obtained by forming a closed loop of these measurements. This was formed by lining up the arrows which represent the fractional frequency measurements y as head-to-head, tail-to-tail or head-to-tail. Figure 1.16b gives his illustration one the Michelson time delay interferometry combination using this method. These loops were enumerated combinatorially using an exhaustive search and he pointed out that the generation of the combinations with 24 links took 10^4 CPU hours [77]. The shortest combinations that he obtained for a real LISA model had 16 link terms. He listed all the second generation TDI combinations with 16 links which contained types resembling the Michelson (X),

Beacon (P), Monitor (E), and Relay (U) observables. One example of the Michelson X-type observables is

$$\begin{aligned} X_1 = {} & y_{132;322'22'3'3} + y_{231;22'22'3'3} + y_{123;2'22'3'3} + y_{321;22'3'3} + y_{123;2'3'3} + y_{321;3'3} \\ & + y_{132;3} + y_{231} - y_{32'1} - y_{123;2'} - y_{231;22'} - y_{132;322'} - y_{231;3'322'} - y_{132;33'322'} \\ & - y_{321;3'33'22'} - y_{123;2'3'33'322'}, \end{aligned} \tag{1.47}$$

where y_{ijk} is called a link and it indicates a reading taken in the direction from i to j to k as recorded by optical bench k over arm j. Transforming this to the match the structure of the Michelson previously used this becomes

$$\begin{aligned} X_1 = {} & \left\{[y_1 + y_{2';3}] - [y_{1'} + y_{3;2'}]\right\} + \left\{[y_{1'} + y_{3;2'}]_{;3'3} - [y_1 + y_{2';3}]_{;22'}\right\} \\ & + \left\{[y_{1'} + y_{3;2'}]_{;22'3'3} - [y_1 + y_{2';3}]_{;3'322'}\right\} \\ & + \left\{[y_1 + y_{2';3}]_{;22'22'3'3} - [y_{1'} + y_{3;2'}]_{;3'33'322'}\right\}. \end{aligned} \tag{1.48}$$

This approach is similar to the conventional method of generating the time delay interferometry observables in that it finds ways of combining the measurements based on their structure that leads to laser frequency noise cancellation. The conventional approach is done manually and uses instinct to determine how to combine them to obtain the laser noise cancellation. The geometric method replaced instinct with a set of rules for combining the basic measurements that became the basis for a computer-based search for the required combinations. So it can be thought of as a computerisation of the conventional approach using a set of rules instead of instinct. The geometric method, unlike the others, had no problems with accounting for the real motions of LISA as this was one of its goals. The other goal was to produce all possible laser noise canceling combinations.

1.5.6 Summary

This section dealt with the two main problems affecting LISA's data which are the overwhelming size of its laser frequency noises and the very large number of overlapping sources. The source confusion problem was dealt with by the Mock LISA Data Challenges (MLDC) while the laser frequency noises were handled by the time delay interferometry observables which are linear combinations of LISA's raw data that result in their cancellation. The original time delay interferometry observables were manually

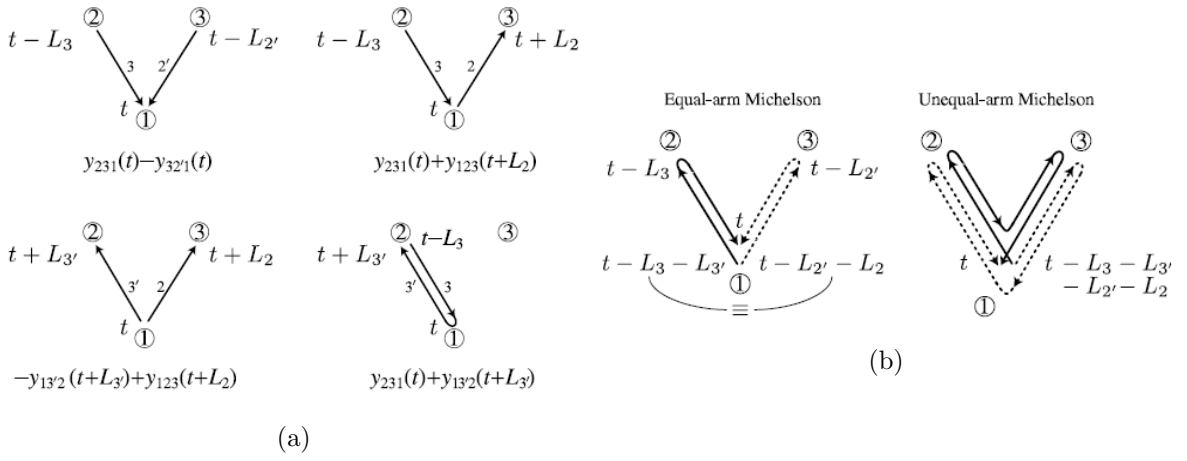

Figure 1.16: The geometric TDI approach of Vallisneri. (a) Illustrates the four different possible ways of canceling the laser phase noise at time t. (b) Illustrates now the method reproduces the cancellation in Michelson TDI observable. Reproduced from Vallisneri [77]

generated and based purely on instinct resulting in a small number of the possible combinations. This was improved on by the computer-based solutions using the algebraic and geometric approaches to the problem. The algebraic approach formulated the problem as a polynomial consisting of the delays in the arms which was viable for static case producing, at most, six variables. However, it did not adapted easily to time varying arm lengths. The geometric approach could be thought of as a computerisation of the manual process in the sense that it obtains the laser noise cancellation by searching for ways of combining the raw data using a set of rules to guide the search instead of instinct. Unlike the algebraic approach, it could produce the required observables even for time varying arm lengths which was one of its goals.

1.6 Simplifying LISA data analysis

The solutions given in the previous section showed that LISA, regardless of these crippling problems, was still a viable project. However, this led to a divide-and-conquer approach which may not be necessary for doing LISA data analysis and the computerisation of the generation of the time delay interferometry observables pointed to the possibility of linking the two techniques. This could lead to not only a simpler analysis process but may also provide a more efficient method of obtaining astronomy from the raw data with its numerous sources and overwhelming laser phase noises.

Recall that the reason these observables was that they are necessary in order to

provide the required sensitivity for obtaining useful information from LISA data [24]. However, explicitly generating these observables may not be the only way to meet this criterion. In trying to find a better approach a question to ask is whether there is another way of doing the analysis without having to create these observables. In other words, is there a process that would transform the raw data which are overwhelmed with laser frequency noise to forms that are free from these noises? Romano and Woan [54] presented such an approach which is based on eigendecomposition and principal components.

1.6.1 Data transformation using eigenvectors

Consider data generated from two variables x and y that have a linear relationship as shown in Figure 1.17a. This data can be transformed to a new basis that results in no correlations as shown in the Figure 1.17b. This kind of transformation re-expresses the data in terms of axes that are aligned with the spread of the values in the plots [61, 37]. In the figure the large spread in the values is indicated by the arrow labeled $v1$ with arrow $v2$ indicating a smaller spread in a direction that is perpendicular to $v1$ which is assumed to be due to measurement noise [61, 37]. This spread of the values for each variable about a mean value can be expressed with a single value called the variance which can be determined from

$$\mathrm{var}(x) = \frac{1}{N}\sum_{i=1}^{N}(x_i - \mu_x)^2, \qquad \mathrm{var}(y) = \frac{1}{N}\sum_{i=1}^{N}(y_i - \mu_y)^2, \tag{1.49}$$

where μ_x and μ_y are the means of x and y, respectively. The linear relationship between the two variables can also be described by a single value called the covariance which can be obtained from

$$\mathrm{cov}(x, y) = \mathrm{cov}(y, x) \;=\; \frac{1}{N}\sum_{i=1}^{N}(x_i - \mu_x)(y_i - \mu_y). \tag{1.50}$$

These values can be conveniently expressed in a 2×2 covariance matrix, $C_{xy}(\tau)$, which can be written as

$$C_{xy}(0) = \begin{bmatrix} \mathrm{var}(x) & \mathrm{cov}(x, y) \\ \mathrm{cov}(x, y) & \mathrm{var}(y) \end{bmatrix}. \tag{1.51}$$

τ is a lag term indicating how the covariances are measured which is zero in this matrix. This assumes that the only non-zero covariances that exists between these variables are

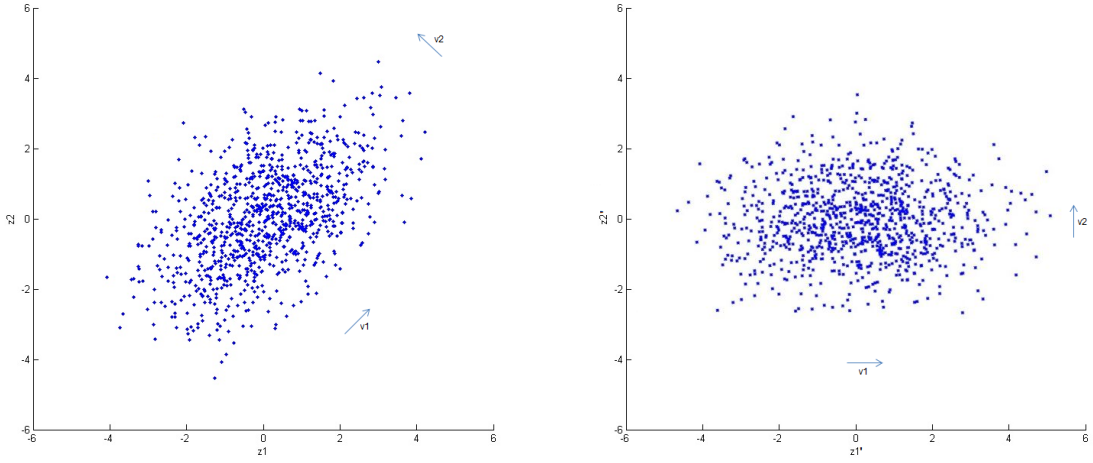

(a) (b)

Figure 1.17: Scatter plot showing correlated (a) and uncorrelated (b) data. The arrows v1 and v2 indicate the directions of the large and small variances respectively in directions that are perpendicular to each other.

when they are aligned exactly that is, it is a comparison between $x_1...x_n$ and $y_1...y_n$. This will be explained in more detail in Chapter 3. It turns out that a certain type of decomposition of the covariance matrix results in a set of vectors that align with the variances in the data. These are known as eigenvectors and the number of these is equal to the size of the matrix. Since the eigenvectors are aligned with the variances in the data their magnitudes, known as eigenvalues, express the variances in the data. The data can be transformed to the new basis through the eigenvectors [61, 37].

1.6.2 Principal component analysis

The fact that the magnitudes of the eigenvalues are related to the variances in the data allows them to be used to determined which of the variables provides important information. Principal component analysis sorts these eigenvalues in descending order of their magnitudes and applies a rank according to the order in which they occur. The largest eigenvalue, associated with the largest variance, is the first principal component and so on. A subset of these principal components can be used to define the data [37].

So the question is whether the eigenvectors can be used to transform the raw data that is overwhelmed with laser phase noise to ones that do not contain the noise. In the data analysis process it is the noise in the LISA's raw data that are used in the statistical inference. The total noise is a combination of correlated and uncorrelated

instrumental noises. The raw data, because they are the outcome of the beating of the lasers of the two optical benches at the end of each arm, will contain common laser frequency noises which will result in correlations occurring between the different data. The number and type of correlations will depend on whether the lasers are allowed to operate independently or phase locked in order to simulate splitting and reflection. The independent noises are those associated with the photodetectors which will be the limiting noises of the antenna. The covariance matrix of the raw data will capture these correlations. The correlations between the laser noises exist at different time offsets so that the covariance matrix will have to account for correlations occurring between the different times of the data. The size of the matrix will reflect the size of the data and so will the number eigenvalues and eigenvectors. After the transformation to the new basis, the data will reflect the characteristic of the eigenvalues with largest containing laser frequency noises while the smallest expected to only contain the photodetector noise.

1.6.3 Principal component example for LISA data - toy model

The technique will be illustrated using the simple model of LISA used in Romano and Woan [54] and will use phase shifts measurements as used in that paper. In their toy example each optical bench data consisted of a common laser phase noise term p, an independent photodetector noise term n_i and a gravitational wave signal h_i. The readings for two photodetectors s_1 and s_2 can be written as

$$s_1(t) = p(t) + n_1(t) + h_1(t), \qquad s_2(t) = p(t) + n_2(t) + h_2(t). \tag{1.52}$$

Rearranging these in terms of the instrumental noises gives

$$s_1 - h_1 = p + n_1, \qquad s_2 - h_2 = p + n_2, \tag{1.53}$$

where the times have been ignored since all terms have the same value. With this simple model the correlations in the data are due to the same noise occurring in the two readings existing at the same time t requiring only the zero lag covariances giving a 2×2 covariance matrix. Assuming that the laser frequency noises have zero means and variances σ_p^2 and that the independent photodetector noises also all have zero means but with variances of σ_n^2, then the variances and cross-covariance of the two photodetector

readings are

$$\begin{aligned}
\mathrm{var}(s_1) &= \langle (p+n_1)(p+n_1) \rangle &&= \langle p^2 \rangle + \langle n_1^2 \rangle = \sigma_p^2 + \sigma_n^2, \\
\mathrm{var}(s_2) &= \langle (p+n_2)(p+n_2) \rangle &&= \langle p^2 \rangle + \langle n_2^2 \rangle = \sigma_p^2 + \sigma_n^2, \\
\mathrm{cov}(s_1, s_2) &= \langle (p+n_1)(p+n_2) \rangle &&= \langle p^2 \rangle \qquad\quad = \quad \sigma_p^2,
\end{aligned} \tag{1.54}$$

and the covariance matrix is

$$C = \begin{bmatrix} \sigma_p^2 + \sigma_n^2 & \sigma_p^2 \\ \sigma_p^2 & \sigma_p^2 + \sigma_n^2 \end{bmatrix}. \tag{1.55}$$

The eigenvalues for this matrix are easy to compute which will be illustrated in Chapter 4. Here, only the values will be given which are $2\sigma_p^2+\sigma_n^2$ and σ_n^2. The eigendecomposition of the covariance matrix will transformed it into another matrix C' with these two values occurring the main diagonal giving

$$C' = \begin{bmatrix} 2\sigma_p^2 + \sigma_n^2 & 0 \\ 0 & \sigma_n^2 \end{bmatrix}. \tag{1.56}$$

The absence of off diagonal terms indicates that there will no longer be any correlations between the two sets of data when they are expressed in the new basis defined by the eigenvectors. The eigenvectors for these eigenvalues are $(1, 1)$ and $(1, -1)$. The method for generating these will also be shown in Chapter 4. The correlated data are transformed to the new basis using a matrix of these eigenvectors by

$$\begin{aligned}
\begin{bmatrix} 1 & 1 \\ 1 & -1 \end{bmatrix} \begin{bmatrix} s_1 - h_1 \\ s_2 - h_2 \end{bmatrix} &= \begin{bmatrix} (s_1 - h_1 + s_2 - h_2) \\ (s_1 - h_1 + s_2 - h_2) \end{bmatrix} \\
&= \begin{bmatrix} (s_1 + s_2) - (h_1 + h_2) \\ (s_1 - s_2) - (h_1 - h_2) \end{bmatrix}.
\end{aligned} \tag{1.57}$$

To see the effects of the transformation on the noises in the data substituting for s_1 and s_2 using Equation 1.52 gives

$$\begin{aligned}
s_1 + s_2 &= p + n_1 + h_1 + p + n_2 + h_2 \\
&= 2p + (n_1 + n_2) + (h_1 + h_2), \\
s_1 - s_2 &= p + n_1 + h_1 - p - n_2 - h_2 \\
&= (n_1 - n_2) + (h_1 - h_2),
\end{aligned} \tag{1.58}$$

where the transformed data have different noise contributions. The one that is required is $s_1 - s_2$ which does not contain any laser frequency noise. Recall that the time delay

interferometry observables are linear combinations of the raw data that lead to the cancellation of laser phase noises. In this example the difference of the two readings $(s_1 - s_2)$ does exactly that and is therefore a simple time delay interferometry observable. So that the principal component approach can be used to generate these observables. The difference between this and the other computer-based approach is that the time delay interferometer observables are generated from the data using the data covariance matrix. The eigendecomposition of this matrix produces the eigenvectors needed for transforming the data into those that lead to the cancellation of the laser frequency noises.

This technique should be able to handle real LISA data since it uses the data and its covariance matrix which will also incorporate the real behaviour of LISA. The covariance matrix will be generated algebraically and its computation is based on knowledge of the arm lengths which is also true for the conventional time delay interferometry observables [77, 78]. The other contributions to the covariance matrix are the instrumental noise variances. These will not be available during the measurements and will be based on assumptions made about the noises.

The technique simplifies the data analysis by using the eigendecomposition of the data covariance matrix in order to obtain the data with the required sensitivity. A potential limitation will be the ease of computing the eigenpairs (eigenvalue with its eigenvector). The more realistic inter-spacecraft readings for LISA will contain two sets of laser frequency noises at different times which can be written as

$$s_i(t) = p_j[t - D_k] - p_i(t) + n_i(t), \tag{1.59}$$

leading to correlations between the noises at different times requiring a covariance matrix that will account for the cross-correlations between the different times and hence will no longer be a simple 2×2 matrix but one that is the size of the data. The effects of the size of the matrix on the computation times using algebraic and numeric methods will investigated in Chapter 6.

The whole point of LISA is to obtain information about gravitational wave sources in its data which is obtained through statistical inference based on the instrumental noises in its data [54]. With the conventional time delay observables this is done on the previously generated observables. The fact that the principal component approach directly

acts on the data means that the "generation" of these observables can be incorporated into the inference which will be illustrated in the next section.

1.6.3.1 Using the principal components in the data analysis

The framework used for the inference in Romano and Woan [54] is Bayesian and in this framework parameters can be assigned probabilities. This will be explained in Chapter 5. The uncertainty in the estimates of the parameters a is obtained from the posterior probability which is defined by Bayes' theorem as

$$p(a|d,M)=\frac{p(a|M)\ p(d|a,M)}{p(d|M)}, \tag{1.60}$$

where d is the data, M is the signal model and $p(a|M)$, $p(d|a,M)$ and $p(d|M)$ are the prior, likelihood and evidence, respectively. For parameter estimation the evidence (the denominator) will be a constant since it is computed for all the values of the parameters using the same model and data. Its effect will be to normalise the posterior probability therefore, it can be ignored. The prior describes the distribution of the values of the parameters. If we assume equal probabilities for all values for the parameters by using a uniform prior then this will also be a constant which can be ignored. With these assumptions Equation 1.60 can be simplified to a proportionality between the posterior probability and the likelihood that is

$$p(a|d,M) \propto p(d|a,M). \tag{1.61}$$

The data appear in the likelihood as noise. If the laser phase noise and the photodetector noises are assumed to be Gaussian which is completely defined by the covariance matrix, then the likelihood function for the noises in the two detectors s_1 and s_2 can be defined as

$$p(\mathbf{s}-\mathbf{h}) = \frac{1}{(2\pi)^{N/2}|C|^{1/2}}\ \exp\Big(-\frac{1}{2}[\mathbf{s}-\mathbf{h}]^T C^{-1}[\mathbf{s}-\mathbf{h}]\Big), \tag{1.62}$$

where $|C|$ is the determinant of the matrix and is a constant. The covariance matrix occurs in the exponential term along with the data as

$$Q = [\mathbf{s}-\mathbf{h}]^T C^{-1}[\mathbf{s}-\mathbf{h}], \tag{1.63}$$

which is where the principal components will enter inference. The eigendecomposition of the covariance matrix used by the principal component approach can be written as

$$CV = V\Lambda, \tag{1.64}$$

where Λ is a diagonal matrix containing the eigenvalues and V is the corresponding matrix of eigenvectors. Rearranging this equation to obtain C gives

$$C = V\Lambda V^{-1}, \tag{1.65}$$

and its inverse is

$$C^{-1} = V^{-1}\Lambda V. \tag{1.66}$$

Inserting this into the Equation 1.63 gives

$$Q = [\mathbf{s} - \mathbf{h}]^T V^{-1}\Lambda V[\mathbf{s} - \mathbf{h}], \tag{1.67}$$

where the product of the eigenvector and the data occurs as $V[\mathbf{s} - \mathbf{h}]$ which is the basis transformation shown in Equation 1.57 that produced the laser noise free data.

Another point to note is that the inverse transforms the principal components. The large values will now become the small. For example, with the noise variances given by $\sigma_p^2 = 100$ and $\sigma_n^2 = 1$ the inverse becomes

$$C^{-1} = \begin{bmatrix} \frac{1}{201} & 0 \\ 0 & \frac{1}{1} \end{bmatrix} = \begin{bmatrix} 0.005 & 0 \\ 0 & 1 \end{bmatrix}. \tag{1.68}$$

The effect on the data is

$$\begin{aligned} &\begin{bmatrix} (s_1 + s_2) - (h_1 + h_2) \\ (s_1 - s_2) - (h_1 - h_2) \end{bmatrix}^T \begin{bmatrix} 0.005 & 0 \\ 0 & 1 \end{bmatrix} \begin{bmatrix} (s_1 + s_2) - (h_1 + h_2) \\ (s_1 - s_2) - (h_1 - h_2) \end{bmatrix} \\ &\qquad = 0.005\big[(s_1 + s_2) - (h_1 + h_2)\big]^2 + \big[(s_1 - s_2) - (h_1 - h_2)\big]^2 \\ &\qquad = 0.005\big[(2p + (n_1 + n_2)\big]^2 + \big[n_1 - n_2\big]^2, \end{aligned} \tag{1.69}$$

which diminishes the contributions from the terms containing the laser noise. The greater the separation between the variances of the two types of noises the smaller will be the contribution from this term. The laser frequency noise is expected to be 10^7 times greater than the detector noise which will result in even smaller values for these in the inverse.

1.6.3.2 Eigendecomposition in the frequency domain

As mentioned previously, the simple model only had common noises at the current time $p(t)$ which resulted in a simple 2×2 covariance matrix. LISA's raw data includes laser noises from two different sources with two different times t and $t - D_i$. This changes the covariance matrix which now has to include the covariances occurring at different times because of the time offset and is reflected by including a lag term τ. The covariance matrix $C(\tau)$ will now depend on the size of the data and the number of eigenvalues will reflect this. So even for a day's data sampled at 1 Hz the number of eigenvalues for the six optical benches will be $\approx 5 \times 10^5$ requiring the decomposition of a very large covariance matrix.

There are methods for generating the eigenvalues that take advantage of the structure of the covariance matrix. For the simple model the structure of the matrix in the time can be defined as a symmetric block banded Toeplitz matrix. In the simplest case this matrix contains sub- and super-diagonals separated from the main by an offset related to the time delay in the data. The separation of the outermost diagonal is defined by the bandwidth. Trench [74, 73] presented a method for generating the eigenvalues that is based on this bandwidth instead of the size of the matrix which could be useful for the time domain covariance matrix.

The frequency domain offers the potential to simplify this as, for the toy model, there are no correlations between frequencies producing a covariance matrix with values occurring in blocks along the main diagonal. The size of the blocks reflect the number of optical benches and for the simple two detector model will be 2. The eigendecomposition of a block diagonal matrix is equal to the eigendecomposition of the individual blocks and so is the inverse. How trivial this is depends on the size of the blocks. For LISA this will reflect the number of optical benches and will therefore be 6×6. This offers the potential to simplify the process by changing it to a block-wise decomposition of smaller matrices. This partitioning of the decomposition also allows the possibility for parallel computation of the eigenpairs.

1.6.4 The scope of this thesis

Romano and Woan [54] applied the method to a simple model for LISA assuming unequal but fixed arm lengths and times were restricted to integer values. The noises were assumed to be stationary with each type having the same values for the variances of σ_p^2 for the laser and σ_n^2 for the photodetector noises. They used a small covariance matrix with only five values for the times from which they obtained nine degenerate eigenvalues that were free from laser phase noise. The degeneracy was due to the equality of the photodetector noise variances. Using a few of the eigenvectors associated with these eigenvalues they were able to generate one Sagnac combination which hinted at a possible link between the eigenvectors and time delay interferometry combinations. In this thesis we not only prove this connection but also that the two approaches to LISA data analysis are equivalent in that they provide the same outcome in terms of the data sensitivity and results for the signal extraction.

1.6.5 Outline

In all the literature about the conventional time delay interferometry observables, because they were manually generated, they are just listed. To our knowledge there are no illustrations of the process of deriving them or explanations of how they work, therefore, we begin by doing this in Chapter 2 using the Sagnac and Michelson time delay interferometry combinations. The effects of LISA's orbital motion on the generation of the time delay interferometry observables is also included to illustrated why the Sagnacs fail to cancel the laser phase noises while the Michelson still cancels them under these conditions. The principal component analysis is performed on the covariance and power spectral density matrices of the instrumental noises in the raw data and Chapter 3 shows how these are generated. The conventional way to do analysis on LISA data is through the time delay interferometry observables which have to be generated first before any inference can be performed. This method also uses these matrices, therefore, Chapter 3 will include a covariance analysis of the AET observables for a comparison with the results using the principal components. The principal components are obtained through the eigendecomposition of the noise covariance and power spectral density matrices which is explained in Chapter 4 using the conventional characteristic equation

method. We also compare the algebraic and numeric computation of the eigenpairs in terms of their computation times and results. In this chapter we prove the relationship between the laser noise free eigenvectors and the time delay interferometry observables in the time and frequency domains. We illustrate the advantage of using the principal component approach in the analysis using a Bayesian approach which is done in Chapter 5. In the same chapter we also include the analysis using the time delay interferometry observables and compare the results from both methods. In Chapter 6 the results of the investigations of a more realistic model of LISA data are presented specifically those related to the noise variances, arm lengths and laser phase-locking as these directly affect the covariance matrix. The aim is to see how the principal components approach handles real LISA data and in doing so determine which of the properties of LISA has the most effect on the eigenvalues. We are particular interested in finding out what would break the method which would mean the prevention of the splitting of the eigenvalues to produce those that are free from laser phase noises which is essential for its success. Our conclusions are presented in Chapter 7.

Chapter 2

Understanding time delay interferometry

This chapter contains the author's interpretation of the cancellation of laser noise using time delay interferometry and how it is used to generate the Sagnac and unequal-arm Michelson observables. The effect of the phase-locking of the lasers on the noise cancellation in these observables is also shown. To illustrate how these observables adapt to real LISA the cancellation is performed with the directional dependence of the arm lengths caused by the rotational motion. This is then used to explain the breaking of the Sagnac observables by the motion of the antenna.

2.1 Laser phase noise cancellation in an unequal-arm Michelson interferometer

One way to understand the laser phase noise problem in LISA and the time delay interferometry approach to canceling this noise is to illustrate what happens in a simple Michelson interferometer when the arms have equal and unequal lengths. Figure 2.1 is a schematic of a conventional Michelson interferometer consisting of a single laser, a beam splitter, a photodetector and two mirrors. The beam from the laser arriving at the beam splitter is divided equally and diverted to the two perpendicular arms. At the end of these arms the beams are reflected by the mirrors back towards the beam splitter where they are redirected towards the photodetector. Since the beam is only separated at the splitter, the optical path lengths will only be measured from that position to the photodetector. The lengths of the arm lengths are given by L_i and the corresponding light travel times are $D_i = L_i/c$ and c is the speed of light.

The laser phase noise p_i associated with a particular arm that arrives at the photodetector (PD) at time t is the same noise that left the laser at a time t minus the total travel time in that arm D_i where $i = \{I, II\}$ is the arm number. The total travel

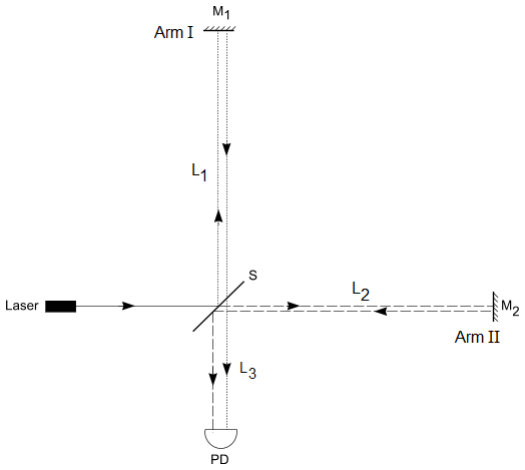

Figure 2.1: Schematic of a conventional Michelson interferometer with orthogonal arms (I, II), a beam splitter (S), two mirrors (M_1, M_2) and a photodetector (PD). The beams are separated for illustration.

times in the arms are

$$D_I = 2D_1 + D_3, \qquad D_{II} = 2D_2 + D_3. \tag{2.1}$$

With equal arm lengths ($D_1 = D_2 = D$) the total times become

$$D_I = D_{II} = 2D + D_3, \tag{2.2}$$

which are the same so that the laser noise arriving at the photodetector for time t will be the same and the phase measurements will be

$$\begin{aligned} s_I^{laser}(t) &= p(t - D_I) \;\; = p(t - 2D - D_3), \\ s_{II}^{laser}(t) &= p(t - D_{II}) = p(t - 2D - D_3). \end{aligned} \tag{2.3}$$

Since they are the same they can be canceled by differencing the two readings giving

$$\begin{aligned} s^{laser}(t) &= s_I^{laser}(t) - s_{II}^{laser}(t) \\ &= p(t - 2D - D_3) - p(t - 2D - D_3) \\ &= 0. \end{aligned} \tag{2.4}$$

With unequal arm lengths the difference in the optical path lengths means that phase measurements recorded at the photodetector at the same time are

$$\begin{aligned} s_I^{laser}(t) &= p(t - D_I) \;\; = p(t - 2D_1 - D_3), \\ s_{II}^{laser}(t) &= p(t - D_{II}) = p(t - 2D_2 - D_3), \end{aligned} \tag{2.5}$$

which will contain different noises because of the different offsets of D_1 and D_2. This means that the direct differencing of the readings for the same time t used with equal

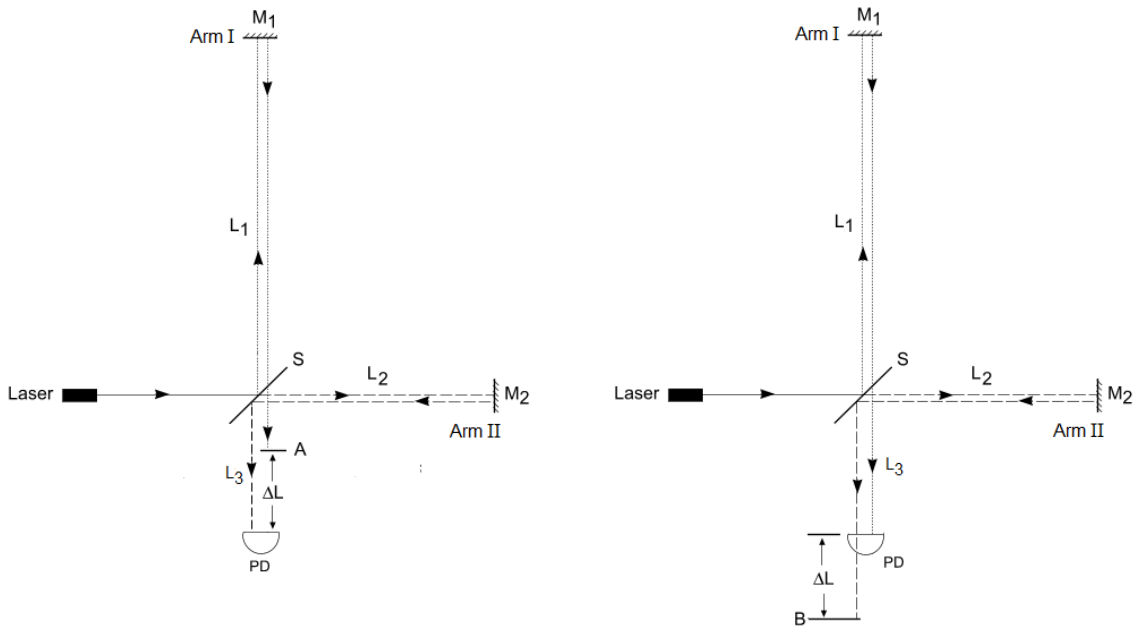

Figure 2.2: Schematic of an unequal-arm Michelson interferometer with a beam splitter (S), mirrors (M1, M2) and photodetector (PD). The arm lengths are $L1$ and $L2$. This difference in arm lengths causes a difference in the arrival times at the photodetector with the beam from the shorter arm arriving before the other.

arm lengths will no longer cancel the laser noise.

2.1.1 Unequal arm laser noise cancellation

The inequality of the arm lengths changes the noises that arrive at the photodetector for a particular time t because they alter the arrival times in each arm. The same noises still exist in the two arms but are just shifted by the difference between their lengths. The noise cancellation can still be achieved but by slightly different methods. The two possible ways of doing this require recording the readings separately in order to track the noise and then difference them.

The first method is to difference the shifted readings of the two arms by a time that is equal to the difference in the arm lengths. This is illustrated in Figure 2.2 where arm I is longer than arm II. In this case when the noise in the arm II (shorter) has arrived at the photodetector the same noise in arm I has only reached a point A which is a distance ΔL from the detector (Figure 2.2a). The noise in arm I will arrive at the detector at a later time $(t + \Delta D)$. To cancel the noise, either difference the reading in Arm I at time t with that in Arm II recorded at an earlier time later time $(t - \Delta D)$

(Figure 2.2b) or difference the reading in Arm II at time t with that of Arm I taken at an later time $(t + \Delta D)$ (Figure 2.2a). For the first case the laser phase noises are

$$s_I^{laser}(t) = p(t), \qquad s_{II}^{laser}(t - \Delta D) = p(t - \Delta D), \tag{2.6}$$

and their difference is

$$\begin{aligned} s_I^{laser}(t) - s_{II}^{laser}(t - \Delta D) &= p(t) - p(t - \Delta D) \\ &= 0, \end{aligned} \tag{2.7}$$

which will result in cancellation. The times will be different but the laser noises will now be the same. The aim is not to have the same times just the same noises.

The second method is to simulate equal arm lengths by making the light travel time in each optical path the same. This can be done by offsetting each reading by the light travel time in the opposite arm. For example, the total time in Arm I is $(2D_1 + D_3)$ and in Arm II it is $(2D_2 + D_3)$ where they differ by twice the times in their respective arms. To equalize the times add the times of the opposite arm so that the times will be $(2D_1 + D_3 + 2D_2)$ for Arm I and $(2D_2 + D_3 + 2D_1)$ for Arm II. The phase readings for each arm will be at times t minus these offsets which are

$$\begin{aligned} s_I^{laser}[t - (2D_1 + D_3 + 2D_2)] &= p(t - 2D_1 - D_3 - 2D_2), \\ s_{II}^{laser}[t - (2D_2 + D_3 + 2D_1)] &= p(t - 2D_2 - D_3 - 2D_1), \end{aligned} \tag{2.8}$$

where the same times result in the same noises. This has the advantage of having same noises with the same times. Practically, since both these methods rely on the differencing of readings taken at earlier and later times they are post-processing techniques. Both methods are used in the time delay interferometry observables.

2.2 Laser noise cancellation using time delay interferometry

The structure of LISA enables it to simulate different types of interferometers such as the Michelson and the Sagnac. The Michelson interferometer compares readings in two arms while the Sagnac compares readings along two closed paths in opposite directions. One way to approach the laser cancellation is to simulate what occurs in

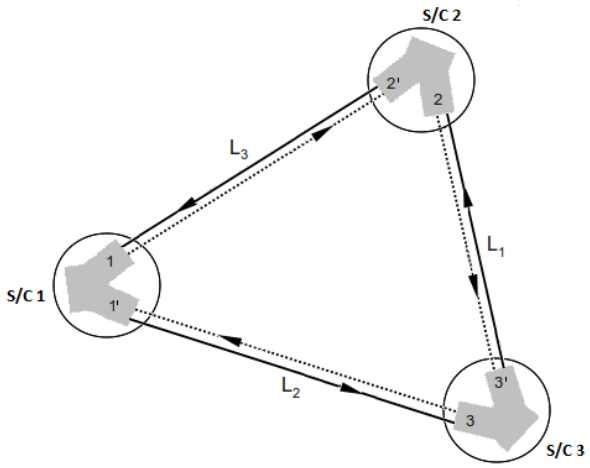

Figure 2.3: A schematic diagram of LISA showing the notation used in the labeling the arms, optical benches and spacecraft.

these interferometers. Initially, the combinations are generated for a stationary rigid LISA array with three arm lengths of L_1, L_2 and L_3 as shown in Figure 2.3. The lasers on each spacecraft are assumed to be phase-locked to each other resulting in only three independent laser phase noises p_1, p_2 and p_3.

Both these assumptions will be relaxed by removing the phase-locking and introducing a rotational motion in the antenna to see the effects on the cancellation of the noise and the creation of the observables. The rotational motion introduces a directional dependence of the arm lengths. The observables that will be generated are the Sagnac ζ and α and the Michleson X.

2.2.1 Fully symmetric Sagnac

Before even simulating either of the interferometers, an examination of the structure of the optical bench readings can give a idea of how to approach the cancellation. The readings for each optical bench is a combination of laser beam received from the other spacecraft at the opposite end of adjacent arm and its local beam. This means that there are two laser phase noises occurring in each reading with times separated by the

light travel times in the arms. The readings for all six benches are

$$\begin{aligned}
s_1(t) &= p_2(t - D_3) - p_1(t), \\
s_{1'}(t) &= p_3(t - D_2) - p_1(t), \\
s_2(t) &= p_3(t - D_1) - p_2(t), \\
s_{2'}(t) &= p_1(t - D_3) - p_2(t), \\
s_3(t) &= p_1(t - D_2) - p_3(t), \\
s_{3'}(t) &= p_2(t - D_1) - p_3(t).
\end{aligned} \tag{2.9}$$

The phase readings s_i with the same numbers are for the same spacecraft with the primed and unprimed numbering indicating the right and left optical benches, respectively. The phase-locking of the lasers on each spacecraft means that the phase noises for their two optical benches are the same and these are reflected in the noises at the current times $p_i(t)$. So that they can be canceled by differencing their readings. Following the convention of subtracting left from right the differenced readings for each spacecraft are

$$\begin{aligned}
s_{1'}(t) - s_1(t) &= p_3(t - D_2) - p_1(t) - p_2(t - D_3) + p_1(t) \\
&= p_3(t - D_2) - p_2(t - D_3), \\
s_{2'}(t) - s_2(t) &= p_1(t - D_3) - p_2(t) - p_3(t - D_1) + p_2(t) \\
&= p_1(t - D_3) - p_3(t - D_1), \\
s_{3'}(t) - s_3(t) &= p_2(t - D_1) - p_3(t) - p_1(t - D_2) + p_3(t) \\
&= p_2(t - D_1) - p_1(t - D_2).
\end{aligned} \tag{2.10}$$

The remaining noises contain two copies of the same noises but with different offsets and with opposite signs. Summing the readings in Equation 2.10 and grouping the same noises gives

$$\begin{aligned}
&[s_{1'}(t) - s_1(t)] + [s_{2'}(t) - s_2(t)] + [s_{3'}(t) - s_3(t)] \\
&\quad = p_1(t - D_3) - p_1(t - D_2) + p_2(t - D_1) - p_2(t - D_3) \\
&\qquad + p_3(t - D_2) - p_3(t - D_1).
\end{aligned} \tag{2.11}$$

This is where the method of equalising the times in the readings by offsetting the

Table 2.1: The noises remaining in Equation 2.11 with their parent optical benches and the offsets needed to cancel them in each reading.

Phase noise	Parent optical bench	Shifted phase noise	Shifted optical bench reading
$p_1(t-D_3)$	$s_{2'}(t)$	$p_1(t-D_3-D_2)$	$s_{2'}(t-D_2)$
$p_1(t-D_2)$	$s_3(t)$	$p_1(t-D_2-D_3)$	$s_3(t-D_3)$
$p_2(t-D_1)$	$s_{3'}(t)$	$p_2(t-D_1-D_3)$	$s_{3'}(t-D_3)$
$p_2(t-D_3)$	$s_1(t)$	$p_2(t-D_3-D_1)$	$s_1(t-D_1)$
$p_3(t-D_2)$	$s_{1'}(t)$	$p_3(t-D_2-D_1)$	$s_{1'}(t-D_1)$
$p_3(t-D_1)$	$s_2(t)$	$p_3(t-D_1-D_2)$	$s_2(t-D_2)$

different light arms is used. For example, for noises $p_1(t-D_3)$ and $p_1(t-D_2)$ this requires offsetting the first by D_2 and the second by D_3. This means offsetting the optical bench readings where the noises originated which, for laser noises $p_1(t-D_3)$ and $p_1(t-D_2)$, are $s_{2'}$ and s_3, respectively. The remaining noises in Equation 2.11 and their parent readings are given in Table 2.1. Applying the shifts as shown in the table gives

$$\begin{aligned}
s_1(t-D_1) &= p_2(t-D_3-D_1) - p_1(t-D_1),\\
s_{1'}(t-D_1) &= p_3(t-D_2-D_1) - p_1(t-D_1),\\
s_2(t-D_2) &= p_3(t-D_1-D_2) - p_2(t-D_2),\\
s_{2'}(t-D_2) &= p_1(t-D_3-D_2) - p_2(t-D_2),\\
s_3(t-D_3) &= p_1(t-D_2-D_3) - p_3(t-D_3),\\
s_{3'}(t-D_3) &= p_2(t-D_1-D_3) - p_3(t-D_3).
\end{aligned} \tag{2.12}$$

This not only shifts the noises we are trying to cancel but also shifts the local noises noises that were canceled. Luckily the local phase noises will still have the same times needed for their cancellation. The process of first differencing the readings on the same spacecraft with these new offsets is repeated and then summed to obtain

$$\begin{aligned}
&[s_{1'}(t-D_1) - s_1(t-D_1)] + [s_{2'}(t-D_2) - s_2(t-D_2)] + [s_{3'}(t-D_3) - s_3(t-D_3)]\\
&\quad = p_3(t-D_2-D_1) - p_1(t-D_1) + p_2(t-D_1-D_3) - p_3(t-D_3)\\
&\qquad + p_1(t-D_3-D_2) - p_2(t-D_2) - p_2(t-D_3-D_1) + p_1(t-D_1)\\
&\qquad - p_3(t-D_1-D_2) + p_2(t-D_2) - p_1(t-D_2-D_3) + p_3(t-D_3)\\
&\quad = 0,
\end{aligned} \tag{2.13}$$

where all the laser noises have been canceled. Grouping the terms in the above combi-

nation in terms of signs gives

$$\begin{aligned}&[s_{1'}(t-D_1)+s_{3'}(t-D_3)+s_{2'}(t-D_2)]\\&\quad-[s_1(t-D_1)+s_2(t-D_2)+s_3(t-D_3)],\end{aligned}\tag{2.14}$$

which simulates a Sagnac interferometer. The switching of $s_{2'}(t)$ and $s_{3'}(t)$ is to show the direction of the path. This arrangement is the fully symmetric Sagnac ζ. The process shows that LISA naturally simulates a Sagnac interferometer. The final equation is

$$\begin{aligned}\zeta(t) = {}& s_{1'}(t-D_1)+s_{3'}(t-D_3)+s_{2'}(t-D_2)\\&- s_1(t-D_1)-s_2(t-D_2)-s_3(t-D_3).\end{aligned}\tag{2.15}$$

This process could have been achieved by simulating a Sagnac interferometer from the outset where the readings are combined as the total paths measured in opposite directions. This is done by differencing the sums of the clockwise and counter-clockwise readings to obtain

$$\begin{aligned}&s_{1'}(t)+s_{3'}(t)+s_{2'}(t)-s_1(t)-s_2(t)-s_3(t)\\&\quad= p_3(t-D_2)-p_1(t)+p_2(t-D_1)-p_3(t)+p_1(t-D_3)-p_2(t)\\&\qquad-p_2(t-D_3)+p_1(t)-p_3(t-D_1)+p_2(t)-p_1(t-D_2)+p_3(t)\\&\quad= p_1(t-D_3)-p_1(t-D_2)+p_2(t-D_1)-p_2(t-D_3)\\&\qquad+p_3(t-D_2)-p_3(t-D_1),\end{aligned}\tag{2.16}$$

which is the same result as in Equation 2.11. To cancel the noises follow the same process that was used for that equation.

2.2.1.1 Laser noise cancellation without phase-locking

The phase-locking of the lasers on each spacecraft had the advantage of allowing the cancellation of their local laser noises by differencing their inter-spacecraft optical bench

readings. With independent lasers the inter-spacecraft readings are

$$\begin{aligned}
s_1(t) &= p_{2'}(t - D_3) - p_1(t), \\
s_{1'}(t) &= p_3(t - D_{2'}) - p_{1'}(t), \\
s_2(t) &= p_{3'}(t - D_1) - p_2(t), \\
s_{2'}(t) &= p_1(t - D_{3'}) - p_{2'}(t), \\
s_3(t) &= p_{1'}(t - D_2) - p_3(t), \\
s_{3'}(t) &= p_2(t - D_{1'}) - p_{3'}(t),
\end{aligned} \tag{2.17}$$

where there are no longer any common noises between the optical benches on the same spacecraft and differencing them will not be useful in canceling any noises. One way to proceed is to try to recover the combination that was derived with phase-locking by starting with that equation which is

$$\begin{aligned}
\zeta(t) = {} & s_{1'}(t - D_1) + s_{3'}(t - D_3) + s_{2'}(t - D_2) \\
& - s_1(t - D_1) - s_2(t - D_2) - s_3(t - D_3),
\end{aligned} \tag{2.18}$$

where the new phase readings are

$$\begin{aligned}
s_1(t - D_1) &= p_{2'}(t - D_3 - D_1) - p_1(t - D_1), \\
s_{1'}(t - D_1) &= p_3(t - D_2 - D_1) - p_{1'}(t - D_1), \\
s_2(t - D_2) &= p_{3'}(t - D_1 - D_2) - p_2(t - D_2), \\
s_{2'}(t - D_2) &= p_1(t - D_3 - D_2) - p_{2'}(t - D_2), \\
s_3(t - D_3) &= p_{1'}(t - D_2 - D_3) - p_3(t - D_3), \\
s_{3'}(t - D_3) &= p_2(t - D_1 - D_3) - p_{3'}(t - D_3).
\end{aligned} \tag{2.19}$$

Substituting these into Equation 2.18 and rearranging the terms to match the times instead of the noises gives

$$\begin{aligned}
& s_{1'}(t - D_1) + s_{3'}(t - D_3) + s_{2'}(t - D_2) - s_1(t - D_1) - s_2(t - D_2) - s_3(t - D_3) \\
& \quad = p_1(t - D_1) - p_{1'}(t - D_1) + p_1(t - D_3 - D_2) - p_{1'}(t - D_2 - D_3) \\
& \qquad + p_2(t - D_2) - p_{2'}(t - D_2) + p_2(t - D_1 - D_3) - \ p_{2'}(t - D_3 - D_1) \\
& \qquad + p_3(t - D_3) - p_{3'}(t - D_3) + p_3(t - D_2 - D_1) - p_{3'}(t - D_1 - D_2).
\end{aligned} \tag{2.20}$$

The noises are different on each spacecraft but have the same times, for example, $p_1(t - D_1)$ and $p_{1'}(t - D_1)$. Canceling the noise now requires the measurements taken between the two optical benches on each spacecraft, the intra-spacecraft readings τ_i, which are

$$\tau_i(t) = p_{i'}(t - d_i) - p_i(t), \qquad \tau_{i'}(t) = p_i(t - d_i) - p_{i'}(t). \tag{2.21}$$

Ignoring the times d_i which are very small ($< 10^{-8}s$), the readings for all six optical benches can be written as

$$\begin{aligned}
\tau_1(t) &= p_{1'}(t) - p_1(t),\\
\tau_{1'}(t) &= p_1(t) - p_{1'}(t),\\
\tau_2(t) &= p_{2'}(t) - p_2(t),\\
\tau_{2'}(t) &= p_2(t) - p_{2'}(t),\\
\tau_3(t) &= p_{3'}(t) - p_3(t),\\
\tau_{3'}(t) &= p_3(t) - p_{3'}(t).
\end{aligned} \tag{2.22}$$

The only non-zero option is to subtract the readings associated with each spacecraft giving

$$\begin{aligned}
\tau_1(t) - \tau_{1'}(t) &= \big[p_{1'}(t) - p_1(t)\big] - \big[p_1(t) - p_{1'}(t)\big]\\
&= 2p_{1'}(t) - 2p_1(t),\\
\tau_2(t) - \tau_{2'}(t) &= \big(p_{2'}(t) - p_2(t)\big) - \big(p_2(t) - p_{2'}(t)\big)\\
&= 2p_{2'}(t) - 2p_2(t),\\
\tau_3(t) - \tau_{3'}(t) &= \big(p_{3'}(t) - p_3(t)\big) - \big(p_3(t) - p_{3'}(t)\big)\\
&= 2p_{3'}(t) - 2p_3(t),
\end{aligned} \tag{2.23}$$

where there are now two copies of each of the noises. To cancel all the noises in Equation 2.20 the internal readings are offset by the appropriate times giving

$$\begin{aligned}
\tau_1(t - D_1) - \tau_{1'}(t - D_1) &= 2p_{1'}(t - D_1) - 2p_1(t - D_1),\\
\tau_2(t - D_2) - \tau_{2'}(t - D_2) &= 2p_{2'}(t - D_2) - 2p_2(t - D_2),\\
\tau_3(t - D_3) - \tau_{3'}(t - D_3) &= 2p_{3'}(t - D_3) - 2p_3(t - D_3),
\end{aligned} \tag{2.24}$$

and

$$\begin{aligned}
\tau_1(t-D_2-D_3)-\tau_{1'}(t-D_2-D_3) &= 2p_{1'}(t-D_2-D_3)-2p_1(t-D_2-D_3),\\
\tau_2(t-D_1-D_3)-\tau_{2'}(t-D_1-D_3) &= 2p_{2'}(t-D_1-D_3)-2p_2(t-D_1-D_3),\\
\tau_3(t-D_1-D_2)-\tau_{3'}(t-D_1-D_2) &= 2p_{3'}(t-D_1-D_2)-2p_3(t-D_1-D_2).
\end{aligned} \tag{2.25}$$

The noises occur in these are twice that required for cancellation. Summing the halves of these differences gives

$$\begin{aligned}
&\frac{1}{2}\big[\tau_1(t-D_1)-\tau_{1'}(t-D_1)\big]+\frac{1}{2}\big[\tau_2(t-D_2)-\tau_{2'}(t-D_2)\big]+\frac{1}{2}\big[\tau_3(t-D_3)-\tau_{3'}(t-D_3)\big]\\
&\quad= p_{1'}(t-D_1)-p_1(t-D_1)+p_{2'}(t-D_2)-p_2(t-D_2)\\
&\qquad+p_{3'}(t-D_3)-p_3(t-D_3),
\end{aligned} \tag{2.26}$$

and

$$\begin{aligned}
&\frac{1}{2}\big[\tau_1(t-D_2-D_3)-\tau_{1'}(t-D_2-D_3)\big]+\frac{1}{2}\big[\tau_2(t-D_1-D_3)-\tau_{2'}(t-D_1-D_3)\big]\\
&\quad+\frac{1}{2}\big[\tau_3(t-D_1-D_2)-\tau_{3'}(t-D_1-D_2)\big]\\
&\quad= p_{1'}(t-D_2-D_3)-p_1(t-D_2-D_3)+p_{2'}(t-D_1-D_3)-p_2(t-D_1-D_3)\\
&\qquad+p_{3'}(t-D_1-D_2)-p_3(t-D_1-D_2),
\end{aligned} \tag{2.27}$$

where the noises appear with opposite signs to the remaining noises in the Equation 2.20. The final noise canceling equation for the ζ with no phase-locking is

$$\begin{aligned}
\zeta(t) = {}& s_{1'}(t-D_1)+s_{3'}(t-D_3)+s_{2'}(t-D_2)-s_1(t-D_1)-s_2(t-D_2)-s_3(t-D_3)\\
&+\frac{1}{2}\big[\tau_1(t-D_1)-\tau_{1'}(t-D_1)+\tau_2(t-D_2)-\tau_{2'}(t-D_2)+\tau_3(t-D_3)\\
&\quad-\tau_{3'}(t-D_3)+\tau_1(t-D_2-D_3)-\tau_{1'}(t-D_2-D_3)+\tau_2(t-D_1-D_3)\\
&\quad-\tau_{2'}(t-D_1-D_3)+\tau_3(t-D_1-D_2)-\tau_{3'}(t-D_1-D_2)\big].
\end{aligned} \tag{2.28}$$

The structure is the same in terms of its inter-spacecraft readings as for phase-locked lasers. Although the ζ observable is the simplest to generate, it has a very low signal response. However, this property has the advantage of allowing it to be used as an instrumental noise analysis observable [20].

2.2.2 The 6-pulse Sagnac α

This will be done by simulating a Sagnac interferometer directly where the differencing is of the sum of the readings in two rings measured in opposite directions. One way to do this for the 6-pulse Sagnacs is sequentially starting with the readings of the two optical benches on the spacecraft that will act as the splitter and then combining it with the readings of the next set of optical benches of the same type (primed or unprimed) in opposite directions. For example, for spacecraft 1 the counter-clockwise path is from $s_{1'}(t)$ to $s_{3'}(t)$ then to $s_{2'}(t)$ and the clockwise path is from $s_1(t)$ to $s_2(t)$ then to $s_3(t)$. The lasers are assumed to be phase-locked on each spacecraft.

For the α Sagnac spacecraft 1 is the beam splitter and the readings are $s_{1'}$ and s_1, which are differenced giving

$$\begin{aligned} s_{1'}(t) - s_1(t) &= [p_3(t - D_2) - p_1(t)] - [p_2(t - D_3) - p_1(t)] \\ &= p_3(t - D_2) - p_2(t - D_3). \end{aligned} \tag{2.29}$$

The next set of readings in the ringed paths are $s_{3'}(t)$ and $s_2(t)$ which when differenced gives

$$s_{3'}(t) - s_2(t) = p_2(t) + p_2(t - D_1) - p_3(t) - p_3(t - D_1), \tag{2.30}$$

where two sets of the same noises (p_2, p_3) occur but at different times. These noises also occur in previously differenced readings therefore, either can be used to cancel them. For example, noises $p_3(t)$ or $p_3(t-D_1)$ in Equation 2.30 can be used to cancel $p_3(t-D_2)$ in Equation 2.29. However, using $p_3(t)$ requires only one offset D_2 while using $p_3(t-D_1)$ requires offsetting it by D_2 and the noise in Equation 2.29 by D_1. This is also the same for the other set of noises in Equation 2.30. For both sets of noises we use the simpler option of shifting the ones at time t which means shifting $s_{3'}(t)$ by D_3 and $s_2(t)$ by D_2 and then differencing these to obtain

$$\begin{aligned} s_{3'}(t - D_2) - s_2(t - D_3) = p_2(t - D_3) + p_2(t - D_1 - D_2) \\ - p_3(t - D_2) - p_3(t - D_1 - D_3). \end{aligned} \tag{2.31}$$

Adding these to Equation 2.29 gives

$$\begin{aligned} s_{1'}(t) - s_1(t) + s_{3'}(t - D_2) - s_2(t - D_3) \\ &= p_3(t - D_2) - p_2(t - D_3) + p_2(t - D_1 - D_2) \\ &\quad - p_3(t - D_2) - p_3(t - D_1 - D_3) \\ &= p_2(t - D_1 - D_2) - p_3(t - D_1 - D_3). \end{aligned} \tag{2.32}$$

The final readings for each ring are $s_{2'}(t)$ and $s_3(t)$ which are

$$s_{2'}(t) = p_1(t - D_3) - p_2(t), \qquad s_3(t) = p_1(t - D_2) - p_3(t) \tag{2.33}$$

where only one set of common noises exist (p_1). Differencing them gives

$$s_{2'}(t) - s_3(t) = p_1(t - D_3) - p_1(t - D_2) - p_2(t) + p_3(t). \tag{2.34}$$

The remaining noises in Equation 2.32 are $p_2(t - D_1 - D_2)$ and $p_3(t - D_1 - D_3)$ and canceling them requires shifting $p_2(t)$ and $p_3(t)$ in Equation 2.34 by $-D_1 - D_2$ and $-D_1 - D_3$, respectively. To do this requires applying the same offsets to $s_{2'}(t)$ and $s_3(t)$ which when differenced gives

$$\begin{aligned} s_{2'}(t - D_1 - D_2) - s_3(t - D_1 - D_3) \\ &= p_1(t - D_3 - D_1 - D_2) - p_2(t - D_1 - D_2) \\ &\quad - p_1(t - D_2 - D_1 - D_3) + p_3(t - D_1 - D_3) \\ &= p_3(t - D_1 - D_3) - p_2(t - D_1 - D_2), \end{aligned} \tag{2.35}$$

where the p_1 noises have been canceled. Adding this to Equation 2.30 gives

$$\begin{aligned} s_{1'}(t) - s_1(t) + s_{3'}(t - D_2) - s_2(t - D_3) + s_{2'}(t - D_1 - D_2) - s_3(t - D_1 - D_3) \\ &= p_2(t - D_1 - D_2) - p_3(t - D_1 - D_3) + p_1(t - D_3 - D_1 - D_2) \\ &\quad - p_2(t - D_1 - D_2) - p_1(t - D_2 - D_1 - D_3) + p_3(t - D_1 - D_3) \\ &= 0. \end{aligned} \tag{2.36}$$

Reordering the combination to reflect the differencing of opposite ringed paths gives

$$\begin{aligned} s_{1'}(t) + s_{3'}(t - D_2) + s_{2'}(t - D_1 - D_2) - s_1(t) - s_2(t - D_3) - s_3(t - D_1 - D_3) \\ &= \alpha(t) \end{aligned} \tag{2.37}$$

The β and γ are derived using spacecraft 2 and spacecraft 3 as the beam splitters, respectively.

2.2.2.1 Laser noise cancellation without phase-locking

Without phase-locking the structure remains the same and the local phase noises are canceled with the internal readings as illustrated for ζ. To show this we adjust the combination which was generated for phase-locking to show the different laser phase noises that now appear and group the noises according to times giving

$$\begin{aligned} s_{1'}(t) + s_{3'}(t-D_2) + s_{2'}(t-D_1-D_2) - s_1(t) - s_2(t-D_3) - s_3(t-D_1-D_3) \\ = \; p_1(t) - p_{1'}(t) + p_1(t-D_3-D_1-D_2) - p_{1'}(t-D_2-D_1-D_3) \\ + p_2(t-D_3) - p_{2'}(t-D_3) + p_2(t-D_1-D_2) - p_{2'}(t-D_1-D_2) \\ + p_3(t-D_2) - p_{3'}(t-D_2) + p_3(t-D_1-D_3) - p_{3'}(t-D_1-D_3) \end{aligned} \tag{2.38}$$

where as expected the noises no longer cancel. However, these can be canceled by using the intra-spacecraft readings with the appropriate offsets. Apply the same process used for ζ and difference the corresponding intra-spacecraft readings τ_i for the noises in Equation 2.34 with the required offsets which will give

$$\begin{aligned} &\tau_1(t) - \tau_{1'}(t)) \\ &\qquad = \; 2p_{1'}(t) - 2p_1(t), \\ &\tau_1(t-D_1-D_2-D_3) - \tau_{1'}(t-D_1-D_2-D_3) \\ &\qquad = \; 2p_{1'}(t-D_1-D_2-D_3) - 2p_1(t-D_1-D_2-D_3), \\ &\tau_2(t-D_3) - \tau_{2'}(t-D_3) \\ &\qquad = \; 2p_{2'}(t-D_3) - 2p_2(t-D_3), \\ &\tau_2(t-D_1-D_2) - \tau_{2'}(t-D_1-D_2) \\ &\qquad = \; 2p_{2'}(t-D_1-D_2) - 2p_2(t-D_1-D_2), \\ &\tau_3(t-D_2) - \tau_{3'}(t-D_2) \\ &\qquad = \; 2p_{3'}(t-D_2) - 2p_3(t-D_2), \\ &\tau_3(t-D_1-D_3) - \tau_{3'}(t-D_1-D_3) \\ &\qquad = \; 2p_{3'}(t-D_1-D_3) - 2p_3(t-D_1-D_3). \end{aligned} \tag{2.39}$$

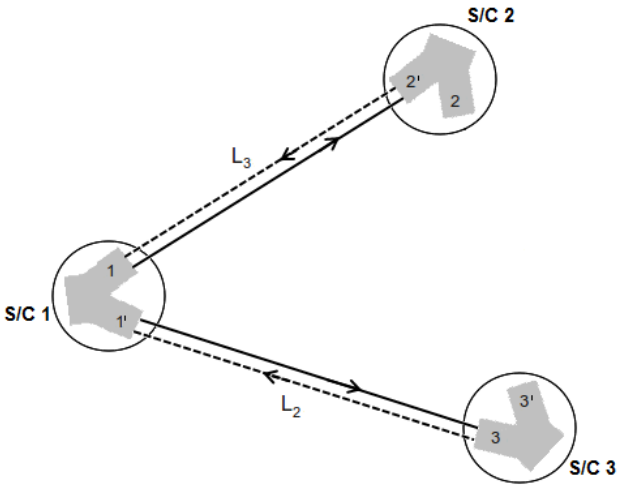

Figure 2.4: Schematic of LISA showing arms L_3 and L_2 used in the unequal-arm Michelson X observable.

The new combination that will cancel all the noises is

$$\begin{aligned} &s_{1'}(t) - s_1(t) + s_{3'}(t - D_2) - s_2(t - D_3) + s_{2'}(t - D_1 - D_2) - s_3(t - D_1 - D_3) \\ &\quad + \frac{1}{2}\big[\tau_1(t) - \tau_{1'}(t)\big] + \frac{1}{2}\big[\tau_1(t - D_1 - D_2 - D_3) - \tau_{1'}(t - D_1 - D_2 - D_3)\big] \\ &\quad + \frac{1}{2}\big[\tau_2(t - D_3) - \tau_{2'}(t - D_3)\big] + \frac{1}{2}\big[\tau_2(t - D_1 - D_2) - \tau_{2'}(t - D_1 - D_2)\big] \\ &\quad + \frac{1}{2}\big[\tau_3(t - D_2) - \tau_{3'}(t - D_2)\big] + \frac{1}{2}\big[\tau_3(t - D_1 - D_3) - \tau_{3'}(t - D_1 - D_3)\big]. \end{aligned} \tag{2.40}$$

Like the Sagnac ζ the structure of the inter-spacecraft readings s_i for the α is not altered as the noise cancellation can be achieved by using the intra-spacecraft readings τ_i.

2.2.3 Unequal-arm Michelson X

The Michelson has a beam splitter with mirrors at the ends of two arms and for LISA this is formed using one of the spacecraft and the two arms adjacent to it. For the X observable spacecraft 1 is the splitter with the arms being L_2 and L_3. The phase readings that are available for this combination are those from the four optical benches at the end of these arms as shown in Figure 2.4 which are 1, 1', 2' and 3. All the optical bench readings are one way measurements therefore no reflection occurs. To simulate reflection we alternate between the optical bench readings at the end of each arm until the noises are canceled. For example, for arm L_3 we alternate between readings s_1 and $s_{2'}$.

Assuming that the lasers on each spacecraft are phase-locked, the four optical bench

readings that are available for a Michelson formed with spacecraft 1 as the beam splitter are

$$\begin{aligned} s_1(t) &= p_2(t - D_3) - p_1(t), \\ s_{1'}(t) &= p_3(t - D_2) - p_1(t), \\ s_{2'}(t) &= p_1(t - D_3) - p_2(t), \\ s_3(t) &= p_1(t - D_2) - p_3(t). \end{aligned} \tag{2.41}$$

To generate the X observable we can use the same first step as for the Sagnac where the two optical bench readings on spacecraft 1 are differenced since it is acting as the splitter which gives

$$\begin{aligned} s_{1'}(t) - s_1(t) &= \big[p_3(t - D_2) - p_1(t)\big] - \big[p_2(t - D_3) - p_1(t)\big] \\ &= p_3(t - D_2) - p_2(t - D_3), \end{aligned} \tag{2.42}$$

where local noises are canceled. To simulate reflection, the next set of available readings that can be used to cancel the remaining noises are those at the ends of the arms adjacent to optical benches $1'$ and 1 which are s_3 and $s_{2'}$, respectively. To cancel the remaining noises in Equation 2.42 $s_{2'}(t)$ is shifted by D_3 and s_3 by D_3 giving

$$\begin{aligned} s_{2'}(t - D_3) &= p_1(t - 2D_3) - p_2(t - D_3), \\ s_3(t - D_2) &= p_1(t - 2D_2) - p_3(t - D_2). \end{aligned} \tag{2.43}$$

Combining these with Equation 2.42 with the appropriate signs gives

$$\begin{aligned} s_{1'}(t) - s_1(t) &- s_{2'}(t - D_3) + s_3(t - D_2) \\ &= p_3(t - D_2) - p_2(t - D_3) - p_1(t - 2D_3) + p_2(t - D_3) \\ &\quad + p_1(t - 2D_2) - p_3(t - D_2) \\ &= p_1(t - 2D_2) - p_1(t - 2D_3). \end{aligned} \tag{2.44}$$

The remaining phase noises are from the same spacecraft but at different times and to equalise the times each is shifted by the time in the other, that is $p_1(t-2D_2)$ by $2D_3$ and $p_1(t - 2D_3)$ by $2D_2$. Continuing with the reflection simulation, this means using s_1 and $s_{1'}$ with the appropriate offsets which are shifting them by $2D_3$ and $2D_3$, respectively

giving

$$\begin{aligned} s_1(t-2D_2) &= p_2(t-D_3-2D_2)-p_1(t-2D_2), \\ s_{1'}(t-2D_3) &= p_3(t-D_2-2D_3)-p_1(t-2D_3). \end{aligned} \tag{2.45}$$

Combining these with the Equation 2.44 with the appropriate signs gives

$$\begin{aligned} &s_{1'}(t)-s_1(t)-s_{2'}(t-D_3)+s_3(t-D_2)+s_1(t-2D_2)-s_{1'}(t-2D_3) \\ &\quad = p_1(t-2D_2)-p_1(t-2D_3)+p_2(t-D_3-2D_2)-p_1(t-2D_2) \\ &\qquad -p_3(t-D_2-2D_3)+p_1(t-2D_3) \\ &\quad = p_2(t-D_3-2D_2)-p_3(t-D_2-2D_3), \end{aligned} \tag{2.46}$$

where two new noises have been introduced. Again, the next available optical benches are the $s_{2'}$ and s_3 which are shifted by D_3+2D_2 and D_2+2D_3, respectively, to obtain the required times for the corresponding noises giving

$$\begin{aligned} s_{2'}(t-D_3-2D_2) &= p_1(t-2D_3-2D_2)-p_2(t-D_3-2D_2), \\ s_3(t-D_2-2D_3) &= p_1(t-2D_2-2D_3)-p_3(t-D_2-2D_3). \end{aligned} \tag{2.47}$$

Combining these with Equation 2.46 with the appropriate signs gives

$$\begin{aligned} &s_{1'}(t)-s_1(t)-s_{2'}(t-D_3)+s_3(t-D_2)+s_1(t-2D_2)-s_{1'}(t-2D_3) \\ &\qquad -s_3(t-D_2-2D_3)+s_{2'}(t-D_3-2D_2) \\ &= p_2(t-D_3-2D_2)-p_3(t-D_2-2D_3) \\ &\qquad -p_1(t-2D_2-2D_3)+p_3(t-D_2-2D_3) \\ &\qquad +p_1(t-2D_3-2D_2)-p_2(t-D_3-2D_2) \\ &= 0, \end{aligned} \tag{2.48}$$

where all the noises have been canceled. Rearranging and grouping according to the readings along each arm gives

$$\begin{aligned} &\big[s_{1'}(t)+s_3(t-D_2)\big]-\big[s_1(t)+s_{2'}(t-D_3)\big]+\big[s_1(t-2D_2)+s_{2'}(t-D_3-2D_2)\big] \\ &\quad -\big[s_{1'}(t-2D_3)+s_3(t-D_2-2D_3)\big], \end{aligned} \tag{2.49}$$

which is the Michelson X combination.

2.2.3.1 Laser noise cancellation without phase-locking

With independent lasers the four optical bench readings are

$$\begin{aligned} s_1(t) &= p_{2'}(t - D_3) - p_1(t), \\ s_{1'}(t) &= p_3(t - D_2) - p_{1'}(t), \\ s_{2'}(t) &= p_1(t - D_3) - p_{2'}(t), \\ s_3(t) &= p_{1'}(t - D_2) - p_3(t). \end{aligned} \tag{2.50}$$

As in the previous section, the two readings on spacecraft 1 ($s_{1'}$, s_1) to obtain

$$s_{1'}(t) - s_1(t) = p_3(t - D_2) - p_{2'}(t - D_3) + p_1(t) - p_{1'}(t), \tag{2.51}$$

where, as expected, this no longer cancel the local laser noises. As was shown for the Sagnac with no phase-locking, this requires the intra-spacecraft readings τ_i. However, the readings for $s_{2'}$ and s_3 contain noise contributions from the two lasers on spacecraft 2 and 3, respectively, so that the only available set of these readings for the X Michelson are those on spacecraft 1 which are τ_1 and $\tau_{1'}$ and their differenced reading is

$$\tau_{1'}(t) - \tau_1(t) = 2p_1(t) - 2p_{1'}(t). \tag{2.52}$$

As before, only half of these noises are required for canceling the noises in Equation 2.51 and subtracting this amount gives

$$\begin{aligned} s_{1'}(t) - s_1(t) - \frac{1}{2}[\tau_{1'}(t) - \tau_1(t)] &= \big[p_3(t - D_2) - p_{2'}(t - D_3) - p_{1'}(t) + p_1(t)\big] \\ &\quad - \big[p_1(t) - p_{1'}(t)\big] \\ &= p_3(t - D_2) - p_{2'}(t - D_3). \end{aligned} \tag{2.53}$$

The same process of alternately combining the readings at the end of each arm with the appropriate delays until all the noises are canceled is used. This means that the next set of readings are $s_{2'}$ and s_3 which are shifted by D_3 and D_2, respectively to obtain the required times for the common noises giving

$$\begin{aligned} s_{2'}(t - D_3) &= p_1(t - 2D_3) - p_{2'}(t - D_3), \\ s_3(t - D_2) &= p_{1'}(t - 2D_2) - p_3(t - D_2), \end{aligned} \tag{2.54}$$

which are combined with Equation 2.53 with the appropriate signs to obtain the cancellation of the p_2 and p_3 noises, that is,

$$\begin{aligned} s_{1'}(t) - s_1(t) - \frac{1}{2}[\tau_{1'}(t) - \tau_1(t)] - s_{2'}(t - D_3) + s_3(t - D_2) \\ = p_3(t - D_2) - p_{2'}(t - D_3) - p_1(t - 2D_3) + p_{2'}(t - D_3) \\ + p_{1'}(t - 2D_2) - p_3(t - D_2) \\ = p_{1'}(t - 2D_2) - p_1(t - 2D_3). \end{aligned} \tag{2.55}$$

The remaining noises are from the same spacecraft but with different times therefore, using the internal readings will not help in their cancellation. The next set of available readings are those of s_1 and $s_{1'}$. Since we are trying to recover the original combination obtained for phase-locked lasers, apply the same offsets by shifting these readings by $2D_2$ and $2D_3$, respectively which gives

$$\begin{aligned} s_1(t - 2D_2) &= p_{2'}(t - D_3 - 2D_2) - p_1(t - 2D_2), \\ s_{1'}(t - 2D_3) &= p_3(t - D_2 - 2D_3) - p_{1'}(t - 2D_3). \end{aligned} \tag{2.56}$$

These are combined with the previous equation to obtain

$$\begin{aligned} s_{1'}(t) - s_1(t) - \frac{1}{2}[\tau_{1'}(t) - \tau_1(t)] - s_{2'}(t - D_3) + s_3(t - D_2) \\ - s_{1'}(t - 2D_3) + s_1(t - 2D_2) \\ = p_{1'}(t - 2D_2) - p_1(t - 2D_3) - p_3(t - D_2 - 2D_3) + p_{1'}(t - 2D_3) \\ + p_{2'}(t - D_3 - 2D_2) - p_1(t - 2D_2) \\ = p_{1'}(t - 2D_2) - p_1(t - 2D_2) - p_{1'}(t - 2D_3) + p_1(t - 2D_3) \\ - p_3(t - D_2 - 2D_3) + p_{2'}(t - D_3 - 2D_2), \end{aligned} \tag{2.57}$$

which does not result in the cancellation of the p_1 and $p_{1'}$ as in the phase-locked case at this stage. However, there are two copies of p_1 and $p_{1'}$ at offsets of $2D_2$ and $2D_3$ which allows for them to be grouped according to the same times that is, $p_{1'}(t - 2D_2), p_1(t - 2D_2)$ and $p_{1'}(t - 2D_3), p_1(t - 2D_3)$. The internal readings can now be used to cancel

these noises and the terms with the required offsets are

$$\begin{aligned}
\tau_1(t-2D_2) &= p_{1'}(t-2D_2) - p_1(t-2D_2),\\
\tau_{1'}(t-2D_2) &= p_1(t-2D_2) - p_{1'}(t-2D_2),\\
\tau_1(t-2D_3) &= p_{1'}(t-2D_3) - p_1(t-2D_3),\\
\tau_{1'}(t-2D_3) &= p_1(t-2D_3) - p_{1'}(t-2D_3),
\end{aligned} \tag{2.58}$$

and their differenced values are

$$\begin{aligned}
\tau_{1'}(t-2D_2) - \tau_1(t-2D_2) &= 2p_1(t-2D_2) - 2p_{1'}(t-2D_2),\\
\tau_{1'}(t-2D_3) - \tau_1(t-2D_3) &= 2p_1(t-2D_3) - 2p_{1'}(t-2D_3).
\end{aligned} \tag{2.59}$$

Subtract half their values and combine them to Equation 2.57 with appropriate signs gives

$$\begin{aligned}
s_{1'}(t) - s_1(t) - \frac{1}{2}\big[\tau_{1'}(t) - \tau_1(t)\big] - s_{2'}(t-D_3) + s_3(t-D_2)& \\
-s_{1'}(t-2D_3) + s_1(t-2D_2) - \frac{1}{2}\big[\tau_{1'}(t-2D_2) - \tau_1(t-2D_2)\big]& \\
-\frac{1}{2}\big[\tau_{1'}(t-2D_3) - \tau_1(t-2D_3)\big]& \\
= p_{1'}(t-2D_2) - p_1(t-2D_2) - p_{1'}(t-2D_3) + p_1(t-2D_3)& \\
-p_3(t-D_2-2D_3) + p_{2'}(t-D_3-2D_2)& \\
-p_{1'}(t-2D_2) + p_1(t-2D_2) + p_{1'}(t-2D_3) - p_1(t-2D_3)& \\
= p_{2'}(t-D_3-2D_2) - p_3(t-D_2-2D_3).&
\end{aligned} \tag{2.60}$$

The next set of available readings are $s_{2'}$ and s_3 which require offsets of $(-D_3-2D_2)$ and $(-D_2-2D_2)$ to match the noises in the previous equation which are

$$\begin{aligned}
s_{2'}(t-D_3-2D_2) &= p_1(t-2D_3-2D_2) - p_{2'}(t-D_3-2D_2),\\
s_3(t-D_2-2D_2) &= p_{1'}(t-2D_2-2D_3) - p_3(t-D_2-2D_3).
\end{aligned} \tag{2.61}$$

Combining these with Equation 2.60 with appropriate signs gives

$$\begin{aligned}
s_{1'}(t) - s_1(t) - \frac{1}{2}\big[\tau_{1'}(t) - \tau_1(t)\big] - s_{2'}(t - D_3) + s_3(t - D_2) \\
-s_{1'}(t - 2D_3) + s_1(t - 2D_2) - \frac{1}{2}\big[\tau_{1'}(t - 2D_2) - \tau_1(t - 2D_2)\big] \\
+\frac{1}{2}\big[\tau_1(t - 2D_3) - \tau_{1'}(t - 2D_3)\big] \\
+s_{2'}(t - D_3 - 2D_2) - s_3(t - D_2 - 2D_3) \\
= p_{2'}(t - D_3 - 2D_2) - p_3(t - D_2 - 2D_3) \\
+p_1(t - 2D_3 - 2D_2) - p_{2'}(t - D_3 - 2D_2) \\
-p_{1'}(t - 2D_2 - 2D_3) + p_3(t - D_2 - 2D_3) \\
= p_1(t - 2D_3 - 2D_2) - p_{1'}(t - 2D_2 - 2D_3). \qquad (2.62)
\end{aligned}$$

The remaining noises are from the same spacecraft with the same times. Again use the internal readings to obtain the noises with the appropriate offsets which are

$$\begin{aligned}
\tau_1(t - 2D_2 - 2D_3) &= p_{1'}(t - 2D_2 - 2D_3) - p_1(t - 2D_2 - 2D_3), \\
\tau_{1'}(t - 2D_2 - 2D_3) &= p_1(t - 2D_2 - 2D_3) - p_{1'}(t - 2D_2 - 2D_3), \qquad (2.63)
\end{aligned}$$

and the differenced reading is

$$\begin{aligned}
\tau_{1'}(t - 2D_2 - 2D_3) - \tau_1(t - 2D_2 - 2D_3) \\
= 2p_1(t - 2D_2 - 2D_3) - 2p_1(t - 2D_2 - 2D_3). \qquad (2.64)
\end{aligned}$$

Adding this to Equation 2.62 gives

$$\begin{aligned}
s_{1'}(t) - s_1(t) - \frac{1}{2}\big[\tau_{1'}(t) - \tau_1(t)\big] - s_{2'}(t - D_3) + s_3(t - D_2) \\
-s_{1'}(t - 2D_3) + s_1(t - 2D_2) - \frac{1}{2}\big[\tau_{1'}(t - 2D_2) - \tau_1(t - 2D_2)\big] \\
-\frac{1}{2}\big[\tau_{1'}(t - 2D_3) - \tau_1(t - 2D_3)\big] \\
+s_{2'}(t - D_3 - 2D_2) - s_3(t - D_2 - 2D_3) \\
+\frac{1}{2}\big[\tau_{1'}(t - 2D_2 - 2D_3) - \tau_1(t - 2D_2 - 2D_3)\big] \\
= p_1(t - 2D_3 - 2D_2) - p_{1'}(t - 2D_2 - 2D_3) \\
-p_1(t - 2D_2 - 2D_3) + p_{1'}(t - 2D_2 - 2D_3) \\
= 0, \qquad (2.65)
\end{aligned}$$

where all the noises have been canceled. The final expression after rearranging and grouping the terms is

$$\begin{aligned} X(t) = {} & [s_{1'}(t) + s_3(t - D_2)] - [s_1(t) + s_{2'}(t - D_3)] + [s_1(t - 2D_2) + s_{2'}(t - D_3 - 2D_2)] \\ & -[s_{1'}(t - 2D_3) + s_3(t - D_2 - 2D_3)] \\ & + \frac{1}{2}\big[\tau_1(t) - \tau_{1'}(t) - \tau_{1'}(t - 2D_2) + \tau_1(t - 2D_2) + \tau_1(t - 2D_3) \\ & \quad -\tau_{1'}(t - 2D_3) + \tau_{1'}(t - 2D_2 - 2D_3) - \tau_1(t - 2D_2 - 2D_3)\big], \end{aligned} \tag{2.66}$$

where, like the Sagnac, the structure did not change with respect to the inter-spacecraft readings. The laser noise cancellation is achieved by incorporating the intra-spacecraft readings.

2.2.4 Summary

In this section, the process of manually generating of the Sagnac α and ζ and Michelson X combinations was illustrated. This was initially done with the lasers locked on each spacecraft and then for independent lasers. The structure of both combinations remained the same in terms of their inter-spacecraft readings with the change being the need for extra readings to cancel the laser phase noises which were obtained from the intra-spacecraft readings.

2.3 The effect of orbital motion on the time delay interferometry observables

This will be demonstrated using the rotational motion only which introduces a dependency on the direction of the measurement of the arm lengths. This difference is indicated by using $L_{i'}$ and L_i for clockwise and counter-clockwise measurements, respectively. The arm lengths are assumed to be static. In this section the assumption will be that lasers are phase-locked on each spacecraft. The time delay interferometry observables that will be illustrated are the Sagnac ζ and the Michelson X.

Table 2.2: The noises remaining in Equation 2.68 with their parent optical benches and the offsets needed to cancel them in each reading.

Phase noise	Parent optical bench	Shifted phase noise	Shifted parent optical bench
$p_1(t-D_{3'})$	$s_{2'}(t)$	$p_1(t-D_{3'}-D_2)$	$s_{2'}(t-D_2)$
$p_1(t-D_2)$	$s_3(t)$	$p_1(t-D_2-D_{3'})$	$s_3(t-D_{3'})$
$p_2(t-D_{1'})$	$s_{3'}(t)$	$p_2(t-D_{1'}-D_3)$	$s_{3'}(t-D_3)$
$p_2(t-D_3)$	$s_1(t)$	$p_2(t-D_3-D_{1'})$	$s_1(t-D_{1'})$
$p_3(t-D_{2'})$	$s_{1'}(t)$	$p_3(t-D_{2'}-D_1)$	$s_{1'}(t-D_1)$
$p_3(t-D_1)$	$s_2(t)$	$p_3(t-D_1-D_{2'})$	$s_2(t-D_{2'})$

2.3.1 Sagnac ζ with orbital motion

The optical bench readings with the different light travel times are

$$\begin{aligned}
s_1(t) &= p_2(t-D_3) - p_1(t),\\
s_{1'}(t) &= p_3(t-D_{2'}) - p_1(t),\\
s_2(t) &= p_3(t-D_{1'}) - p_2(t),\\
s_{2'}(t) &= p_1(t-D_{3'}) - p_2(t),\\
s_3(t) &= p_1(t-D_{2'}) - p_3(t),\\
s_{3'}(t) &= p_2(t-D_{1'}) - p_3(t).
\end{aligned} \tag{2.67}$$

The different offsets caused by the directional dependence means that adjusting the final equation obtained for phase-locked lasers to account for this cannot be done. Instead we start by simulating a Sagnac by differencing the readings in the opposite arms as done in Equation 2.16 to obtain

$$\begin{aligned}
&s_{1'}(t) + s_{3'}(t) + s_{2'}(t) - s_1(t) - s_2(t) - s_3(t)\\
&\quad= p_3(t-D_{2'}) - p_1(t) + p_2(t-D_{1'}) - p_3(t) + p_1(t-D_{3'}) - p_2(t)\\
&\qquad\quad - p_2(t-D_3) + p_1(t) - p_3(t-D_1) + p_2(t)\\
&\qquad\quad - p_1(t-D_2) + p_3(t)\\
&\quad= p_1(t-D_{3'}) - p_1(t-D_2) + p_2(t-D_{1'}) - \ p_2(t-D_3)\\
&\qquad\quad + p_3(t-D_{2'}) - p_3(t-D_1).
\end{aligned} \tag{2.68}$$

The difference in the arm lengths means that there are now six different offsets in the result. The remaining noises with their parent optical bench are given in columns 1 and 2 of Table 2.2 and the offsets that need to be applied to these to cancel the noises are

given in columns 3 and 4. The new readings with these offsets are

$$\begin{aligned}
s_1(t - D_{1'}) &= p_2(t - D_3 - D_{1'}) - p_1(t - D_{1'}),\\
s_{1'}(t - D_1) &= p_3(t - D_{2'} - D_1) - p_1(t - D_1),\\
s_2(t - D_{2'}) &= p_3(t - D_1 - D_{2'}) - p_2(t - D_{2'}),\\
s_{2'}(t - D_2) &= p_1(t - D_{3'} - D_2) - p_2(t - D_2),\\
s_3(t - D_{3'}) &= p_1(t - D_2 - D_{3'}) - p_3(t - D_{3'}),\\
s_{3'}(t - D_3) &= p_2(t - D_{1'} - D_3) - p_3(t - D_3).
\end{aligned} \tag{2.69}$$

Rewriting Equation 2.68 with these shifts gives

$$\begin{aligned}
&s_{1'}(t - D_1) + s_{3'}(t - D_3) + s_{2'}(t - D_2) - s_1(t - D_{1'}) - s_2(t - D_{2'}) - s_3(t - D_{3'})\\
&\quad = p_3(t - D_{2'} - D_1) - p_1(t - D_1) + p_2(t - D_{1'} - D_3) - p_3(t - D_3)\\
&\qquad + p_1(t - D_{3'} - D_2) - p_2(t - D_2) - p_2(t - D_3 - D_{1'})\\
&\qquad + p_1(t - D_{1'}) - p_3(t - D_1 - D_{2'}) + p_2(t - D_{2'})\\
&\qquad - p_1(t - D_2 - D_{3'}) + p_3(t - D_{3'})\\
&\quad = p_1(t - D_{1'}) - p_1(t - D_1) + p_2(t - D_{2'}) - p_2(t - D_2)\\
&\qquad + p_3(t - D_{3'}) - p_3(t - D_3),
\end{aligned} \tag{2.70}$$

which no longer leads to the cancellation of all the noises because the noises have different offsets reflecting the directional dependency, for example, $p_1(t - D_1)$ and $p_1(t - D_{1'})$. The internal readings τ_i are useful when the noises on the same spacecraft are at the same times but this does not happen in Equation 2.70 therefore they cannot be used to solve the problem as was done for the independent lasers in Section 2.2.1.1.

This has illustrated why the ζ Sagnac combination does not survive rotational motion. This is also true of the 6-pulse Sagnacs. This failure with rotation of the antenna can also be illustrated intuitively. In an actual Sagnac interferometer if the total length of the opposite loops are not the same then the noises arriving at the beam splitter will no longer be the same.

2.3.2 Unequal-arm Michelson X with orbital motion

The equations for the optical benches needed for the unequal-arm Michelson with new offsets are

$$\begin{aligned} s_1(t) &= p_2(t - D_3) - p_1(t), \\ s_{1'}(t) &= p_3(t - D_{2'}) - p_1(t), \\ s_{2'}(t) &= p_1(t - D_{3'}) - p_2(t), \\ s_3(t) &= p_1(t - D_2) - p_3(t). \end{aligned} \tag{2.71}$$

Differencing the readings on spacecraft 1 with the new offsets gives

$$\begin{aligned} s_{1'}(t) - s_1(t) &= p_3(t - D_{2'}) - p_1(t) - p_2(t - D_3) + p_1(t) \\ &= p_3(t - D_{2'}) - p_2(t - D_3). \end{aligned} \tag{2.72}$$

Offsetting $s_{2'}(t)$ by D_3 and $s_3(t)$ by $D_{2'}$ gives

$$\begin{aligned} s_{2'}(t - D_3) &= p_1(t - D_{3'} - D_3) - p_2(t - D_3), \\ s_3(t - D_{2'}) &= p_1(t - D_2 - D_{2'}) - p_3(t - D_{2'}). \end{aligned} \tag{2.73}$$

Combining these with Equation 2.72 gives

$$\begin{aligned} s_{1'}(t) - s_1(t) &- s_{2'}(t - D_3) + s_3(t - D_{2'}) \\ &= p_3(t - D_{2'}) - p_2(t - D_3) - p_1(t - D_{3'} - D_3) + p_2(t - D_3) \\ &\quad + p_1(t - D_2 - D_{2'}) - p_3(t - D_{2'}) \\ &= p_1(t - D_2 - D_{2'}) - p_1(t - D_{3'} - D_3). \end{aligned} \tag{2.74}$$

The difference in the clockwise and counter-clockwise times means that the $2D_2$ and $2D_3$ offsets are replaced by $-D_2 - D_{2'}$ and $-D_{3'} - D_3$, respectively. The next set of readings with the appropriate offsets are

$$\begin{aligned} s_1(t - D_2 - D_{2'}) &= p_2(t - D_3 - D_2 - D_{2'}) - p_1(t - D_2 - D_{2'}), \\ s_{1'}(t - D_{3'} - D_3) &= p_3(t - D_2 - D_{3'} - D_3) - p_1(t - D_{3'} - D_3), \end{aligned} \tag{2.75}$$

which are combine with the previous equations to obtain

$$\begin{aligned} s_{1'}(t) - s_1(t) - s_{2'}(t - D_3) + s_3(t - D_{2'}) - s_{1'}(t - D_{3'} - D_3) + s_1(t - D_2 - D_{2'}) \\ = \quad & p_1(t - D_2 - D_{2'}) - p_1(t - D_{3'} - D_3) - p_3(t - D_{2'} - D_{3'} - D_3) \\ & + p_1(t - D_{3'} - D_3) + p_2(t - D_3 - D_2 - D_{2'}) - p_1(t - D_2 - D_{2'}) \\ = \quad & p_2(t - D_3 - D_2 - D_{2'}) - p_3(t - D_{2'} - D_{3'} - D_3). \end{aligned} \tag{2.76}$$

The next set of readings from spacecraft 2 and 3 for canceling these are

$$\begin{aligned} s_{2'}(t - D_3 - D_2 - D_{2'}) &= p_1(t - D_{3'} - D_3 - D_2 - D_{2'}) - \ p_2(t - D_3 - D_2 - D_{2'}), \\ s_3(t - D_{2'} - D_{3'} - D_3) &= p_1(t - D_2 - D_{2'} - D_3 - D_{3'}) - p_3(t - D_{2'} - D_{3'} - D_3), \end{aligned} \tag{2.77}$$

which are combined with Equation 2.76 to give

$$\begin{aligned} s_{1'}(t) - s_1(t) - s_{2'}(t - D_{3'}) + s_3(t - D_2) - s_{1'}(t - D_{3'} - D_3) + s_1(t - D_2 - D_{2'}) \\ & + s_{2'}(t - D_3 - D_2 - D_{2'}) - s_3(t - D_{2'} - D_{3'} - D_3) \\ = p_2(t - D_3 - D_2 - D_{2'}) - p_3(t - D_{2'} - D_{3'} - D_3) \\ & + p_1(t - D_{3'} - D_3 - D_2 - D_{2'}) - \ p_2(t - D_3 - D_2 - D_{2'}) \\ & - p_1(t - D_2 - D_{2'} - D_3 - D_{3'}) + p_3(t - D_{2'} - D_3 - D_{3'}) \\ = 0. \end{aligned} \tag{2.78}$$

The unequal-arm Michelson retains its structure even when the directional differences are accounted for. Its flexibility is due to the $2D_i$ terms occurring in their non-rotating expressions which are replaced by the $D_i + D_{i'}$ to account for the directional differences.

2.4 Summary

The laser phase noise in LISA presents a problem because of the inequality of the lengths of its arms. Laser phase noise cancellation using time delay interferometry was illustrated using a simple unequal-arm Michelson interferometer to explain the problem caused by the inequality and how this can be resolved. With unequal arms the same noises do not appear at the photodetectors at the same time but they still exist in the different arms just at different times. To accomplish the laser noise cancellation in this case the readings in each arm have to be obtained separately to allow the noises to be

tracked in the different arms. Once the readings are located they are differenced to cancel the noise. Two methods were shown for locating the same reading in the arms. The obvious method was to difference the readings by the exact difference between the arm lengths ΔL. The other was to simulate an equal arm interferometer by offsetting the measurement in each arm by the length in the other. The conventional time delay interferometry uses both methods.

We illustrated how these techniques for cancelling the laser noises are was used to generate the conventional time delay interferometry observables. This was illustrated using the Sagnac (ζ, α) and unequal-arm Michelson X using a simple model of LISA as a stationary rigid array with the two lasers on each spacecraft phase-locked together. Under these conditions the laser noise free combinations could be generated with only the inter-spacecraft readings which are the readings taken along the arms. We then illustrated the effect of removing phase-locking of the lasers had on the generation of the combinations. The result was that this did not affect the structure of the combinations in terms of the how the inter-spacecraft readings were combined, however, the internal readings τ_i were now required for the laser phase noise cancellation. This was true for both the Sagnac and Michelson combinations.

The toy model initially assumed stationary static arm lengths. We illustrated what happened to these combinations when the motion of the LISA is taken into account. This was done with the directional dependence of the arm lengths that occurs with the rotational motion of the antenna. For this we assumed that the different measurements were static. The effect was illustrated with the Sagnac ζ and the Michelson X combinations with spacecraft phase-locking. The directional differences in the offsets broke the symmetry of the ζ. The Michelson X combination, however, survived because the $2D$ offset in some of terms was able to incorporate the different offsets by becoming the sum of the different offsets, that is, $D_i + D_{i'}$.

In using this method the relaxation of the assumptions meant manually regenerating the combinations making it an inefficient process which is the main reason for only a few combinations being generated. The potential to generate all these combinations and provide a more efficient way of generating them led to the computer-based methods such as the algebraic and the geometric methods mentioned in Chapter 1. Although not all the combinations would be needed, being able to generate them would offer the possibil-

ity of obtaining those with better sensitivities to gravitational wave signals for use in the data analysis process. The principal component approach is another computer-based method that improves on these by incorporating the laser noise cancellation into the inference process removing the need to generate the laser noise free data before doing the analysis. This method is based on eigendecomposition of the raw data covariance and the power spectral density matrices therefore, in the following chapter we will illustrate how these are generated.

Chapter 3

Generating the covariance and power spectral density matrices for LISA data

The principal components are obtained from the raw data covariance or power spectral density matrices. In this chapter we generate the covariances and power spectral densities required for creating these matrices. We also include the power spectral densities for the optimal *AET* observables as our analysis will include the conventional approach for comparison.

3.1 Basic functions

Ideally the covariance matrix would be derived directly from the noises using the auto-covariance and cross-covariance functions obtained from their time series. However, because there is no way to simultaneously and independently observe the noises the covariance functions are generated algebraically and the values are computed based on assumptions made about the noise characteristics[1].

3.1.1 Covariance functions

Auto-covariance

If the noise is represented by a discrete random variable X_i with values given by x_i then the auto-covariance which expresses the mutual relationships between the different values can be determined using

$$C_{XX}(k) = \text{cov}(X_i, X_{i+k}) = \frac{1}{N}\sum_{i=1}^{n}\Big[\big(x_i - \langle X_i\rangle\big)\,\big(x_{i+k} - \langle X_{i+k}\rangle\big)\Big], \tag{3.1}$$

where $i = \{1, 2, ..., n\}$ and $k = \{0, 1, ..., n-1\}$. k is the lag term specifying the separation between the values of X. A simpler version of this equation will be used which is

[1]The information sources for this section were [34] and [62]

obtained by expanding the product giving

$$\begin{aligned} C_{XX}(k) &= \frac{1}{N}\sum_{i=1}^{n}\left[x_i x_{i+k} - x_i\langle X_{i+k}\rangle - \langle X_i\rangle x_{i+k} + \langle X_i\rangle\langle X_{i+k}\rangle\right] \\ &= \frac{1}{N}\sum_{i=1}^{n}\left[x_i x_{i+k}\right] - \frac{1}{N}\sum_{i=1}^{n}\left[x_i\langle X_{i+k}\rangle\right] - \frac{1}{N}\sum_{i=1}^{n}\left[\langle X_i\rangle x_{i+k}\right] \\ &\quad + \frac{1}{N}\sum_{i=1}^{n}\left[\langle X_i\rangle\langle X_{i+k}\rangle\right] \\ &= \left\langle X_i X_{i+k}\right\rangle - \left\langle X_i\right\rangle\left\langle X_{i+k}\right\rangle, \end{aligned} \tag{3.2}$$

where $\langle X_i X_{i+k}\rangle$ is the mean of the squared values and $\langle X_i\rangle\langle X_{i+k}\rangle$ is the square of the means. The auto-covariance is a one to one comparison between the values of the full time series X_i with values from sections of the time series X_{i+k} where $i+k$ is the starting point for the partial series. The covariances are computed for all values of k to cover the length of the time series. For zero lag the auto-covariance gives the variance of the full time series and from Equation 3.2 this is

$$C_{XX}(0) = \mathrm{cov}(X_i, X_i) = \mathrm{var}[X] = \left\langle X_i^2\right\rangle - \left\langle X_i\right\rangle^2. \tag{3.3}$$

There will also be variances for portions of the time series X_{i+k} given by

$$\mathrm{cov}(X_{i+k}, X_{i+k}) = \mathrm{var}[X_{i+k}] = \left\langle X_{i+k}^2\right\rangle - \left\langle X_{i+k}\right\rangle^2. \tag{3.4}$$

If the means are assumed to be zero Equations 3.2 and 3.4 become

$$C_{XX}(k) = \left\langle X_i\ X_{i+k}\right\rangle, \qquad C_{XX}(0) = \left\langle X_i^2\right\rangle. \tag{3.5}$$

In matrix format these can be written as

$$C_{XX} = \begin{bmatrix} \mathrm{var}(X_1) & \mathrm{cov}(X_1, X_2) & \cdots & \mathrm{cov}(X_1, X_n) \\ \mathrm{cov}(X_2, X_1) & \mathrm{var}(X_2) & \cdots & \mathrm{cov}(X_2, X_n) \\ \vdots & \vdots & \ddots & \vdots \\ \mathrm{cov}(X_n, X_1) & \mathrm{cov}(X_n, X_2) & \cdots & \mathrm{var}(X_n) \end{bmatrix}, \tag{3.6}$$

where the variances are the values along the main diagonal and the auto-covariances everywhere else.

Cross-covariance

The cross-covariances expresses relationships between different time series. For two discrete time series represented by two random variables X and Y with values of x_i and

y_i, respectively, the cross-covariance can be defined as

$$\begin{aligned} C_{XY}(k) = \mathrm{cov}(X_i, Y_{i+k}) &= \big\langle (x_i - \langle X_i \rangle)\,(y_{i+k} - \langle Y_{i+k} \rangle) \big\rangle \\ &= \big\langle X_i\, Y_{i+k} \big\rangle - \big\langle X_i \big\rangle \big\langle Y_{i+k} \big\rangle, \end{aligned} \tag{3.7}$$

which with zero means becomes

$$C_{XY}(k) = \big\langle X_i\, Y_{i+k} \big\rangle, \qquad C_{XY}(0) = \big\langle X_i\, Y_i \big\rangle. \tag{3.8}$$

The cross-covariance matrix is

$$C_{XY}(k) = \begin{bmatrix} \mathrm{cov}(X_1, Y_1) & \mathrm{cov}(X_1, Y_2) & \cdots & \mathrm{cov}(X_1, Y_n) \\ \mathrm{cov}(X_2, Y_1) & \mathrm{cov}(X_2, Y2) & \cdots & \mathrm{cov}(X_2, Y_n) \\ \vdots & \vdots & \ddots & \vdots \\ \mathrm{cov}(X_n, Y_1) & \mathrm{cov}(X_n, Y_2) & \cdots & \mathrm{cov}(X_n, Y_n) \end{bmatrix}, \tag{3.9}$$

where, as for the auto-covariance matrix, the zero lag terms are along the main diagonal with the others providing the off-diagonal values.

The combined covariance matrix

Combining the auto-covariance and the cross-covariance matrices produces a block matrix which is

$$C = \begin{bmatrix} C_{11} & C_{12} & \cdots & C_{1n} \\ C_{21} & C_{22} & \cdots & C_{2n} \\ \vdots & \vdots & \ddots & \vdots \\ C_{n1} & C_{n2} & \cdots & C_{nn} \end{bmatrix}, \tag{3.10}$$

where C_{ij} are blocks. The size of the blocks depends on the number of variables. The diagonal C_{ii} and off-diagonal C_{ij} blocks are given by

$$C_{ii} = \begin{bmatrix} \mathrm{var}(X_i) & \mathrm{cov}(X_i, Y_i) \\ \mathrm{cov}(X_i, Y_i) & \mathrm{var}(Y_i) \end{bmatrix}, \quad C_{ij} = \begin{bmatrix} \mathrm{cov}(X_i, X_j) & \mathrm{cov}(X_i, Y_j) \\ \mathrm{cov}(Y_i, X_j) & \mathrm{cov}(Y_i, Y_j) \end{bmatrix}. \tag{3.11}$$

3.1.2 Power spectral densities

In the frequency domain this is expressed in terms of the auto-power and cross-power spectral densities which defines how the power of the signal is distributed with frequency. These can be obtained from their corresponding covariance functions through the Fourier transform. The Wiener-Khinchin theorem gives the relationship between

the autocorrelation function $R_{XX}(k)$ and the auto-power spectral density which is

$$S_{XX}(k) = \sum_{k=-\infty}^{\infty} R_{XX}(n)\, e^{-2\pi ikn/N}. \tag{3.12}$$

The auto-correlation function is related to the auto-covariance function by

$$C_{XX}k = R_{XX}(k) - \langle X_i \rangle \langle X_{i+k} \rangle \tag{3.13}$$

with zero means they are the same. So that the Wiener-Khinchin is also true for the auto-covariance function. It can be extended to include the cross-correlations and the cross-power spectral densities are obtained by

$$S_{XY}(k) = \sum_{k=-\infty}^{\infty} R_{XY}(n)\, e^{-2\pi ikn/N} \tag{3.14}$$

where the relationship between the cross-correlation and the auto-covariance functions [34] is

$$C_{XY}(k) = R_{XY}(k) - \langle X_i \rangle \langle Y_{i+k} \rangle. \tag{3.15}$$

Power spectral density matrix

Unlike covariances which can occur between different times generally there are no correlations between different frequencies. The complex spectra means that the computation of the power spectral densities involves the use of complex conjugates and the auto-power and cross-power spectral densities are defined as

$$\begin{aligned} S_{XX}(f) &= \mathrm{var}[\widetilde{X}(f)] = \mathrm{cov}[\widetilde{X}(f), \widetilde{X}^*(f)], \\ S_{XY}(f) &= \mathrm{cov}[\widetilde{X}(f), \widetilde{Y}^*(f)], \end{aligned} \tag{3.16}$$

where $\widetilde{X}^*(f)$ is the complex conjugate of $\widetilde{X}(f)$. The lack of correlations between different frequencies mean that the power spectral density matrices are diagonal. The auto- and cross-power spectral densities matrices are respectively

$$C_{XX} = \begin{bmatrix} S_{XX}(1) & 0 & \cdots & 0 \\ 0 & S_{XX}(2) & \cdots & 0 \\ \vdots & \vdots & \ddots & \vdots \\ 0 & 0 & \cdots & S_{XX}(n) \end{bmatrix}, \tag{3.17}$$

and

$$C_{XY} = \begin{bmatrix} S_{XY}(1) & 0 & \cdots & 0 \\ 0 & S_{XY}(2) & \cdots & 0 \\ \vdots & \vdots & \ddots & \vdots \\ 0 & 0 & \cdots & S_{XY}(n) \end{bmatrix}. \tag{3.18}$$

As is the case for the time domain covariance matrices the combined matrix will be a block matrix with the size of the blocks dependent on the number of variables. The combined matrix and blocks are

$$C = \begin{bmatrix} C_{11} & 0 & \cdots & 0 \\ 0 & C_{22} & \cdots & 0 \\ \vdots & \vdots & \ddots & \vdots \\ 0 & 0 & \cdots & C_{nn} \end{bmatrix}. \tag{3.19}$$

and

$$C_{ii} = \begin{bmatrix} S_{XX}(i) & S_{XY}(i) \\ S_{XY}(i) & S_{YY}(i) \end{bmatrix}. \tag{3.20}$$

3.2 Raw data covariance and power spectral density matrices

LISA data consist of time series from the six optical benches monitoring the three arms. Each optical bench reading is a beating of the beam of local laser with that received from the other bench at the end of the adjacent arm and will therefore contain two laser noises and the noise from the recording photodetector. The inter-spacecraft raw data in terms of noise contributions can be written as

$$s_i(t) = p_{j'}(t - D_k) - p_i(t) + n_i(t), \tag{3.21}$$

where p_i and p_j are the laser phase noises from the receiving and transmitting optical benches and n_i is the photodetector noise of the receiving optical bench [6]. The noises are assumed to be random therefore, correlations between readings will only occur if the same noise occurs in different readings. For example, the two optical bench readings

$(s_i,\, s_{j'})$ at the end of arm k can be written as

$$\begin{aligned} s_i(t_a) &= p_{j'}(t_a - D_k) - p_i(t_a) + n_i(t_a), \\ s_{j'}(t_b) &= p_i(t_b - D_k) - p_{j'}(t_b) + n_{j'}(t_b), \end{aligned} \tag{3.22}$$

where they both contain the same noises p_i and $p_{j'}$ but they have times that differ by the same offset D_k. This will cause correlations between the two readings when $t_a - t_b = \pm D_k$. This will also occur between the readings at the ends of the other two arms.

In this representation of the noises in the data the laser noises are assumed to be acting independently. With LISA there is the option of locking the phases of the lasers, that is, phase-locking. Two other possibilities are locking the lasers on each spacecraft together which will allow of the simulation of a beam splitter on each spacecraft, or locking all the lasers to one (master) which allows for splitting and reflection. As expected phase-locking will increase the number of correlations between the different readings. The interesting option is the latter which will not only cause correlation between the different optical bench readings but also within in the readings themselves. With this option the lasers will all be acting as one therefore, $p_i = p$ and Equation 3.21 will become

$$s_i(t) = p(t - D_k) - p(t) + n_i(t),$$

where there will also be correlations between the lasers in the readings at times t and $t - D_k$.

3.2.1 LISA toy model assumptions

The assumptions that will be used for computing the covariances are that the laser phase and shot noises are both white Gaussian processes with zero means and variances of σ_p^2 and σ_n^2, respectively. The conditions for correlations for these noises are

$$\text{Rule 1} \qquad \langle n_a[t_c] n_b[t_d] \rangle = \delta_{ab}\delta_{cd}\sigma_n^2, \tag{3.23}$$

$$\text{Rule 2} \qquad \langle n_a[t_c] p_b[t_d] \rangle = 0, \tag{3.24}$$

where δ_{ab} and δ_{cd} are Dirac delta functions [54] which are given by

$$\delta_{ab} = \begin{cases} 1, & \text{if } a = b, \\ 0, & \text{if } a \neq b, \end{cases} \qquad \text{and} \qquad \delta_{cd} = \begin{cases} 1, & \text{if } c = d, \\ 0, & \text{if } c \neq d. \end{cases} \tag{3.25}$$

For independent lasers or for those locked on each spacecraft correlations between the lasers requires both the optical bench numbers and times have to match. The condition for correlations is

$$\text{Rule 3} \qquad \langle p_a[t_c] p_b[t_d] \rangle = \delta_{ab}\delta_{cd}\sigma_p^2. \tag{3.26}$$

When they are all locked they will act as a single laser and the optical bench number no longer becomes necessary. Correlations occur when the times are the same therefore

$$\text{Rule 4} \qquad \langle p[t_c] p[t_d] \rangle = \delta_{cd}\sigma_p^2. \tag{3.27}$$

3.2.2 Generating the covariance matrices

With the assumption of zero means for the noises the definition for the auto-covariance and cross-covariance functions that will be used are

$$\text{cov}(X_i, X_i) = \big\langle X_i \; X_i \big\rangle, \qquad \text{cov}(X_i, Y_i) = \big\langle X_i \; Y_i \big\rangle. \tag{3.28}$$

The inter-spacecraft readings with the three phase-locking options are listed in Table 3.1 for equal and unequal arm lengths. The labeling and locations of the optical benches, arms and spacecraft are shown in Figure 3.1.

3.2.2.1 Covariances with no laser phase-locking

For independent lasers the contributions for the combined laser phase and photodetector noises in the inter-spacecraft readings can be written as

$$s_i(t) = p_{j'}(t - D_k) - p_i(t) + n_i(t), \tag{3.29}$$

where the primed subscript is used to distinguish between the two lasers on each spacecraft.

Table 3.1: Optical bench time series showing the expressions for the laser phase and photodetector noises in each optical bench reading for the different phase-locking options and with unequal and equal arm lengths.

Phase locking	Phase	Time series	
		Unequal arms($D_i = L_i/c$)	Equal arms $D = L/c$
None	$s_1(t)$	$p_{2'}(t-D_3) - p_1(t) + n_1(t)$	$p_{2'}(t-D) - p_1(t) + n_1(t)$
	$s_{1'}(t)$	$p_3(t-D_2) - p_{1'}(t) + n_{1'}(t)$	$p_3(t-D) - p_{1'}(t) + n_{1'}(t)$
	$s_2(t)$	$p_{3'}(t-D_1) - p_2(t) + n_2(t)$	$p_{3'}(t-D) - p_2(t) + n_2(t)$
	$s_{2'}(t)$	$p_1(t-D_3) - p_{2'}(t) + n_{2'}(t)$	$p_1(t-D) - p_{2'}(t) + n_{2'}(t)$
	$s_3(t)$	$p_{1'}(t-D_2) - p_3(t) + n_3(t)$	$p_{1'}(t-D) - p_3(t) + n_3(t)$
	$s_{3'}(t)$	$p_2(t-D_1) - p_{3'}(t) + n_{3'}(t)$	$p_2(t-D) - p_{3'}(t) + n_{3'}(t)$
Spacecraft	$s_1(t)$	$p_2(t-D_3) - p_1(t) + n_1(t)$	$p_2(t-D) - p_1(t) + n_1(t)$
	$s_{1'}(t)$	$p_3(t-D_2) - p_1(t) + n_{1'}(t)$	$p_3(t-D) - p_1(t) + n_{1'}(t)$
	$s_2(t)$	$p_3(t-D_1) - p_2(t) + n_2(t)$	$p_3(t-D) - p_2(t) + n_2(t)$
	$s_{2'}(t)$	$p_1(t-D_3) - p_2(t) + n_{2'}(t)$	$p_1(t-D) - p_2(t) + n_{2'}(t)$
	$s_3(t)$	$p_1(t-D_2) - p_3(t) + n_3(t)$	$p_1(t-D) - p_3(t) + n_3(t)$
	$s_{3'}(t)$	$p_2(t-D_1) - p_3(t) + n_{3'}(t)$	$p_2(t-D) - p_3(t) + n_{3'}(t)$
All	$s_1(t)$	$p(t-D_3) - p(t) + n_1(t)$	$p(t-D) - p(t) + n_1(t)$
	$s_{1'}(t)$	$p(t-D_2) - p(t) + n_{1'}(t)$	$p(t-D) - p(t) + n_{1'}(t)$
	$s_2(t)$	$p(t-D_1) - p(t) + n_2(t)$	$p(t-D) - p(t) + n_2(t)$
	$s_{2'}(t)$	$p(t-D_3) - p(t) + n_{2'}(t)$	$p(t-D) - p(t) + n_{2'}(t)$
	$s_3(t)$	$p(t-D_2) - p(t) + n_3(t)$	$p(t-D) - p(t) + n_3(t)$
	$s_{3'}(t)$	$p(t-D_1) - p(t) + n_{3'}(t)$	$p(t-D) - p(t) + n_{3'}(t)$

Auto-covariance

Using the reading for the left optical bench on spacecraft 1, for independent lasers this can be written as

$$s_1(t) = p_{2'}(t-D_3) - p_1(t) + n_1(t), \tag{3.30}$$

and its auto-covariance function is defined as

$$\begin{aligned}
\mathrm{cov}[s_1(t_1), s_1(t_2)] &= \Big\langle \big[p_{2'}(t_1-D_3) - p_1(t_2) + n_1(t_a)\big] \times \big[p_{2'}(t_2-D_3) - p_1(t_2) + n_1(t_2)\big] \Big\rangle \\
&= \big\langle p_{2'}(t_1-D_3)\, p_{2'}(t_2-D_3)\big\rangle - \big\langle p_{2'}(t_1-D_3)\, p_1(t_2)\big\rangle \\
&\quad + \big\langle p_{2'}(t_1-D_3)\, n_1(t_2)\big\rangle - \big\langle p_1(t_1)\, p_{2'}(t_2-D_3)\big\rangle \\
&\quad + \big\langle p_1(t_1)\, p_1(t_2)\big\rangle - \big\langle p_1(t_1)\, n_1(t_2)\big\rangle + n_1(t_1)\, p_{2'}(t_2-D_3)\big\rangle \\
&\quad - \big\langle n_1(t_1)\, p_1(t_2)\big\rangle + \big\langle n_1(t_1)\, n_1(t_2)\big\rangle.
\end{aligned} \tag{3.31}$$

There are no correlations between the laser phase and photodetector noises (Rule 2) nor between the different lasers (Rule 3) therefore Equation 3.31 becomes

$$\begin{aligned}
\mathrm{cov}[s_1(t_1), s_1(t_2)] &= \big\langle p_{2'}(t_1-D_3)\, p_{2'}(t_2-D_3)\big\rangle + \big\langle p_1(t_1)\, p_1(t_2)\big\rangle \\
&\quad + \big\langle n_1(t_1)\, n_1(t_2)\big\rangle.
\end{aligned} \tag{3.32}$$

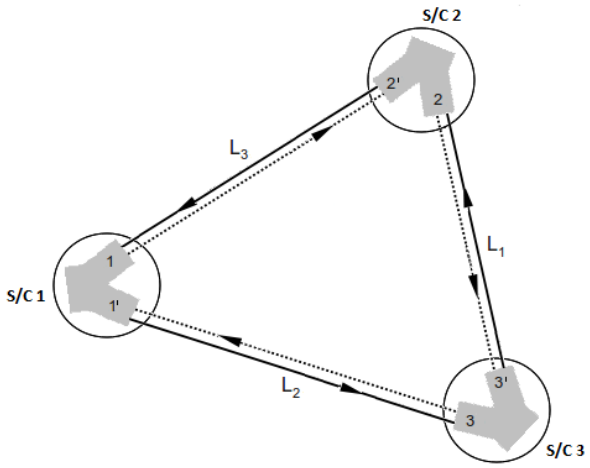

Figure 3.1: A schematic diagram of LISA illustrating the positions and labels of the arms (L_i), optical benches (i, i') and spacecraft (S/C i).

Correlations will only exist when the times are the same, therefore setting $t_1, t_2 = t$ in Equation 3.32 gives

$$\begin{aligned}\mathrm{cov}[s_1(t), s_1(t)] &= \left\langle p_{2'}^2(t - D_3)\right\rangle + \left\langle p_1^2(t)\right\rangle + \left\langle n_1^2(t)\right\rangle \\ &= \mathrm{var}[s_1(t)]. \end{aligned} \tag{3.33}$$

Indicating that the only auto-covariance when the lasers are not phase-locked is for zero lag which is just the variance. Substituting the values for the variances of the different noises into Equation 3.33 gives

$$\mathrm{var}[s_1(t)] = 2\sigma_p^2 + \sigma_n^2. \tag{3.34}$$

For the illustrations in the following sections only the contributions from the correlated noises will be listed that is, terms that are combinations of p_i and n_i or p_i and p_j will be ignored.

Cross-covariances

For independent lasers, the only cross-correlations that will exist are between the raw data from optical benches at the ends of the same arm because only these will contain common laser phase noises. The readings for the optical benches at the end of arm L_3 are

$$\begin{aligned} s_1(t) &= p_{2'}(t - D_3) - p_1(t) + n_1(t), \\ s_{2'}(t) &= p_1(t - D_3) - p_{2'}(t) + n_{2'}(t), \end{aligned} \tag{3.35}$$

where the same laser noises occur in both readings but at different times and their cross-covariance is

$$\begin{aligned}\mathrm{cov}[s_1(t_1), s_{2'}(t_2)] &= \big\langle \big[p_{2'}(t_1 - D_3) - p_1(t_1) + n_1(t_1)\big] \times \big[p_1(t_2 - D_3) - p_{2'}(t_2) + n_{2'}(t_2)\big] \big\rangle \\ &= -\big\langle p_{2'}(t_1 - D_3)\, p_{2'}(t_2)\big\rangle - \big\langle p_1(t_1)\, p_1(t_2 - D_3)\big\rangle. \end{aligned} \tag{3.36}$$

The same noises exist at different times which are offset by the same value (D_3). For $t_2 = t_1 - D_3$ the covariance is

$$\begin{aligned}\mathrm{cov}[s_1(t_1), s_{2'}(t_1 - D_3)] &= -\big\langle p_{2'}(t_1 - D_3)\, p_{2'}(t_1 - D_3)\big\rangle - \big\langle p_1(t_1)\, p_1(t_1 - 2D_3)\big\rangle \\ &= -\big\langle p^2_{2'}(t_1 - D_3)\big\rangle \\ &= -\sigma_p^2, \end{aligned} \tag{3.37}$$

and for $t_1 = t_2 - D_3$ it is

$$\begin{aligned}\mathrm{cov}[s_1(t_2 - D_3), s_{2'}(t_2)] &= -\big\langle p_{2'}(t_2 - 2D_3)\, p_{2'}(t_2)\big\rangle - \big\langle p_1(t_2 - D_3)\, p_1(t_2 - D_3)\big\rangle \\ &= -\big\langle p^2_1(t_2 - D_3)\big\rangle \\ &= -\sigma_p^2, \end{aligned} \tag{3.38}$$

where the contributions are from different optical benches in each case.

Equal arm lengths

For independent lasers the structure of the expressions are not greatly affected by the nature of the arm lengths. The difference is in the location of the correlations which instead of being at the three values given by D_i will only occur at one location determined by D. The equations for the auto-covariance and the cross-covariance with equal arms are easily obtained from Equations 3.33 and 3.36. The auto-covariance with equal arm lengths is

$$\begin{aligned}\mathrm{var}[s_1(t)] &= \big\langle p^2_{2'}(t - D)\big\rangle + \big\langle p^2_1(t)\big\rangle + \big\langle n^2_1(t)\big\rangle \\ &= 2\sigma_p^2 + \sigma_n^2. \end{aligned} \tag{3.39}$$

The cross-covariance between s_1 and $s_{2'}$ with equal arms is

$$\mathrm{cov}[s_1(t_1), s_{2'}(t_2)] = -\big\langle p_{2'}(t_1 - D)\, p_{2'}(t_2)\big\rangle - \big\langle p_1(t_1)\, p_1(t_2 - D)\big\rangle, \tag{3.40}$$

with the covariances occurring at times $t_1 = t_2 - D$ and $t_2 = t_1 - D$.

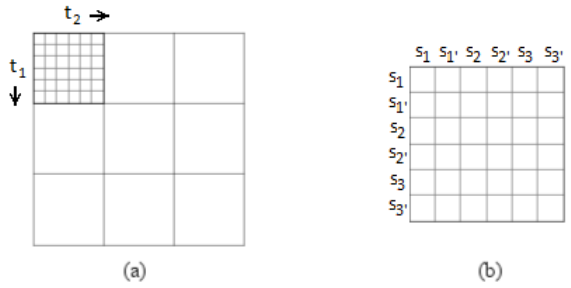

Figure 3.2: A diagram illustrating the block structure of the covariance matrix showing the times in (a) and the labeling of the blocks in (b) where s_i are the optical bench readings.

Summary

The auto- and cross-covariances for all the raw data with no laser phase-locking are given in Figure 3.4 where they are arranged in 6×6 blocks to mimic the block in the covariance matrix shown in Figure 3.2. In Figure 3.4 the times are located at the right edge of the blocks. The results for equal and unequal arm lengths are given. For independent lasers, the auto-covariances when the times are the same, which are the blocks along the main diagonal of the matrix, are restricted to the main diagonal of each block. The values for different times produce two diagonals in the blocks above and below the main diagonal of the block. However, this structure will only occur when the arm lengths are equal. For different arm lengths the correlations will occur in three different blocks because of the three different offsets (D_1, D_2, D_3) occurring in the values. The differences are illustrated in Figure 3.3.

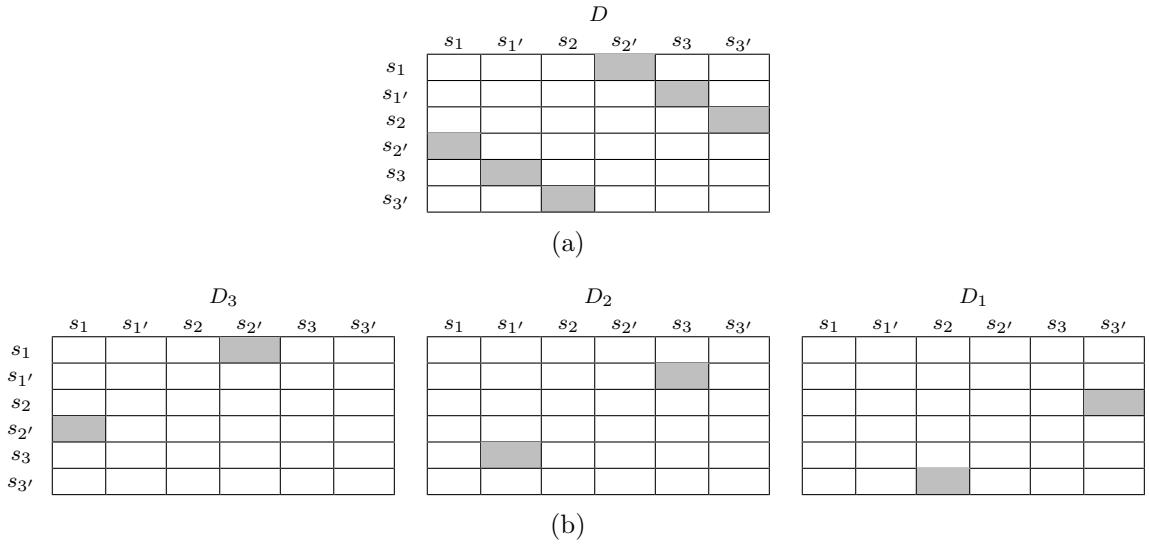

Figure 3.3: The structure of the blocks when the times are not equal illustrating the changes for (a) equal (D) and (b) unequal arm (D_1, D_2, D_3) lengths. The different offsets are shown above the blocks.

(a) SAME TIMES ($t_1 = t_2 = t$)
Unequal arms ($D_i = L_i/c$)

	$s_1(t)$	$s_{1'}(t)$	$s_2(t)$	$s_{2'}(t)$	$s_3(t)$	$s_{3'}(t)$
$s_1(t)$	$\langle p^2_{2'}(t-D_3)\rangle$ $+\langle p^2_1(t)\rangle + \langle n^2_1(t)\rangle$	0	0	0	0	0
$s_{1'}(t)$	0	$\langle p^2_3(t-D_2)\rangle$ $+\langle p^2_{1'}(t)\rangle + \langle n^2_{1'}(t)\rangle$	0	0	0	0
$s_2(t)$	0	0	$\langle p^2_{3'}(t-D_1)\rangle$ $+\langle p^2_2(t)\rangle + \langle n^2_2(t)\rangle$	0	0	0
$s_{2'}(t)$	0	0	0	$\langle p^2_1(t-D_3)\rangle$ $+\langle p^2_{2'}(t)\rangle + \langle n^2_{2'}(t)\rangle$	0	0
$s_3(t)$	0	0	0	0	$\langle p^2_{1'}(t-D_2)\rangle$ $+\langle p^2_3(t)\rangle + \langle n^2_3(t)\rangle$	0
$s_{3'}(t)$	0	0	0	0	0	$\langle p^2_2(t-D_1)\rangle$ $+\langle p^2_{3'}(t)\rangle + \langle n^2_1(t)\rangle$

Equal arm ($\mathbf{D = L/c}$)

	$s_1(t)$	$s_{1'}(t)$	$s_2(t)$	$s_{2'}(t)$	$s_3(t)$	$s_{3'}(t)$
$s_1(t_1)$	$\langle p^2_{2'}(t-D)\rangle$ $+\langle p^2_1(t)\rangle + \langle n^2_1(t)\rangle$	0	0	0	0	0
$s_{1'}(t)$	0	$\langle p^2_3(t-D)\rangle$ $+\langle p^2_{1'}(t)\rangle + \langle n^2_{1'}(t)\rangle$	0	0	0	0
$s_2(t)$	0	0	$\langle p^2_{3'}(t-D)\rangle$ $+\langle p^2_2(t)\rangle + \langle n^2_2(t)\rangle$	0	0	0
$s_{2'}(t)$	0	0	0	$\langle p^2_1(t-D)\rangle$ $+\langle p^2_{2'}(t)\rangle + \langle n^2_{2'}(t)\rangle$	0	0
$s_3(t)$	0	0	0	0	$\langle p^2_{1'}(t-D)\rangle$ $+\langle p^2_3(t)\rangle + \langle n^2_3(t)\rangle$	0
$s_{3'}(t)$	0	0	0	0	0	$\langle p^2_2(t-D)\rangle$ $+\langle p^2_{3'}(t)\rangle + \langle n^2_1(t)\rangle$

(b) DIFFERENT TIMES ($t_1 \neq t_2$)
Unequal arms ($D_i = L_i/c$)

	$s_1(t_2)$	$s_{1'}(t_2)$	$s_2(t_2)$	$s_{2'}(t_2)$	$s_3(t_2)$	$s_{3'}(t_2)$
$s_1(t_1)$	0	0	0	$-\langle p_1(t_1)p_1(t_2-D_3)\rangle$ $-\langle p_{2'}(t_1-D_3)p_{2'}(t_2)\rangle$	0	0
$s_{1'}(t_1)$	0	0	0	0	$\langle p_{1'}(t_1)p_{1'}(t_2-D_2)\rangle$ $-\langle p_3(t_1-D_2)p_3(t_2)\rangle$	0
$s_2(t_1)$	0	0	0	0	0	$\langle p_2(t_1)p_2(t_2-D_1)\rangle$ $-\langle p_{3'}(t_1-D_1)p_{3'}(t_2)\rangle$
$s_{2'}(t_1)$	$-\langle p_1(t_1-D_3)p_1(t_2)\rangle$ $-\langle p_{2'}(t_1)p_{2'}(t_2-D_3)\rangle$	0	0	0	0	0
$s_3(t_1)$	0	$\langle p_{1'}(t_1-D_2)p_{1'}(t_2)\rangle$ $-\langle p_3(t_1)p_3(t_2-D_2)\rangle$	0	0	0	0
$s_{3'}(t_1)$	0	0	$\langle p_2(t_1-D_1)p_2(t_2)\rangle$ $-\langle p_{3'}(t_1)p_{3'}(t_2-D_1)\rangle$	0	0	0

Equal arms ($\mathbf{D = L/c}$)

	$s_1(t_2)$	$s_{1'}(t_2)$	$s_2(t_2)$	$s_{2'}(t_2)$	$s_3(t_2)$	$s_{3'}(t_2)$
$s_1(t_1)$	0	0	0	$-\langle p_1(t_1)p_1(t_2-D)\rangle$ $-\langle p_{2'}(t_1-D)p_{2'}(t_2)\rangle$	0	0
$s_{1'}(t_1)$	0	0	0	0	$\langle p_{1'}(t_1)p_{1'}(t_2-D)\rangle$ $-\langle p_3(t_1-D)p_3(t_2)\rangle$	0
$s_2(t_1)$	0	0	0	0	0	$\langle p_2(t_1)p_2(t_2-D)\rangle$ $-\langle p_{3'}(t_1-D)p_{3'}(t_2)\rangle$
$s_{2'}(t_1)$	$-\langle p_1(t_1-D)p_1(t_2)\rangle$ $-\langle p_{2'}(t_1)p_{2'}(t_2-D)\rangle$	0	0	0	0	0
$s_3(t_1)$	0	$\langle p_{1'}(t_1-D)p_{1'}(t_2)\rangle$ $-\langle p_3(t_1)p_3(t_2-D)\rangle$	0	0	0	0
$s_{3'}(t_1)$	0	0	$\langle p_2(t_1-D)p_2(t_2)\rangle$ $-\langle p_{3'}(t_1)p_{3'}(t_2-D)\rangle$	0	0	0

Figure 3.4: Raw data covariances when all lasers are operating independently, that is, the lasers are not phase-locked. The blocks are grouped according to equal times (top) and unequal times (bottom). The expressions in the cells are the noise covariances between the optical benches.

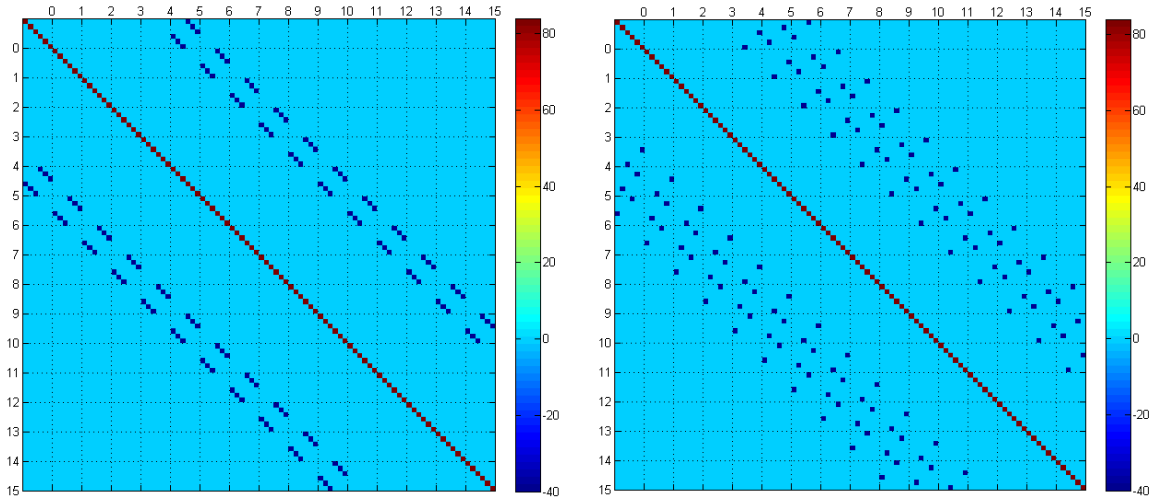

(a) (b)

Figure 3.5: Samples of the raw data covariance matrices for no laser phase-locking with (a) equal and (a) unequal arm lengths.

Sample covariance matrices for independent lasers

The values used for generating the covariances matrices are given in Table 3.2. These were chosen to allow illustration of the structure of the matrices in a small space, therefore, they do not represent real values for LISA. The range of values that the divisions cover in the colour scheme used to display the matrices in the figures is set by MATLAB. Differences between the covariances that are less than these division will not show up in the figures. The values for the noise variances were chosen to overcome this problem. This is more relevant for the case where all the lasers are locked but for consistency the same values are used for all the phase locking options.

Samples of the covariance matrices for independent lasers with equal and unequal arm lengths are shown in Figure 3.5. The times are listed at the top and left hand side of the figures. The matrices are both symmetric about the main diagonal with entries occurring in 6×6 blocks. As expected, with equal arm lengths the matrix has three diagonals with the blocks on the main diagonal having values only along their main diagonal. The other diagonals are offset from the main diagonal of the matrix by the light travel time in the arm length D. For unequal arm lengths the main diagonal of the matrix is still the same but the two diagonals obtained for equal arms have now been split into three diagonals at offsets of 4, 5 and 6 which are the light travel times in the different arms.

Table 3.2: Values used for generating the covariances for all sample matrices.

Variable	Value
Laser frequency noise variance, σ_p^2	40
Photodetector noise variance, σ_n^2	4
Arm lengths (seconds)	
Equal, D	5
Unequal, D_i	4, 5, 6

3.2.2.2 Covariances with laser phase-locking on each spacecraft

When the lasers are phase-locked on each spacecraft the readings for the two optical benches on a spacecraft can be written as

$$\begin{aligned} s_i(t) &= p_j(t - D_k) - p_i(t) + n_i(t), \\ s_{i'}(t) &= p_k(t - D_j) - p_i(t) + n_{i'}(t), \end{aligned} \tag{3.41}$$

where correlations will now exist between them. There will also be correlations between the raw data from the optical bench on one spacecraft and those from the two optical benches on the spacecraft at the end of the adjacent arm. This happens because of they will now contain the same laser noises. For example, the readings for spacecraft j which is at the end of arm L_k are $s_j(t)$ and $s_{j'}(t)$ which are

$$\begin{aligned} s_{j'}(t) &= p_i(t - D_k) - p_j(t) + n_{j'}(t), \\ s_j(t) &= p_k(t - D_i) - p_j(t) + n_j(t), \end{aligned} \tag{3.42}$$

where the common laser phase noise p_j is also present in $s_i(t)$ in Equation 3.41.

Auto-covariances

The auto-covariance will be the same as for the independent lasers with the only change being the dropping of the primed notation for the laser noises. Since there still only two different noises in the readings only the variance will have non-zero values which for unequal arm lengths is

$$\text{var}[s_1(t)] = \left\langle p_2^2(t - D_3) \right\rangle + \left\langle p_1^2(t) \right\rangle + \left\langle n_1^2(t) \right\rangle, \tag{3.43}$$

with values of $2\sigma_p^2 + \sigma_n^2$ in each case which is the same as for independent lasers. With equal arm lengths the only change is the replacement of D_3 with D.

Cross-covariances

This will be computed for only three combinations of readings to illustrate the different types correlations between the optical benches. This will be between the raw data from the optical benches on spacecraft 1, between those at the end of arm L_3 and between the right optical bench of spacecraft 1 and the left optical bench of spacecraft 2. The equations for these optical benches with spacecraft locking are

$$\begin{aligned} s_1(t) &= p_2(t - D_3) - p_1(t) + n_1(t), \\ s_{1'}(t) &= p_3(t - D_2) - p_1(t) + n_{1'}(t), \\ s_2(t) &= p_3(t - D_1) - p_2(t) + n_2(t), \\ s_{2'}(t) &= p_1(t - D_3) - p_2(t) + n_{2'}(t). \end{aligned} \tag{3.44}$$

The cross-covariance between the raw data form the optical benches on spacecraft 1 is

$$\begin{aligned} \mathrm{cov}[s_1(t_1), s_{1'}(t_2)] &= \big\langle \big[p_2(t_1 - D_3) - p_1(t_1) + n_1(t_1)\big] \times \big[p_3(t_2 - D_2) - p_1(t_2) + n_{1'}(t_2)\big] \big\rangle \\ &= \big\langle p_1(t_1)\, p_1(t_2) \big\rangle. \end{aligned} \tag{3.45}$$

which will result in correlations when the times are equal giving

$$\begin{aligned} \mathrm{cov}[s_1(t), s_{i'}(1)] &= \big\langle p_1^2(t) \big\rangle \\ &= \sigma_p^2. \end{aligned} \tag{3.46}$$

Since these do not have any offset times the result will be same for equal arm lengths.

The cross-covariance between the raw data from the optical benches at the end of arm L_3 which are $s_1(t)$ and $s_{2'}(t)$ is

$$\begin{aligned} \mathrm{cov}[s_1(t_1), s_{2'}(t_2)] &= \big\langle \big[p_2(t_1 - D_3) - p_1(t_1) + n_1(t_1)\big] \times \big[p_1(t_2 - D_3) - p_2(t_2) + n_{2'}(t_2)\big] \big\rangle \\ &= -\big\langle p_2(t_1 - D_3)\, p_2(t_2) \big\rangle - \big\langle p_1(t_1)\, p_1(t_2 - D_3) \big\rangle, \end{aligned} \tag{3.47}$$

where the only difference between this and the independent lasers is the absence of the primed values. This will give values of $-\sigma_p^2$ which will occur at offsets of $t_1 - t_2 = \pm D_3$. The only change with equal arm lengths is that the offsets are just D.

The cross-covariance between the raw data from the right optical bench of spacecraft 1 and that from the left optical bench of spacecraft 2 is

$$\begin{aligned} \mathrm{cov}[s_{1'}(t_1), s_2(t_2)] &= \big\langle \big[p_3(t_1 - D_2) - p_1(t_1) + n_{1'}(t_1)\big] \times \big[p_3(t_2 - D_1) - p_2(t_2) + n_2(t_2)\big] \big\rangle \\ &= \big\langle p_3(t_1 - D_2)\, p_3(t_2 - D_1) \big\rangle, \end{aligned} \tag{3.48}$$

where the correlation exist at two offset times of $t_1 - D_2$ and $t_2 - D_3$. The correlation will occur at $t_1 - t_2 = \pm(D_3 - D_2)$ with values of σ_p^2. This time there is a difference with the equal arm lengths which is

$$\text{cov}[s_{1'}(t_1), s_2(t_2)] = \big\langle p_3(t_1 - D)\; p_3(t_2 - D) \big\rangle. \tag{3.49}$$

where, because of the equal offsets, the only times that correlations will occur are when the times are equal which is

$$\begin{aligned} \text{cov}[s_{1'}(t), s_2(t)] &= \big\langle p_3^2(t) \big\rangle \\ &= \sigma_p^2. \end{aligned} \tag{3.50}$$

With equal arm lengths this correlation occurs in the block on the main diagonal of the matrix but with unequal arm lengths it occurs at a time that is the difference of the offsets $D_3 - D_2$ shifting it away from the main diagonal.

Summary

The locking of the lasers on each spacecraft increases the number of correlations between the raw data which appears in the matrix as an increase in the density of the blocks as illustrated in Figure 3.6. For the unequal arm lengths, although all the values are placed in the same block in Figure 3.6, the correlations will not all occur in one block.

Sample covariance matrices

Figure 3.7 shows samples of the covariance matrices for equal and unequal arm lengths where the variances and arm lengths are the same as used for independent lasers. For equal arm lengths the number of diagonals is the same but with more values in each block, that is, the density of the blocks has increased as expected. For unequal arm lengths the number of correlations in the other diagonals has also increased and so has the number of diagonals with two appearing close to the main diagonal which are due to differences of the offsets $D_i - D_j$.

(a) SAME TIMES ($\mathbf{t_1 = t_2 = t}$)

Unequal arms ($\mathbf{D_i = L_i/c}$)

	$s_1(t)$	$s_{1'}(t)$	$s_2(t)$	$s_{2'}(t)$	$s_3(t)$	$s_{3'}(t)$
$s_1(t)$	$\langle p_2^2(t-D_3)\rangle$ $+\langle p_1^2(t)\rangle + \langle n_1^2(t)\rangle$	$\langle p_1^2(t)\rangle$	0	0	0	0
$s_{1'}(t)$	$\langle p_1^2(t)\rangle$	$\langle p_3^2(t-D_2)\rangle$ $+\langle p_1^2(t)\rangle + \langle n_{1'}^2(t)\rangle$	0	0	0	0
$s_2(t)$	0	0	$\langle p_3^2(t-D_1)\rangle$ $+\langle p_2^2(t)\rangle + \langle n_2^2(t)\rangle$	$\langle p_2^2(t)\rangle$	0	0
$s_{2'}(t)$	0	0	$\langle p_2^2(t)\rangle$	$\langle p_1^2(t-D_3)\rangle$ $+\langle p_2^2(t)\rangle + \langle n_{2'}^2(t)\rangle$	0	0
$s_3(t)$	0	0	0	0	$\langle p_1^2(t-D_2)\rangle$ $+\langle p_3^2(t)\rangle + \langle n_3^2(t)\rangle$	$\langle p_3^2(t)\rangle$
$s_{3'}(t)$	0	0	0	0	$\langle p_3^2(t)\rangle$	$\langle p_2^2(t-D_1)\rangle$ $+\langle p_3^2(t)\rangle + \langle n_1^2(t)\rangle$

Equal arms ($\mathbf{D = L/c}$)

	$s_1(t)$	$s_{1'}(t)$	$s_2(t)$	$s_{2'}(t)$	$s_3(t)$	$s_{3'}(t)$
$s_1(t)$	$\langle p_2^2(t-D)\rangle$ $+\langle p_1^2(t)\rangle + \langle n_1^2(t)\rangle$	$\langle p_1^2(t)\rangle$	0	0	0	$\langle p_2^2(t-D)\rangle$
$s_{1'}(t)$	$\langle p_1^2(t)\rangle$	$\langle p_3^2(t-D)\rangle$ $+\langle p_1^2(t)\rangle + \langle n_{1'}^2(t)\rangle$	$\langle p_3^2(t-D)\rangle$	0	0	0
$s_2(t)$	0	$\langle p_3^2(t-D)\rangle$	$\langle p_3^2(t-D)\rangle$ $+\langle p_2^2(t)\rangle + \langle n_2^2(t)\rangle$	$\langle p_2^2(t)\rangle$	0	0
$s_{2'}(t)$	0	0	$\langle p_2^2(t)\rangle$	$\langle p_1^2(t-D)\rangle$ $+\langle p_2^2(t)\rangle + \langle n_{2'}^2(t)\rangle$	$\langle p_1^2(t-D)\rangle$	0
$s_3(t)$	0	0	0	$\langle p_1^2(t-D)\rangle$	$\langle p_1^2(t-D)\rangle$ $+\langle p_3^2(t)\rangle + \langle n_3^2(t)\rangle$	$\langle p_3^2(t)\rangle$
$s_{3'}(t)$	$\langle p_2^2(t-D)\rangle$	0	0	0	$\langle p_3^2(t)\rangle$	$\langle p_2^2(t-D)\rangle$ $+\langle p_3^2(t)\rangle + \langle n_1^2(t)\rangle$

(b) DIFFERENT TIMES ($\mathbf{t_1 \neq t_2}$)

Unequal arms ($\mathbf{D_i = L_i/c}$)

	$s_1(t_2)$	$s_{1'}(t_2)$	$s_2(t_2)$	$s_{2'}(t_2)$	$s_3(t_2)$	$s_{3'}(t_2)$
$s_1(t_1)$	0	0	$-\langle p_2(t_1-D_3)p_2(t_2)\rangle$	$-\langle p_1(t_1)p_1(t_2-D_3)\rangle$ $-\langle p_1(t_1-D_3)p_1(t_2)\rangle$	$-\langle p_1(t_1)p_1(t_2-D_2)\rangle$	$\langle p_2(t_1-D_3)p_2(t_2-D_1)\rangle$
$s_{1'}(t_1)$	0	0	$\langle p_3(t_1-D_2)p_3(t_2-D_1)\rangle$	$-\langle p_1(t_1)p_1(t_2-D_3)\rangle$	$-\langle p_1(t_1)p_1(t_2-D_2)\rangle$ $-\langle p_3(t_1-D_2)p_3(t_2)\rangle$	$-\langle p_3(t_1-D_2)p_3(t_2)\rangle$
$s_2(t_1)$	$\langle p_2(t_1-D_3)p_2(t_2)\rangle$	$-\langle p_3(t_1-D_1)p_3(t_2-D_2)\rangle$	0	0	$-\langle p_3(t_1-D_1)p_3(t_2)\rangle$	$-\langle p_2(t_1)p_2(t_2-D_1)\rangle$ $-\langle p_3(t_1-D_1)p_3(t_2)\rangle$
$s_{2'}(t_1)$	$-\langle p_1(t_1-D_3)p_1(t_2)\rangle$ $-\langle p_2(t_1)p_2(t_2-D_3)\rangle$	$-\langle p_1(t_1-D_3)p_1(t_2)\rangle$	0	0	$\langle p_1(t_1-D_3)p_1(t_2-D_2)\rangle$	$-\langle p_2(t_1)p_2(t_2-D_1)\rangle$
$s_3(t_1)$	$-\langle p_1(t_1-D_2)p_1(t_2)\rangle$	$-\langle p_1(t_1-D_2)p_1(t_2)\rangle$ $-\langle p_3(t_1)p_3(t_2-D_2)\rangle$	$-\langle p_3(t_1)p_3(t_2-D_1)\rangle$	$\langle p_1(t_1-D_2)p_1(t_2-D_3)\rangle$	0	0
$s_{3'}(t_1)$	$\langle p_2(t_1-D_1)p_2(t_2-D_3)\rangle$	$-\langle p_3(t_1)p_3(t_2-D_2)\rangle$	$-\langle p_2(t_1-D_1)p_2(t_2)\rangle$ $-\langle p_3(t_1)p_3(t_2-D_1)\rangle$	$-\langle p_2(t_1-D_1)p_2(t_2)\rangle$	0	0

Equal arms ($\mathbf{D = L/c}$)

	s_1t_2	$s_{1'}t_2$	s_2t_2	$s_{2'}t_2$	s_3t_2	$s_{3'}t_2$
$s_1(t_1)$	0	0	$-\langle p_2(t_1-D)p_2(t_2)\rangle$	$-\langle p_1(t_1)p_1(t_2-D)\rangle$ $-\langle p_1(t_1-D)p_1(t_2)\rangle$	$-\langle p_1(t_1)p_1(t_2-D)\rangle$	0
$s_{1'}(t_1)$	0	0	0	$-\langle p_1(t_1)p_1(t_2-D)\rangle$	$-\langle p_1(t_1)p_1(t_2-D)\rangle$ $-\langle p_3(t_1-D)p_3(t_2)\rangle$	$-\langle p_3(t_1-D)p_3(t_2)\rangle$
$s_2(t_1)$	$\langle p_2(t_1)p_2(t_2-D)\rangle$	0	0	0	$-\langle p_3(t_1-D)p_3(t_2)\rangle$	$-\langle p_2(t_1)p_2(t_2-D)\rangle$ $-\langle p_3(t_1-D)p_3(t_2)\rangle$
$s_{2'}(t_1)$	$-\langle p_1(t_1-D)p_1(t_2)\rangle$ $-\langle p_2(t_1)p_2(t_2-D)\rangle$	$-\langle p_1(t_1-D)p_1(t_2)\rangle$	0	0	0	$-\langle p_2(t_1)p_2(t_2-D)\rangle$
$s_3(t_1)$	$-\langle p_1(t_1-D)p_1(t_2)\rangle$	$-\langle p_1(t_1-D)p_1(t_2)\rangle$ $-\langle p_3(t_1)p_3(t_2-D)\rangle$	$-\langle p_3(t_1)p_3(t_2-D)\rangle$	0	0	0
$s_{3'}(t_1)$	0	$-\langle p_3(t_1)p_3(t_2-D)\rangle$	$-\langle p_2(t_1-D)p_2(t_2)\rangle$ $-\langle p_3(t_1)p_3(t_2-D)\rangle$	$-\langle p_2(t_1-D)p_2(t_2)\rangle$	0	0

Figure 3.6: The covariances for the raw data when the lasers are phase-locked on each spacecraft for unequal (top) and equal (bottom) arms.

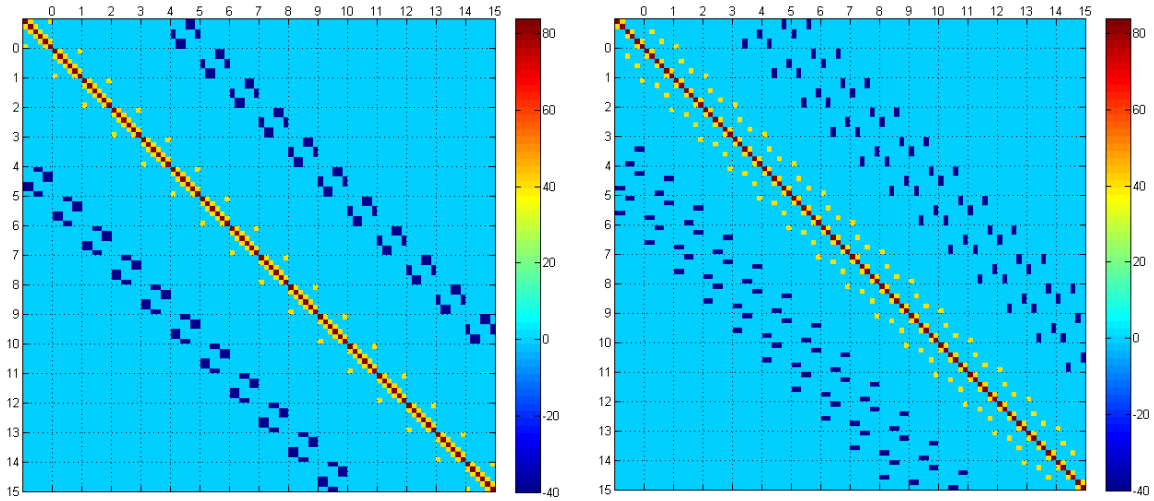

(a) (b)

Figure 3.7: Sample raw data covariance matrices with lasers that are phase-locked on each spacecraft and with (a) equal and (b) unequal arm lengths.

3.2.2.3 Covariances with all lasers phase-locked to a master

When the lasers are all locked to a master they will all have the same noises and the readings will reflect this by having no subscripts associated with the laser noises p. The raw data with all the lasers locked can be written as

$$s_i(t) = p(t - D_k) - p(t) + n_i(t), \tag{3.51}$$

where the two laser noises in the readings are now the same but with different offsets. This will introduce correlations within the same readings ans also with all the other readings.

Auto-covariances

Using the raw data from the left optical bench on spacecraft 1 as an example, with all lasers locked it is

$$s_1(t) = p(t - D_3) - p(t) + n_1(t), \tag{3.52}$$

and its auto-covariance is

$$\begin{aligned} \mathrm{cov}[s_1(t_1), s_1(t_2)] &= \Big\langle \big[p(t_1 - D_3) - p(t_1) + n_1(t_1)\big] \times \big[p(t_2 - D_3) - p(t_2) + n_1(t_2)\big] \Big\rangle \\ &= \big\langle p(t_1 - D_3)\, p(t_2 - D_3) \big\rangle - \big\langle p(t_1 - D_3)\, p(t_2) \big\rangle - \big\langle p(t_1)\, p(t_2 - D_3) \big\rangle \\ &\quad + \big\langle p(t_1)\, p(t_2) \big\rangle + \big\langle n_1(t_1)\, n_1(t_2) \big\rangle, \end{aligned} \tag{3.53}$$

where there are four different times for correlations. For equal times $t_1, t_2 = t$ the auto-covariance for unequal arm lengths is

$$\begin{aligned}\mathrm{cov}[s_1(t)] = \mathrm{var}[s_1(t)] &= \big\langle p^2(t - D_3)\big\rangle + \big\langle p^2(t)\big\rangle + \big\langle n_1^2(t)\big\rangle, \\ &= 2\sigma_p^2 + \sigma_n^2, \end{aligned} \tag{3.54}$$

giving the same structure and values for the variances as the other two phase-locking options. The difference here is that correlations have been introduced between the laser phase noises in the same time series. The different times of these noises in the readings cause correlations away from the main diagonal where $t_a \neq t_b$. The only change with equal arm lengths is that the correlations occur at D instead of D_3.

For times that are not the same $t_a \neq t_b$, the covariance for these are

$$\mathrm{cov}[s_1(t_1), s_1(t_2)] = -\big\langle p(t_1 - D_3)\, p(t_2)\big\rangle - \big\langle p(t_1)\, p(t_2 - D_3)\big\rangle, \tag{3.55}$$

with values of $-\sigma_p^2$ when $t_1 = t_2 - D_3$ and $t_2 = t_1 - D_3$. With equal arm lengths the correlations occur at D instead of D_3 with the same value $-\sigma_p^2$.

Cross-covariances

The illustrations will be done with the raw data from the same optical benches that were used for space craft locked lasers which are those on spacecraft 1 since the structure of the cross-covariances are the same for the rest of the optical benches but with different offsets. The equations for these with all the lasers locked together are

$$\begin{aligned} s_1(t) &= p(t - D_3) - p(t) + n_1(t), \\ s_{1'}(t) &= p(t - D_2) - p(t) + n_{1'}(t), \end{aligned} \tag{3.56}$$

The covariances between the raw data from spacecraft 1 is

$$\begin{aligned}\mathrm{cov}[s_1(t_1), s_{1'}(t_2)] &= \big\langle \big[p(t_1 - D_3) - p(t_1) + n_1(t_1)\big] \times \big[p(t_2 - D_2) - p(t_2) + n_{1'}(t_2)\big]\big\rangle \\ &= \big\langle p(t_1 - D_3)\, p(t_2 - D_2)\big\rangle - \big\langle p(t_1 - D_3)\, p(t_2)\big\rangle \\ &\quad -\big\langle p(t_1)\, p(t_2 - D_2)\big\rangle + \big\langle p(t_1)\, p(t_2)\big\rangle. \end{aligned} \tag{3.57}$$

For $t_1, t_2 = t$ the cross-covariance is

$$\begin{aligned}\mathrm{cov}[s_1(t), s_{1'}(t)] &= \big\langle p^2(t)\big\rangle \\ &= \sigma_p^2, \end{aligned} \tag{3.58}$$

which will be in the blocks along the main diagonal of the matrix but away from the main diagonal of the individual blocks. For $t_1 \neq t_2$ the covariance is

$$\begin{aligned}\mathrm{cov}[s_1(t_1), s_{1'}(t_2)] = \big\langle p(t_1 - D_3)\, p(t_2 - D_2)\big\rangle - \big\langle p(t_1 - D_3)\, p(t_2)\big\rangle \\ -\big\langle p(t_1)\, p(t_2 - D_2)\big\rangle,\end{aligned} \tag{3.59}$$

with correlation occurring at three different times. For $t_1 = t_2 - D_2$ and $t_2 = t_1 - D_3$ the covariances are

$$\begin{aligned}\mathrm{cov}[s_1(t_2 - D_2), s_{1'}(t_2)] &= -\big\langle p^2(t_2 - D_2)\big\rangle, \\ \mathrm{cov}[s_1(t_1), s_{1'}(t_1 - D_3)] &= -\big\langle p^2(t_1 - D_3)\big\rangle,\end{aligned} \tag{3.60}$$

with both having values of $-\sigma_p^2$. For the combinations with two offsets substituting $t_1 = t - D_2$ and $t_2 = t - D_3$ gives

$$\begin{aligned}\mathrm{cov}[s_1(t - D_2), s_{1'}(t - D_3)] &= \big\langle p^2(t - D_2 - D_3)\big\rangle \\ &= \sigma_p^2,\end{aligned} \tag{3.61}$$

where the correlations occur at sums of the offsets in readings $D_2 + D_3$. With equal arm lengths the change will be in Equation 3.61 where the equal arm lengths will shift the correlations to the main where the times are equal.

Summary

The covariances for all the raw data are shown in Figure 3.8 where overall the densities of the blocks have increased and for equal arms they are completely filled.

Sample covariance matrices

Figure 3.9 show the sample matrices where, as expected, the densities of the matrices have increased for both equal and unequal arm lengths. For equal arm lengths there are still three diagonals as seen in the corresponding matrices for the independent and spacecraft locked lasers but in this case all blocks are now filled. For unequal arm lengths only the blocks along the main diagonal are full. There is also an increase in density of the diagonals close the main.

(a) SAME TIMES ($\mathbf{t_1 = t_2 = t}$)
Unequal arms ($\mathbf{D_i = L_i/c}$)

	$s_1(t)$	$s_{1'}(t)$	$s_2(t)$	$s_{2'}(t)$	$s_3(t)$	$s_{3'}(t)$
$s_1(t)$	$\langle p^2(t-D_3)\rangle$ $+\langle p^2(t)\rangle + \langle n_1^2(t)\rangle$	$\langle p^2(t)\rangle$	$\langle p^2(t)\rangle$	$\langle p^2(t)\rangle$	$\langle p^2(t)\rangle$	$\langle p^2(t)\rangle$
$s_{1'}(t)$	$\langle p^2(t)\rangle$	$\langle p^2(t-D_2)\rangle$ $+\langle p^2(t)\rangle + \langle n_{1'}^2(t)\rangle$	$\langle p^2(t)\rangle$	$\langle p^2(t)\rangle$	$\langle p^2(t)\rangle$	$\langle p^2(t)\rangle$
$s_2(t)$	$\langle p^2(t)\rangle$	$\langle p^2(t)\rangle$	$\langle p^2(t-D_1)\rangle$ $+\langle p^2(t)\rangle + \langle n_2^2(t)\rangle$	$\langle p^2(t)\rangle$	$\langle p^2(t)\rangle$	$\langle p^2(t)\rangle$
$s_{2'}(t)$	$\langle p^2(t)\rangle$	$\langle p^2(t)\rangle$	$\langle p^2(t)\rangle$	$\langle p^2(t-D_3)\rangle$ $+\langle p^2(t)\rangle + \langle n_{2'}^2(t)\rangle$	$\langle p^2(t)\rangle$	$\langle p^2(t)\rangle$
$s_3(t)$	$\langle p^2(t)\rangle$	$\langle p^2(t)\rangle$	$\langle p^2(t)\rangle$	$\langle p^2(t)\rangle$	$\langle p^2(t-D_2)\rangle$ $+\langle p^2(t)\rangle + \langle n_3^2(t)\rangle$	$\langle p^2(t)\rangle$
$s_{3'}(t)$	$\langle p^2(t)\rangle$	$\langle p^2(t)\rangle$	$\langle p^2(t)\rangle$	$\langle p^2(t)\rangle$	$\langle p^2(t)\rangle$	$\langle p^2(t-D_1)\rangle$ $+\langle p^2(t)\rangle + \langle n_1^2(t)\rangle$

Equal arms ($\mathbf{D = L/c}$)

	$s_1(t)$	$s_{1'}(t)$	$s_2(t)$	$s_{2'}(t)$	$s_3(t)$	$s_{3'}(t)$
$s_1(t)$	$\langle p^2(t-D)\rangle$ $+\langle p^2(t)\rangle + \langle n_1^2(t)\rangle$	$\langle p^2(t)\rangle + \langle p^2(t-D)\rangle$	$\langle p^2(t)\rangle + \langle p^2(t-D)\rangle$	$\langle p^2(t)\rangle + \langle p^2(t-D)\rangle$	$\langle p^2(t)\rangle + \langle p^2(t-D)\rangle$	$\langle p^2(t)\rangle + \langle p^2(t-D)\rangle$
$s_{1'}(t)$	$\langle p^2(t)\rangle + \langle p^2(t-D)\rangle$	$\langle p^2(t-D)\rangle$ $+\langle p^2(t)\rangle + \langle n_{1'}^2(t)\rangle$	$\langle p^2(t)\rangle + \langle p^2(t-D)\rangle$	$\langle p^2(t)\rangle + \langle p^2(t-D)\rangle$	$\langle p^2(t)\rangle + \langle p^2(t-D)\rangle$	$\langle p^2(t)\rangle + \langle p^2(t-D)\rangle$
$s_2(t)$	$\langle p^2(t)\rangle + \langle p^2(t-D)\rangle$	$\langle p^2(t)\rangle + \langle p^2(t-D)\rangle$	$\langle p^2(t-D)\rangle$ $+\langle p^2(t)\rangle + \langle n_2^2(t)\rangle$	$\langle p^2(t)\rangle + \langle p^2(t-D)\rangle$	$\langle p^2(t)\rangle + \langle p^2(t-D)\rangle$	$\langle p^2(t)\rangle + \langle p^2(t-D)\rangle$
$s_{2'}(t)$	$\langle p^2(t)\rangle + \langle p^2(t-D)\rangle$	$\langle p^2(t)\rangle + \langle p^2(t-D)\rangle$	$\langle p^2(t)\rangle + \langle p^2(t-D)\rangle$	$\langle p^2(t-D)\rangle$ $+\langle p^2(t)\rangle + \langle n_{2'}^2(t)\rangle$	$\langle p^2(t)\rangle + \langle p^2(t-D)\rangle$	$\langle p^2(t)\rangle + \langle p^2(t-D)\rangle$
$s_3(t)$	$\langle p^2(t)\rangle + \langle p^2(t-D)\rangle$	$\langle p^2(t)\rangle + \langle p^2(t-D)\rangle$	$\langle p^2(t)\rangle + \langle p^2(t-D)\rangle$	$\langle p^2(t)\rangle + \langle p^2(t-D)\rangle$	$\langle p^2(t-D)\rangle$ $+\langle p^2(t)\rangle + \langle n_3^2(t)\rangle$	$\langle p^2(t)\rangle + \langle p^2(t-D)\rangle$
$s_{3'}(t)$	$\langle p^2(t)\rangle + \langle p^2(t-D)\rangle$	$\langle p^2(t)\rangle + \langle p^2(t-D)\rangle$	$\langle p^2(t)\rangle + \langle p^2(t-D)\rangle$	$\langle p^2(t)\rangle + \langle p^2(t-D)\rangle$	$\langle p^2(t)\rangle + \langle p^2(t-D)\rangle$	$\langle p^2(t-D)\rangle$ $+\langle p^2(t)\rangle + \langle n_1^2(t)\rangle$

(b) DIFFERENT TIMES ($\mathbf{t_1 \neq t_2}$)
Unequal arms ($\mathbf{D_i = L_i/c}$)

	$s_1(t_2)$	$s_{1'}(t_2)$	$s_2(t_2)$	$s_{2'}(t_2)$	$s_3(t_2)$	$s_{3'}(t_2)$
$s_1(t_1)$	$-\langle p(t_1-D_3)\,p(t_2)\rangle$ $-\langle p(t_a)\,p(t_b-D_3)\rangle$	$-\langle p(t_1)p(t_2-D_2)\rangle$ $-\langle p(t_1-D_3)p(t_2)\rangle$ $+\langle p(t_1-D_3)p(t_2-D_2)\rangle$	$-\langle p(t_1)p(t_2-D_1)\rangle$ $-\langle p(t_1-D_3)p(t_2)\rangle$ $+\langle p(t_1-D_3)p(t_2-D_1)\rangle$	$-\langle p(t_1-D_3)p(t_2)\rangle$ $-\langle p(t_1)p(t_2-D_3)\rangle$ $+\langle p(t_1-D_3)p(t_2-D_3)\rangle$	$-\langle p(t_1)p(t_2-D_2)\rangle$ $-\langle p(t_1-D_3)p(t_2)\rangle$ $+\langle p(t_1-D_3)p(t_2-D_2)\rangle$	$-\langle p(t_1)p(t_2-D_1)\rangle$ $-\langle p(t_1-D_3)p(t_2)\rangle$ $+\langle p(t_1-D_3)p(t_2-D_1)\rangle$
$s_{1'}(t_1)$	$-\langle p(t_1-D_2)p(t_2)\rangle$ $-\langle p(t_1)p(t_2-D_3)\rangle$ $+\langle p(t_1-D_2)p(t_2-D_3)$	$-\langle p(t_1-D_2)\,p(t_2)\rangle$ $-\langle p(t_a)\,p(t_b-D_2)\rangle$	$-\langle p(t_1)p(t_2-D_1)\rangle$ $-\langle p(t_1-D_2)p(t_2)\rangle$ $+\langle p(t_1-D_2)p(t_2-D_1)\rangle$	$-\langle p(t_1-D_2)p(t_2)\rangle$ $-\langle p(t_1)p(t_2-D_3)\rangle$ $+\langle p(t_1-D_2)p(t_2-D_3)\rangle$	$-\langle p(t_1-D_2)p(t_2)\rangle$ $-\langle p(t_1)p(t_2-D_2)\rangle$ $+\langle p(t_1-D_2)p(t_2-D_2)\rangle$	$-\langle p(t_1)p(t_2-D_2)\rangle$ $-\langle p(t_1-D_2)p(t_2)\rangle$ $+\langle p(t_1-D_2)p(t_2-D_2)\rangle$
$s_2(t_1)$	$-\langle p(t_1-D_1)p(t_2)\rangle$ $-\langle p(t_1)p(t_2-D_3)\rangle$ $+\langle p(t_1-D_1)p(t_2-D_3)\rangle$	$-\langle p(t_1-D_1)p(t_2)\rangle$ $-\langle p(t_1)p(t_2-D_2)\rangle$ $+\langle p(t_1-D_1)p(t_2-D_2)\rangle$	$-\langle p(t_1-D_1)\,p(t_2)\rangle$ $-\langle p(t_a)\,p(t_b-D_1)\rangle$	$-\langle p(t_1-D_1)p(t_2)\rangle$ $-\langle p(t_1)p(t_2-D_3)\rangle$ $+\langle p(t_1-D_1)p(t_2-D_3)\rangle$	$-\langle p(t_1-D_1)p(t_2)\rangle$ $-\langle p(t_1)p(t_2-D_2)\rangle$ $+\langle p(t_1-D_1)p(t_2-D_2)\rangle$	$-\langle p(t_1-D_1)p(t_2)\rangle$ $-\langle p(t_1)p(t_2-D_1)\rangle$ $+\langle p(t_1-D_1)p(t_2-D_1)\rangle$
$s_{2'}(t_1)$	$-\langle p(t_1)p(t_2-D_3)\rangle$ $-\langle p(t_1-D_3)p(t_2)\rangle$ $+\langle p(t_1-D_3)p(t_2-D_3)\rangle$	$-\langle p(t_1)p(t_2-D_2)\rangle$ $-\langle p(t_1-D_3)p(t_2)\rangle$ $+\langle p(t_1-D_3)p(t_2-D_2)\rangle$	$-\langle p(t_1)p(t_2-D_1)\rangle$ $-\langle p(t_1-D_3)p(t_2)\rangle$ $+\langle p(t_1-D_3)p(t_2-D_1)\rangle$	$-\langle p(t_1-D_3)\,p(t_2)\rangle$ $-\langle p(t_a)\,p(t_b-D_3)\rangle$	$-\langle p(t_1)p(t_2-D_2)\rangle$ $-\langle p(t_1-D_3)p(t_2)\rangle$ $+\langle p(t_1-D_3)p(t_2-D_2)\rangle$	$-\langle p(t_1)p(t_2-D_1)\rangle$ $-\langle p(t_1-D_3)p(t_2)\rangle$ $+\langle p(t_1-D_3)p(t_2-D_1)\rangle$
$s_3(t_1)$	$-\langle p(t_1-D_2)p(t_2)\rangle$ $-\langle p(t_1)p(t_2-D_3)\rangle$ $+\langle p(t_1-D_2)p(t_2-D_3)\rangle$	$-\langle p(t_1)p(t_2-D_2)\rangle$ $-\langle p(t_1-D_2)p(t_2)\rangle$ $+\langle p(t_1-D_2)p(t_2-D_2)\rangle$	$-\langle p(t_1)p(t_2-D_1)\rangle$ $-\langle p(t_1-D_2)p(t_2)\rangle$ $+\langle p(t_1-D_2)p(t_2-D_1)\rangle$	$-\langle p(t_1)p(t_2-D_1)\rangle$ $-\langle p(t_1)p(t_2-D_3)\rangle$ $+\langle p(t_1-D_2)p(t_2-D_3)\rangle$	$-\langle p(t_1-D_2)\,p(t_2)\rangle$ $-\langle p(t_a)\,p(t_b-D_2)\rangle$	$-\langle p(t_1)p(t_2-D_1)\rangle$ $-\langle p(t_1-D_2)p(t_2)\rangle$ $+\langle p(t_1-D_2)p(t_2-D_1)\rangle$
$s_{3'}(t_1)$	$-\langle p(t_1-D_1)p(t_2)\rangle$ $-\langle p(t_1)p(t_2-D_3)\rangle$ $+\langle p(t_1-D_1)p(t_2-D_3)\rangle$	$-\langle p(t_1-D_2)p(t_2)\rangle$ $-\langle p(t_1)p(t_2-D_2)\rangle$ $+\langle p(t_1-D_2)p(t_2-D_2)\rangle$	$-\langle p(t_1)p(t_2-D_1)\rangle$ $-\langle p(t_1-D_1)p(t_2)\rangle$ $+\langle p(t_1-D_1)p(t_2-D_1)\rangle$	$-\langle p(t_1-D_1)p(t_2)\rangle$ $-\langle p(t_1)p(t_2-D_3)\rangle$ $+\langle p(t_1-D_1)p(t_2-D_3)\rangle$	$-\langle p(t_1-D_1)p(t_2)\rangle$ $-\langle p(t_1)p(t_2-D_2)\rangle$ $+\langle p(t_1-D_1)p(t_2-D_2)\rangle$	$-\langle p(t_1-D_1)\,p(t_2)\rangle$ $-\langle p(t_a)\,p(t_b-D_1)\rangle$

Equal arms ($\mathbf{D = L/c}$)

	$s_1(t_2)$	$s_{1'}(t_2)$	$s_2(t_2)$	$s_{2'}(t_2)$	$s_3(t_2)$	$s_{3'}(t_2)$
$s_1(t_1)$	$-\langle p(t_1-D)\,p(t_2)\rangle$ $-\langle p(t_1)\,p(t_2-D)\rangle$	$-\langle p(t_1)p(t_2-D)\rangle$ $-\langle p(t_1-D)p(t_2)\rangle$	$-\langle p(t_1)p(t_2-D)\rangle$ $-\langle p(t_1-D)p(t_2)\rangle$	$-\langle p(t_1-D)p(t_2)\rangle$ $-\langle p(t_1)p(t_2-D)\rangle$	$-\langle p(t_1)p(t_2-D)\rangle$ $-\langle p(t_1-D)p(t_2)\rangle$	$-\langle p(t_1)p(t_2-D)\rangle$ $-\langle p(t_1-D)p(t_2)\rangle$
$s_{1'}(t_1)$	$-\langle p(t_1-D)p(t_2)\rangle$ $-\langle p(t_1)p(t_2-D)\rangle$	$-\langle p(t_1-D)\,p(t_2)\rangle$ $-\langle p(t_1)\,p(t_2-D)\rangle$	$-\langle p(t_1)p(t_2-D)\rangle$ $-\langle p(t_1-D)p(t_2)\rangle$	$-\langle p(t_1-D)p(t_2)\rangle$ $-\langle p(t_1)p(t_2-D)\rangle$	$-\langle p(t_1-D)p(t_2)\rangle$ $-\langle p(t_1)p(t_2-D)\rangle$	$-\langle p(t_1)p(t_2-D)\rangle$ $-\langle p(t_1-D)p(t_2)\rangle$
$s_2(t_1)$	$-\langle p(t_1-D)p(t_2)\rangle$ $-\langle p(t_1)p(t_2-D)\rangle$	$-\langle p(t_1-D)p(t_2)\rangle$ $-\langle p(t_1)p(t_2-D)\rangle$	$-\langle p(t_1-D)\,p(t_2)\rangle$ $-\langle p(t_1)\,p(t_2-D)\rangle$	$-\langle p(t_1-D)p(t_2)\rangle$ $-\langle p(t_1)p(t_2-D)\rangle$	$-\langle p(t_1-D)p(t_2)\rangle$ $-\langle p(t_1)p(t_2-D)\rangle$	$-\langle p(t_1-D)p(t_2)\rangle$ $-\langle p(t_1)p(t_2-D)\rangle$
$s_{2'}(t_1)$	$-\langle p(t_1)p(t_2-D)\rangle$ $-\langle p(t_1-D)p(t_2)\rangle$	$-\langle p(t_1)p(t_2-D)\rangle$ $-\langle p(t_1-D)p(t_2)\rangle$	$-\langle p(t_1)p(t_2-D)\rangle$ $-\langle p(t_1-D)p(t_2)\rangle$	$-\langle p(t_1)p(t_2-D)\rangle$ $-\langle p(t_1)\,p(t_2-D)\rangle$	$-\langle p(t_1)p(t_2-D)\rangle$ $-\langle p(t_1-D)p(t_2)\rangle$	$-\langle p(t_1)p(t_2-D)\rangle$ $-\langle p(t_1-D)p(t_2)\rangle$
$s_3(t_1)$	$-\langle p(t_1-D)p(t_2)\rangle$ $-\langle p(t_1)p(t_2-D)\rangle$	$-\langle p(t_1)p(t_2-D)\rangle$ $-\langle p(t_1-D)p(t_2)\rangle$	$-\langle p(t_1)p(t_2-D)\rangle$ $-\langle p(t_1-D)p(t_2)\rangle$	$-\langle p(t_1)p(t_2-D)\rangle$ $-\langle p(t_1)p(t_2-D)\rangle$	$-\langle p(t_1-D)\,p(t_2)\rangle$ $-\langle p(t_1)\,p(t_2-D)\rangle$	$-\langle p(t_1)p(t_2-D)\rangle$ $-\langle p(t_1-D)p(t_2)\rangle$
$s_{3'}(t_1)$	$-\langle p(t_1-D)p(t_2)\rangle$ $-\langle p(t_1)p(t_2-D)\rangle$	$-\langle p(t_1)p(t_2-D)\rangle$ $-\langle p(t_1-D)p(t_2)\rangle$	$-\langle p(t_1)p(t_2-D)\rangle$ $-\langle p(t_1-D)p(t_2)\rangle$	$-\langle p(t_1)p(t_2-D)\rangle$ $-\langle p(t_1)p(t_2-D)\rangle$	$-\langle p(t_1)p(t_2-D)\rangle$ $-\langle p(t_1)p(t_2-D)\rangle$	$-\langle p(t_1-D_3)\,p(t_2)\rangle$ $-\langle p(t_1)\,p(t_2-D)\rangle$

Figure 3.8: Raw data covariances with all lasers phased locked to a master for unequal (top) and equal (bottom) arm lengths.

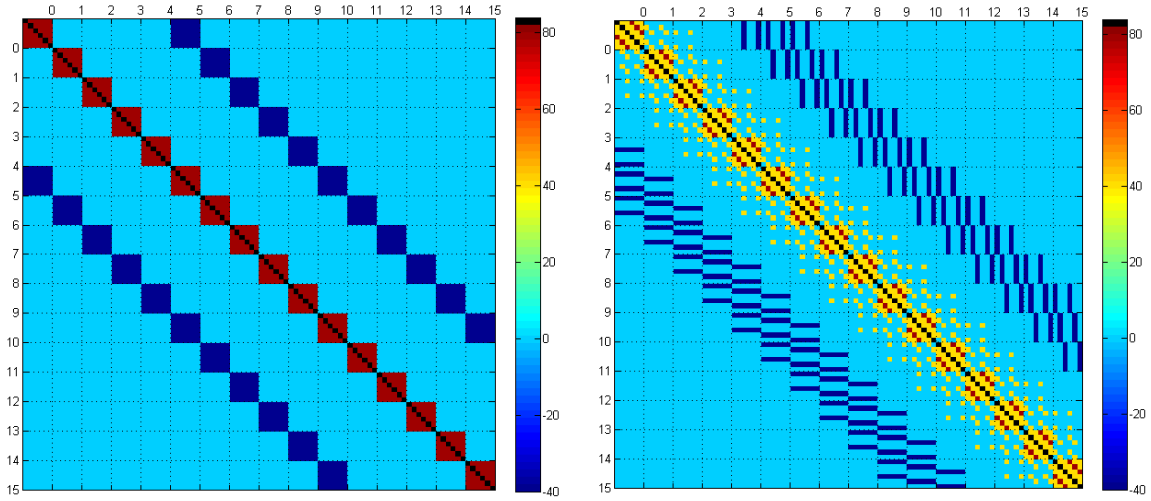

(a) (b)

Figure 3.9: Sample raw data covariance matrices with lasers that are phase-locked on each spacecraft and with (a) equal and (b) unequal arm lengths.

3.2.3 Power spectral density matrix

The process is similar to that used for computing the time domain covariances. First the spectra for the optical bench readings are obtained from the Fourier transform of the time series. Using the general equation for the optical bench time series which can be written as

$$s_l(t) = p_j(t - D_k) - p_l(t) + n_l(t), \tag{3.62}$$

where l and j are the optical bench numbers and k is the number for the arm. Here l is used to avoid confusion with the imaginary number i. The corresponding spectrum is

$$\widetilde{s}_l(f) = \widetilde{p}_{j'}(f)\, e^{-2\pi i f D_k} - \widetilde{p}_l(f) + \widetilde{n}_l(f), \tag{3.63}$$

where $\widetilde{s}_l(f)$ represents the Fourier transform of $s_l(t)$ which is

$$\widetilde{s}_l(f) = \mathcal{F}[s_l(t)] = \int_{-\infty}^{\infty} s_l(t) e^{-2\pi i f t} dt. \tag{3.64}$$

The offset D_k in the time series corresponds to a phase shift $e^{-2\pi i f D_k}$ in the spectrum. The list of all the raw data spectra for equal and unequal arm lengths is given in Table 3.3. As was done for the time series the generation of the power spectral densities will be illustrated with a few examples for the different phase-locking options and for equal and unequal arm lengths.

Table 3.3: Raw data spectra showing the expressions for different types of phase-locking with unequal and equal arm lengths.

Phase-locking	Spectrum	Contributions	
		Unequal arms($D_i = L_i/c$)	Equal arms $D = L/c$
None	$\widetilde{s}_1(f)$	$\widetilde{p}_{2'}(f)\, e^{-2\pi i f D_3} - \widetilde{p}_1(f) + \widetilde{n}_1(f)$	$\widetilde{p}_{2'}(f)\, e^{-2\pi i f D} - \widetilde{p}_1(f) + \widetilde{n}_1(f)$
	$\widetilde{s}_{1'}(f)$	$\widetilde{p}_3(f)\, e^{-2\pi i f D_2} - \widetilde{p}_{1'}(f) + \widetilde{n}_{1'}(f)$	$\widetilde{p}_3(f)\, e^{-2\pi i f D} - \widetilde{p}_{1'}(f) + \widetilde{n}_{1'}(t)$
	$\widetilde{s}_2(f)$	$\widetilde{p}_{3'}(f)\, e^{-2\pi i f D_1} - \widetilde{p}_2(f) + \widetilde{n}_2(f)$	$\widetilde{p}_{3'}(f)\, e^{-2\pi i f D} - \widetilde{p}_2(f) + \widetilde{n}_2(f)$
	$\widetilde{s}_{2'}(f)$	$p_1(f)\, e^{-2\pi i f D_3} - p_{2'}(t) + \widetilde{n}_{2'}(f)$	$\widetilde{p}_1(f)\, e^{-2\pi i f D} - \widetilde{p}_{2'}(f) + \widetilde{n}_{2'}(f)$
	$\widetilde{s}_3(f)$	$\widetilde{p}_{1'}(f)\, e^{-2\pi i f D_2} - \widetilde{p}_3(f) + \widetilde{n}_3(f)$	$\widetilde{p}_{1'}(f)\, e^{-2\pi i f D} - \widetilde{p}_3(f) + \widetilde{n}_3(f)$
	$\widetilde{s}_{3'}(f)$	$\widetilde{p}_2(f)\, e^{-2\pi i f D_1} - \widetilde{p}_{3'}(f) + \widetilde{n}_{3'}(f)$	$\widetilde{p}_2(f)\, e^{-2\pi i f D} - \widetilde{p}_{3'}(f) + \widetilde{n}_{3'}(f)$
Spacecraft	$\widetilde{s}_1(f)$	$\widetilde{p}_2(f)\, e^{-2\pi i f D_3} - \widetilde{p}_1(f) + \widetilde{n}_1(f)$	$\widetilde{p}_2(f)\, e^{-2\pi i f D} - \widetilde{p}_1(f) + \widetilde{n}_1(f)$
	$\widetilde{s}_{1'}(f)$	$\widetilde{p}_3(f)\, e^{-2\pi i f D_2} - \widetilde{p}_1(t) + \widetilde{n}_{1'}(f)$	$\widetilde{p}_3(f)\, e^{-2\pi i f D} - \widetilde{p}_1(f) + \widetilde{n}_{1'}(f)$
	$\widetilde{s}_2(f)$	$\widetilde{p}_3(f)\, e^{-2\pi i f D_1} - \widetilde{p}_2(t) + \widetilde{n}_2(f)$	$\widetilde{p}_3(f)\, e^{-2\pi i f D} - \widetilde{p}_2(f) + \widetilde{n}_2(f)$
	$\widetilde{s}_{2'}(f)$	$\widetilde{p}_1(f)\, e^{-2\pi i f D_3} - \widetilde{p}_2(t) + \widetilde{n}_{2'}(f)$	$\widetilde{p}_1(f)\, e^{-2\pi i f D} - \widetilde{p}_2(f) + \widetilde{n}_{2'}(f)$
	$\widetilde{s}_3(f)$	$\widetilde{p}_1(f)\, e^{-2\pi i f D_2} - \widetilde{p}_3(t) + \widetilde{n}_3(f)$	$\widetilde{p}_1(f)\, e^{-2\pi i f D} - \widetilde{p}_3(f) + \widetilde{n}_3(f)$
	$\widetilde{s}_{3'}(f)$	$\widetilde{p}_2(f)\, e^{-2\pi i f D_1} - \widetilde{p}_3(t) + \widetilde{n}_{3'}(f)$	$\widetilde{p}_2(f)\, e^{-2\pi i f D} - \widetilde{p}_3(f) + \widetilde{n}_{3'}(f)$
All	$\widetilde{s}_1(f)$	$\widetilde{p}(f)\, e^{-2\pi i f D_3} - \widetilde{p}(t) + \widetilde{n}_1(f)$	$\widetilde{p}(f)\, e^{-2\pi i f D} - \widetilde{p}(f) + \widetilde{n}_1(f)$
	$\widetilde{s}_{1'}(f)$	$\widetilde{p}(f)\, e^{-2\pi i f D_2} - \widetilde{p}(t) + \widetilde{n}_{1'}(f)$	$\widetilde{p}(f)\, e^{-2\pi i f D} - \widetilde{p}(f) + \widetilde{n}_{1'}(f)$
	$\widetilde{s}_2(f)$	$\widetilde{p}(f)\, e^{-2\pi i f D_1} - \widetilde{p}(t) + \widetilde{n}_2(f)$	$\widetilde{p}(f)\, e^{-2\pi i f D} - \widetilde{p}(f) + \widetilde{n}_2(f)$
	$\widetilde{s}_{2'}(f)$	$\widetilde{p}(f)\, e^{-2\pi i f D_3} - \widetilde{p}(t) + \widetilde{n}_{2'}(f)$	$\widetilde{p}(f)\, e^{-2\pi i f D} - \widetilde{p}(f) + \widetilde{n}_{2'}(f)$
	$\widetilde{s}_3(f)$	$\widetilde{p}(f)\, e^{-2\pi i f D_2} - \widetilde{p}(t) + \widetilde{n}_3(f)$	$\widetilde{p}(f)\, e^{-2\pi i f D} - \widetilde{p}(f) + \widetilde{n}_3(f)$
	$\widetilde{s}_{3'}(f)$	$\widetilde{p}(f)\, e^{-2\pi i f D_1} - \widetilde{p}(t) + \widetilde{n}_{3'}(f)$	$\widetilde{p}(f)\, e^{-2\pi i f D} - \widetilde{p}(f) + \widetilde{n}_{3'}(f)$

3.2.3.1 Power spectral densities with no laser phase-locking

As shown in the time domain the only optical benches that will have common laser phase noises for when the lasers are not phase-locked are those at the end of an arm. For arm L_3 these are s_1 and $s_{2'}$ which are

$$\begin{aligned}\widetilde{s}_1(f) &= \widetilde{p}_{2'}(f)\, e^{-2\pi i f D_3} - \widetilde{p}_1(f) + \widetilde{n}_1(f),\\ \widetilde{s}_{2'}(f) &= \widetilde{p}_1(f)\, e^{-2\pi i f D_3} - \widetilde{p}_{2'}(f) + \widetilde{n}_{2'}(f).\end{aligned} \tag{3.65}$$

For the power spectral densities only the optical bench numbers will be used, that is, S_{ij} instead of $S_{s_i s_j}$.

Auto-power spectra

For optical bench s_1 the auto-power spectral density is

$$\begin{aligned}S_{11}(f) &= \left\langle [\tilde{p}_{2'}(f) e^{-2\pi i f D_3} - \tilde{p}_1(f) + \tilde{n}_1(f)] \times [\tilde{p}^*_{2'}(f) e^{2\pi i f D_3} - \tilde{p}^*_1(f) + \tilde{n}^*_1(f)] \right\rangle\\ &= \left\langle \tilde{p}^2_{2'}(f) \right\rangle + \left\langle \tilde{p}^2_1(f) \right\rangle + \left\langle \tilde{n}^2_1(f) \right\rangle,\end{aligned} \tag{3.66}$$

which has the same structure as the time domain auto-covariance. Substituting the values for the variances which are σ_p^2 and σ_n^2 gives

$$S_{11}(f) = 2\sigma_p^2 + \sigma_n^2. \tag{3.67}$$

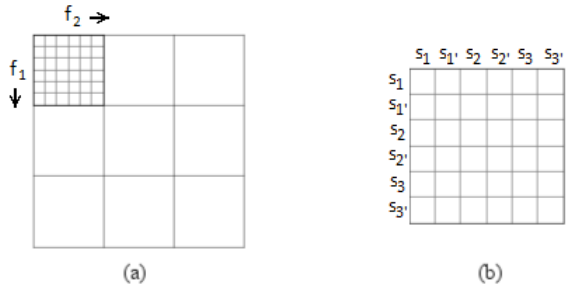

Figure 3.10: A diagram illustrating the block structure of the covariance matrix showing the frequencies in (a) and the labeling of the blocks in (b) where s_i are the optical bench readings.

For equal arm lengths the result is the same.

Cross-power spectra

The cross-power spectral density between the optical benches s_1 and $s_{2'}$ is

$$\begin{aligned} S_{12'}(f) &= \left\langle [\tilde{p}_{2'}(f)e^{-2\pi i f D_3} - \tilde{p}_1(f) + \tilde{n}_1(f)] \times [\tilde{p}_1^*(f)e^{2\pi i f D_3} - \tilde{p}_{2'}^*(f) + \tilde{n}_{2'}^*(f)] \right\rangle \\ &= -\left\langle \tilde{p}_{2'}^2(f) \right\rangle e^{-2\pi i f D_3} - \left\langle \tilde{p}_1^2(f) \right\rangle e^{2\pi i f D_3}. \end{aligned} \tag{3.68}$$

Substituting the values for the variances gives

$$S_{12'}(f) = -\sigma_p^2 \left[e^{-2\pi i f D_3} + e^{2\pi i f D_3} \right], \tag{3.69}$$

where they differ from the time domain by having an exponential term. With equal arm lengths the only change is in the offset.

Summary

As was done for the covariance matrices, the values for all the power spectral densities are given in 6×6 blocks in Figure 3.11 to match the structure in the matrix which is shown in Figure 3.10. With no correlations between frequencies these blocks occur along the main diagonal of the matrix. Unlike the time domain the structure of the blocks will be the actual structure in the matrix as the time offset gives a phase shift and not a shift off the main diagonal as in the time domain. For no phase-locking, like the time domain, the non-zero values of the power-spectral densities in the individual blocks will only occur along the main diagonal and two other diagonals. The difference in the frequency domain is that these are now combined in the same block. Also, the power spectral density matrices will contain two sets of values of either the combined imaginary and real components or the magnitude and phases.

Unequal arms ($\mathbf{D_i = L_i/c}$)

	$s_1(f)$	$s_{1'}(f)$	$s_2(f)$	$s_{2'}(f)$	$s_3(f)$	$s_{3'}(f)$
$s_1(f)$	$\langle\widetilde{p}_{2'}^2(f)\rangle$ $+\langle\widetilde{p}_1^2(f)\rangle + \langle\widetilde{n}_1^2(f)\rangle$	0	0	$-\langle\widetilde{p}_1^2(f)\rangle\, e^{2\pi i f D_3}$ $-\langle\widetilde{p}_{2'}^2(f)\rangle\, e^{-2\pi i f D_3}$	0	0
$s_{1'}(f)$	0	$\langle\widetilde{p}_3^2(f)\rangle$ $+\langle\widetilde{p}_{1'}^2(f)\rangle + \langle\widetilde{n}_{1'}^2(f)\rangle$	0	0	$-\langle\widetilde{p}_{1'}^2(f)\rangle\, e^{2\pi i f D_2}$ $-\langle\widetilde{p}_3^2(f)\rangle\, e^{-2\pi i f D_2}$	0
$s_2(f)$	0	0	$\langle\widetilde{p}_{3'}^2(f)\rangle$ $+\langle\widetilde{p}_2^2(f)\rangle + \langle\widetilde{n}_2^2(f)\rangle$	0	0	$-\langle\widetilde{p}_2^2(f)\rangle\, e^{2\pi i f D_1}$ $-\langle\widetilde{p}_{3'}^2(f)\rangle\, e^{-2\pi i f D_1}$
$s_{2'}(f)$	$-\langle\widetilde{p}_1^2(f)\rangle\, e^{-2\pi i f D_3}$ $-\langle\widetilde{p}_{2'}^2(f)\rangle\, e^{2\pi i f D_3}$	0	0	$\langle\widetilde{p}_1^2(f)\rangle$ $+\langle\widetilde{p}_{2'}^2(f)\rangle + \langle\widetilde{n}_{2'}^2(f)\rangle$	0	0
$s_3(f)$	0	$-\langle\widetilde{p}_{1'}^2(f)\rangle\, e^{-2\pi i f D_2}$ $-\langle\widetilde{p}_3^2(f)\rangle\, e^{2\pi i f D_2}$	0	0	$\langle\widetilde{p}_{1'}^2(f)\rangle$ $+\langle\widetilde{p}_3^2(f)\rangle + \langle\widetilde{n}_3^2(f)\rangle$	0
$s_{3'}(f)$	0	0	$-\langle\widetilde{p}_2^2(f)\rangle\, e^{-2\pi i f D_1}$ $-\langle\widetilde{p}_{3'}^2(f)\rangle\, e^{2\pi i f D_1}$	0	0	$\langle\widetilde{p}_2^2(f)\rangle$ $+\langle\widetilde{p}_{3'}^2(f)\rangle + \langle\widetilde{n}_1^2(f)\rangle$

Equal arms ($\mathbf{D = L/c}$)

	$s_1(f)$	$s_{1'}(f)$	$s_2(f)$	$s_{2'}(f)$	$s_3(f)$	$s_{3'}(f)$
$s_1(f)$	$\langle\widetilde{p}_{2'}^2(f)\rangle$ $+\langle\widetilde{p}_1^2(f)\rangle + \langle\widetilde{n}_1^2(f)\rangle$	0	0	$-\langle\widetilde{p}_1^2(f)\rangle\, e^{2\pi i f D}$ $-\langle\widetilde{p}_{2'}^2(f)\rangle\, e^{-2\pi i f D}$	0	0
$s_{1'}(f)$	0	$\langle\widetilde{p}_3^2(f)\rangle$ $+\langle\widetilde{p}_{1'}^2(f)\rangle + \langle\widetilde{n}_{1'}^2(f)\rangle$	0	0	$-\langle\widetilde{p}_{1'}^2(f)\rangle\, e^{2\pi i f D}$ $-\langle\widetilde{p}_3^2(f)\rangle\, e^{-2\pi i f D}$	0
$s_2(f)$	0	0	$\langle\widetilde{p}_{3'}^2(f)\rangle$ $+\langle\widetilde{p}_2^2(f)\rangle + \langle\widetilde{n}_2^2(f)\rangle$	0	0	$-\langle\widetilde{p}_2^2(f)\rangle\, e^{2\pi i f D}$ $-\langle\widetilde{p}_{3'}^2(f)\rangle\, e^{-2\pi i f D}$
$s_{2'}(f)$	$-\langle\widetilde{p}_1^2(f)\rangle\, e^{-2\pi i f D}$ $-\langle\widetilde{p}_{2'}^2(f)\rangle\, e^{2\pi i f D}$	0	0	$\langle\widetilde{p}_1^2(f)\rangle$ $+\langle\widetilde{p}_{2'}^2(f)\rangle + \langle\widetilde{n}_{2'}^2(f)\rangle$	0	0
$s_3(f)$	0	$-\langle\widetilde{p}_{1'}^2(f)\rangle\, e^{-2\pi i f D}$ $-\langle\widetilde{p}_3^2(f)\rangle\, e^{2\pi i f D}$	0	0	$\langle\widetilde{p}_{1'}^2(f)\rangle$ $+\langle\widetilde{p}_3^2(f)\rangle + \langle\widetilde{n}_3^2(f)\rangle$	0
$s_{3'}(f)$	0	0	$-\langle\widetilde{p}_2^2(f)\rangle\, e^{-2\pi i f D}$ $-\langle\widetilde{p}_{3'}^2(f)\rangle\, e^{2\pi i f D}$	0	0	$\langle\widetilde{p}_2^2(f)\rangle$ $+\langle\widetilde{p}_{3'}^2(f)\rangle + \langle\widetilde{n}_1^2(f)\rangle$

Figure 3.11: Raw data power spectral densities for unequal and equal arm lengths and no phase-locking of the lasers

Sample power spectral density matrices

The values used for generating the matrices are given in Table 3.4. The values for the arm lengths were chosen to avoid integer values occurring in the exponential terms with the integer frequencies used in the computations. The sample matrices are given in Figure 3.12 showing the magnitudes and phases. The matrices containing the magnitudes show the three diagonals in each block. The values in the phase matrices are just values of π which is equivalent to a zero phase shift. For these there are no values along the main diagonal as there are no phase shifts in their values. As expected the magnitudes are same for both types of arm lengths. The phases should show differences in the values along the diagonals however, the small differences between the values do not result in any noticeable variations in the matrix.

Table 3.4: Values used for generating the power spectral densities for all sample matrices.

Variable	Value
Laser frequency noise variance, σ_p^2	40
Photodetector noise variance, σ_n^2	4
Arm lengths (seconds)	
Equal, D	5.3
Unequal, D_i	5.3, 6.3, 7.3

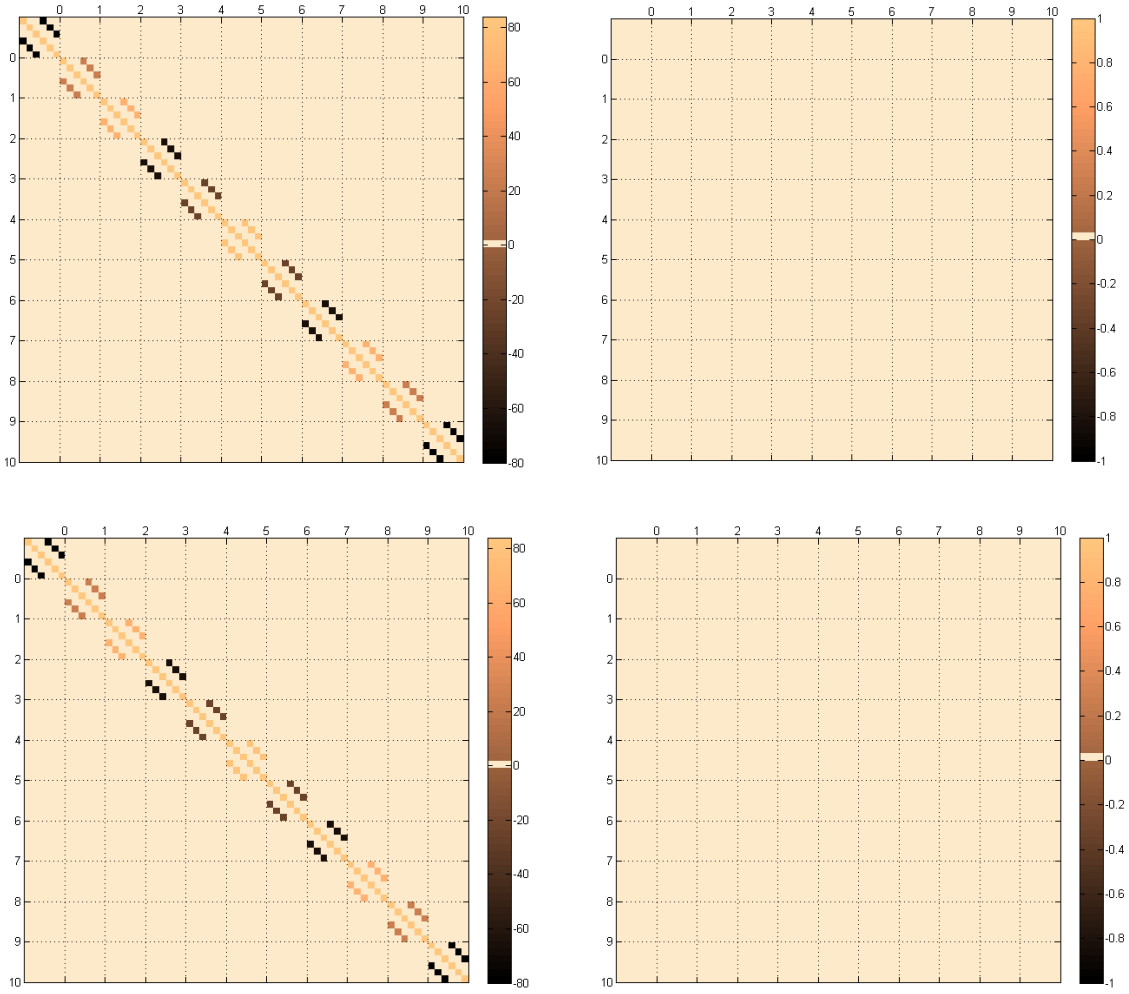

Figure 3.12: Sample raw data power spectral density matrices for independent lasers showing the magnitudes (left) and phases (right) for equal (top) and unequal (bottom) arm lengths.

3.2.3.2 Power spectral densities with laser phase-locking on each spacecraft

Some of the different types of correlations will be illustrated using the optical benches on spacecraft 1 and the spacecraft 2 which are

$$\begin{aligned}
\widetilde{s}_1(f) &= \widetilde{p}_2(f)\, e^{-2\pi i f D_3} - \widetilde{p}_1(f) + \widetilde{n}_1(f), \\
\widetilde{s}_{1'}(f) &= \widetilde{p}_3(f)\, e^{-2\pi i f D_2} - \widetilde{p}_1(f) + \widetilde{n}_{1'}(f), \\
\widetilde{s}_2(f) &= \widetilde{p}_3(f)\, e^{-2\pi i f D_1} - \widetilde{p}_2(f) + \widetilde{n}_2(f), \\
\widetilde{s}_{2'}(f) &= \widetilde{p}_1(f)\, e^{-2\pi i f D_3} - \widetilde{p}_2(f) + \widetilde{n}_{2'}(f).
\end{aligned} \tag{3.70}$$

The full set of power spectral densities are given in Figure 3.13.

Auto-power spectra

The auto-power spectral density for optical bench 1 with unequal arm lengths is

$$\begin{aligned} S_{11}(f) &= \left\langle [\widetilde{p}_2(f)e^{-2\pi i f D_3} - \widetilde{p}_1(f) + \widetilde{n}_1(f)] \times [\widetilde{p}_2^*(f)e^{2\pi i f D_3} - \widetilde{p}_1^*(f) + \widetilde{n}_1^*(f)] \right\rangle \\ &= \left\langle \widetilde{p}_2^2(f) \right\rangle + \left\langle \widetilde{p}_1^2(f) \right\rangle + \left\langle \widetilde{n}_1^2(f) \right\rangle \\ &= 2\sigma_p^2 + \sigma_n^2, \end{aligned} \tag{3.71}$$

which is the same as for no phase-locking and will also be the same for equal arm lengths since the offset does not appear in the final value.

Cross-power spectra

As in the case for lasers that are not phase-locked, the only other correlation that exists is between the optical benches at the end of each arm. For arm L_3 the cross-power spectral density with unequal arm lengths this is

$$\begin{aligned} S_{12'}(f) &= \left\langle [\widetilde{p}_2(f)e^{-2\pi i f D_3} - \widetilde{p}_1(f) + \widetilde{n}_1(f)] \times [\widetilde{p}_1^*(f)e^{2\pi i f D_3} - \widetilde{p}_2^*(f) + \tilde{n}_{2'}^*(f)] \right\rangle \\ &= -\left\langle \widetilde{p}_2^2(f) \right\rangle e^{-2\pi i f D_3} - \left\langle \widetilde{p}_1^2(f) \right\rangle e^{2\pi i f D_3} \\ &= -\sigma_p^2 \left[e^{-2\pi i f D_3} + e^{2\pi i f D_3} \right], \end{aligned} \tag{3.72}$$

which is the same as for no phase-locking and with equal arm lengths the result is the same but with offsets of D.

The cross-power spectral density for the optical benches on the spacecraft 1 with unequal arm lengths is

$$\begin{aligned} S_{11'}(f) &= \left\langle [\widetilde{p}_2(f)e^{-2\pi i f D_3} - \widetilde{p}_1(f) + \widetilde{n}_1(f)] \times [\widetilde{p}_3(f)e^{-2\pi i f D2} - \widetilde{p}_1(f) + \widetilde{n}_{1'}(f)] \right\rangle \\ &= \left\langle \widetilde{p}_1^2(f) \right\rangle \\ &= \sigma_p^2. \end{aligned} \tag{3.73}$$

For equal arm lengths the structure is the same but with offset of D and value is the same. The cross-power spectral density for the left optical bench on spacecraft 1 ($\widetilde{s}_{1'}$) and the right optical bench on spacecraft 2 ($\widetilde{s}_2$) with unequal arm lengths is

$$\begin{aligned} S_{1'2}(f) &= \left\langle [\widetilde{p}_3(f)e^{-2\pi i f D_2} - \widetilde{p}_1(f) + \widetilde{n}_{1'}(f)] \times [\widetilde{p}_3^*(f)e^{2\pi i f D_1} - \widetilde{p}_2^*(f) + \widetilde{n}_2^*(f)] \right\rangle \\ &= \left\langle \widetilde{p}_3^2(f) \right\rangle e^{-2\pi i f (D_2 - D_1)} \\ &= \sigma_p^2 \, e^{-2\pi i f (D_2 - D_1)}. \end{aligned} \tag{3.74}$$

Unequal arms ($\mathbf{D_i = L_i/c}$)

	$s_1(f)$	$s_{1'}(f)$	$s_2(f)$	$s_{2'}(f)$	$s_3(f)$	$s_{3'}(f)$
$s_1(f)$	$\langle\widetilde{p}_2^2(f)\rangle$ $+\langle\widetilde{p}_1^2(f)\rangle + \langle\widetilde{n}_1^2(f)\rangle$	$\langle p_1^2(f)\rangle$	$-\langle\widetilde{p}_2^2(f)\rangle\, e^{-2\pi i f D_3}$	$-\langle\widetilde{p}_1^2(f)\rangle\, e^{2\pi i f D_3}$ $-\langle\widetilde{p}_2^2(f)\rangle\, e^{-2\pi i f D_3}$	$-\langle\widetilde{p}_1^2(f)\rangle\, e^{2\pi i f D_2}$	$\langle\widetilde{p}_2^2(f)\rangle\, e^{2\pi i f(D_1-D_3)}$
$s_{1'}(f)$	$\langle p_1^2(f)\rangle$	$\langle\widetilde{p}_3^2(f)\rangle$ $+\langle\widetilde{p}_1^2(f)\rangle + \langle\widetilde{n}_{1'}^2(f)\rangle$	$\langle\widetilde{p}_3^2(f)\rangle\, e^{2\pi i f(D_1-D_2)}$	$-\langle\widetilde{p}_1^2(f)\rangle\, e^{2\pi i f D_3}$	$-\langle\widetilde{p}_1^2(f)\rangle\, e^{2\pi i f D_2}$ $-\langle\widetilde{p}_3^2(f)\rangle\, e^{-2\pi i f D_2}$	$-\langle\widetilde{p}_3^2(f)\rangle\, e^{-2\pi i f D_2}$
$s_2(f)$	$-\langle\widetilde{p}_2^2(f)\rangle\, e^{2\pi i f D_3}$	$\langle\widetilde{p}_3^2(f)\rangle\, e^{-2\pi i f(D_1-D_2)}$	$\langle\widetilde{p}_3^2(f)\rangle$ $+\langle\widetilde{p}_2^2(f)\rangle + \langle\widetilde{n}_2^2(f)\rangle$	$\langle\widetilde{p}_2^2(f)\rangle$	$-\langle\widetilde{p}_3^2(f)\rangle\, e^{-2\pi i f D_1}$	$-\langle\widetilde{p}_2^2(f)\rangle\, e^{2\pi i f D_1}$ $-\langle\widetilde{p}_3^2(f)\rangle\, e^{-2\pi i f D_1}$
$s_{2'}(f)$	$-\langle\widetilde{p}_1^2(f)\rangle\, e^{-2\pi i f D_3}$ $-\langle\widetilde{p}_2^2(f)\rangle\, e^{2\pi i f D_3}$	$-\langle\widetilde{p}_1^2(f)\rangle\, e^{-2\pi i f D_3}$	$\langle\widetilde{p}_2^2(f)\rangle$	$\langle\widetilde{p}_1^2(f)\rangle$ $+\langle\widetilde{p}_2^2(f)\rangle + \langle\widetilde{n}_{2'}^2(f)\rangle$	$\langle\widetilde{p}_1^2(f)\rangle\, e^{2\pi i f(D_2-D_3)}$	$-\langle\widetilde{p}_2^2(f)\rangle\, e^{2\pi i f D_1}$
$s_3(f)$	$-\langle\widetilde{p}_1^2(f)\rangle\, e^{-2\pi i f D_2}$	$-\langle\widetilde{p}_1^2(f)\rangle\, e^{-2\pi i f D_2}$ $-\langle\widetilde{p}_3^2(f)\rangle\, e^{2\pi i f D_2}$	$-\langle\widetilde{p}_3^2(f)\rangle\, e^{2\pi i f D_1}$	$\langle\widetilde{p}_1^2(f)\rangle\, e^{-2\pi i f(D_2-D_3)}$	$\langle\widetilde{p}_1^2(f)\rangle$ $+\langle\widetilde{p}_3^2(f)\rangle + \langle\widetilde{n}_3^2(f)\rangle$	$\langle\widetilde{p}_3^2(f)\rangle$
$s_{3'}(f)$	$\langle\widetilde{p}_2^2(f)\rangle\, e^{-2\pi i f(D_1-D_3)}$	$-\langle\widetilde{p}_3^2(f)\rangle\, e^{2\pi i f D_2}$	$-\langle\widetilde{p}_2^2(f)\rangle\, e^{-2\pi i f D_1}$ $-\langle\widetilde{p}_3^2(f)\rangle\, e^{2\pi i f D_1}$	$-\langle\widetilde{p}_2^2(f)\rangle\, e^{-2\pi i f D_1}$	$\langle\widetilde{p}_3^2(f)\rangle$	$\langle\widetilde{p}_2^2(f)\rangle$ $+\langle\widetilde{p}_3^2(f)\rangle + \langle\widetilde{n}_1^2(f)\rangle$

Equal arms ($\mathbf{D = L/c}$)

	$s_1(f)$	$s_{1'}(f)$	$s_2(f)$	$s_{2'}(f)$	$s_3(f)$	$s_{3'}(f)$
$s_1(f)$	$\langle\widetilde{p}_2^2(f)\rangle$ $+\langle\widetilde{p}_1^2(f)\rangle + \langle\widetilde{n}_1^2(f)\rangle$	$\langle\widetilde{p}_1^2(f)\rangle$	$-\langle\widetilde{p}_2^2(f)\rangle\, e^{-2\pi i f D}$	$-\langle\widetilde{p}_1^2(f)\rangle\, e^{2\pi i f D}$ $-\langle\widetilde{p}_2^2(f)\rangle\, e^{-2\pi i f D}$	$-\langle\widetilde{p}_1^2(f)\rangle\, e^{2\pi i f D}$	$\langle\widetilde{p}_2^2(f)\rangle$
$s_{1'}(f)$	$\langle\widetilde{p}_1^2(f)\rangle$	$\langle\widetilde{p}_3^2(f)\rangle$ $+\langle\widetilde{p}_1^2(f)\rangle + \langle\widetilde{n}_{1'}^2(f)\rangle$	$\langle\widetilde{p}_3^2(f)\rangle$	$-\langle\widetilde{p}_1^2(f)\rangle\, e^{2\pi i f D}$	$-\langle\widetilde{p}_1^2(f)\rangle\, e^{2\pi i f D}$ $-\langle\widetilde{p}_3^2(f)\rangle\, e^{-2\pi i f D_2}$	$-\langle\widetilde{p}_3^2(f)\rangle\, e^{-2\pi i f D_2}$
$s_2(f)$	$-\langle\widetilde{p}_2^2(f)\rangle\, e^{2\pi i f D}$	$\langle\widetilde{p}_3^2(f)\rangle$	$\langle\widetilde{p}_3^2(f)\rangle$ $+\langle\widetilde{p}_2^2(f)\rangle + \langle\widetilde{n}_2^2(f)\rangle$	$\langle\widetilde{p}_2^2(f)\rangle$	$-\langle\widetilde{p}_3^2(f)\rangle\, e^{-2\pi i f D}$	$-\langle\widetilde{p}_2^2(f)\rangle\, e^{2\pi i f D}$ $-\langle\widetilde{p}_3^2(f)\rangle\, e^{-2\pi i f D}$
$s_{2'}(f)$	$-\langle\widetilde{p}_1^2(f)\rangle\, e^{-2\pi i f D}$ $-\langle\widetilde{p}_2^2(f)\rangle\, e^{2\pi i f D}$	$-\langle\widetilde{p}_1^2(f)\rangle\, e^{-2\pi i f D}$	$\langle\widetilde{p}_2^2(f)\rangle$	$\langle\widetilde{p}_1^2(f)\rangle$ $+\langle\widetilde{p}_2^2(f)\rangle + \langle\widetilde{n}_{2'}^2(f)\rangle$	$\langle\widetilde{p}_1^2(f)\rangle$	$-\langle\widetilde{p}_2^2(f)\rangle\, e^{2\pi i f D}$
$s_3(f)$	$-\langle\widetilde{p}_1^2(f)\rangle\, e^{-2\pi i f D}$	$-\langle\widetilde{p}_1^2(f)\rangle\, e^{-2\pi i f D}$ $-\langle\widetilde{p}_3^2(f)\rangle\, e^{2\pi i f D}$	$-\langle\widetilde{p}_3^2(f)\rangle\, e^{2\pi i f D}$	$\langle\widetilde{p}_1^2(f)\rangle$	$\langle\widetilde{p}_1^2(f)\rangle$ $+\langle\widetilde{p}_3^2(f)\rangle + \langle\widetilde{n}_3^2(f)\rangle$	$\langle\widetilde{p}_3^2(f)\rangle$
$s_{3'}(f)$	$\langle\widetilde{p}_2^2(f)\rangle$	$-\langle\widetilde{p}_3^2(f)\rangle\, e^{2\pi i f D}$	$-\langle\widetilde{p}_2^2(f)\rangle\, e^{-2\pi i f D}$ $-\langle\widetilde{p}_3^2(f)\rangle\, e^{2\pi i f D}$	$-\langle\widetilde{p}_2^2(f)\rangle\, e^{-2\pi i f D}$	$\langle\widetilde{p}_3^2(f)\rangle$	$\langle\widetilde{p}_2^2(f)\rangle$ $+\langle\widetilde{p}_3^2(f)\rangle + \langle\widetilde{n}_1^2(f)\rangle$

Figure 3.13: Raw data power spectral densities with lasers that are phased-locked on each space craft for unequal (top) and equal (bottom) arms

Here the exponential term includes the difference of the time offsets which will disappear with equal arm lengths.

Summary

The values for all the power spectral densities are given in Figure 3.13. The difference caused by the locking of the lasers on each spacecraft is to produce correlations between all the optical benches resulting in full blocks.

Sample power spectral density matrices

The sample raw data power spectral density matrices for the spacecraft phase-locked lasers are given in Figure 3.14 showing the magnitudes and phases for unequal and equal arm lengths. The matrices for the different types of arm lengths have magnitudes that are same with the phases showing small differences.

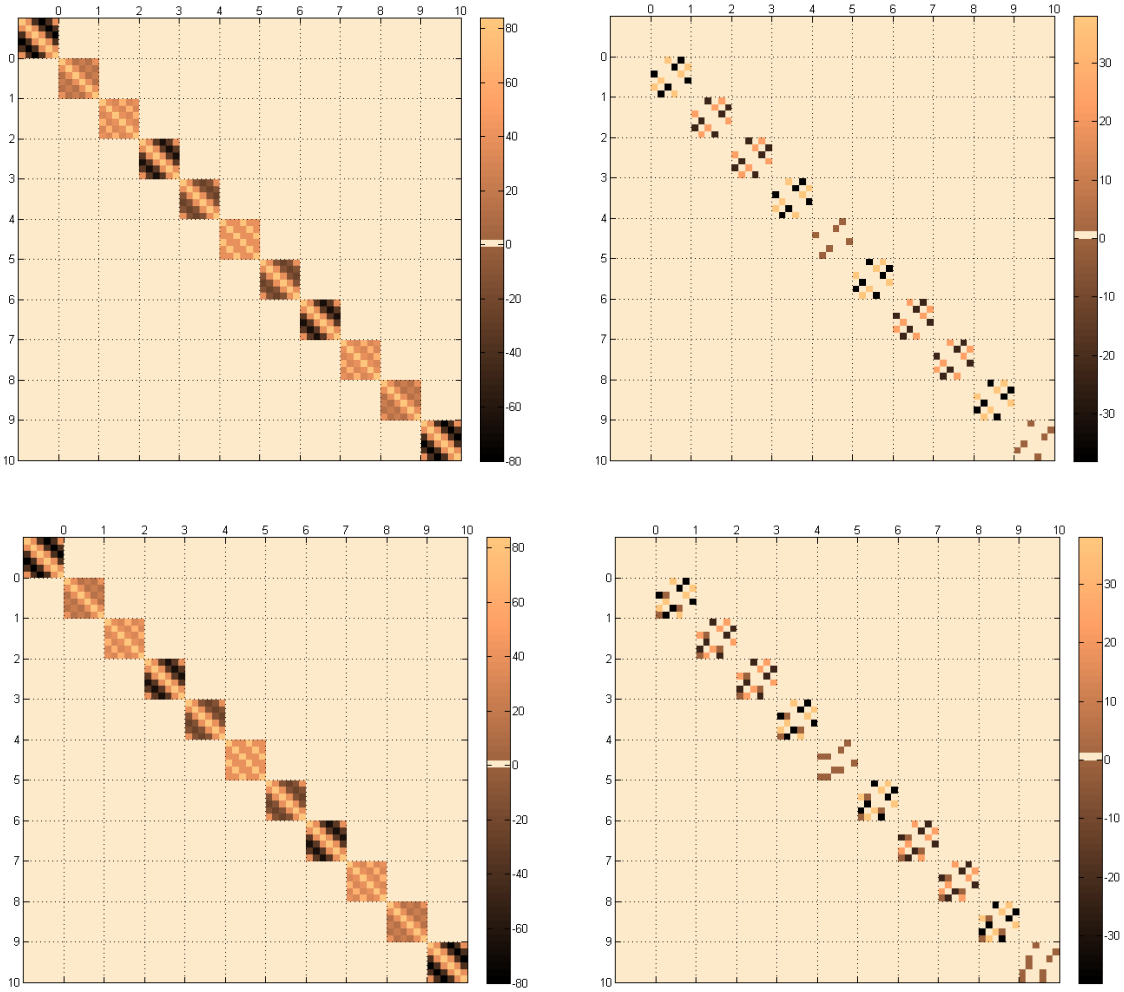

Figure 3.14: Sample raw data power spectral density matrices with the lasers that are phase-locked on each spacecraft showing the magnitudes (left) and phases (right) for equal (top) and unequal (bottom) arm lengths.

3.2.3.3 Power spectral densities with all lasers phase-locked

The spectra for the readings on spacecraft 1 and 2 which are

$$\begin{aligned}
\widetilde{s}_1(f) &= \widetilde{p}(f)\, e^{-2\pi i f D_3} - \widetilde{p}(f) + \widetilde{n}_1(f), \\
\widetilde{s}_{1'}(f) &= \widetilde{p}(f)\, e^{-2\pi i f D_2} - \widetilde{p}(f) + \widetilde{n}_{1'}(f), \\
\widetilde{s}_2(f) &= \widetilde{p}(f)\, e^{-2\pi i f D_1} - \widetilde{p}(f) + \widetilde{n}_2(f), \\
\widetilde{s}_{2'}(f) &= \widetilde{p}(f)\, e^{-2\pi i f D_3} - \widetilde{p}(f) + \widetilde{n}_{2'}(f).
\end{aligned} \tag{3.75}$$

The power spectral densities for all the raw data are given in Table 3.5 and not in a 6×6 blocks as done for the others as the equations are too long.

Auto-power spectra

The auto-power spectral density for optical bench 1 is

$$\begin{aligned} S_{11}(f) &= \left\langle \left[\widetilde{p}(f)e^{-2\pi i f D_3} - \widetilde{p}(f) + \widetilde{n}_1(f)\right] \times \left[\widetilde{p}^*(f)e^{2\pi i f D_3} - \widetilde{p}^*(f) + \widetilde{n}_1^*(f)\right]\right\rangle \\ &= \left\langle \widetilde{p}^2(f)\right\rangle \left[2 - e^{-2\pi i f D_3} - e^{2\pi i f D_3}\right] + \left\langle \widetilde{n}_1^2(f)\right\rangle \\ &= \sigma_p^2\left[2 - e^{-2\pi i f D_3} - e^{2\pi i f D_3}\right] + \sigma_n^2, \end{aligned} \tag{3.76}$$

with the only change for equal arm lengths being the the offsets to D.

Cross-power spectra

For the raw data from the optical benches at the end of arm L_3 the cross-power spectral density is

$$\begin{aligned} S_{12'}(f) &= \left\langle \left[\widetilde{p}(f)e^{-2\pi i f D_3} - \widetilde{p}(f) + \widetilde{n}_1(f)\right] \times \left[\widetilde{p}^*(f)e^{2\pi i f D_3} - \widetilde{p}^*(f) + \widetilde{n}_{2'}^*(f)\right]\right\rangle \\ &= \left\langle \widetilde{p}^2(f)\right\rangle \left[2 - e^{-2\pi i f D_3} - e^{2\pi i f D_3}\right] \\ &= \sigma_p^2\left[2 - e^{-2\pi i f D_3} - e^{2\pi i f D_3}\right], \end{aligned} \tag{3.77}$$

which has the same structure as the auto-power spectral density for the laser phase noises but contains no photodetector noise. With equal arm lengths the only change is with the offsets changing to D.

The cross-power spectral density for the optical benches on the same spacecraft is

$$\begin{aligned} S_{11'}(f) &= \left\langle \left[\widetilde{p}(f)e^{-2\pi i f D_3} - \widetilde{p}(f) + \widetilde{n}_1(f)\right] \times \left[\widetilde{p}^*(f)e^{2\pi i f D_2} - \widetilde{p}^*(f) + \widetilde{n}_{1'}^*(f)\right]\right\rangle \\ &= \left\langle \widetilde{p}^2(f)\right\rangle \left[1 + e^{-2\pi i f (D_3 - D_2)} - e^{-2\pi i f D_3} - e^{2\pi i f D_3}\right] \\ &= \sigma_p^2\left[1 + e^{-2\pi i f (D_3 - D_2)} - e^{-2\pi i f D_3} - e^{2\pi i f D_2}\right]. \end{aligned} \tag{3.78}$$

With equal arm lengths there is a slight change in the structure to

$$S_{11'}(f) = \left\langle \widetilde{p}^2(f)\right\rangle \left[2 - e^{-2\pi i f D} - e^{2\pi i f D}\right] \tag{3.79}$$

which is the same as for cross-power spectral densities between $\widetilde{s}_1$ and $\widetilde{s}_{2'}$ with the same value.

Summary

All the values for the raw data power spectral densities are given in Table 3.5 which are the values for the blocks along the main diagonal. The values that will be on the

Table 3.5: Raw data power spectral densities for equal and unequal arm lengths.

Power spectra	Expressions	
	Unequal arm lengths	Equal arm lengths
$S_{11}(f)$	$\langle\tilde{p}^2(f)\rangle\left[2-e^{-2\pi ifD_3}-e^{2\pi ifD_3}\right]+\langle\tilde{n}_1^2(f)\rangle$	$\langle\tilde{p}^2(f)\rangle\left[2-e^{-2\pi ifD}-e^{2\pi ifD}\right]+\langle\tilde{n}_1^2(f)\rangle$
$S_{1'1'}(f)$	$\langle\tilde{p}^2(f)\rangle\left[2-e^{-2\pi ifD_2}-e^{2\pi ifD_2}\right]+\langle\tilde{n}_{1'}^2(f)\rangle$	$\langle\tilde{p}^2(f)\rangle\left[2-e^{-2\pi ifD}-e^{2\pi ifD}\right]+\langle\tilde{n}_{1'}^2(f)\rangle$
$S_{22}(f)$	$\langle\tilde{p}^2(f)\rangle\left[2-e^{-2\pi ifD_1}-e^{2\pi ifD_1}\right]+\langle\tilde{n}_2^2(f)\rangle$	$\langle\tilde{p}^2(f)\rangle\left[2-e^{-2\pi ifD}-e^{2\pi ifD}\right]+\langle\tilde{n}_2^2(f)\rangle$
$S_{2'2'}(f)$	$\langle\tilde{p}^2(f)\rangle\left[2-e^{-2\pi ifD_3}-e^{2\pi ifD_3}\right]+\langle\tilde{n}_{2'}^2(f)\rangle$	$\langle\tilde{p}^2(f)\rangle\left[2-e^{-2\pi ifD}-e^{2\pi ifD}\right]+\langle\tilde{n}_{2'}^2(f)\rangle$
$S_{33}(f)$	$\langle\tilde{p}^2(f)\rangle\left[2-e^{-2\pi ifD_2}-e^{2\pi ifD_2}\right]+\langle\tilde{n}_3^2(f)\rangle$	$\langle\tilde{p}^2(f)\rangle\left[2-e^{-2\pi ifD}-e^{2\pi ifD}\right]+\langle\tilde{n}_3^2(f)\rangle$
$S_{3'3'}(f)$	$\langle\tilde{p}^2(f)\rangle\left[2-e^{-2\pi ifD_1}-e^{2\pi ifD_1}\right]+\langle\tilde{n}_{3'}^2(f)\rangle$	$\langle\tilde{p}^2(f)\rangle\left[2-e^{-2\pi ifD}-e^{2\pi ifD}\right]+\langle\tilde{n}_{3'}^2(f)\rangle$
$S_{12'}(f)$	$\langle\tilde{p}^2(f)\rangle\left[2-e^{-2\pi ifD_3}-e^{2\pi ifD_3}\right]$	$\langle\tilde{p}^2(f)\rangle\left[2-e^{-2\pi ifD}-e^{2\pi ifD}\right]$
$S_{1'3}(f)$	$\langle\tilde{p}^2(f)\rangle\left[2-e^{-2\pi ifD_2}-e^{2\pi ifD_2}\right]$	$\langle\tilde{p}^2(f)\rangle\left[2-e^{-2\pi ifD}-e^{2\pi ifD}\right]$
$S_{23'}(f)$	$\langle\tilde{p}^2(f)\rangle\left[2-e^{-2\pi ifD_1}-e^{2\pi ifD_1}\right]$	$\langle\tilde{p}^2(f)\rangle\left[2-e^{-2\pi ifD}-e^{2\pi ifD}\right]$
$S_{11'}(f)$	$\langle\tilde{p}^2(f)\rangle\left[1+e^{-2\pi if(D_3-D_2)}-e^{-2\pi ifD_3}-e^{2\pi ifD_2}\right]$	$\langle\tilde{p}^2(f)\rangle\left[2-e^{-2\pi ifD}-e^{2\pi ifD}\right]$
$S_{22'}(f)$	$\langle\tilde{p}^2(f)\rangle\left[1+e^{-2\pi if(D_1-D_3)}-e^{-2\pi ifD_1}-e^{2\pi ifD_3}\right]$	$\langle\tilde{p}^2(f)\rangle\left[2-e^{-2\pi ifD}-e^{2\pi ifD}\right]$
$S_{33'}(f)$	$\langle\tilde{p}^2(f)\rangle\left[1+e^{-2\pi if(D_2-D_1)}-e^{-2\pi ifD_2}-e^{2\pi ifD_1}\right]$	$\langle\tilde{p}^2(f)\rangle\left[2-e^{-2\pi ifD}-e^{2\pi ifD}\right]$
$S_{12}(f)$	$\langle\tilde{p}^2(f)\rangle\left[1+e^{-2\pi if(D_3-D_1)}-e^{-2\pi ifD_3}-e^{2\pi ifD_1}\right]$	$\langle\tilde{p}^2(f)\rangle\left[2-e^{-2\pi ifD}-e^{2\pi ifD}\right]$
$S_{13}(f)$	$\langle\tilde{p}^2(f)\rangle\left[1+e^{-2\pi if(D_3-D_2)}-e^{-2\pi ifD_3}-e^{2\pi ifD_2}\right]$	$\langle\tilde{p}^2(f)\rangle\left[2-e^{-2\pi ifD}-e^{2\pi ifD}\right]$
$S_{23}(f)$	$\langle\tilde{p}^2(f)\rangle\left[1+e^{-2\pi if(D_1-D_2)}-e^{-2\pi ifD_1}-e^{2\pi ifD_2}\right]$	$\langle\tilde{p}^2(f)\rangle\left[2-e^{-2\pi ifD}-e^{2\pi ifD}\right]$
$S_{1'2'}(f)$	$\langle\tilde{p}^2(f)\rangle\left[1+e^{-2\pi if(D_2-D_3)}-e^{-2\pi ifD_2}-e^{2\pi ifD_3}\right]$	$\langle\tilde{p}^2(f)\rangle\left[2-e^{-2\pi ifD}-e^{2\pi ifD}\right]$
$S_{1'3'}(f)$	$\langle\tilde{p}^2(f)\rangle\left[1+e^{-2\pi if(D_2-D_1)}-e^{-2\pi ifD_2}-e^{2\pi ifD_1}\right]$	$\langle\tilde{p}^2(f)\rangle\left[2-e^{-2\pi ifD}-e^{2\pi ifD}\right]$
$S_{2'3'}(f)$	$\langle\tilde{p}^2(f)\rangle\left[1+e^{-2\pi if(D_3-D_1)}-e^{-2\pi ifD_3}-e^{2\pi ifD_1}\right]$	$\langle\tilde{p}^2(f)\rangle\left[2-e^{-2\pi ifD}-e^{2\pi ifD}\right]$
$S_{13'}(f)$	$\langle\tilde{p}^2(f)\rangle\left[1+e^{-2\pi if(D_3-D_1)}-e^{-2\pi ifD_3}-e^{2\pi ifD_1}\right]$	$\langle\tilde{p}^2(f)\rangle\left[2-e^{-2\pi ifD}-e^{2\pi ifD}\right]$
$S_{21'}(f)$	$\langle\tilde{p}^2(f)\rangle\left[1+e^{-2\pi if(D_1-D_2)}-e^{-2\pi ifD_1}-e^{2\pi ifD_2}\right]$	$\langle\tilde{p}^2(f)\rangle\left[2-e^{-2\pi ifD}-e^{2\pi ifD}\right]$
$S_{32'}(f)$	$\langle\tilde{p}^2(f)\rangle\left[1+e^{-2\pi if(D_2-D_3)}-e^{-2\pi ifD_2}-e^{2\pi ifD_3}\right]$	$\langle\tilde{p}^2(f)\rangle\left[2-e^{-2\pi ifD}-e^{2\pi ifD}\right]$

main diagonals of these blocks are the auto-power spectral densities which are the first six rows in the table. With equal arm lengths the laser noise contributions all have the same structure.

Sample raw data power spectral density matrices

The sample matrices are given in Figure 3.15 where the values for the auto-power spectral densities show up as a diagonal in the blocks and the matrices. One interesting feature is the nature of the blocks for frequencies that do not contain any contribution from the laser phase noises, for example, blocks 1 and 11. This is because the laser noises in the equations have two basic structures $[2-e^{-2\pi ifD_i}-e^{2\pi ifD_i}]$ and $[1+e^{-2\pi if(D_i-D_j)}-e^{-2\pi ifD_i}-e^{2\pi ifD_j}]$ which both sum to zero when the exponential terms are equal to 1.

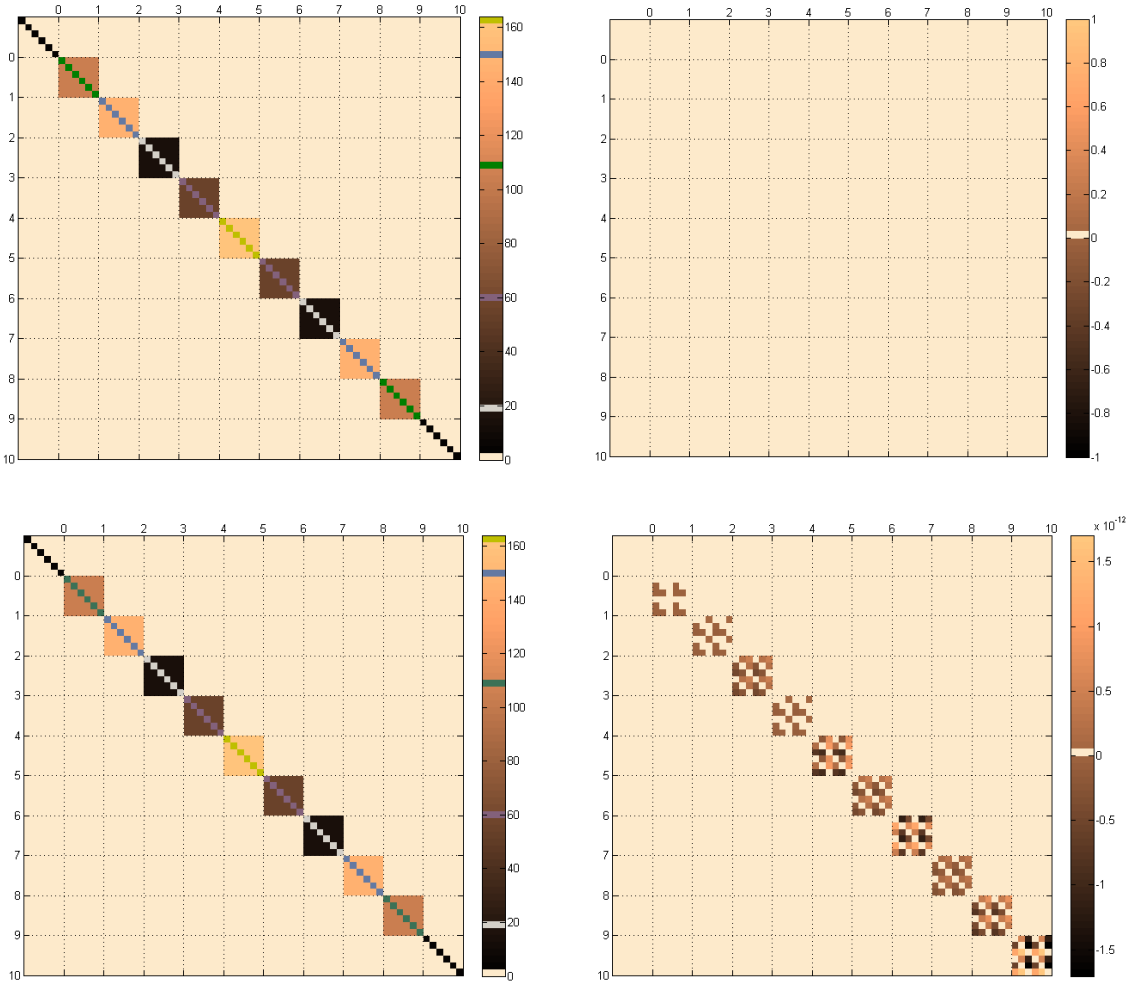

Figure 3.15: Sample raw data power spectral density matrices for lasers that are all phase-locked to a master showing the magnitudes (left) and phases (right) for equal (top) and unequal arm lengths (bottom).

3.2.4 A comparison of the covariance and power spectral density matrices

The instrumental noises in our toy model of LISA data that was used for generating covariance and power spectral density matrices were the laser phase and photodetector noises. The raw data from each of the six optical benches included the laser phase noises from the local laser and from the other laser at the end of the same arm and, the noise from the local photodetector. Both of these noises were assumed to be independent and random therefore correlations only occurred if the same noise occurred in the different readings. For the photodetector noises this meant that the correlations only occurred between readings from the same optical bench at the same times, that is, only auto-correlations existed for these noises. In the covariance matrix these only occur along

the main diagonal. The times of the two laser phase noises each reading are t for the local laser and $t - D_i$ for the laser beam arriving from the optical bench at the other end of arm. The offset D_i is the light travel time in arm i. The correlations reflected these times with possible locations being on the main diagonal, where the times are the same, and at times shifted from the main diagonal by offsets of D_i or a difference of two offsets of $D_i - D_j$. For the laser phase noises the correlations between the readings depended on how the lasers were phase-locked with the main outcome being an increase in the number of correlations which increased the density of the matrix.

The samples of the covariance matrices generated in this chapter are reproduced in Figures 3.16. The entries in these matrices are all 6×6 blocks corresponding to the number of optical benches therefore, the description of the structure relates to the blocks and not the elements. The properties of LISA that were demonstrated were the arm lengths and the phase-locking of the lasers. The options for the arms included static equal and unequal lengths and those for the phase locking the included (i) no locking, (ii) locking of the two lasers on each together and (iii) locking all lasers to a single (master) laser. In all cases the variances of the laser phase and photodetector noises were kept constant with each type having the same values.

As expected, in the covariance matrices the equal arm lengths resulted in three diagonals with the two diagonals away from the main located at offsets equal to the light travel time in the arms which is shown in Figures 3.16a, 3.16c 3.16e. The diagonals away from the main showed the correlations between the laser phase noises with times of t and $t - D$ while those on the main diagonal are between noises with the same times. With equal arm lengths, the effect of increasing the number of lasers that were phase-locked was just an increase in the density of the blocks. With three different arm lengths the diagonals away from the main are split into three diagonals which is shown in Figures 3.16b, 3.16d and 3.16f. These produced correlations between times t and $t - D_i$ which occurred at offsets of D_i. The effects of the phase-locking, in this case, was more pronounced than for the equal arm lengths. Apart from increasing the number of correlations, it also produced correlations between the laser phase noises with different shifted times of $t - D_i$ and $t - D_j$. These correlations are located at times that are differences of these offsets $(D_i - D_j)$ and are the values occurring close to the main diagonal in Figures 3.16d and 3.16f. The power spectral density matrices have simpler

structures than the covariance matrices because there are no correlations between the different frequencies. The lack of correlations produced matrices that were all block diagonals as shown in Figure 3.17. The time offsets in the covariance matrices occur as phase shifts in the power spectral density matrices. Increasing the number of lasers that are phase-locked also increased the density of the blocks in these matrices.

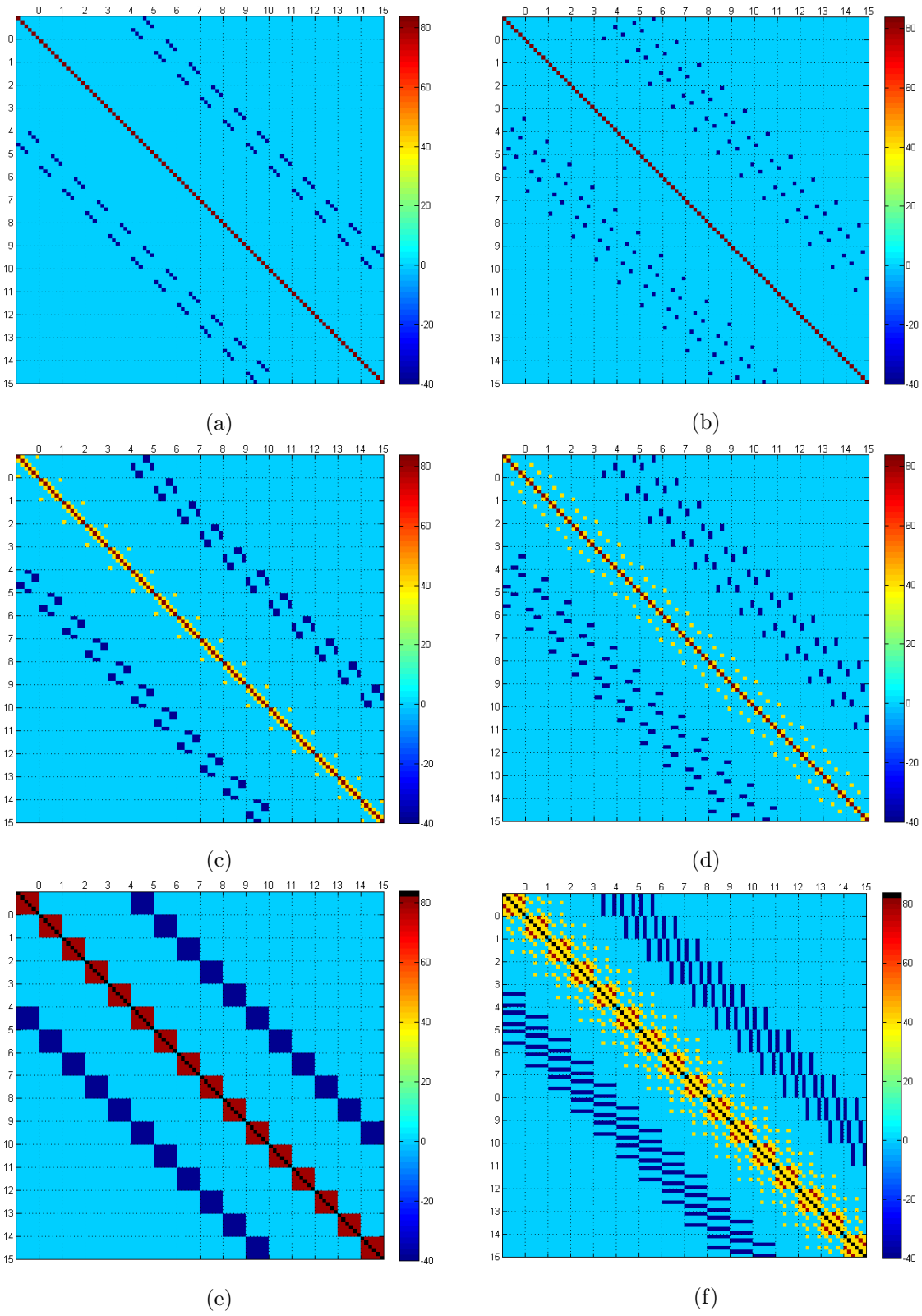

Figure 3.16: Sample raw data covariance matrices for laser options of no phase-locking (top), phase-locking on each spacecraft (middle) and all locked to a master.

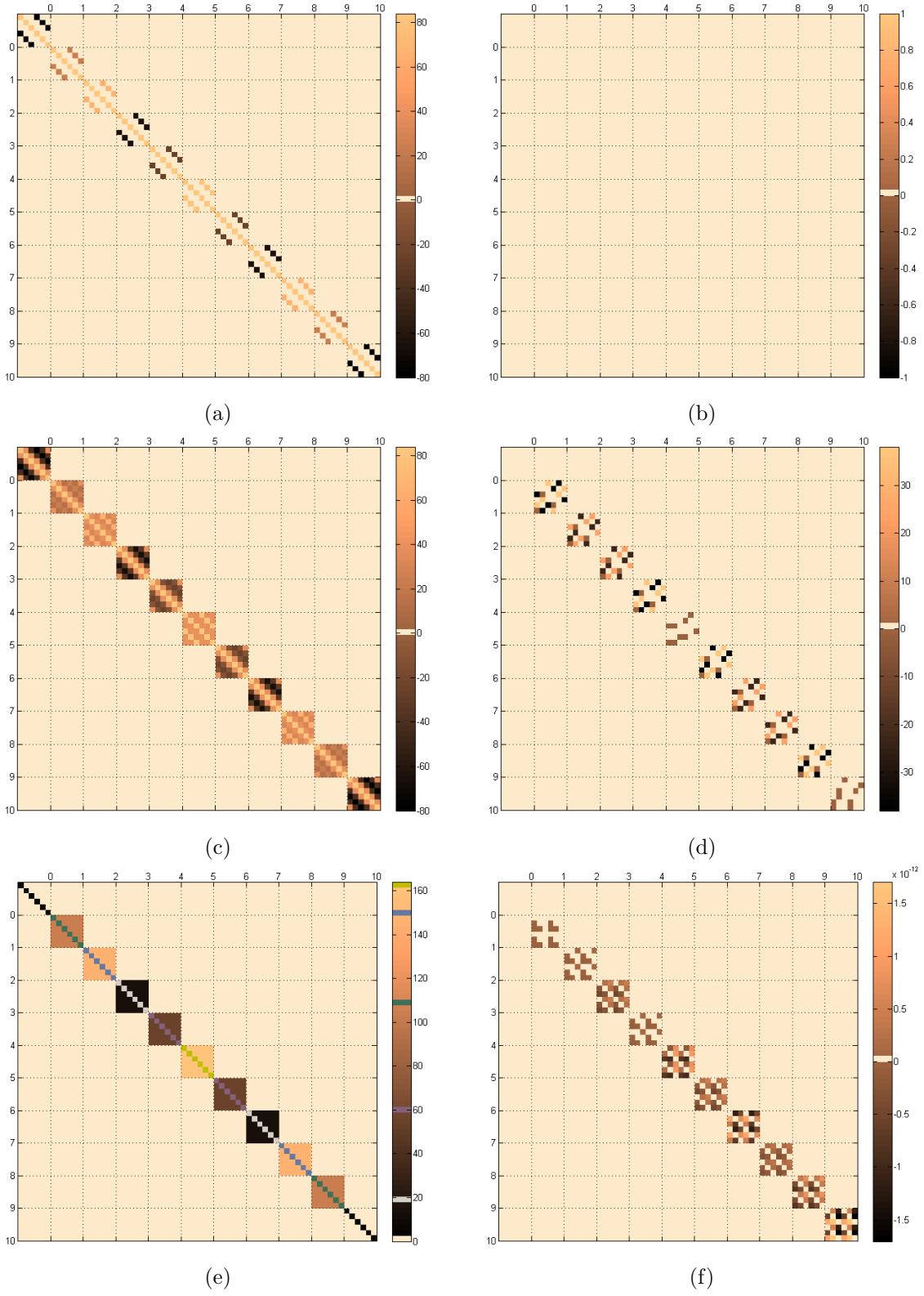

Figure 3.17: Sample raw data power spectral density matrices showing the magnitudes and phases for no phase-locking (top), phase-locking on each spacecraft (middle) and all phase-locked to a master (bottom).

Table 3.6: AET noise spectra

Amplitude spectra	Noise contributions
$A(f)$	$\frac{1}{\sqrt{2}}\{\widetilde{n}_1(f)\left[1-e^{-2\pi i f D_2}\right]-\widetilde{n}_{1'}(f)\left[1-e^{-2\pi i f(D_1+D_3)}\right]+\widetilde{n}_2(f)\left[e^{-2\pi i f D_3}-e^{-2\pi i f(D_2+D_3)}\right]$ $+\widetilde{n}_{2'}(f)\left[e^{-2\pi i f D_1}-e^{-2\pi i f(D_1+D_2)}\right]-\widetilde{n}_3(f)\left[1-e^{-2\pi i f(D_1+D_3)}\right]+\widetilde{n}_{3'}(f)\left[1-e^{-2\pi i f D_2}\right]\}$
$E(f)$	$\frac{1}{\sqrt{6}}\{-\widetilde{n}_1(f)\left[1-e^{-2\pi i f D_2}-2e^{-2\pi i f(D_1+D_2)}\right]+\widetilde{n}_{1'}(f)\left[1-2e^{-2\pi i f D_3}+e^{-2\pi i f(D_1+D_3}\right]$ $+\widetilde{n}_2(f)\left[2-e^{-2\pi i f D_3}-e^{-2\pi i f(D_2+D_3)}\right]-\widetilde{n}_{2'}(f)\left[2-e^{-2\pi i f D_1}-e^{-2\pi i f(D_1-D_2)}\right]$ $-\widetilde{n}_3(f)\left[1-2e^{-2\pi i f D_1}+e^{-2\pi i f(D_1+D_3)}\right]+\widetilde{n}_{3'}(f)\left[1+e^{-2\pi i f D_2}-2e^{-2\pi i f(D_2+D_3)}\right]\}$
$T(f)$	$\frac{1}{\sqrt{3}}\{-\widetilde{n}_1(f)\left[1+e^{-2\pi i f D_2}+e^{-2\pi i f(D_1+D_2)}\right]+\widetilde{n}_{1'}(f)\left[1+e^{-2\pi i f D_3}+e^{-2\pi i f(D_1+D_3)}\right]$ $-\widetilde{n}_2(f)\left[1+e^{-2\pi i f D_3}+e^{-2\pi i f(D_2+D_3)}\right]+\widetilde{n}_{2'}(f)\left[1+e^{-2\pi i f D_1}+e^{-2\pi i f(D_1+D_2)}\right]$ $-\widetilde{n}_3(f)\left[1+e^{-2\pi i f D_1}+e^{-2\pi i f(D_1+D_3)}\right]+\widetilde{n}_{3'}(f)\left[1+e^{-2\pi i f D_2}+e^{-2\pi i f(D_2+D_3)}\right]\}$

3.3 The power spectral densities for AET.

For the static array assumption of LISA the laser phase noises are completely canceled in the time delay interferometry observables. This is the main difference between the computation of the covariance functions for the time delay interferometry observables and for the raw data. The laser phase-locking which is important for the raw data will not have any effect on the time delay interferometry covariances since the correlations in them will be due to the remaining noises which, in our toy model, are the photodetector noises. The illustrations will only include an example of an auto-power and a cross-power spectral density. The noise contributions for the amplitude spectra for the AET observables are given in Table 3.6. The auto-power spectral density for the A combination can be computed from

$$\begin{aligned}
S_{AA}(f) = \Big\langle \frac{1}{\sqrt{2}}\Big\{ & \widetilde{n}_1(f)\left[1-e^{-2\pi i f D_2}\right]-\widetilde{n}_{1'}(f)\left[1-e^{-2\pi i f(D_3+D_1)}\right]+ \\
& +\widetilde{n}_2(f)\left[e^{-2\pi i f D_3}-e^{-2\pi i f(D_3+D_2)}\right]+\widetilde{n}_{2'}(f)\left[e^{-2\pi D_1}-e^{-2\pi i f(D_1+D_2)}\right] \\
& -\widetilde{n}_3(f)\left[1-e^{-2\pi i f(D_1+D_3)}\right]+\widetilde{n}_{3'}(f)\left[1-e^{-2\pi i f D_2}\right]\Big\} \\
& \times\frac{1}{\sqrt{2}}\Big\{\widetilde{n}_1^*(f)\left[1-e^{2\pi i f D_2}\right]-\widetilde{n}_{1'}^*(f)\left[1-e^{2\pi i f(D_3+D_1)}\right]+ \\
& +\widetilde{n}_2^*(f)\left[e^{2\pi i f D_3}-e^{2\pi i f(D_3+D_2)}\right]+\widetilde{n}_{2'}^*(f)\left[e^{2\pi D_1}-e^{2\pi i f(D_1+D_2)}\right] \\
& -\widetilde{n}_3^*(f)\left[1-e^{2\pi i f(D_1+D_3)}\right]+\widetilde{n}_{3'}^*(f)\left[1-e^{2\pi i f D_2}\right]\Big\}\Big\rangle \\
= \frac{1}{2}\Big\{ & \left[\left\langle\widetilde{n}_1^2(f)\right\rangle+\left\langle\widetilde{n}_2^2(f)\right\rangle+\left\langle\widetilde{n}_{2'}^2(f)\right\rangle+\left\langle\widetilde{n}_{3'}^2(f)\right\rangle\right]\left[2-e^{-2\pi i f D_2}-e^{2\pi i f D_2}\right] \\
& +\left[\left\langle\widetilde{n}_{1'}^2(f)\right\rangle+\left\langle\widetilde{n}_3^2(f)\right\rangle\right]\left[2-e^{-2\pi i f(D_3+D_1)}-e^{2\pi i f(D_3+D_1)}\right]\Big\} \qquad (3.80)
\end{aligned}$$

Table 3.7: AET power spectral densities.

Power spectra	Noise contributions
$S_{AA}(f)$	$\frac{1}{2}\{\left[\langle\tilde{n}_1^2(f)\rangle + \langle\tilde{n}_{2'}^2(f)\rangle + \langle\tilde{n}_{3'}^2(f)\rangle\right]\left[2 - e^{2\pi i f D_2} - e^{-2\pi i f D_2}\right]$ $+ \left[\langle\tilde{n}_{1'}^2(f)\rangle + \langle\tilde{n}_3^2(f)\rangle\right]\left[2 - e^{2\pi i f(D_1+D_3)} - e^{-2\pi i f(D_1+D_3)}\right]\}$
$S_{EE}(f)$	$\frac{1}{6}\{\left[\langle\tilde{n}_1^2(f)\rangle + \langle\tilde{n}_{2'}^2(f)\rangle\right]\left[6 - 2e^{2\pi i f D_1} - 2e^{-2\pi i f D_1} + e^{2\pi i f D_2} + e^{-2\pi i f D_2} - 2e^{2\pi i f(D_1+D_2)} - 2e^{-2\pi i f(D_1+D_2)}\right]$ $+\left[\langle\tilde{n}_2^2(f)\rangle + \langle\tilde{n}_{3'}^2(f)\right]\left[6 + e^{2\pi i f D_2} + e^{-2\pi i f D_2} - 2e^{2\pi i f D_3} - 2e^{-2\pi i f D_3} - 2e^{2\pi i f(D_2+D_3)} - 2e^{-2\pi i f(D_2+D_3)}\right]$ $+\left[\langle\tilde{n}_3^2(f)\rangle\langle\tilde{n}_{1'}^2(f)\rangle\right]\left[6 - 2e^{2\pi i f D_1} - 2e^{-2\pi i f D_1} - 2e^{2\pi i f D_3} - 2e^{-2\pi i f D_3} + e^{2\pi i f(D_1+D_3)} + e^{-2\pi i f(D_1+D_3)}\right]\}$
$S_{TT}(f)$	$\frac{1}{3}\{\left[\langle\tilde{n}_1^2(f)\rangle + \langle\tilde{n}_{2'}^2(f)\rangle\right]\left[3 + e^{2\pi i f D_1} + e^{-2\pi i f D_1} + e^{2\pi i f D_2} + e^{-2\pi i f D_2} + e^{2\pi i f(D_1+D_2)} + e^{-2\pi i f(D_1+D_2)}\right]$ $+\left[\langle\tilde{n}_2^2(f)\rangle + \langle\tilde{n}_{3'}^2(f)\rangle\right]\left[3 + e^{2\pi i f D_2} + e^{-2\pi i f D_2} + e^{2\pi i f D_3} + e^{-2\pi i f D_3} + e^{2\pi i f(D_2+D_3)} + e^{-2\pi i f(D_2+D_3)}\right]$ $+\left[\langle\tilde{n}_3^2(f)\rangle + \langle\tilde{n}_{1'}^2(f)\rangle\right]\left[3 + e^{2\pi i f D_1} + e^{-2\pi i f D_1} + e^{2\pi i f D_3} + e^{-2\pi i f D_3} + e^{2\pi i f(D_1+D_3)} + e^{-2\pi i f(D_1+D_3)}\right]\}$
$S_{AE}(f)$	$\frac{1}{\sqrt{12}}\{ -\langle\tilde{n}_1^2(f)\rangle\left[2e^{2\pi i f D_1} + e^{2\pi i f D_2} - e^{-2\pi i f D_2} - 2e^{2\pi i f(D_1+D_2)}\right]$ $-\langle\tilde{n}_{1'}^2(f)\rangle\left[2e^{-2\pi i f D_1} - 2e^{2\pi i f D_3} + e^{2\pi i f(D_1+D_3)} - e^{-2\pi i f(D_1+D_3)}\right]$ $-\langle\tilde{n}_2^2(f)\rangle\left[e^{2\pi i f D_2} - e^{-2\pi i f D_2} - 2e^{-2\pi i f D_3} + 2e^{-2\pi i f(D_2+D_3)}\right]$ $-\langle\tilde{n}_{2'}^2(f)\rangle\left[2e^{-2\pi i f D_1} - e^{2\pi i f D_2} + e^{-2\pi i f D_2} - 2e^{-2\pi i f(D_1+D_2)}\right]$ $-\langle\tilde{n}_3^2(f)\rangle\left[2e^{2\pi i f D_1} - 2e^{-2\pi i f D_3} - e^{2\pi i f(D_1+D_3)} + e^{-2\pi i f(D_1+D_3)}\right]$ $+\langle\tilde{n}_{3'}^2(f)\rangle\left[e^{2\pi i f D_2} - e^{-2\pi i f D_2} + 2e^{2\pi i f D_3} - 2e^{2\pi i f(D_2+D_3)}\right]\}$
$S_{AT}(f)$	$\frac{1}{\sqrt{6}}\{\langle\tilde{n}_1^2(f)\rangle\left[e^{2\pi i f D_1} - e^{2\pi i f D_2} + e^{-2\pi i f D_2} - e^{2\pi i f(D_1+D_2)}\right]$ $+\langle\tilde{n}_{1'}^2(f)\rangle\left[e^{-2\pi i f D_1} - e^{2\pi i f D_3} - e^{2\pi i f(D_1+D_3)} + e^{-2\pi i f(D_1+D_3)}\right]$ $-\langle\tilde{n}_2^2(f)\rangle\left[e^{2\pi i f D_2} - e^{-2\pi i f D_2} + e^{-2\pi i f D_3} - e^{-2\pi i f(D_2+D_3)}\right]$ $+\langle\tilde{n}_{2'}^2(f)\rangle\left[e^{-2\pi i f D_1} + e^{2\pi i f D_2} - e^{-2\pi i f D_2} - e^{-2\pi i f(D_1+D_2)}\right]$ $+\langle\tilde{n}_3^2(f)\rangle\left[e^{2\pi i f D_1} - e^{-2\pi i f D_3} + e^{2\pi i f(D_1+D_3)} - e^{-2\pi i f(D_1+D_3)}\right]$ $+\langle\tilde{n}_{3'}^2(f)\rangle\left[e^{2\pi i f D_2} - e^{-2\pi i f D_2} - e^{2\pi i f D_3} + e^{2\pi i f(D_2+D_3)}\right]\}$
$S_{ET}(f)$	$\frac{1}{3\sqrt{2}}\{\langle\tilde{n}_1^2(f)\rangle\left[e^{2\pi i f D_1} - 2e^{-2\pi i f D_1} + e^{2\pi i f D_2} + e^{-2\pi i f D_2} + e^{2\pi i f(D_1+D_2)} - 2e^{-2\pi i f(D_1+D_2)}\right]$ $+\langle\tilde{n}_{1'}^2(f)\rangle\left[e^{-2\pi i f D_1} - 2e^{2\pi i f D_1} + e^{2\pi i f D_3} - 2e^{-2\pi i f D_3} + e^{2\pi i f(D_1+D_3)} + e^{-2\pi i f(D_1+D_3)}\right]$ $+\langle\tilde{n}_2^2(f)\rangle\left[e^{2\pi i f D_2} + e^{-2\pi i f D_2} - 2e^{2\pi i f D_3} + e^{-2\pi i f D_3} - 2e^{2\pi i f(D_2+D_3)} + e^{-2\pi i f(D_2+D_3)}\right]$ $+\langle\tilde{n}_{2'}^2(f)\rangle\left[e^{-2\pi i f D_1} - 2e^{2\pi i f D_1} + e^{2\pi i f D_2} + e^{-2\pi i f D_2} - 2e^{2\pi i f(D_1+D_2)} + e^{-2\pi i f(D_1+D_2)}\right]$ $+\langle\tilde{n}_3^2(f)\rangle\left[e^{2\pi i f D_1} - 2e^{-2\pi i f D_1} - 2e^{2\pi i f D_3} + e^{-2\pi i f D_3} + e^{2\pi i f(D_1+D_3)} + e^{-2\pi i f(D_1+D_3)}\right]$ $+\langle\tilde{n}_{3'}^2(f)\rangle\left[e^{2\pi i f D_2} + e^{-2\pi i f D_2} + e^{2\pi i f D_3} - 2e^{-2\pi i f D_3} + e^{2\pi i f(D_2+D_3)} - 2e^{-2\pi i f(D_2+D_3)}\right]\}$

and substituting the values for the variances gives

$$S_{AA}(f) = \sigma_n^2\left[6 - 2e^{2\pi i f D_2} - 2e^{-2\pi i f D_2} - e^{2\pi i f(D_3+D_1)} - e^{-2\pi i f(D_3+D_1)}\right]. \quad (3.81)$$

With equal arm lengths there are no major changes just a replacement of the D_i with D in Equations 3.80 and 3.81. The cross-power spectral density is computed in a similar manner. The results for all the power spectral densities are given in Table 3.7. Samples of the power spectral density matrices are given in Figure 3.18 showing the real and imaginary values for equal and unequal arm lengths where frequencies and readings are arranged as shown in Figure 3.19.

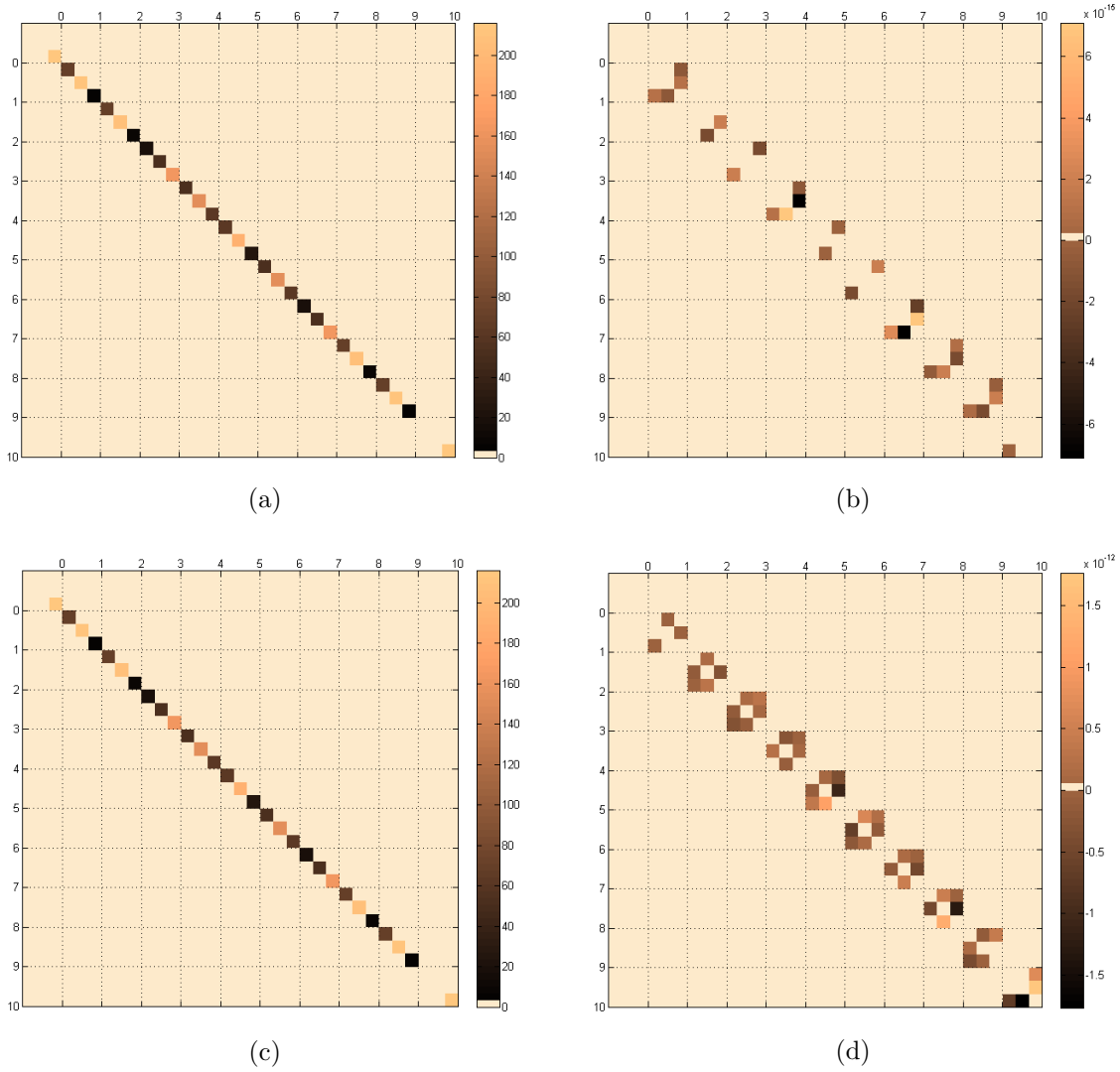

Figure 3.18: Sample *AET* power spectral density matrices showing the real (left) and imaginary (right) values for photodetector noise variances of $\sigma_n^2 = 1$. The matrices are for equal arm lengths of $D = 5.3$ (top) and unequal arm lengths of $D = \{5.3, 6.3, 7.3\}$ (bottom).

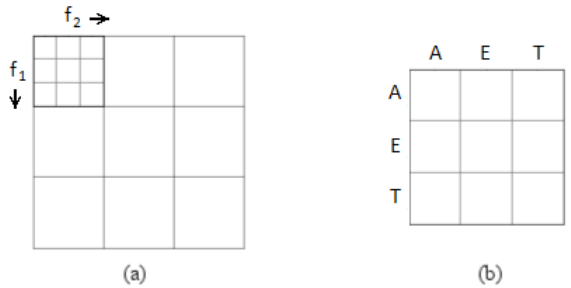

Figure 3.19: A diagram illustrating the block structure of the power spectral density matrix for AET showing the frequencies in (a) and the labeling of the blocks in (b).

3.4 Summary

In this chapter we generated the covariance and power spectral density matrices for the raw data which are the sources of the principal components. The configuration of

LISA used for these was that of stationary rigid array. The power spectral densities for the optimal AET observables were also generated. Results were obtained for equal and unequal arm lengths and, in the case of the raw data, for the three different laser phase-locking options. Sample covariance power spectral density matrices were generated. In the next chapter we will perform the eigendecomposition of the raw data covariance and power spectral density matrices and prove the connection between the laser phase noise free eigenvectors and the time delay interferometry observables in both the time and frequency domains.

Chapter 4

The principal components - time delay interferometry connection

In this chapter we show the connection between the principal components and time delay interferometry observables in both the time and frequency domains. For this we used a toy model of LISA with small covariance and power spectral density matrices using small arm lengths and equal variances for each noise type. We begin with a brief explanation of eigenvalues and eigenvectors and illustrate the conventional method for generating them. We also compare algebraic and numeric methods for computing them with respect to the values produced and the speed of computation.

4.1 Eigenvectors and eigenvalues

An eigenvector $\mathbf{v}$ is a vector that transforms a square matrix A into another vector which is the same or a multiple of itself. The transformation is a linear operation that can be written as

$$A\mathbf{v} = \lambda\mathbf{v}, \tag{4.1}$$

where the coefficient λ is the eigenvalue associated with the eigenvector. The number of eigenvalues generated are equal to the size of the matrix. The eigenvectors will be mutually independent but will only be orthogonal if the eigenvalues of the matrix are all unique. The eigenvalues for a matrix that have multiple occurrences are called degenerate.

The conventional way to determine the eigenvalues and eigenvectors is by finding the solution of Equation 4.1 using the homogeneous form which is

$$A\mathbf{v} - \lambda\mathbf{v} = \big(A - \lambda I\big)\mathbf{v} = 0, \tag{4.2}$$

where I is the unit matrix [53]. The only non-trivial solution for this is when $\big(A - \lambda I\big)$

is equal to zero which is solved using the determinant giving

$$|A - \lambda I| = 0, \tag{4.3}$$

where | | indicates the determinant [53]. This equation is called the characteristic equation which is a polynomial in λ of the same size as the matrix A giving the same number of roots [53]. Expanding Equation 4.3 gives

$$|A - \lambda I| = \begin{vmatrix} a_{11} - \lambda & a_{12} & \cdots & a_{1n} \\ a_{21} & a_{22} - \lambda & \cdots & a_{2n} \\ \vdots & \vdots & \vdots & \\ a_{n1} & a_{n2} & \cdots & a_{nn} - \lambda \end{vmatrix} = 0, \tag{4.4}$$

where a_{ij} are the elements of A. The eigenvectors are found by solving the Equation 4.1 for each eigenvalue.

4.1.1 Determination of the eigenvalues and eigenvectors for a LISA - toy model example

When the matrix is a data covariance matrix the eigenvectors align with the variances in the data. In the toy model data that Romano and Woan [54] used the phase measurements consisted of a single laser noise $p(t)$, photodetector noise $n_i(t)$ and signal $h_i(t)$ which can be written as

$$s_i = h_i(t) + p(t) + n_i(t). \tag{4.5}$$

The covariance matrix is based on the noises in the data, therefore, rearranging this gives

$$s_i(t) - h_i(t) = p(t) + n_i(t), \tag{4.6}$$

which for two photodetetors s_1 and s_2 gives

$$\begin{aligned} s_1 - h_1 &= p + n_1, \\ s_2 - h_2 &= p + n_2, \end{aligned} \tag{4.7}$$

where, because the terms have the same times, they have been dropped. With photodetector noises variances of σ_n^2 and laser phase noise variances of σ_p^2 the variances of s_1 and s_2 have the same value of $2\sigma_p^2 + \sigma_n^2$. Since there are no time offsets for the data the

covariance matrix C is simple with no lags and is defined as

$$C = \begin{bmatrix} \sigma_p^2 + \sigma_n^2 & \sigma_p^2 \\ \sigma_p^2 & \sigma_p^2 + \sigma_n^2. \end{bmatrix}.$$

The characteristic equation for this matrix is

$$\begin{aligned} |C - \lambda I| &= \begin{vmatrix} [(\sigma_p^2 + \sigma_n^2) - \lambda] & \sigma_p^2 \\ \sigma_p^2 & [(\sigma_p^2 + \sigma_n^2) - \lambda] \end{vmatrix} \\ &= \left[(\sigma_p^2 + \sigma_n^2) - \lambda\right]^2 - (\sigma_p^2)^2 \\ &= 0, \end{aligned} \tag{4.8}$$

which easily factorises into

$$\left[(\sigma_p^2 + \sigma_n^2) - \lambda\right]^2 - (\sigma_p^2)^2 = \Big\{ \left[(\sigma_p^2 + \sigma_n^2) - \lambda\right] - \sigma_p^2 \Big\} \Big\{ \left[(\sigma_p^2 + \sigma_n^2) - \lambda\right] + \sigma_p^2 \Big\}.$$

The two equations to be solved are

$$\begin{aligned} \sigma_p^2 + \sigma_n^2 - \lambda - \sigma_p^2 &= 0, \\ \sigma_p^2 + \sigma_n^2 - \lambda + \sigma_p^2 &= 0, \end{aligned} \tag{4.9}$$

giving solutions of $\lambda = \sigma_n^2$ and $\lambda = 2\sigma_p^2 + \sigma_n^2$, respectively. The eigenvalues are combined in a matrix Λ as

$$\Lambda = \begin{bmatrix} 2\sigma_p^2 + \sigma_n^2 & 0 \\ 0 & \sigma_n^2 \end{bmatrix}, \tag{4.10}$$

where they occur on the diagonal of the matrix. The matrix version of Equation 4.1 is

$$CV = V\Lambda, \tag{4.11}$$

where V is the matrix containing the eigenvectors, respectively. The occurrence of the V on both sides means that the matrix of eigenvalues Λ is equivalent to the covariance matrix C. Since this matrix is diagonal this means that the eigendecompostion diagonalised the covariance matrix. The corresponding eigenvectors are found by solving Equation 4.1 for each eigenvalue. The equations with the eigenvalues are

$$\begin{bmatrix} \sigma_p^2 + \sigma_n^2 & \sigma_p^2 \\ \sigma_p^2 & \sigma_p^2 + \sigma_n^2 \end{bmatrix} \begin{bmatrix} v_{11} \\ v_{12} \end{bmatrix} = 2\sigma_p^2 + \sigma_n^2 \begin{bmatrix} v_{11} \\ v_{12} \end{bmatrix}, \tag{4.12}$$

$$\begin{bmatrix} \sigma_p^2 + \sigma_n^2 & \sigma_p^2 \\ \sigma_p^2 & \sigma_p^2 + \sigma_n^2 \end{bmatrix} \begin{bmatrix} v_{21} \\ v_{22} \end{bmatrix} = \sigma_n^2 \begin{bmatrix} v_{21} \\ v_{22} \end{bmatrix}, \tag{4.13}$$

where v_{ij} are the elements of the eigenvector matrix. Equations 4.12 and 4.13 give consistent sets with general solutions of $v_{11} = v_{12}$ and $v_{21} = -v_{22}$. The eigenvectors are $\mathbf{v}_1 = [k \;\; k]$ and $\mathbf{v}_2 = [k \;\; -k]$ where k is non-zero number [53]. For $k = 1$ the vectors are $\mathbf{v}_1 = [1 \;\; 1]$ and $\mathbf{v}_2 = [1 \;\; -1]$ and the matrix is

$$V = \begin{bmatrix} 1 & 1 \\ 1 & -1 \end{bmatrix}, \tag{4.14}$$

with the eigenvectors arranged in columns.

4.1.2 Algebraic and numeric computations of the eigenvalues and eigenvectors

In the toy model example the eigenvalues were determined using the characteristic equation which requires the computation of the determinant of the matrix. The problem with this is that this scales badly with matrix size since the computation of the determinant is non-trivial for full matrices of sizes greater than three. The software package that we used for generating the eigenpairs (eigenvalues and eigenvectors) was MATLAB which has functions for algebraic and numeric solutions. To illustrate the difference in the computation times between the two methods and also to show how badly the algebraic approach scales with matrix size, the eigenpairs were computed for covariance matrices of different sizes with the values of the other properties that determined the matrix kept constant. Table 4.1 lists sample algebraic and numeric computation times for matrix sizes (n) ranging from 30 to 18000 which are plotted in Figure 4.1. The numeric computation of the 18000×18000 matrix took approximately 420 s which is roughly the time it took the algebraic computation of only a 48×48 matrix.[1]

In terms of the values and number of degenerate eigenvalues, both methods seem to produce the same results. The values of all the eigenvalues were checked for one matrix and their rounded values were found to be the same. For generating the time delay interferometry combinations the exact solutions were required for the eigenvectors, therefore, the the algebraic solutions were only used for this purpose.

[1] Computed on saturn (x86, 64bit, 1200MHz)

Table 4.1: Examples of the computation times for the eigenvalues and eigenvectors from algebraic and numeric solutions obtained using MATLAB.

(a) Algebraic

Number of timestamps	Computation time (s)
5	12.982
6	56.353
7	215.740
8	501.246
10	2289.314
11	4243.665
12	8208.799
13	12314.336
14	19402.763
15	31757.095

(b) Numeric

Number of timestamps	Computation time (s)
5	0.00046
6	0.00056
7	0.00062
10	0.00073
11	0.00077
12	0.00107
14	0.00124
15	0.00165
20	0.00272
40	0.00701
100	0.04304
300	0.44765
501	1.64426
800	7.08202
1600	62.41153
3000	435.86898

4.1.3 Independence and orthogonality of the eigenvectors

Independence indicates that there are no linear combinations of all the eigenvectors that will sum to zero. This can be written as

$$x_1\mathbf{e}_1 + x_2\mathbf{e}_2 + \cdots + x_n\mathbf{e}_n = \mathbf{0} \tag{4.15}$$

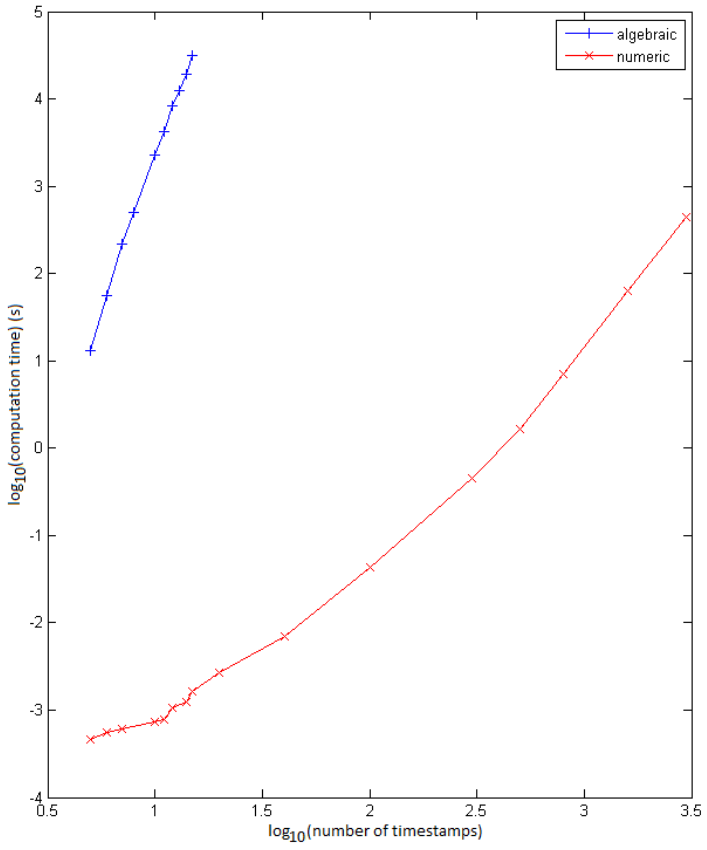

Figure 4.1: The plot of the algebraic and numeric computation times for the values in Table 4.1.

Table 4.2: The contributions from the raw data for the Sagnac α and ζ for times $t = \{1, ..., 5\}$ and offsets $D = \{1, 2, 3\}$.

OB#	α[5]	ζ[5]
s_1 (1)	0	0
$s_{1'}$(1)	0	0
s_2 (1)	0	0
$s_{2'}$(1)	0	0
s_3 (1)	-1	1
$s_{3'}$(1)	0	0
s_1 (2)	0	0
$s_{1'}$(2)	0	0
s_2 (2)	-1	0
$s_{2'}$(2)	1	0
s_3 (2)	0	-1
$s_{3'}$(2)	0	1
s_1 (3)	0	0
$s_{1'}$(3)	0	0
s_2 (3)	0	-1
$s_{2'}$(3)	0	0
s_3 (3)	0	0
$s_{3'}$(3)	1	0
s_1 (4)	0	-1
$s_{1'}$(4)	0	1
s_2 (4)	0	0
$s_{2'}$(4)	0	0
s_3 (4)	0	0
$s_{3'}$(4)	0	0
s_1 (5)	-1	0
$s_{1'}$(5)	1	0
s_2 (5)	0	0
$s_{2'}$(5)	0	0
s_3 (5)	0	0
$s_{3'}$(5)	0	0

where x_i are coefficients and $\mathbf{0}$ is the null vector [53]. For independent vectors the only combination that will lead to the null vector is the trivial solution where all the coefficients are zero. For the eigenvectors to be mutually orthogonal their inner products must be equal to zero, that is,

$$\mathbf{e}_i \cdot \mathbf{e}_j = 0. \tag{4.16}$$

If the eigenvalues for the covariance matrix are all unique their eigenvectors will be independent and orthogonal. In the case of degenerate eigenvalues the eigenvectors will be independent but not necessarily orthogonal.

4.2 Generating the Sagnac observables

Determining the set of eigenvectors that will produce the required time delay interferometer combination can be obtained by solving a set of linear equations which can be

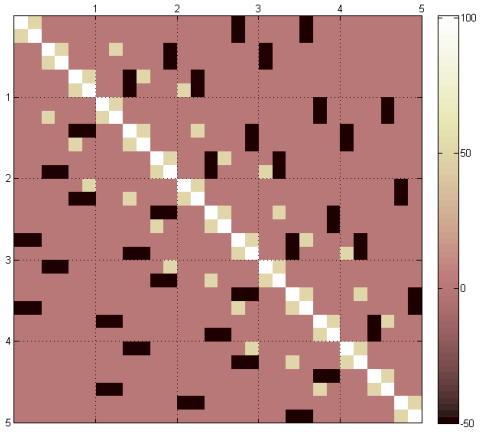

Figure 4.2: The covariance matrix of Romano and Woan with variances of $\sigma_p^2 = 50$ and $\sigma_n^2 = 1$, times of $t = \{1, 2, 3, 4, 5\}$ and offsets of $D = \{1, 2, 3\}$.

written as

$$x_1\mathbf{e}_1 + x_2\mathbf{e}_2 + \cdots + x_n\mathbf{e}_n = \mathbf{b}, \tag{4.17}$$

where x_i are scalar coefficients, $\mathbf{e}_i$ are the eigenvectors of size $n \times 1$, $\mathbf{b}$ is a $n \times 1$ vector containing the corresponding values needed for each time delay interferometry combinations. In matrix form this can be written as

$$A\mathbf{x} = \mathbf{b}, \tag{4.18}$$

where A is the matrix of eigenvectors as columns, $\mathbf{x}$ is a column vector of coefficients and $\mathbf{b}$ the column vector containing the target values which will reflect the structure of the matrix. Examples for $\mathbf{b}$ values for $\alpha(5)$ and $\alpha(5)$ are given in Table 4.2. The solution will be obtained by

$$\mathbf{x} = A^{-1}\mathbf{b}, \tag{4.19}$$

which can be done directly in MATLAB using the left divide operator

$$\mathbf{x} = A\backslash\mathbf{b}, \tag{4.20}$$

or using *linsolve* function.

Table 4.3: The degenerate eigenvalues for the covariance matrix in Figure 4.2 used in Romano and Woan [54].

OB#	$\mathbf{e}_1$	$\mathbf{e}_2$	$\mathbf{e}_3$	$\mathbf{e}_4$	$\mathbf{e}_5$	$\mathbf{e}_6$	$\mathbf{e}_7$	$\mathbf{e}_8$	$\mathbf{e}_9$
s_1 (1)	0	0	0	0	0	0	0	0	0
$s_{1'}$(1)	0	0	0	0	0	0	0	0	0
s_2 (1)	0	0	0	0	0	1	0	0	0
$s_{2'}$(1)	0	0	0	0	0	0	0	0	0
s_3 (1)	0	0	0	1	0	0	0	0	0
$s_{3'}$(1)	0	1	0	0	0	0	0	0	0
s_1 (2)	0	0	0	0	0	0	0	0	0
$s_{1'}$(2)	0	0	0	0	0	-1	0	0	0
s_2 (2)	0	0	0	0	0	0	1	0	0
$s_{2'}$(2)	0	0	0	-1	0	0	0	0	0
s_3 (2)	1	0	0	0	0	-1	0	0	0
$s_{3'}$(2)	0	0	0	0	0	0	0	0	1
s_1 (3)	0	-1	0	0	0	0	0	0	0
$s_{1'}$(3)	0	1	0	1	0	0	-1	0	0
s_2 (3)	1	0	0	0	0	0	0	0	0
$s_{2'}$(3)	-1	0	0	0	0	1	0	0	0
s_3 (3)	0	0	1	0	0	0	0	0	0
$s_{3'}$(3)	0	0	0	0	0	0	0	1	0
s_1 (4)	0	0	0	0	0	1	0	0	-1
$s_{1'}$(4)	0	0	0	0	0	-1	0	0	1
s_2 (4)	0	0	1	-1	0	0	1	0	0
$s_{2'}$(4)	0	0	-1	0	0	0	0	0	0
s_3 (4)	0	0	0	0	1	0	0	0	0
$s_{3'}$(4)	0	0	0	0	0	1	0	0	0
s_1 (5)	0	0	0	-1	0	0	1	-1	0
$s_{1'}$(5)	0	0	0	1	0	0	-1	1	0
s_2 (5)	0	0	0	0	1	1	0	0	0
$s_{2'}$(5)	0	0	0	0	-1	-1	0	0	0
s_3 (5)	0	0	0	1	0	0	0	-1	0
$s_{3'}$(5)	0	0	0	-1	0	0	0	1	0

4.2.1 Results for the covariance matrix given in Romano and Woan

Romano and Woan [54] were able to produce the Sagnac α time delay interferometry observable from the laser phase noise from the eigenvectors obtained from a 1×5 covariance matrix with times $t = \{1, 2, 3, 4, 5\}$ and offsets $D = \{1, 2, 3\}$. The matrix and the laser noise free eigenvectors that they obtained are given in Figure 4.2 and Table 4.3, respectively.

Table 4.4: The values for the current and shifted times appearing in the Sagnac observables for $t = \{1, 2, 3, 4, 5\}$ and $D_i = \{1, 2, 3\}$ as used by Romano and Woan.

t	$t - D_1$	$t - D_2$	$t - D_3$	$t - D_1 - D_2$	$t - D_1 - D_3$	$t - D_2 - D_3$
1	0	-1	-2	-2	-3	-4
2	1	0	-1	-1	-2	-3
3	2	1	0	0	-1	-2
4	3	2	1	1	0	-1
5	4	3	2	2	1	0

4.2.1.1 Solutions for the Sagnac α and ζ

The inter-spacecraft phase measurements for the Sagnac observables can be written as

$$\begin{aligned}
\alpha(t) &= s_{1'}(t) + s_{2'}(t - D_1 - D_2) + s_{3'}(t - D_2) - s_1(t) - s_2(t - D_3) - s_3(t - D_1 - D_3),\\
\beta(t) &= s_{1'}(t - D_3) + s_{2'}(t) + s_{3'}(t - D_2 - D_3) - s_1(t - D_2 - D_1) - s_2(t) - s_3(t - D_1),\\
\gamma(t) &= s_{1'}(t - D_3 - D_1) + s_{2'}(t - D_1) + s_{3'}(t) - s_1(t - D_2) - s_2(t - D_3 - D_2) - s_3(t),\\
\zeta(t) &= s_{1'}(t - D_1) + s_{2'}(t - D_2) + s_{3'}(t - D_3) - s_1(t - D_1) - s_2(t - D_2) - s_3(t - D_3).
\end{aligned} \tag{4.21}$$

The values for the times occurring in the Sagnacs are given in Table 4.4 for $t = \{1, 2, 3, 4, 5\}$ and $D_i = \{1, 2, 3\}$ where they range from -4 to 5. If the covariance matrix is restricted to positive values including zero, the only time that will have offsets occurring with all these values is $t = 5$. The values for all the Sagnacs for this time are

$$\begin{aligned}
\alpha(5) &= s_{1'}(5) + s_{2'}(2) + s_{3'}(3) - s_1(5) - s_2(2) - s_3(1),\\
\beta(5) &= s_{1'}(2) + s_{2'}(5) + s_{3'}(0) - s_1(2) - s_2(5) - s_3(4),\\
\gamma(5) &= s_{1'}(1) + s_{2'}(4) + s_{3'}(5) - s_1(3) - s_2(0) - s_3(5),\\
\zeta(5) &= s_{1'}(4) + s_{2'}(3) + s_{3'}(2) - s_1(4) - s_2(3) - s_3(2).
\end{aligned} \tag{4.22}$$

The matrix used by Romano and Woan did not include a zero value, therefore, the only combinations that could be generated are the $\alpha(5)$ and $\zeta(5)$. Their solution for $\alpha(5)$ was $-\mathbf{e}_4 - \mathbf{e}_7 + \mathbf{e}_8$. From Table 4.3 the equations for these are

$$\begin{aligned}
\mathbf{e}_4 &= s_3(1) - s_{2'}(2) + s_{1'}(3) - s_2(4) - s_1(5) + s_{1'}(5) + s_3(5) - s_{3'}(5),\\
\mathbf{e}_7 &= s_2(2) - s_{1'}(3) + s_2(4) + s_1(5) - s_{1'}(5) - s_3(5) + s_{3'}(5),\\
\mathbf{e}_8 &= s_{3'}(3) - s_1(5) + s_{1'}(5),
\end{aligned} \tag{4.23}$$

which gives

$$\begin{aligned}
-\mathbf{e}_4 - \mathbf{e}_7 + \mathbf{e}_8 = & -s_3(1) + s_{2'}(2) - s_{1'}(3) + s_2(4) + s_1(5) - s_{1'}(5) - s_3(5) + s_{3'}(5) \\
& - s_2(2) + s_{1'}(3) - s_2(4) - s_1(5) + s_{1'}(5) + s_3(5) - s_{3'}(5) \\
& + s_{3'}(3) - s_1(5) + s_{1'}(5) \\
= & \, s_{1'}(5) + s_{2'}(2) + s_{3'}(3) - s_1(5) - s_2(2) - s_3(1) \\
\equiv & \, \alpha(5). \qquad (4.24)
\end{aligned}$$

This matches the values for $\alpha(5)$ in Equation 4.22. $\zeta(5)$ can also be obtained by combining eigenvectors $\mathbf{e}_1$ and $\mathbf{e}_9$ of Table 4.3 for which the contributions from the raw data are

$$\begin{aligned}
\mathbf{e}_1 &= s_3(2) + s_2(3) - s_{2'}(3), \\
\mathbf{e}_9 &= s_{3'}(2) - s_1(4) + s_{1'}(4), \qquad (4.25)
\end{aligned}$$

and differencing them gives

$$\begin{aligned}
\zeta(5) &= -\mathbf{e}_1 + \mathbf{e}_9 \\
&= -s_3(2) - s_2(3) + s_{2'}(3) + s_{3'}(2) - s_1(4) + s_{1'}(4) \\
&= s_{1'}(4) + s_{2'}(3) + s_{3'}(2) - s_1(4) - s_2(3) - s_3(2). \qquad (4.26)
\end{aligned}$$

We have illustrated that two Sagnacs can be obtained from the laser noise free eigenvectors of the covariance matrix for the times presented by Romano and Woan. The conclusion from this is that the limitations came from the matrix size and times which did not allow for a zero value, therefore, it should be possible to generate the other Sagnacs by using a larger matrix.

4.2.1.2 Results for a 6×6 matrix

To investigate this, a new covariance matrix was generated for times of $t = \{0, 1, 2, 3, 4, 5\}$ with the same offsets used by Romano and Woan. This matrix is shown in Figure 4.3 where, because of the symmetric Toeplitz structure, the only difference from the previous matrix in Figure 4.2 is the size of the matrix. The degenerate eigenvectors for this matrix obtained from MATLAB's *eig* function are listed in Table 4.5. From this set of eigenvectors we were able to obtain solutions for all the Sagnacs for time $t = 5$. The

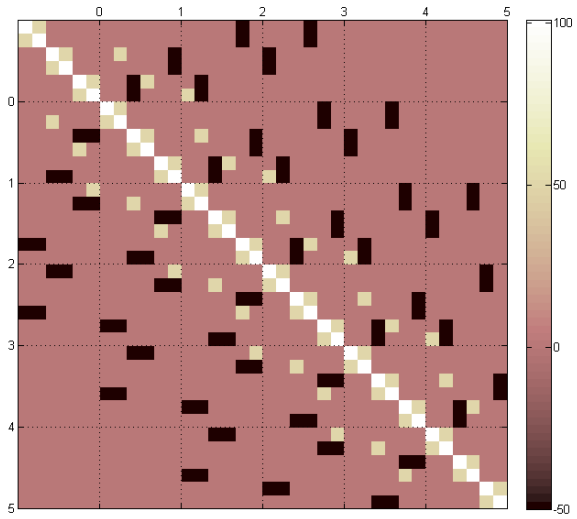

Figure 4.3: The covariance matrix for times of $t = \{0, ..., 9\}$ and offsets of $D = \{1, 2, 3, 4\}$ with variances of $\sigma_p^2 = 50$ and $\sigma_n^2 = 1$.

solutions are

$$\begin{aligned} \alpha(5) &= \mathbf{e}_3 + \mathbf{e}_6 + \mathbf{e}_{10}, \qquad & \beta(5) &= \mathbf{e}_2 + \mathbf{e}_{11}, \\ \gamma(5) &= \mathbf{e}_8 + \mathbf{e}_{12}, & \zeta(5) &= \mathbf{e}_5 + \mathbf{e}_7. \end{aligned} \tag{4.27}$$

For example, for ζ the raw data contributions for eigenvectors $\mathbf{e}_5$ and $\mathbf{e}_7$ are

$$\mathbf{e}_5 = -s_3(2) - s_2(3) + s_2(3), \qquad \mathbf{e}_7 = s_{3'}(2) - s_1(4) + s_{1'}(4), \tag{4.28}$$

and summing them gives

$$\begin{aligned} \mathbf{e}_5 + \mathbf{e}_7 &= -s_3(2) - s_2(3) + s_{2'}(3) + s_{3'}(2) - s_1(4) + s_{1'}(4) \\ &= s_{1'}(4) + s_{2'}(3) + s_{3'}(2) - s_1(4) - s_3(2) - s_2(3) \\ &= \zeta(5). \end{aligned} \tag{4.29}$$

The six phase readings occurring in the four Sagnacs in Equation 4.22 do not have any overlapping times for the same optical benches. Also, the solutions for the four Sagnacs in Equation 4.27 do not have any overlapping eigenvectors which could reflect this independence for same times. This will be investigated further in the next section.

Independence and orthogonality of the eigenvectors

The set of eigenvectors in Table 4.3 and 4.5 were determined to be all mutually independent but they are not all orthogonal. This is expected as they are associated with

Table 4.5: The degenerate eigenvalues for times $t = \{0, ..., 5\}$ and offsets $D = \{1, 2, 3\}$.

OB#	$\mathbf{e}_1$	$\mathbf{e}_2$	$\mathbf{e}_3$	$\mathbf{e}_4$	$\mathbf{e}_5$	$\mathbf{e}_6$	$\mathbf{e}_7$	$\mathbf{e}_8$	$\mathbf{e}_9$	$\mathbf{e}_{10}$	$\mathbf{e}_{11}$	$\mathbf{e}_{12}$
s_1 (0)	0	0	0	0	0	0	0	0	0	0	0	0
$s_{1'}$(0)	0	0	0	0	0	0	0	0	0	0	0	0
s_2 (0)	0	0	0	0	0	1	0	0	0	-1	0	-1
$s_{2'}$(0)	0	0	0	0	0	0	0	0	0	0	0	0
s_3 (0)	-1	0	0	0	0	0	0	0	0	0	0	0
$s_{3'}$(0)	0	1	0	0	0	0	0	0	1	0	0	0
s_1 (1)	0	0	0	0	0	0	0	0	0	0	0	0
$s_{1'}$(1)	0	0	0	0	0	-1	0	0	0	1	0	1
s_2 (1)	-1	0	0	0	0	0	0	0	1	0	0	0
$s_{2'}$(1)	1	0	0	0	0	0	0	0	0	0	0	0
s_3 (1)	0	0	-1	0	0	0	0	0	0	0	0	0
$s_{3'}$(1)	0	0	0	1	0	1	0	0	0	-1	0	0
s_1 (2)	0	-1	0	0	0	0	0	0	-1	0	0	0
$s_{1'}$(2)	0	1	0	0	0	0	0	0	0	0	0	0
s_2 (2)	0	0	-1	0	0	1	0	0	0	-1	0	0
$s_{2'}$(2)	0	0	1	0	0	0	0	0	0	0	0	0
s_3 (2)	0	0	0	0	-1	0	0	0	0	0	0	0
$s_{3'}$(2)	0	0	0	0	0	0	1	0	1	0	0	0
s_1 (3)	0	0	0	-1	0	0	0	0	0	0	0	-1
$s_{1'}$(3)	0	0	0	1	0	0	0	0	0	0	0	0
s_2 (3)	0	0	0	0	-1	0	0	0	1	0	0	0
$s_{2'}$(3)	0	0	0	0	1	0	0	0	0	0	0	0
s_3 (3)	0	0	0	0	0	-1	0	-1	0	1	0	1
$s_{3'}$(3)	0	0	0	0	0	1	0	0	0	0	0	0
s_1 (4)	0	0	0	0	0	0	-1	0	0	0	0	0
$s_{1'}$(4)	0	0	0	0	0	0	1	0	0	0	0	0
s_2 (4)	0	0	0	0	0	0	0	-1	0	0	0	1
$s_{2'}$(4)	0	0	0	0	0	0	0	1	0	0	0	0
s_3 (4)	0	0	0	0	0	0	0	0	-1	0	-1	0
$s_{3'}$(4)	0	0	0	0	0	0	0	0	1	0	0	0
s_1 (5)	0	0	0	0	0	0	0	0	0	-1	0	0
$s_{1'}$(5)	0	0	0	0	0	0	0	0	0	1	0	0
s_2 (5)	0	0	0	0	0	0	0	0	0	0	-1	0
$s_{2'}$(5)	0	0	0	0	0	0	0	0	0	0	1	0
s_3 (5)	0	0	0	0	0	0	0	0	0	0	0	-1
$s_{3'}$(5)	0	0	0	0	0	0	0	0	0	0	0	1

eigenvalues that are degenerate. For example, in Table 4.3 eigenvectors $\mathbf{e}_1$ and $\mathbf{e}_2$ both form non-zero inner products with $\mathbf{e}_4$ and so does $\mathbf{e}_4$ with $\mathbf{e}_1$,$\mathbf{e}_2$, $\mathbf{e}_3$ and $\mathbf{e}_7$. The majority of the eigenvectors in that table were not orthogonal. Table 4.5 had more orthogonal eigenvectors which could be linked to how they were generated as their non-zero values have patterns that do not occur in those of Table 4.3.

4.2.2 Results for offsets of $D_i = \{2, 3, 4\}$

This section contains the results for a different set of offsets and times that will allow the generation of combinations for different times from the same matrix. To obtain the Sagnac combinations for a specific set of offsets, the largest time value for the covariance

matrix must be equal to or greater than the maximum time offset in the combinations. For offsets of $D_i = \{2, 3, 4\}$ the maximum offset in the Sagnac combinations is $D_2+D_3 = 7$, therefore, the top value in the range of times of the covariance matrix must not be less than this value. If the times are restricted to positive values including zero, these only occur for $t = 7$ as shown in Table 4.6 therefore, to illustrate the generation of the Sagnacs for more than a single time value we extended the times up to 9 which will allow for three times values of 7, 8 and 9. The times needed for the phase measurements for the optical benches in the Sagnacs for these times are also included in Table 4.6. The covariance matrix is given in Figure 4.4 and its degenerate eiegnvectors are listed in Table 4.7. The equations for the Sagancs for $t = \{7, 8, 9\}$ are

$$\begin{aligned}
\alpha(7) &= s_{1'}(7) + s_{2'}(2) + s_{3'}(4) - s_1(7) - s_2(3) - s_3(1),\\
\beta(7) &= s_{1'}(3) + s_{2'}(7) + s_{3'}(0) - s_1(2) - s_2(7) - s_3(5),\\
\gamma(7) &= s_{1'}(1) + s_{2'}(5) + s_{3'}(7) - s_1(4) - s_2(0) - s_3(7),\\
\zeta(7) &= s_{1'}(5) + s_{2'}(4) + s_{3'}(3) - s_1(5) - s_2(4) - s_3(3),\\
\\
\alpha(8) &= s_{1'}(8) + s_{2'}(3) + s_{3'}(5) - s_1(8) - s_2(4) - s_3(2),\\
\beta(8) &= s_{1'}(4) + s_{2'}(8) + s_{3'}(1) - s_1(3) - s_2(8) - s_3(6),\\
\gamma(8) &= s_{1'}(2) + s_{2'}(6) + s_{3'}(8) - s_1(5) - s_2(1) - s_3(8),\\
\zeta(8) &= s_{1'}(6) + s_{2'}(5) + s_{3'}(4) - s_1(6) - s_2(5) - s_3(4),\\
\\
\alpha(9) &= s_{1'}(9) + s_{2'}(4) + s_{3'}(6) - s_1(9) - s_2(5) - s_3(3),\\
\beta(9) &= s_{1'}(5) + s_{2'}(9) + s_{3'}(2) - s_1(4) - s_2(9) - s_3(7),\\
\gamma(9) &= s_{1'}(3) + s_{2'}(7) + s_{3'}(9) - s_1(6) - s_2(2) - s_3(9),\\
\zeta(9) &= s_{1'}(7) + s_{2'}(6) + s_{3'}(5) - s_1(7) - s_2(6) - s_3(5).
\end{aligned} \tag{4.30}$$

From this set of eigenvectors we were able to obtain solutions for all the Sagnacs listed in Equation 4.30. The solutions are

$$\begin{aligned}
\alpha(7) &= \mathbf{e}_5 + \mathbf{e}_{12}, & \alpha(8) &= \mathbf{e}_8 + \mathbf{e}_{15}, & \alpha(9) &= \mathbf{e}_4 + \mathbf{e}_{11} + \mathbf{e}_{18},\\
\beta(7) &= \mathbf{e}_2 + \mathbf{e}_{13}, & \beta(8) &= \mathbf{e}_3 + \mathbf{e}_{16}, & \beta(9) &= \mathbf{e}_6 + \mathbf{e}_{19},\\
\gamma(7) &= \mathbf{e}_7 + \mathbf{e}_{14}, & \gamma(8) &= \mathbf{e}_1 + \mathbf{e}_{10} + \mathbf{e}_{17}, & \gamma(9) &= \mathbf{e}_2 + \mathbf{e}_{13} + \mathbf{e}_{20},\\
\zeta(7) &= \mathbf{e}_4 + \mathbf{e}_6, & \zeta(8) &= \mathbf{e}_5 + \mathbf{e}_7 + \mathbf{e}_9, & \zeta(9) &= \mathbf{e}_8 + \mathbf{e}_{10} + \mathbf{e}_{12}.
\end{aligned} \tag{4.31}$$

Table 4.6: The values for the current and shifted times appearing in the Sagnac observables for $t = \{0, \ldots, 9\}$ and $D_i = \{2, 3, 4\}$.

t	$t - D_1$	$t - D_2$	$t - D_3$	$t - D_1 - D_2$	$t - D_1 - D_3$	$t - D_2 - D_3$
0	-2	-3	-4	-5	-6	-7
1	-1	-2	-3	-4	-5	-6
2	0	-1	-2	-3	-4	-5
3	1	0	-1	-2	-3	-4
4	2	1	0	-1	-2	-3
5	3	2	1	0	-1	-2
6	4	3	2	1	0	-1
7	5	4	3	2	1	0
8	6	5	4	3	2	1
9	7	6	5	4	3	2

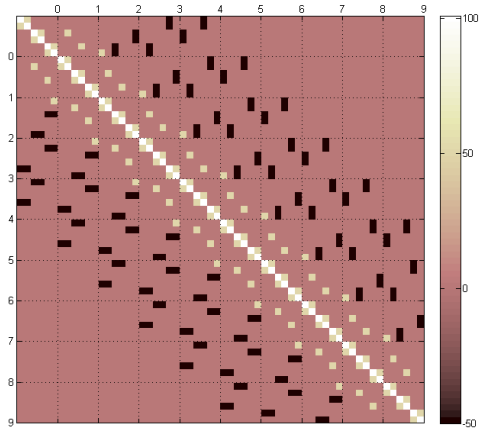

Figure 4.4: The covariance matrix for times of $t = \{0, ..., 9\}$ and offsets of $D = \{2, 3, 4\}$ and variances of $\sigma_p^2 = 50$ and $\sigma_n^2 = 1$.

The difference with this method of generating time delay interferometry observables is that the combinations are generated for specific times and not for a general time t. This means that the combinations of eigenvectors that work for one time value are not the same for another as shown in Equation 4.31.

Table 4.7: The time domain degenerate eigenvectors eigenvectors for time $t = \{0, ..., 9\}$, offsets $D = \{2, 3, 4\}$ and variances $\sigma_p^2 = 50$ and $\sigma_n^2 = 1$.

OB#	$\mathbf{e}_1$	$\mathbf{e}_2$	$\mathbf{e}_3$	$\mathbf{e}_4$	$\mathbf{e}_5$	$\mathbf{e}_6$	$\mathbf{e}_7$	$\mathbf{e}_8$	$\mathbf{e}_9$	$\mathbf{e}_{10}$	$\mathbf{e}_{11}$	$\mathbf{e}_{12}$	$\mathbf{e}_{13}$	$\mathbf{e}_{14}$	$\mathbf{e}_{15}$	$\mathbf{e}_{16}$	$\mathbf{e}_{17}$	$\mathbf{e}_{18}$	$\mathbf{e}_{19}$	$\mathbf{e}_{20}$
s_1 (0)	0	0	0	0	0	0	0	0	0	0	0	0	0	0	0	0	0	0	0	0
$s_{1'}$(0)	0	0	0	0	0	0	0	0	0	0	0	0	0	0	0	0	0	0	0	0
s_2 (0)	0	0	0	0	1	0	-1	0	0	1	0	-1	0	0	0	0	-1	0	0	0
$s_{2'}$(0)	0	0	0	0	0	0	0	0	0	0	0	0	0	0	0	0	0	0	0	0
s_3 (0)	-1	0	0	-1	0	1	1	0	-1	0	0	0	0	-1	0	0	1	1	-1	0
$s_{3'}$(0)	1	0	0	0	0	0	0	1	0	-1	0	0	1	0	-1	0	0	0	0	-1
s_1 (1)	0	0	0	0	0	0	0	0	0	0	0	0	0	0	0	0	0	0	0	0
$s_{1'}$(1)	0	0	0	0	-1	0	1	0	0	-1	0	1	0	0	0	0	1	0	0	0
s_2 (1)	-1	0	0	0	0	0	0	0	0	0	0	0	0	0	0	0	0	0	0	0
$s_{2'}$(1)	1	0	0	1	0	-1	-1	0	1	0	0	0	0	1	0	0	-1	-1	1	0
s_3 (1)	0	-1	0	-1	-1	1	1	1	0	-1	0	0	1	-1	-1	0	1	1	-1	0
$s_{3'}$(1)	0	1	0	0	0	0	0	0	0	0	1	0	-1	0	0	1	0	-1	0	0
s_1 (2)	-1	0	0	0	0	0	0	-1	0	1	0	0	-1	0	1	0	0	0	0	1
$s_{1'}$(2)	1	0	0	0	0	0	0	0	0	0	0	0	0	0	0	0	0	0	0	0
s_2 (2)	0	-1	0	-1	0	1	1	1	-1	-1	0	0	1	-1	-1	0	1	1	-1	-1
$s_{2'}$(2)	0	1	0	1	1	-1	-1	-1	0	1	0	0	-1	1	1	0	-1	-1	1	0
s_3 (2)	0	0	-1	-1	-1	1	1	0	0	-1	1	1	0	-1	-1	1	1	0	-1	0
$s_{3'}$(2)	0	0	1	0	1	0	-1	0	0	1	0	-1	0	1	0	-1	-1	0	1	0
s_1 (3)	0	-1	0	0	0	0	0	0	0	0	-1	0	1	0	0	-1	0	1	0	0
$s_{1'}$(3)	0	1	0	0	0	0	0	0	0	0	0	0	0	0	0	0	0	0	0	0
s_2 (3)	0	0	-1	-1	-1	1	1	1	0	-1	1	0	0	-1	-1	1	1	0	-1	0
$s_{2'}$(3)	0	0	1	1	1	-1	-1	0	0	1	-1	-1	0	1	1	-1	-1	0	1	0
s_3 (3)	0	0	0	-1	0	0	0	0	0	0	0	0	0	0	0	0	0	0	0	0
$s_{3'}$(3)	0	0	0	1	0	0	-1	0	1	0	0	0	0	1	0	0	0	-1	0	0
s_1 (4)	0	0	-1	0	0	0	0	0	0	0	0	0	0	-1	0	1	0	0	-1	0
$s_{1'}$(4)	0	0	1	0	0	0	0	0	0	0	0	0	0	0	0	0	0	0	0	0
s_2 (4)	0	0	0	-1	0	0	0	0	0	0	1	0	0	0	-1	0	0	0	0	0
$s_{2'}$(4)	0	0	0	1	0	0	0	0	0	0	0	0	0	0	0	0	0	0	0	0
s_3 (4)	0	0	0	0	-1	0	0	0	0	-1	0	1	0	0	0	0	1	0	0	0
$s_{3'}$(4)	0	0	0	0	1	0	0	0	0	0	0	0	0	0	0	0	0	0	0	0
s_1 (5)	0	0	0	0	0	-1	0	0	0	0	0	0	0	0	0	0	-1	0	1	0
$s_{1'}$(5)	0	0	0	0	0	1	0	0	0	0	0	0	0	0	0	0	0	0	0	0
s_2 (5)	0	0	0	0	0	0	-1	0	0	0	0	0	0	1	0	0	0	-1	0	0
$s_{2'}$(5)	0	0	0	0	0	0	1	0	0	0	0	0	0	0	0	0	0	0	0	0
s_3 (5)	0	0	0	0	0	0	0	-1	0	0	0	0	-1	0	1	0	0	0	0	1
$s_{3'}$(5)	0	0	0	0	0	0	0	1	0	0	0	0	0	0	0	0	0	0	0	0
s_1 (6)	0	0	0	0	0	0	0	0	-1	0	0	0	0	0	0	0	0	0	0	-1
$s_{1'}$(6)	0	0	0	0	0	0	0	0	1	0	0	0	0	0	0	0	0	0	0	0
s_2 (6)	0	0	0	0	0	0	0	0	0	-1	0	0	0	0	0	0	1	0	0	0
$s_{2'}$(6)	0	0	0	0	0	0	0	0	0	1	0	0	0	0	0	0	0	0	0	0
s_3 (6)	0	0	0	0	0	0	0	0	0	0	-1	0	0	0	0	-1	0	1	0	0
$s_{3'}$(6)	0	0	0	0	0	0	0	0	0	0	1	0	0	0	0	0	0	0	0	0
s_1 (7)	0	0	0	0	0	0	0	0	0	0	0	-1	0	0	0	0	0	0	0	0
$s_{1'}$(7)	0	0	0	0	0	0	0	0	0	0	0	1	0	0	0	0	0	0	0	0
s_2 (7)	0	0	0	0	0	0	0	0	0	0	0	0	-1	0	0	0	0	0	0	1
$s_{2'}$(7)	0	0	0	0	0	0	0	0	0	0	0	0	1	0	0	0	0	0	0	0
s_3 (7)	0	0	0	0	0	0	0	0	0	0	0	0	0	-1	0	0	0	0	-1	0
$s_{3'}$(7)	0	0	0	0	0	0	0	0	0	0	0	0	0	1	0	0	0	0	0	0
s_1 (8)	0	0	0	0	0	0	0	0	0	0	0	0	0	0	-1	0	0	0	0	0
$s_{1'}$(8)	0	0	0	0	0	0	0	0	0	0	0	0	0	0	1	0	0	0	0	0
s_2 (8)	0	0	0	0	0	0	0	0	0	0	0	0	0	0	0	-1	0	0	0	0
$s_{2'}$(8)	0	0	0	0	0	0	0	0	0	0	0	0	0	0	0	1	0	0	0	0
s_3 (8)	0	0	0	0	0	0	0	0	0	0	0	0	0	0	0	0	-1	0	0	0
$s_{3'}$(8)	0	0	0	0	0	0	0	0	0	0	0	0	0	0	0	0	1	0	0	0
s_1 (9)	0	0	0	0	0	0	0	0	0	0	0	0	0	0	0	0	0	-1	0	0
$s_{1'}$(9)	0	0	0	0	0	0	0	0	0	0	0	0	0	0	0	0	0	1	0	0
s_2 (9)	0	0	0	0	0	0	0	0	0	0	0	0	0	0	0	0	0	0	-1	0
$s_{2'}$(9)	0	0	0	0	0	0	0	0	0	0	0	0	0	0	0	0	0	0	1	0
s_3 (9)	0	0	0	0	0	0	0	0	0	0	0	0	0	0	0	0	0	0	0	-1
$s_{3'}$(9)	0	0	0	0	0	0	0	0	0	0	0	0	0	0	0	0	0	0	0	1

4.2.2.1 Eigenvectors and correlations in the Sagnac observables

In the eigenvector combinations for the Sagnacs given in Equation 4.31 there are some combinations that have common eigenvectors. These occur between different combinations at different times, for example, the eigenvector combinations for $\alpha(7)$ and $\zeta(8)$ are

$$\begin{aligned}\alpha(7) &= \mathbf{e}_5 + \mathbf{e}_{12},\\ \zeta(8) &= \mathbf{e}_5 + \mathbf{e}_7 + \mathbf{e}_9.\end{aligned} \tag{4.32}$$

which both contain the eigenvector $\mathbf{e}_5$. This could indicate correlations between the two Sagnacs for those times. However, this depends on whether any of the terms in $\mathbf{e}_5$ survive in the $\zeta(8)$ as it may just be used to cancel the unwanted terms in the other eigenvectors in order to obtain those needed for $\zeta(8)$. The eigenvector used for generating this Sagnac are

$$\begin{aligned}\mathbf{e}_5 &= s_2(0) - s_{1'}(1) + s_{2'}(2) - s_2(3) - s_3(1) - s_3(2) + s_{3'}(2) + s_{2'}(3) - s_3(4) + s_{3'}(4),\\ \mathbf{e}_7 &= -s_2(0) + s_{1'}(1) - s_{2'}(2) + s_2(3) + s_3(1) + s_3(2) - s_{3'}(2) - s_{2'}(3) - s_2(5) + s_{2'}(5)\\ &\quad + s_3(0) - s_{2'}(1) + s_2(2) - s_{3'}(3)\\ \mathbf{e}_9 &= -s_3(0) + s_{2'}(1) - s_2(2) + s_{3'}(3) - s_1(6) + s_{1'}(6),\end{aligned} \tag{4.33}$$

where they have been aligned to show the terms that will cancel. The final combination will contain two terms from each eigenvector giving

$$\zeta(8) = -s_3(4) + s_{3'}(4) - s_2(5) + s_{2'}(5) - s_1(6) + s_{1'}(6), \tag{4.34}$$

where the common optical bench between the two is $s_{3'}(4)$. A list of the Sagnacs and their common eigenvectors is given in Table 4.8. Also, in Table 4.9 the correlated Sagnacs are listed with their common optical bench readings. All the Sagnacs with common eigenvectors are correlated but not all the correlated Sagnacs in Table 4.9 have common eigenvectors.

4.3 Generating the *AET* observables

The *AET* observables were generated in the frequency domain therefore, in this section we investigate the connection between these and the eigenvectors of the raw data power

Table 4.8: Sagnacs with common eigenvectors.

Sagnacs	Eigenvectors
$\alpha(7)$, $\zeta(8)$	$\mathbf{e}_5$
$\alpha(7)$, $\zeta(9)$	$\mathbf{e}_{12}$
$\beta(7)$, $\gamma(9)$	$\mathbf{e}_2$, $\mathbf{e}_{13}$
$\gamma(7)$, $\zeta(8)$	$\mathbf{e}_7$
$\zeta(7)$, $\alpha(9)$	$\mathbf{e}_4$
$\zeta(7)$, $\beta(9)$	$\mathbf{e}_6$
$\alpha(8)$, $\zeta(9)$	$\mathbf{e}_8$
$\gamma(8)$, $\zeta(9)$	$\mathbf{e}_{10}$

Table 4.9: Correlations between the Sagnacs for times $t = \{7, 8, 9\}$.

Sagnacs	Common terms
$\alpha(7)$, $\zeta(8)$	$s_{3'}(4)$
$\alpha(7)$, $\zeta(9)$	$s_1(7)$, $s_{1'}(7)$
$\beta(7)$, $\gamma(9)$	$s_{1'}(3)$, $s_{2'}(7)$
$\beta(7)$, $\zeta(9)$	$s_3(5)$
$\gamma(7)$, $\zeta(8)$	$s_{2'}(5)$
$\gamma(7)$, $\beta(9)$	$s_1(4)$, $s_3(7)$
$\zeta(7)$, $\alpha(8)$	$s_2(4)$
$\zeta(7)$, $\gamma(8)$	$s_1(5)$
$\zeta(7)$, $\alpha(9)$	$s_{2'}(4)$, $s_3(3)$
$\zeta(7)$, $\beta(9)$	$s_{1'}(5)$
$\alpha(8)$, $\zeta(9)$	$s_{3'}(5)$
$\gamma(8)$, $\zeta(9)$	$s_{2'}(6)$
$\zeta(8)$, $\alpha(9)$	$s_2(5)$
$\zeta(8)$, $\gamma(9)$	$s_1(6)$

spectral density matrix. The A, E and T spectra can be written as a combination of the phase reading $\widetilde{s}_i(f)$ and a complex gain $G_i(f)$. For example, A can be written as

$$\begin{aligned} A(f) = \frac{1}{\sqrt{2}}\big\{&\widetilde{n}_1(f)\big[1 - e^{-2\pi i f D_2}\big] - \widetilde{n}_{1'}(f)\big[1 - e^{-2\pi i f (D_1+D_3)}\big] \\ &+\widetilde{n}_2(f)\big[e^{-2\pi i f D_3} - e^{-2\pi i f (D_2+D_3)}\big] + \widetilde{n}_{2'}(f)\big[e^{-2\pi i f D_1} - e^{-2\pi i f (D_1+D_2)}\big] \\ &- \widetilde{n}_3(f)\big[1 - e^{-2\pi i f (D_1+D_3)}\big] + \widetilde{n}_{3'}(f)\big[1 - e^{-2\pi i f D_2}\big]\big\}. \end{aligned} \tag{4.35}$$

The complex gains are the terms in square brackets associated with each bench and Equation 4.35 can be rewritten as

$$\begin{aligned} A(f) = \frac{1}{\sqrt{2}}\Big[&\widetilde{s}_1(f)G_1(f) - \widetilde{s}_{1'}(f)G_{1'}(f) + \widetilde{s}_2(f)G_2(f) + \widetilde{s}_{2'}(f)G_{2'}(f) \\ &-\widetilde{s}_3(f)G_3(f) + \widetilde{s}_{3'}(f)G_{3'}(f)\Big]. \end{aligned} \tag{4.36}$$

Table 4.10: The complex gains for AET.

Observable	Optical bench	Gain
$\widetilde{A}(f)$	$\tilde{s}_1\,(f)$	$1-e^{-2\pi i f D_2}$
	$\tilde{s}_{1'}(f)$	$-1+e^{-2\pi i f (D_1+D_3)}$
	$\tilde{s}_2\,(f)$	$e^{-2\pi i f D_3}-e^{-2\pi i f (D_2+D_3)}$
	$\tilde{s}_{2'}(f)$	$e^{-2\pi i f D_1}-e^{-2\pi i f (D_1+D_2)}$
	$\tilde{s}_3\,(f)$	$-1+e^{-2\pi i f (D_1+D_3)}$
	$\tilde{s}_{3'}(f)$	$1-e^{-2\pi i f D_2}$
$\widetilde{E}(f)$	$\tilde{s}_1\,(f)$	$-1-e^{-2\pi i f D_2}+2e^{-2\pi i f (D_1+D_2)}$
	$\tilde{s}_{1'}(f)$	$1-2e^{-2\pi i f D_3}+e^{-2\pi i f (D_1+D_3}$
	$\tilde{s}_2\,(f)$	$2-e^{-2\pi i f D_3}-e^{-2\pi i f (D_2+D_3)}$
	$\tilde{s}_{2'}(f)$	$-2+e^{-2\pi i f D_1}+e^{-2\pi i f (D_1+D_2)}$
	$\tilde{s}_3\,(f)$	$-1+2e^{-2\pi i f D_1}-e^{-2\pi i f (D_1+D_3)}$
	$\tilde{s}_{3'}(f)$	$1+e^{-2\pi i f D_2}-2e^{-2\pi i f (D_2+D_3)}$
$\widetilde{T}(f)$	$\tilde{s}_1\,(f)$	$-1-e^{-2\pi i f D_2}-e^{-2\pi i f (D_1+D_2)}$
	$\tilde{s}_{1'}(f)$	$1+e^{-2\pi i f D_3}+e^{-2\pi i f (D_1+D_3)}$
	$\tilde{s}_2\,(f)$	$-1-e^{-2\pi i f D_3}-e^{-2\pi i f (D_2+D_3)}$
	$\tilde{s}_{2'}(f)$	$1+e^{-2\pi i f D_1}+e^{-2\pi i f (D_1+D_2)}$
	$\tilde{s}_3\,(f)$	$-1-e^{-2\pi i f D_1}-e^{-2\pi i f (D_1+D_3)}$
	$\tilde{s}_{3'}(f)$	$1+e^{-2\pi i f D_2}+e^{-2\pi i f (D_2+D_3)}$

The gains for the observables are listed given in Table 4.10. For generating the AET observables these gains are the target values for the vector $\mathbf{b}$ in Equation 4.19. The normalising fractions associated them will not be included in the computations.

4.3.1 Results

The eigenpairs were generated from the real and imaginary power spectral density matrix with laser phase noise variance of $\sigma_p^2 = 50$ and photodetector noise variance $\sigma_n^2 = 1$, respectively. Three different sets of offsets were used which are $D_i = \{2, 3, 4\}$, $D_i = \{2.5, 3.5, 4.5\}$ and $D_i = \{2.125, 3.125, 4.125\}$.

4.3.1.1 Solutions for integer offsets $D = \{2, 3, 4\}$

The real and imaginary power spectral density matrices for offsets $D_i = \{2, 3, 4\}$ are given in Figure 4.5. The blocks in the real matrix are all the same and those in the imaginary matrix have values that are very small 10^{-13} which will be assumed to be zero. The eigenpairs can therefore be generated from just one of the bocks in the real matrix. The values of the first blocks (S_{11}) of both matrices will be used and these are given in Table 4.11a. The small size of the blocks makes it easy to list all the eigenvalues and eigenvectors, including those with laser phase noises, which are given in Table 4.11b where the two distinct values are clearly seen. The laser noise free eigenvectors are

Table 4.11: The real and imaginary values for the blocks of the power spectral density matrix for offsets $D_i = \{2, 3, 4\}$ (a) with their corresponding eigenpairs (b).

(a) Power spectral densities.

	Real						Imaginary					
$\tilde{s}_1$ (0)	101	50	-50	-100	-50	50	0	0	0	0	0	0
$\tilde{s}_{1'}(0)$	50	101	50	-50	-100	-50	0	0	0	0	0	0
$\tilde{s}_2$ (0)	-50	50	101	50	-50	-100	0	0	0	0	0	0
$\tilde{s}_{2'}(0)$	-100	-50	50	101	50	-50	0	0	0	0	0	0
$\tilde{s}_3$ (0)	-50	-100	-50	50	101	50	0	0	0	0	0	0
$\tilde{s}_{3'}(0)$	50	-50	-100	-50	50	101	0	0	0	0	0	0

(b) Eigenvalues (λ_i) and eigenvectors ($\mathbf{v}_i$, $\mathbf{e}_i$).

λ_1	λ_2	λ_3	λ_4	λ_5	λ_6	OB#	$\mathbf{v}_1$	$\mathbf{v}_2$	$\mathbf{e}_1$	$\mathbf{e}_2$	$\mathbf{e}_3$	$\mathbf{e}_4$
301	0	0	0	0	0	$\tilde{s}_1$ (0)	-1	1	1	1	0	-1
0	301	0	0	0	0	$\tilde{s}_{1'}(0)$	-1	0	-1	0	1	1
0	0	1	0	0	0	$\tilde{s}_2$ (0)	0	-1	1	0	0	0
0	0	0	1	0	0	$\tilde{s}_{2'}(0)$	1	-1	0	1	0	0
0	0	0	0	1	0	$\tilde{s}_3$ (0)	1	0	0	0	1	0
0	0	0	0	0	1	$\tilde{s}_{3'}(0)$	0	1	0	0	0	1

Table 4.12: The complex gains for AET for integer offsets $D = \{2, 3, 4\}$.

OB#	$\widetilde{A}(1)$	$\widetilde{E}(1)$	$\widetilde{T}(1)$
$\tilde{s}_1$ (0)	0	0	-3
$\tilde{s}_{1'}(0)$	0	0	3
$\tilde{s}_2$ (0)	0	0	-3
$\tilde{s}_{2'}(0)$	0	0	3
$\tilde{s}_3$ (0)	0	0	-3
$\tilde{s}_{3'}(0)$	0	0	3

labeled $\mathbf{e}_i$ and those with laser phase noises are labeled $\mathbf{v}_i$. The eigenvalues of interest are the degenerate ones, $\lambda_i = 1$, and their corresponding eigenvectors are given by $\mathbf{e}_i$. The four degenerate eigenvalues are all independent but only $\mathbf{e}_2$ and $\mathbf{e}_3$ are orthogonal.

Since the power spectral densities are the same for all frequencies the equations for these can be written in terms of f giving

$$\begin{aligned}
\mathbf{e}_1 &= \tilde{s}_1(f) - \tilde{s}_{1'}(f) + \tilde{s}_2(f), \\
\mathbf{e}_2 &= \tilde{s}_1(f) + \tilde{s}_{2'}(f), \\
\mathbf{e}_3 &= \tilde{s}_{1'}(f) + \tilde{s}_3(f), \\
\mathbf{e}_4 &= -\tilde{s}_1(f) + \tilde{s}_{1'}(f) + \tilde{s}_{3'}(f).
\end{aligned} \tag{4.37}$$

For these offsets the complex gains for frequencies $f = \{0, .., 5\}$ are all the same which are given in Table 4.12 where only the T combinations has non-zero values. This is because of the structure of the A and E observables and the even numbers of π being

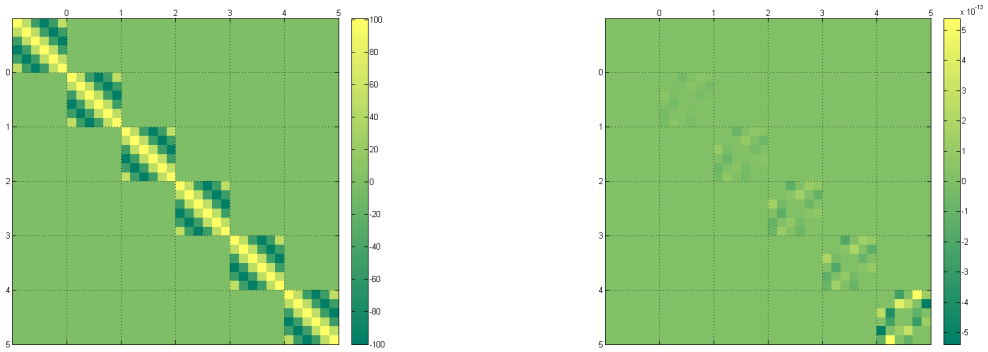

(a) (b)

Figure 4.5: The optical bench (a) real and (b) imaginary power spectral density matrices for frequencies $f = \{0, ..., 5\}$, offsets $D = \{2, 3, 4\}$ and laser phase and photodetector noise variances of $\sigma_p^2 = 50$ and $\sigma_n^2 = 1$, respectively.

produced in the exponential terms by the integer values. The solution for T is

$$\begin{aligned}
\widetilde{T}(f) &= -3\mathbf{e}_1 + 3\mathbf{e}_2 - 3\mathbf{e}_3 + 3e_4 \\
&= -3\big[\mathbf{e}_1 - \mathbf{e}_2 + \mathbf{e}_3 - \mathbf{e}_4\big] \\
&= -3\big[\tilde{s}_1(f) - \tilde{s}_{1'}(f) + \tilde{s}_2(f) - \tilde{s}_1(f) - \tilde{s}_{2'}(f) \\
&\qquad + \tilde{s}_{1'}(f) + \tilde{s}_3(f) + \tilde{s}_1(f) - \tilde{s}_{1'}(f) - \tilde{s}_{3'}(f)\big] \\
&= -3\big[\tilde{s}_1(f) - \tilde{s}_{1'}(f) + \tilde{s}_2(f) - \tilde{s}_{2'}(f) + \tilde{s}_3(f) - \tilde{s}_{2'}(f)\big].
\end{aligned} \tag{4.38}$$

4.3.1.2 Solutions for real offsets

The previous results showed that having integer offsets and integer frequencies produced real values for the power spectral densities of all the blocks with only the T combinations having non-zero values. To obtain non-zero values for the A and E real offsets were used. This was done for two sets of values in which one set provided only real power spectral densities and the other a combination of real and imaginary values.

Solutions for $D_i = \{2.5, 3.5, 4.5\}$

The real and imaginary matrices for the power spectral densities matrices for these offsets are given in Figure 4.6. For these offsets, there are two sets of values for the blocks in the real matrix reflecting the even and odd frequencies. The real values for even frequencies are the same result as those for integer offsets. The imaginary values are

Table 4.13: (a) The real and imaginary values for the block S_{11} and S_{22} of the power spectral density matrix for offsets $D = \{2.5, 3.5, 4.5\}$. The eigenvalue and eigevectors for these blocks are given in (b) and (c), respectively.

(a) Power spectral densities.

	Real						Imaginary					
$\tilde{s}_1\,(0)$	101	50	-50	-100	-50	50	0	0	0	0	0	0
$\tilde{s}_{1'}(0)$	50	101	50	-50	-100	-50	0	0	0	0	0	0
$\tilde{s}_2\,(0)$	-50	50	101	50	-50	-100	0	0	0	0	0	0
$\tilde{s}_{2'}(0)$	-100	-50	50	101	50	-50	0	0	0	0	0	0
$\tilde{s}_3\,(0)$	-50	-100	-50	50	101	50	0	0	0	0	0	0
$\tilde{s}_{3'}(0)$	50	-50	-100	-50	50	101	0	0	0	0	0	0
$\tilde{s}_1\,(1)$	101	50	50	100	50	50	0	0	0	0	0	0
$\tilde{s}_{1'}(1)$	50	101	50	50	100	50	0	0	0	0	0	0
$\tilde{s}_2\,(1)$	50	50	101	50	50	100	0	0	0	0	0	0
$\tilde{s}_{2'}(1)$	100	50	50	101	50	50	0	0	0	0	0	0
$\tilde{s}_3\,(1)$	50	100	50	50	101	50	0	0	0	0	0	0
$\tilde{s}_{3'}(1)$	50	50	100	50	50	101	0	0	0	0	0	0

(b) Eigenvalues (λ_i) and eigenvectors ($\mathbf{v}_i, \mathbf{e}_i$) for block S_{11}.

λ_1	λ_2	λ_3	λ_4	λ_5	λ_6	OB#	$\mathbf{v}_1$	$\mathbf{v}_2$	$\mathbf{e}_1$	$\mathbf{e}_2$	$\mathbf{e}_3$	$\mathbf{e}_4$
301	0	0	0	0	0	$\tilde{s}_1\,(0)$	-1	1	1	1	0	-1
0	301	0	0	0	0	$\tilde{s}_{1'}(0)$	-1	0	-1	0	1	1
0	0	1	0	0	0	$\tilde{s}_2\,(0)$	0	-1	1	0	0	0
0	0	0	1	0	0	$\tilde{s}_{2'}(0)$	1	-1	0	1	0	0
0	0	0	0	1	0	$\tilde{s}_3\,(0)$	1	0	0	0	1	0
0	0	0	0	0	1	$\tilde{s}_{3'}(0)$	0	1	0	0	0	1

(c) Eigenvalues (λ_i) and eigenvectors ($\mathbf{v}_i, \mathbf{e}_i$) for block S_{22}.

λ_1	λ_2	λ_3	λ_4	λ_5	λ_6	OB#	$\mathbf{v}_1$	$\mathbf{v}_2$	$\mathbf{v}_3$	$\mathbf{e}_1$	$\mathbf{e}_2$	$\mathbf{e}_3$
401	0	0	0	0	0	$\tilde{s}_1\,(1)$	1	-1	-1	-1	0	0
0	101	0	0	0	0	$\tilde{s}_{1'}(1)$	1	1	0	0	-1	0
0	0	101	0	0	0	$\tilde{s}_2\,(1)$	1	0	1	0	0	-1
0	0	0	1	0	0	$\tilde{s}_{2'}(1)$	1	-1	-1	1	0	0
0	0	0	0	1	0	$\tilde{s}_3\,(1)$	1	1	0	0	1	0
0	0	0	0	0	1	$\tilde{s}_{3'}(1)$	1	0	1	0	0	1

similar to those obtained for integer offsets with values $\approx 10^{-13}$ which will be rounded to 0. The values for both even and odd frequencies are from blocks S_{11} and S_{22} which are given in Table 4.13 (a). The complete set of eigenvalues and eigenvectors are given in Table 4.13 (b) and (c).

The eigenpairs for S_{11} where $f = 0$ are the same as for the integer values. For block S_{22} there are three laser noise free eigenvectors which are mutually independent and

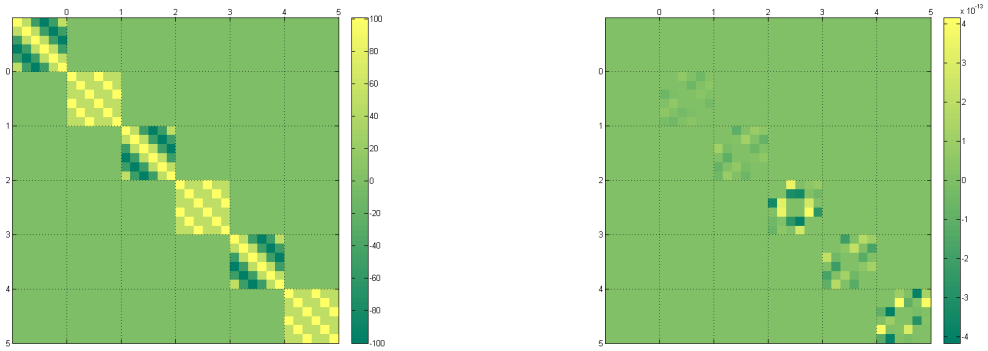

(a) (b)

Figure 4.6: The (a) real and (b) imaginary power spectral density matrices for frequencies $f = \{0, ..., 5\}$, offsets $D = \{2.5, 3.5, 4.5\}$ and laser phase and photodetector noise variances of $\sigma_p^2 = 50$ and $\sigma_n^2 = 1$, respectively.

orthogonal. The equations for these are

$$\mathbf{e}_1 = -\tilde{s}_1(1) + \tilde{s}_{2'}(1), \qquad \mathbf{e}_2 = -\tilde{s}_{1'}(1) + \tilde{s}_3(1), \qquad \mathbf{e}_3 = -\tilde{s}_2(1) + \tilde{s}_{3'}(1). \tag{4.39}$$

The gains for A, E and T for both blocks S_{11} and S_{22} are given in Table 4.14. The solutions for block S_{22} are

$$\begin{aligned}
\widetilde{A}(1) &= -2\mathbf{e}_1 + 2\mathbf{e}_3 \\
&= 2\tilde{s}_1(1) - 2\tilde{s}_{2'}(1) - 2\tilde{s}_2(1) + 2\tilde{s}_{3'}(1)), \\
\widetilde{E}(1) &= -2\mathbf{e}_1 - 4\mathbf{e}_2 - 2\mathbf{e}_3 \\
&= 2\tilde{s}_1(1) + 4\tilde{s}_{1'}(1) + 2\tilde{s}_2(1) - 2\tilde{s}_{2'}(1) - 4\tilde{s}_3(1)) - 2\tilde{s}_{3'}(1), \\
\widetilde{T}(1) &= \mathbf{e}_1 - \mathbf{e}_2 + \mathbf{e}_3 \\
&= -\tilde{s}_1(1) + \tilde{s}_{1'}(1) - \tilde{s}_2(1) + \tilde{s}_{2'}(1) - \tilde{s}_3(1) + \tilde{s}_{3'}(1).
\end{aligned} \tag{4.40}$$

Table 4.14: The complex gains for AET for integer offsets $D = \{2.5, 3.5, 4.5\}$.

OB#	$\widetilde{A}(0)$	$\widetilde{E}(0)$	$\widetilde{T}(0)$	OB#	$\widetilde{A}(1)$	$\widetilde{E}(1)$	$\widetilde{T}(1)$
$\tilde{s}_1\ (0)$	0	0	-3	$\tilde{s}_1\ (1)$	2	2	-1
$\tilde{s}_{1'}(0)$	0	0	3	$\tilde{s}_{1'}(1)$	0	4	1
$\tilde{s}_2\ (0)$	0	0	-3	$\tilde{s}_2\ (1)$	-2	2	-1
$\tilde{s}_{2'}(0)$	0	0	3	$\tilde{s}_{2'}(1)$	-2	-2	1
$\tilde{s}_3\ (0)$	0	0	-3	$\tilde{s}_3\ (1)$	0	-4	-1
$\tilde{s}_{3'}(0)$	0	0	3	$\tilde{s}_{3'}(1)$	2	-2	1

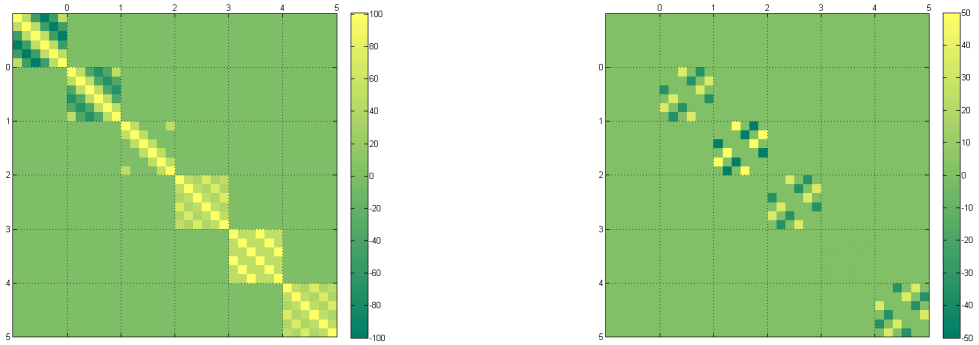

(a) (b)

Figure 4.7: The real (a) and imaginary (b) matrices for the power spectral density matrices for frequencies $f = \{0, 1, 2, 3, 4, 5\}$, offsets $D = \{2.125, 3.125, 4.125\}$ (e,f) and laser phase and photodetector noise variances of $\sigma_p^2 = 50$ and $\sigma_n^2 = 1$, respectively.

Solutions for $D = \{2.125, 3.125, 4.125\}$

These offsets were chosen to give multiples of $\pi/4$ in the exponential terms which give real and imaginary values of 0.7071 ($= \sqrt{2}/2$). The hope was that there would be algebraic solutions for these values.

The real and imaginary matrices for the power spectral densities for these offsets are given in Figure 4.7 and the values for all the blocks are given in Table 4.15. The gains for A, E and T for these offsets are given in Table 4.16. With these offsets imaginary values were obtained for some of the blocks. Blocks for frequencies of 0 and 4 overlap with those in the previous sets. The focus will be on those blocks with imaginary values which are those for frequencies which are 1, 2, 3 and 5 in order to obtain both algebraic and numeric solutions with them.

Algebraic solution

For an algebraic solution the block for $f = 2$ was used and the values for the eigenvalues and eigenvectors are given in Table 4.17. The laser noise free eigenvectors are

$$\begin{aligned}
\mathbf{e}_1 &= -\tilde{s}_1(2) + (1+i)\ \tilde{s}_{1'}(2) - (1+i)\tilde{s}_2 + \tilde{s}_{2'}(2), \\
\mathbf{e}_2 &= -(1-i)\ \tilde{s}_1(2) + \tilde{s}_{1'}(2) - (1+i)\ \tilde{s}_2 + \tilde{s}_3(2), \\
\mathbf{e}_3 &= -(1-i)\ \tilde{s}_1(2) + (1-i)\ \tilde{s}_{1'}(2) - \tilde{s}_2(2) + \tilde{s}_{3'}(2).
\end{aligned} \tag{4.41}$$

For example, the solution for A is

Table 4.15: The real and imaginary (rounded to nearest integer) values for the blocks of the power spectral density matrix for offsets $D = \{2.125, 3.125, 4.125\}$.

	Real						Imaginary					
$\tilde{s}_1\,(0)$	101	50	-50	-100	-50	50	0	0	0	0	0	0
$\tilde{s}_{1'}(0)$	50	101	50	-50	-100	-50	0	0	0	0	0	0
$\tilde{s}_2\,(0)$	-50	50	101	50	-50	-100	0	0	0	0	0	0
$\tilde{s}_{2'}(0)$	-100	-50	50	101	50	-50	0	0	0	0	0	0
$\tilde{s}_3\,(0)$	-50	-100	-50	50	101	50	0	0	0	0	0	0
$\tilde{s}_{3'}(0)$	50	-50	-100	-50	50	101	0	0	0	0	0	0
$\tilde{s}_1\,(1)$	101	50	-35	-71	-35	50	0	0	35	0	-35	0
$\tilde{s}_{1'}(1)$	50	101	50	-35	-71	-35	0	0	0	-35	0	35
$\tilde{s}_2\,(1)$	-35	50	101	50	-35	-71	-35	0	0	0	35	0
$\tilde{s}_{2'}(1)$	-71	-35	50	101	50	-35	0	35	0	0	0	-35
$\tilde{s}_3\,(1)$	-35	-71	-35	50	101	50	35	0	-35	0	0	0
$\tilde{s}_{3'}(1)$	50	-35	-71	-35	50	101	0	-35	0	35	0	0
$\tilde{s}_1\,(2)$	101	50	0	0	0	50	0	0	50	0	-50	0
$\tilde{s}_{1'}(2)$	50	101	50	0	0	0	0	0	0	-50	0	50
$\tilde{s}_2\,(2)$	0	50	101	50	0	0	-50	0	0	0	50	0
$\tilde{s}_{2'}(2)$	0	0	50	101	50	0	0	50	0	0	0	-50
$\tilde{s}_3\,(2)$	0	0	0	50	101	50	50	0	-50	0	0	0
$\tilde{s}_{3'}(2)$	50	0	0	0	50	101	0	-50	0	50	0	0
$\tilde{s}_1\,(3)$	101	50	35	71	35	50	0	0	35	0	-35	0
$\tilde{s}_{1'}(3)$	50	101	50	35	71	35	0	0	0	-35	0	35
$\tilde{s}_2\,(3)$	35	50	101	50	35	71	-35	0	0	0	35	0
$\tilde{s}_{2'}(3)$	71	35	50	101	50	35	0	35	0	0	0	-35
$\tilde{s}_3\,(3)$	35	71	35	50	101	50	35	0	-35	0	0	0
$\tilde{s}_{3'}(3)$	50	35	71	35	50	101	0	-35	0	35	0	0
$\tilde{s}_1\,(4)$	101	50	50	100	50	50	0	0	0	0	0	0
$\tilde{s}_{1'}(4)$	50	101	50	50	100	50	0	0	0	0	0	0
$\tilde{s}_2\,(4)$	50	50	101	50	50	100	0	0	0	0	0	0
$\tilde{s}_{2'}(4)$	100	50	50	101	50	50	0	0	0	0	0	0
$\tilde{s}_3\,(4)$	50	100	50	50	101	50	0	0	0	0	0	0
$\tilde{s}_{3'}(4)$	50	50	100	50	50	101	0	0	0	0	0	0
$\tilde{s}_1\,(5)$	101	50	35	71	35	50	0	0	-35	0	35	0
$\tilde{s}_{1'}(5)$	50	101	50	35	71	35	0	0	0	35	0	-35
$\tilde{s}_2\,(5)$	35	50	101	50	35	71	35	0	0	0	-35	0
$\tilde{s}_{2'}(5)$	71	35	50	101	50	35	0	-35	0	0	0	35
$\tilde{s}_3\,(5)$	35	71	35	50	101	50	-35	0	35	0	0	0
$\tilde{s}_{3'}(5)$	50	35	71	35	50	101	0	35	0	-35	0	0

$$
\begin{aligned}
\widetilde{A}(2) &= (1+i)\,\mathbf{e}_1 - 2\mathbf{e}_2 + (1-i)\,\mathbf{e}_3 \\
&= -(1+i)\tilde{s}_1(2) + (1+i)^2\,\tilde{s}_{1'}(2) - (1+i)^2\tilde{s}_2(2) + (1+i)\tilde{s}_{2'}(2) \\
&\qquad +2(1-i)\,\tilde{s}_1(2) - 2\tilde{s}_{1'}(2) + 2(1+i)\,\tilde{s}_2(2) - 2\tilde{s}_3(2) \\
&\qquad -(1-i)^2\,\tilde{s}_1(2) + (1-i)^2\,\tilde{s}_{1'}(2) - (1-i)\tilde{s}_2(2) + (1-i)\tilde{s}_{3'}(2) \\
&= \big[-(1+i) + 2(1-i) - (1-i)^2\big]\tilde{s}_1(2) + \big[(1+i)^2 - 2 + (1-i)^2\big]\tilde{s}_{1'}(2) \\
&\qquad -\big[(1+i)^2 - 2(1+i) + (1-i)\big]\tilde{s}_2(2) + (1+i)\tilde{s}_{2'} - 2\tilde{s}_3 + (1-i)s_{3'}(2) \\
&= \big[-1-i+2-2i+2i\big]\tilde{s}_1(2) + \big[2i-2-2i\big]\tilde{s}_{1'}(2) \\
&\qquad -\big[2i-2-2i+1-i\big]s_2 + (1+i)s_{2'}(2) - 2\tilde{s}_3(2) + (1-i)\tilde{s}_{3'} \\
&= (1-i)\tilde{s}_1(2) - 2\tilde{s}_{1'}(2) + (1+i)\tilde{s}_2(2) + (1+i)\tilde{s}_{2'}(2) \\
&\qquad -2\tilde{s}_3(2) + (1-i)\tilde{s}_{3'}(2). \qquad (4.42)
\end{aligned}
$$

Table 4.16: The complex gains for AET for $f = \{0, ..., 5\}$ and offsets $D = \{2.125, 3.125, 4.125\}$.

OB	$\widetilde{A}$	$\widetilde{E}$	$\widetilde{T}$
$\tilde{s}_1\,(0)$	0	0	-3
$\tilde{s}_{1'}(0)$	0	0	3
$\tilde{s}_2\,(0)$	0	0	-3
$\tilde{s}_{2'}(0)$	0	0	3
$\tilde{s}_3\,(0)$	0	0	-3
$\tilde{s}_{3'}(0)$	0	0	3
$\tilde{s}_1\,(1)$	0.2929 - 0.7071i	-1.7071 + 1.2929i	-1.7071 - 1.7071i
$\tilde{s}_{1'}(1)$	-1.0000 + 1.0000i	-0.4142 - 0.4142i	1.7071 + 1.7071i
$\tilde{s}_2\,(1)$	0.7071 - 0.2929i	1.2929 - 1.7071i	-1.7071 - 1.7071i
$\tilde{s}_{2'}(1)$	0.7071 - 0.2929i	-1.2929 + 1.7071i	1.7071 + 1.7071i
$\tilde{s}_3\,(1)$	-1.0000 + 1.0000i	0.4142 + 0.4142i	-1.7071 - 1.7071i
$\tilde{s}_{3'}(1)$	0.2929 - 0.7071i	1.7071 - 1.2929i	1.7071 + 1.7071i
$\tilde{s}_1\,(2)$	1 - 1i	-3 - 1i	0 - 1i
$\tilde{s}_{1'}(2)$	-2 + 0i	0 - 2i	0 + 1i
$\tilde{s}_2\,(2)$	1 + 1i	3 - 1i	0 - 1i
$\tilde{s}_{2'}(2)$	1 + 1i	-3 + 1i	0 + 1i
$\tilde{s}_3\,(2)$	-2 + 0i	0 + 2i	0 - 1i
$\tilde{s}_{3'}(2)$	1 - 1i	3 + 1i	0 + 1i
$\tilde{s}_1\,(3)$	1.7071 - 0.7071i	-0.2929 - 2.7071i	-0.2929 + 0.2929i
$\tilde{s}_{1'}(3)$	-1.0000 - 1.0000i	2.4142 - 2.4142i	0.2929 - 0.2929i
$\tilde{s}_2\,(3)$	-0.7071 + 1.7071i	2.7071 + 0.2929i	-0.2929 + 0.2929i
$\tilde{s}_{2'}(3)$	-0.7071 + 1.7071i	-2.7071 - 0.2929i	0.2929 - 0.2929i
$\tilde{s}_3\,(3)$	-1.0000 - 1.0000i	-2.4142 + 2.4142i	-0.2929 + 0.2929i
$\tilde{s}_{3'}(3)$	1.7071 - 0.7071i	0.2929 + 2.7071i	0.2929 - 0.2929i
$\tilde{s}_1\,(4)$	2	2	-1
$\tilde{s}_{1'}(4)$	0	4	1
$\tilde{s}_2\,(4)$	-2	2	-1
$\tilde{s}_{2'}(4)$	-2	-2	1
$\tilde{s}_3\,(4)$	0	-4	-1
$\tilde{s}_{3'}(4)$	2	-2	1
$\tilde{s}_1\,(5)$	1.7071 + 0.7071i	-0.2929 + 2.7071i	-0.2929 - 0.2929i
$\tilde{s}_{1'}(5)$	-1.0000 + 1.0000i	2.4142 + 2.4142i	0.2929 + 0.2929i
$\tilde{s}_2\,(5)$	-0.7071 - 1.7071i	2.7071 - 0.2929i	-0.2929 - 0.2929i
$\tilde{s}_{2'}(5)$	-0.7071 - 1.7071i	-2.7071 + 0.2929i	0.2929 + 0.2929i
$\tilde{s}_3\,(5)$	-1.0000 + 1.0000i	-2.4142 - 2.4142i	-0.2929 - 0.2929i
$\tilde{s}_{3'}(5)$	1.7071 + 0.7071i	0.2929 - 2.7071i	0.2929 + 0.2929i

The solutions for E and T are

$$\widetilde{E}(2) = (-1+i)\,\mathbf{e}_1 + 2\mathbf{e}_2 + (3+i)\,\mathbf{e}_3,$$
$$\widetilde{T}(2) = i\,\mathbf{e}_1 - i\,\mathbf{e}_2 + i\,\mathbf{e}_3. \tag{4.43}$$

Table 4.17: The eigenvalues and eigenvectors for block $f = 2$ for offsets $D = \{2.125, 3.125, 4.125\}$.

Eigenvalues						Eigenvectors						
λ_1	λ_2	λ_3	λ_4	λ_5	λ_6	OB#	$\mathbf{v}_1$	$\mathbf{v}_2$	$\mathbf{v}_3$	$\mathbf{e}_1$	$\mathbf{e}_2$	$\mathbf{e}_3$
201	0	0	0	0	0	$\tilde{s}_1\,(2)$	1	-1-i	1+i	-1	-1+i	-1+i
0	201	0	0	0	0	$\tilde{s}_{1'}(2)$	1-i	-1	1+i	1+i	1	1-i
0	0	201	0	0	0	$\tilde{s}_2\,(2)$	1-i	-1+i	1	-1-i	-1-i	-1
0	0	0	1	0	0	$\tilde{s}_{2'}(2)$	1	0	0	1	0	0
0	0	0	0	1	0	$\tilde{s}_3\,(2)$	0	1	0	0	1	0
0	0	0	0	0	1	$\tilde{s}_{3'}(2)$	0	0	1	0	0	1

Table 4.18: The degenerate eigenvectors for block $f = \{1, 3, 5\}$ for offsets $D = \{2.125, 3.125, 4.125\}$.

(a)

OB#	$\mathbf{e}_1$	$\mathbf{e}_2$	$\mathbf{e}_3$
$\tilde{s}_1\,(1)$	0.4082	0.5570 + 0.0079i	-0.1518 + 0.0016i
$\tilde{s}_{1'}(1)$	-0.4082	-0.3651 - 0.0730i	-0.3668 - 0.2452i
$\tilde{s}_2\,(1)$	0.4082	-0.1689 + 0.2469i	0.4914 + 0.0490i
$\tilde{s}_{2'}(1)$	-0.4082	0.4776 + 0.0730i	-0.1994 + 0.2452i
$\tilde{s}_3\,(1)$	0.4082	-0.3881 - 0.2547i	-0.3395 - 0.0506i
$\tilde{s}_{3'}(1)$	-0.4082	-0.1125 + 0.0000i	0.5663 + 0.0000i

(b)

OB#	$\mathbf{e}_1$	$\mathbf{e}_2$	$\mathbf{e}_3$
$\tilde{s}_1\,(2)$	-0.0419 + 0.5507i	0.1050 - 0.1313i	0.4082
$\tilde{s}_{1'}(2)$	-0.1568 + 0.0174i	-0.2594 - 0.4911i	-0.4082
$\tilde{s}_2\,(2)$	-0.4774 - 0.3069i	-0.0763 + 0.0732i	0.4082
$\tilde{s}_{2'}(2)$	0.0229 - 0.0174i	-0.3022 + 0.4911i	-0.4082
$\tilde{s}_3\,(2)$	0.5193 - 0.2438i	-0.0288 + 0.0581i	0.4082
$\tilde{s}_{3'}(2)$	0.1339 + 0.0000i	0.5616 + 0.0000i	-0.4082

(c)

OB#	$\mathbf{e}_1$	$\mathbf{e}_2$	$\mathbf{e}_3$
$\tilde{s}_1\,(3)$	-0.0419 - 0.5507i	0.1050 + 0.1313i	0.4082
$\tilde{s}_{1'}(3)$	-0.1568 - 0.0174i	-0.2594 + 0.4911i	-0.4082
$\tilde{s}_2)\,(3)$	-0.4774 + 0.3069i	-0.0763 - 0.0732i	0.4082
$\tilde{s}_{2'}(3)$	0.0229 + 0.0174i	-0.3022 - 0.4911i	-0.4082
$\tilde{s}_3\,(3)$	0.5193 + 0.2438i	-0.0288 - 0.0581i	0.4082
$\tilde{s}_{3'}(3)$	0.1339 + 0.0000i	0.5616 + 0.0000i	-0.4082

Numeric solution

The laser noise free eigenvectors for blocks with frequencies $f = \{1, 3, 5\}$ are given in Table 4.18. The solutions for AET using these eigenvectors are

$$\widetilde{A}(1) = (0.6746 - 1.7142i)\,\mathbf{e}_2 + (0.6512 - 1.5892i)\,\mathbf{e}_3,$$

$$\widetilde{E}(1) = (-2.3501 + 1.8237i)\,\mathbf{e}_2 + (2.5478 - 1.9208i)\,\mathbf{e}_3,$$

$$\widetilde{T}(1) = (-4.1815 - 4.1815i)\,\mathbf{e}_1,$$

$$\widetilde{A}(3) = (-0.6006 - 2.5994i)\,\mathbf{e}_1 + (3.1829 - 0.6392i)\,\mathbf{e}_2,$$

$$\widetilde{E}(3) = (-5.1417 + 2.2762i)\ \mathbf{e}_1 + (1.7477 + 4.2776i)\ \mathbf{e}_2,$$
$$\widetilde{T}(3) = (-0.7175 + 0.7175i)\ \mathbf{e}_3,$$

$$\widetilde{A}(5) = (-0.6006 + 2.5994i)\ \mathbf{e}_1 - (3.1829 + 0.6392i)\ \mathbf{e}_2,$$
$$\widetilde{E}(5) = (-5.1417 - 2.2762i)\ \mathbf{e}_1 + (1.7477 - 4.2776i)\ \mathbf{e}_2,$$
$$\widetilde{T}(5) = (-0.7175 - 0.7175i)\ \mathbf{e}_3. \tag{4.44}$$

The same results were obtained for $f = \{3, 5\}$ with blocks that contain the same real values but different imaginary values for the power spectral densities (Table 4.15). This seems to indicate that the eigenvalues and eigenvectors can obtained from the real power spectral density matrix. This might also indicate the possibility of using only the magnitude spectral densities, however, unlike the real values they do not retain the signs of the values which are needed, for example, blocks $f = 1$ and $f = 3$. The eigenvalues for these blocks are (301,301,1,1,1,1) and (401,101,101,1,1,1) where the number of degenerate values are different.

4.4 Summary

In this chapter we proved the connection between the eigenvalues that are free from laser phase noises with the time domain Sagnac and the frequency domain *AET* observables. In the time domain using integer values for the offsets allowed the eigenpairs to be generated algebraically. This was only possible for very small matrices since the computation times increased rapidly with the increase in the size of the matrix. The algebraic computation times for a small 90×90 matrix was approximately 9 hrs. In the frequency domain the structure of the matrix is a block diagonal and the algebraic computation can be done on each block separately which, in theory, should lead to shorter reasonable times. However, the conventional method of generating the eigenvalues depends on the determinant of the matrix which is not trivial to compute for matrices with sizes greater than three. In the frequency domain the speed of the computation will depend on the size and structure of the blocks. For the raw data the size of the blocks is the same as in the time domain which is 6×6 for which the computation of the determinant for algebraic solutions will still not be trivial in general. However, the partitioning of the eigendecompostion makes parallel computation possible which would

be useful for both methods.

Obtaining LISA data with the required sensitivity for the analysis is accomplished by transforming the raw data using the laser noise free eigenvectors which are determined from the eigenvalues. It is the transformation of the data that is important therefore, exact solutions may not be needed for the generation of the eigenpairs. In this case numeric solutions were obtained for which the computation times remained reasonably low. For example, for the largest matrix which was 18000×18000 the computation time was 7 m. For this time, the size of the matrix that the algebraic computation could produce a solution was for a 48×48 matrix. The comparison of the number and values of the eigenvalues obtained from both methods were the same. The difference was that the numeric solutions gave eigenvectors with that had contributions from most of the optical benches and times.

In this chapter we used toy models to obtain algebraic solutions in order to determine the connection between the laser noise free eigenvectors and time delay interferometry combinations. We adjusted the model slightly to include real values for the arm lengths from which we were still able to obtain the distinct groups. In Chapter 6 the model will be extended even further to handle more realistic LISA data including some mentioned in Romano and Woan. The success of this approach relies on the splitting of the values into the two distinct groups, therefore in that chapter we will be checking whether this will still be the case when using real data. Before doing this, however, we will show how the principal components approach is used in the data analysis and how it compares with the conventional approach using the time delay interferometry observables. This will be done in the next chapter.

Chapter 5

Bayesian-principal component analysis for LISA data

Recall that the reason for the time delay interferometry observables is to achieve the required sensitivity for LISA that will allow astronomy to be obtained from its data. The main obstruction to achieving this goal is the overwhelming laser phase noises for which the time delay interferometry observables were developed which are linear combination of the raw data that leads to the cancellation of the noises. The data analysis is done using these observables which have to be generated before any analysis is performed. Romano and Woan introduced the principal components approach for producing the data with the necessary sensitivity required for the analysis. In the last chapter we proved the connection between these principal components and the time delay interferometry observables. In this chapter we illustrate the use of these components in the data analysis and show that they produce the same results as the conventional method using the time delay interferometry observables. This will be performed on a toy model of LISA raw data consisting of a single monochromatic source buried in white stationary Gaussian noises. The signal will be characterised only by its waveform parameters of amplitude, frequency and phase with the latter two assumed to be known. Bayesian inference will be used to estimate the amplitude of the signal in the raw data.

Since the data are time series the inference is initially done using these however, the frequency domain offers some advantages particularly the possibility of identifying the frequencies of the signals and of simplifying the matrix inversion and eigendecomposition because of the diagonal nature of the power spectral density matrix. For this reason the inference is also performed in this domain. The results from these will be compared with that obtained using the conventional approach with the optimal AET observables.

5.1 Bayesian inference

The Bayesian approach to statistical inference uses probability to define uncertainty which expresses either incomplete knowledge or unpredictability due to randomness [45]. It is performed on real data which are the outcomes of observations and therefore they are fixed. The variable quantities, which are the target of the inference, are the unknown parameters that produce the data and the uncertainties in the estimates of their values are defined with probability distributions. This differs from the frequentist approach where the unknown parameters are fixed and the data are random outcomes. Probabilities are assigned to reflect the possibility of different realisations of the data based on a particular parameter value which is based on hypothetical data [79].

5.1.1 Bayes' theorem

The mathematical formulation of Bayesian inference is Bayes' theorem which is defined by Bretthorst [16] as

$$p(H|D,I) = \frac{p(D|H,I)p(H|I)}{p(D|I)}. \tag{5.1}$$

Following Bretthorst, the outcome of the inference is the posterior probability $p(H|D,I)$ which expresses the probability of the hypothesis H given the data D and some prior information I. The prior information defines what is known about the phenomena that generated the data. The prior probability $p(H|I)$ describes what is known about the hypothesis based only on information obtained before considering the data. The posterior provides information after considering the data. The direct probability $p(D|H,I)$ generally expresses the probability of the data given the hypothesis and the prior information. However, what this represents depends on what is kept constant in the computations. When the hypothesis is evaluated for different sets of data this is a sampling probability distribution but when different hypotheses are evaluated using the same data it is a likelihood function. The prior probability of the data $p(D|I)$ is the probability of the data based only on the prior information and it is also called the marginal probability, the global likelihood or the evidence.

Weinberg [79] points out that it is the relationship between the posterior and the prior probabilities that is the value of the Bayesian analysis since it provides informa-

tion about the hypothesis before and after considering the data. This also allows the updating of the estimates when new data are acquired resulting in a sequential application of Bayes' theorem where the posterior probability obtained from one experiment is used as the prior probability for the next experiment. It provides a way to learn from experience by including new data/information [45]. Another advantage of the Bayesian approach is the ability to handle nuisance parameters which are those that are needed for the computation but are not the required outcome of the inference. This is handled through a process of marginalisation where the computation are performed for all values of the nuisance parameter.

5.1.2 Bayesian parameter estimation

In the inference the hypothesis is posed as a question about the values of the parameters that could be responsible for the observed data for which the prior information I will contain a model M for the data [5]. For parameter estimation Equation 5.1 can be written as

$$p(\mathbf{a}|\mathbf{d}, M) = \frac{p(\mathbf{d}|\mathbf{a}, M)\, p(\mathbf{a}|M)}{p(\mathbf{d}|M)}, \tag{5.2}$$

where $p(\mathbf{d}|\mathbf{a}, M)$ is the likelihood, $p(\mathbf{a}|M)$ is the prior and is the $p(\mathbf{d}|M)$ evidence. The parameters and data are given by $\mathbf{a} = \{a_1, ..., a_k\}$ and $\mathbf{d} = \{d_1, ..., d_n\}$, respectively.

5.1.2.1 The posterior probability

As the outcome of the inference, the posterior probability $p(\mathbf{a}|\mathbf{d}, M)$ will be a distribution of the probabilities of the possible values of the parameters responsible for the data. The results of the inference can be expressed by reporting the whole distribution or just summary statistics from it, for example, the mean and variance [79].

5.1.2.2 The likelihood

The likelihood $p(\mathbf{d}|\mathbf{a}, M)$ is the point where the data enters the inference. For model-based inference this is evaluated for different values of the parameters for the same data and therefore, it is a likelihood function $L(\mathbf{a}; \mathbf{D}, M)$. The inference will be based on the noises in the data with parameters and model defined by statistics and probability distributions.

The statistical models express the probability of the joint occurrence of the values in the observations. If the noise in the data are represented by $\mathbf{d} = \{d_1, d_2, \ldots, d_n\}$ and if the individual values are all mutually independent, the probability of their joint occurrence can be expressed as

$$\begin{aligned} p_{\mathbf{d}}(d_1, ..., d_n) &= p(d_1)\; p(d_2) \cdots p(d_d) \\ &= \prod_{i=1}^{n} p(d_i). \end{aligned} \tag{5.3}$$

With dependencies between the values, the joint probability distribution will contain conditional probabilities which is given by

$$\begin{aligned} p_{\mathbf{d}}(d_1, ..., d_n) &= p(d_1)\; p(d_2|d_1) \cdots p(d_n|d_1, \ldots, d_{n-1}) \\ &= p(d_1) \prod_{i=2}^{n} p(d_i|d_1, \ldots, d_{n-1}). \end{aligned} \tag{5.4}$$

Although the focus is on the noises, the aim is the extraction of the signals buried in the noise. The noise models and their parameters are assumed to be previously known and are used to infer the signal parameters based on knowledge of the different waveforms expected in the data.

5.1.3 Simplifying Bayes' theorem

The computation of the posterior probability using Bayes' theorem as given in Equation 5.2 can be expressed as a proportionality depending only on the likelihood, that is,

$$p(\mathbf{a}|\mathbf{d}, M) \propto p(\mathbf{d}|\mathbf{a}, M). \tag{5.5}$$

This depends on the properties of the evidence and assumptions made about the prior. This will be illustrated in the following sections.

5.1.3.1 The evidence

In the context of parameter estimation, the evidence $p(\mathbf{d}|M)$, the denominator in Equation 5.2, is computed for a fixed model and fixed data which can be obtained from

$$p(\mathbf{d}|\mathbf{a}, M) = \sum_i p(\mathbf{d}|\mathbf{a}_i, M)\; p(\mathbf{a}_i|M). \tag{5.6}$$

where it is the probability of the data summed over all the values of the parameters giving a global value for the parameters (global likelihood) or a marginal value for the

data (marginal likelihood) [33]. The likelihood gives results for a particular value of the parameter while the evidence is evaluated for all values of the parameter. So for parameter estimation this will be a constant and its effect would be to normalise the posterior probability ensuring that it sums or integrates to unity [15]. The product of the posterior distribution with a constant does not change its mean value or the structure of the distribution, therefore, it can be ignored and Equation 5.2 reduces to a proportionality containing the prior and likelihood becoming

$$p(\mathbf{a}|\mathbf{d}, M) \propto p(\mathbf{d}|\mathbf{a}, M)\, p(\mathbf{a}|M). \tag{5.7}$$

5.1.3.2 The prior

This is the term that can greatly affects the outcome of the inference as it describes the distribution of the values of the parameters which can have different statistics and shapes. In our toy model we will be assuming equal probabilities of all values for the parameter being estimated which can be defined using a flat or uniform prior. This will also be constant for which the product with the likelihood function will also not change the structure or location of the mean of the resulting posterior probability distribution. Ignoring the prior reduces Equation 5.7 to

$$p(\mathbf{a}|D, M) \propto p(\mathbf{d}|\mathbf{a}, M) \tag{5.8}$$

which will be the form used in the analysis of LISA data.

5.1.4 The likelihood for the raw data

The raw data time series with the two lasers on each spacecraft phase-locked can be written as

$$s_i(t_a) = p_j(t_a - D_k) - p_i(t_a) + n_i(t_a) + h_i(t_a), \tag{5.9}$$

where p_i, n_i, h_i represent the contributions from the laser phase noises, the photodetector noises and the gravitational waves, respectively. The subscripts i and j indicate the optical bench number and k the arm of the antenna. The likelihood is based on the noises in the data and these are obtained from Equation 5.9 by subtracting the signal

$h_i(t)$ giving

$$\begin{aligned} s_i(t_a) - h_i(t_a) &= p_j(t_a - D_k) - p_i(t_a) + n_i(t_a) \\ &= d_i(t_a), \end{aligned} \tag{5.10}$$

which is a linear combination of the three different noises. In the toy model each of these noises are assumed to be independent Gaussian processes with no correlations between their values at different times. This means that there are no correlations between the same optical bench readings at different times (auto-correlations) but there are cross-correlations between the different optical bench readings because of the presence of the same noises in the different readings.

The joint probability distribution for each reading d_i will be the product of independent Gaussian distributions. The probability distribution of a linear combination of independent Gaussian processes is another Gaussian with mean and variance equal to the sum of the individual means and variances. The distribution for the noises in each optical bench data is therefore $\mathbf{d} \sim \mathcal{N}(0, 2\sigma_d^2)$ where $\sigma_d^2 = 2\sigma_p^2 + \sigma_n^2$ expressing the joint probability distribution of the combined noises in each optical bench data and the likelihood is

$$\begin{aligned} L(a; \mathbf{d}_i, M) &= \prod_{l=1}^{m} p(d_i(t_l)) \\ &= \prod_{l=1}^{m} \Big(\frac{1}{2\pi(2\sigma_p^2 + \sigma_n^2)}\Big)^{1/2} \exp\Big(- \frac{1}{2} \frac{(d_i(t_l))^2}{2\sigma_p^2 + \sigma_n^2}\Big) \\ &= \Big(\frac{1}{2\pi(2\sigma_p^2 + \sigma_n^2)}\Big)^{m/2} \exp\Big(- \frac{1}{2} \sum_{l=1}^{m} \frac{(d_i(t_l))^2}{2\sigma_p^2 + \sigma_n^2}\Big), \end{aligned} \tag{5.11}$$

which is a multivariate Gaussian. Here $\mathbf{d}_i = \{d_i(t_1), \ldots d_i(t_m)\}$ with the subscript i indicating the optical bench number. In matrix form this can be written as

$$L(a; \mathbf{d}_i, M) = \frac{1}{(2\pi)^{N/2}|C|^{1/2}} \exp\Big(- \frac{1}{2} \mathbf{d}_i^T C^{-1} \mathbf{d}_i\Big), \tag{5.12}$$

where C is the covariance matrix for each optical bench expressing the correlations between the values at different times, $|C|$ is the determinant of the matrix and N is the total number of values. For the individual optical bench readings the matrix will be diagonal with the values along the main diagonal being the variance which is $2\sigma_p^2 + \sigma_n^2$. The inference is performed using all six readings simultaneously and with phase-locking of the lasers on each spacecraft there will be correlations between the readings of the

different optical benches requiring conditional distributions. The likelihood for all six readings Equation 5.12 becomes

$$L(a;\mathbf{d},M)=\frac{1}{(2\pi)^N|C|^{1/2}}\exp\Big(-\frac{1}{2}\,\mathbf{d}^TC^{-1}\mathbf{d}\Big), \tag{5.13}$$

where $\mathbf{d}$ is a $6m\times 1$ vector of the raw data from all the six optical benches grouped in blocks of six where the order is $1,1',2,2',3,3'$. This covariance matrix is the block matrix that was generated in Chapter 3.

5.1.4.1 Computing the likelihood

The values that will be used for the noise variances in the our toy model will be chosen to allow for easy identification of the laser noise free eigenvectors and will have values integer values with a large separation between them for example, $\sigma_p^2=100$ and $\sigma_n^2=1$. This leads to very small values in the terms outside the exponential in the multivariate Gaussian function in Equation 5.13 for any appreciable sized matrix. For a 10×10 diagonal matrix the determinant is $\approx 10^{33}$ for which the inverse is $\approx 10^{-33}$. Since these do not change in the parameter estimation the computation of the likelihood function will be based only on the last term in the equation which is called the likelihood kernel [33] and Equation 5.13 can be rewritten as

$$L(a;\mathbf{d},M)\propto\exp\Big(-\frac{1}{2}\,\mathbf{d}^TC^{-1}\mathbf{d}\Big). \tag{5.14}$$

The values within the exponential will also be small and to compensate for this the relative likelihood $\mathcal{L}_R$ will be computed and plotted instead of the likelihood where it is given relative to the maximum estimate of the parameter [33]. This is computed from

$$L_R(a;\mathbf{d})=\frac{L(a;\mathbf{d})}{L(\hat{a}_{ML};\mathbf{d})}. \tag{5.15}$$

The aim of the analysis is to obtain an estimate of the amplitude of the signal buried in the raw data using the data generated by the principal components. Since we will be using relative likelihood values we will only be able to compare the values obtained and not their probabilities.

5.1.4.2 Incorporating the principal components

The target of the principal component analysis is the covariance matrix in Equation 5.13. Recall that the principal components are obtained from the eigendecomposition

of this matrix which can be expressed as

$$CV = V\Lambda, \tag{5.16}$$

where V and Λ are the matrix of eigenvectors and eigenvalues, respectively.

$$C = V\Lambda V^{-1}. \tag{5.17}$$

The inverse of the covariance matrix is required which can be written as

$$\begin{aligned} C^{-1} &= (V\Lambda V^{-1})^{-1} \\ &= V^T\Lambda V, \end{aligned} \tag{5.18}$$

where the $V^{-1} = V^T$. This is substituted into Equation **??**

$$L(a; \mathbf{d}, M) \propto \exp\Big[-\frac{1}{2} (V\mathbf{d})^T \Lambda^{-1} (V\mathbf{d}) \Big], . \tag{5.19}$$

5.2 Bayesian inference using the raw science data

In this section the results of the inference using the principal component approach for dealing with the laser phase noises are given including details of how the data are simulated. This is done in the time and frequency domains. In order to compare the estimates of the amplitude values from both domains the spectra will be generated from the raw data time series using the MATLAB *fft* function.

5.2.1 Simulating the raw data time series

Recall that time series for the raw data can be written as

$$s_i(t) = p_j(t - D_k) - p_i(t) + n_i(t) + h_i(t), \tag{5.20}$$

where each reading is a combination of the noises associated with the receiving optical bench (p_i, n_i), the delayed phase noise of the transmitting optical bench (p_j) and the strain produced by the gravitational wave h_i in the arm between them.

5.2.1.1 The laser phase and photodetector noises

The noise contributions for all the optical benches with the laser on each spacecraft phase-locked to each other are

$$\begin{aligned}
s_1^{noise}(t) &= p_2(t-D_3) - p_1(t) + n_1(t), \quad s_{1'}^{noise}(t) = p_3(t-D_2) - p_1(t) + n_{1'}(t), \\
s_2^{noise}(t) &= p_3(t-D_1) - p_2(t) + n_2(t), \quad s_{2'}^{noise}(t) = p_1(t-D_3) - p_2(t) + n_{2'}(t), \\
s_3^{noise}(t) &= p_1(t-D_2) - p_3(t) + n_3(t), \quad s_{3'}^{noise}(t) = p_2(t-D_1) - p_3(t) + n_{3'}(t), \quad (5.21)
\end{aligned}$$

where there will only be three independent lasers with phases noises of p_1, p_2 and p_3 with the numbers indicating the spacecraft. Each laser phase noise occurs in readings at the current time t and at two shifted times related to the arms adjacent to the parent spacecraft requiring three copies of each noise. The time series are simulated with three independent random Gaussian sequences with zero means and variances σ_p^2 generated with the MATLAB *randn* function. The time series for the laser noises with the time offsets are generated from the current time series by shifting them according to the corresponding offsets. The photodetector noises are all independent with each occuring only once in the data at time t. These are simulated with six independent random Gaussian sequences with zero means and variance σ_n^2 also using the *randn* function.

5.2.1.2 Gravitational wave signal

The contributions from the signals in the optical bench data are

$$s_i^{gw}(t) = h_i(t), \quad (5.22)$$

where $h_i(t)$ is the phase reading associated with the strain produced in the arm adjacent to optical bench i by the gravitational wave $\mathbf{h}(t)$. The equations for signal responses were obtained from Armstrong, Estabrook and Tinto [6] where the gravitational signal $\mathbf{h}(t)$ is assumed to be a transverse traceless plane wave. The motion and orientation of the wave is described by an orthonormal propagation frame with unit vectors $\hat{\mathbf{i}}$, $\hat{\mathbf{j}}$ and $\hat{\mathbf{k}}$ with the direction of motion being parallel to $\hat{\mathbf{k}}$. The wave is a combination of two polarisations $h_+(t)$ and $h_\times(t)$ given by

$$\mathbf{h}(t) = h_+(t)\mathbf{e}_+ + h_\times(t)\mathbf{e}_\times, \quad (5.23)$$

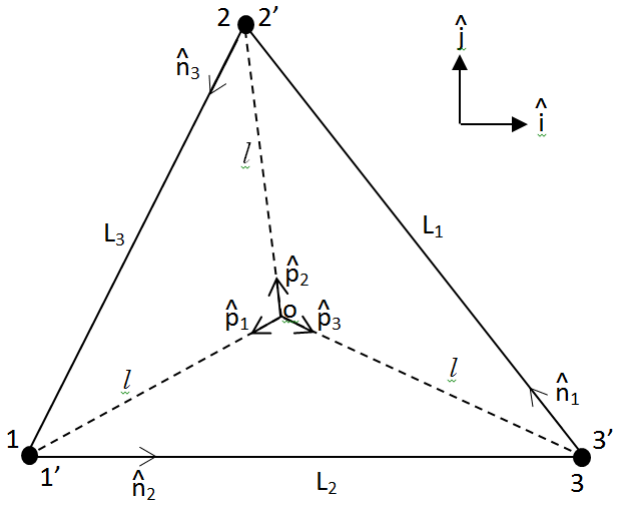

Figure 5.1: A schematic diagram of the plane of LISA showing notation and the location of the vectors used in deriving the gravitational wave responses based on [6].

where $\mathbf{e}_+$ and $\mathbf{e}_\times$ are tensors that are transverse to $\hat{\mathbf{k}}$ and traceless. For the orthonormal frame these can be expressed as

$$e_+ = \begin{pmatrix} 1 & 0 & 0 \\ 0 & -1 & 0 \\ 0 & 0 & 0 \end{pmatrix}, \qquad e_\times = \begin{pmatrix} 0 & 1 & 0 \\ 1 & 0 & 0 \\ 0 & 0 & 0 \end{pmatrix}, \tag{5.24}$$

and Equation 5.23 becomes

$$\mathbf{h}(t) = \begin{pmatrix} h_+(t) & 0 & 0 \\ 0 & -h_+(t) & 0 \\ 0 & 0 & 0 \end{pmatrix} + \begin{pmatrix} 0 & h_\times(t) & 0 \\ h_\times(t) & 0 & 0 \\ 0 & 0 & 0 \end{pmatrix}. \tag{5.25}$$

In Armstrong et. al. [6] the wave is assumed to be a first-order spatial metric perturbation occurring at point O which is a point in plane of the antenna that is equidistant from the three spacecraft as shown in Figure 5.1. The distance from this point to three spacecraft is l and the orientation to the spacecraft is defined by three unit vectors $\hat{\mathbf{p}}_i$ that are in the antenna's plane. The orientation of the wave with respect to the antenna given by μ_i which is the dot product of the $\hat{\mathbf{k}}$ and $\hat{\mathbf{p}}_i$ that is

$$\mu_i = \hat{\mathbf{k}} \cdot \hat{\mathbf{p}}_i. \tag{5.26}$$

The expressions given for the responses for the optical benches on spacecraft 1 are

$$h_1(t) = \big[1 + \frac{d}{D_3}\big(\mu_1 - \mu_2\big)\big]\big[\Psi_3(t - \mu_2 d - D_3) - \Psi_3(t - \mu_1 d)\big], \tag{5.27}$$

$$h_{1'}(t) = \big[1 - \frac{d}{D_2}\big(\mu_3 - \mu_1\big)\big]\big[\Psi_2(t - \mu_3 d - D_2) - \Psi_2(t - \mu_1 d)\big], \tag{5.28}$$

where $D_i = L_i/c$ is the light travel time in each arm and $d = l/c$ is the travel time from O to each spacecraft. The function $\Psi_i(t)$ describes the orientation of the wave to the arms with respect to the unit vectors $\hat{\mathbf{n}}_i$ along each arm and is given by

$$\Psi_i(t) = \frac{1}{2}\frac{\hat{\mathbf{n}}_i \cdot \mathbf{h}(t) \cdot \hat{\mathbf{n}}_i}{1 - (\hat{\mathbf{k}} \cdot \hat{\mathbf{n}}_i)^2}. \tag{5.29}$$

From the above, the responses for the optical benches on the other spacecraft were generated and determined to be

$$h_2(t) = \big[1 + \frac{d}{D_1}\big(\mu_2 - \mu_3\big)\big]\big[\Psi_1(t - \mu_3 d - D_1) - \Psi_1(t - \mu_2 d)\big], \tag{5.30}$$

$$h_{2'}(t) = \big[1 - \frac{d}{D_3}\big(\mu_1 - \mu_2\big)\big]\big[\Psi_3(t - \mu_1 d - D_3) - \Psi_3(t - \mu_2 d)\big], \tag{5.31}$$

$$h_3(t) = \big[1 + \frac{d}{D_1}\big(\mu_2 - \mu_3\big)\big]\big[\Psi_1(t - \mu_2 d - D_1) - \Psi_1(t - \mu_3 d)\big], \tag{5.32}$$

$$h_{3'}(t) = \big[1 - \frac{d}{D_2}\big(\mu_3 - \mu_1\big)\big]\big[\Psi_2(t - \mu_1 d - D_2) - \Psi_2(t - \mu_3 d)\big], \tag{5.33}$$

where Ψ_i for all the optical benches are defined as

$$\begin{aligned}
\Psi_1(t - \mu_2 d - D_1) &= \frac{1}{2}\frac{\hat{\mathbf{n}}_1 \cdot \mathbf{h}(t - \mu_2 d - D_1) \cdot \hat{\mathbf{n}}_1}{1 - (\hat{\mathbf{k}} \cdot \hat{\mathbf{n}}_1)^2}, \quad \Psi_1(t - \mu_3 d) = \frac{1}{2}\frac{\hat{\mathbf{n}}_1 \cdot \mathbf{h}(t - \mu_3 d) \cdot \hat{\mathbf{n}}_1}{1 - (\hat{\mathbf{k}} \cdot \hat{\mathbf{n}}_1)^2}, \\
\Psi_1(t - \mu_3 d - D_1) &= \frac{1}{2}\frac{\hat{\mathbf{n}}_1 \cdot \mathbf{h}(t - \mu_3 d - D_1) \cdot \hat{\mathbf{n}}_1}{1 - (\hat{\mathbf{k}} \cdot \hat{\mathbf{n}}_1)^2}, \quad \Psi_1(t - \mu_2 d) = \frac{1}{2}\frac{\hat{\mathbf{n}}_1 \cdot \mathbf{h}(t - \mu_2 d) \cdot \hat{\mathbf{n}}_1}{1 - (\hat{\mathbf{k}} \cdot \hat{\mathbf{n}}_1)^2}, \\
\Psi_2(t - \mu_1 d - D_2) &= \frac{1}{2}\frac{\hat{\mathbf{n}}_2 \cdot \mathbf{h}(t - \mu_1 d - D_2) \cdot \hat{\mathbf{n}}_2}{1 - (\hat{\mathbf{k}} \cdot \hat{\mathbf{n}}_2)^2}, \quad \Psi_2(t - \mu_3 d) = \frac{1}{2}\frac{\hat{\mathbf{n}}_2 \cdot \mathbf{h}(t - \mu_3 d) \cdot \hat{\mathbf{n}}_2}{1 - (\hat{\mathbf{k}} \cdot \hat{\mathbf{n}}_2)^2} \\
\Psi_2(t - \mu_3 d - D_2) &= \frac{1}{2}\frac{\hat{\mathbf{n}}_2 \cdot \mathbf{h}(t - \mu_3 d - D_2) \cdot \hat{\mathbf{n}}_2}{1 - (\hat{\mathbf{k}} \cdot \hat{\mathbf{n}}_2)^2}, \quad \Psi_2(t - \mu_1 d) = \frac{1}{2}\frac{\hat{\mathbf{n}}_2 \cdot \mathbf{h}(t - \mu_1 d) \cdot \hat{\mathbf{n}}_2}{1 - (\hat{\mathbf{k}} \cdot \hat{\mathbf{n}}_2)^2}, \\
\Psi_3(t - \mu_1 d - D_3) &= \frac{1}{2}\frac{\hat{\mathbf{n}}_3 \cdot \mathbf{h}(t - \mu_1 d - D_3) \cdot \hat{\mathbf{n}}_3}{1 - (\hat{\mathbf{k}} \cdot \hat{\mathbf{n}}_3)^2}, \quad \Psi_3(t - \mu_2 d) = \frac{1}{2}\frac{\hat{\mathbf{n}}_3 \cdot \mathbf{h}(t - \mu_2 d) \cdot \hat{\mathbf{n}}_3}{1 - (\hat{\mathbf{k}} \cdot \hat{\mathbf{n}}_3)^2}, \\
\Psi_3(t - \mu_2 d - D_3) &= \frac{1}{2}\frac{\hat{\mathbf{n}}_3 \cdot \mathbf{h}(t - \mu_2 d - D_3) \cdot \hat{\mathbf{n}}_3}{1 - (\hat{\mathbf{k}} \cdot \hat{\mathbf{n}}_3)^2}, \quad \Psi_3(t - \mu_1 d) = \frac{1}{2}\frac{\hat{\mathbf{n}}_3 \cdot \mathbf{h}(t - \mu_1 d) \cdot \hat{\mathbf{n}}_3}{1 - (\hat{\mathbf{k}} \cdot \hat{\mathbf{n}}_3)^2}.
\end{aligned} \tag{5.34}$$

Simplifying the responses

In our simulation the signal will be assumed to contain only the plus polarisation and the vectors $\hat{\mathbf{i}}$ and $\hat{\mathbf{j}}$ are aligned with the direction of its perturbations. Assuming that the gravitational wave is traveling in a direction perpendicular to the plane of the antenna, then $\mu_i = \hat{\mathbf{k}} \cdot \hat{\mathbf{n}}_i = 0$ and expressions in the Equation 5.34 reduce to

$$\begin{aligned}
\Psi_1(t) &= \frac{1}{2}\hat{\mathbf{n}}_1 \cdot \mathbf{h}(t) \cdot \hat{\mathbf{n}}_1, \qquad & \Psi_1(t - D_1) &= \frac{1}{2}\hat{\mathbf{n}}_1 \cdot \mathbf{h}(t - D_1) \cdot \hat{\mathbf{n}}_1, \\
\Psi_2(t) &= \frac{1}{2}\hat{\mathbf{n}}_2 \cdot \mathbf{h}(t) \cdot \hat{\mathbf{n}}_2, \qquad & \Psi_2(t - D_2) &= \frac{1}{2}\hat{\mathbf{n}}_2 \cdot \mathbf{h}(t - D_2) \cdot \hat{\mathbf{n}}_2, \\
\Psi_3(t) &= \frac{1}{2}\hat{\mathbf{n}}_3 \cdot \mathbf{h}(t) \cdot \hat{\mathbf{n}}_3, \qquad & \Psi_3(t - D_3) &= \frac{1}{2}\hat{\mathbf{n}}_3 \cdot \mathbf{h}(t - D_3) \cdot \hat{\mathbf{n}}_3.
\end{aligned} \tag{5.35}$$

Inserting these into Equations 5.28 and 5.33 gives

$$\begin{aligned}
h_1(t) &= \Psi_3(t - D_3) - \Psi_3(t) = \frac{1}{2}\big[\hat{\mathbf{n}}_3 \cdot \mathbf{h}(t - D_3) \cdot \hat{\mathbf{n}}_3 - \hat{\mathbf{n}}_3 \cdot \mathbf{h}(t) \cdot \hat{\mathbf{n}}_3\big], \\
h_{1'}(t) &= \Psi_2(t - D_2) - \Psi_2(t) = \frac{1}{2}\big[\hat{\mathbf{n}}_2 \cdot \mathbf{h}(t - D_2) \cdot \hat{\mathbf{n}}_2 - \hat{\mathbf{n}}_2 \cdot \mathbf{h}(t) \cdot \hat{\mathbf{n}}_2\big], \\
h_2(t) &= \Psi_1(t - D_1) - \Psi_1(t) = \frac{1}{2}\big[\hat{\mathbf{n}}_1 \cdot \mathbf{h}(t - D_1) \cdot \hat{\mathbf{n}}_1 - \hat{\mathbf{n}}_1 \cdot \mathbf{h}(t) \cdot \hat{\mathbf{n}}_1\big], \\
h_{2'}(t) &= \Psi_3(t - D_3) - \Psi_3(t) = \frac{1}{2}\big[\hat{\mathbf{n}}_3 \cdot \mathbf{h}(t - D_3) \cdot \hat{\mathbf{n}}_3 - \hat{\mathbf{n}}_3 \cdot \mathbf{h}(t) \cdot \hat{\mathbf{n}}_3\big], \\
h_3(t) &= \Psi_2(t - D_2) - \Psi_2(t) = \frac{1}{2}\big[\hat{\mathbf{n}}_2 \cdot \mathbf{h}(t - D_2) \cdot \hat{v}_2 - \hat{\mathbf{n}}_2 \cdot \mathbf{h}(t) \cdot \hat{\mathbf{n}}_2\big], \\
h_{3'}(t) &= \Psi_1(t - D_1) - \Psi_1(t) = \frac{1}{2}\big[\hat{\mathbf{n}}_1 \cdot \mathbf{h}(t - D_1) \cdot \hat{\mathbf{n}}_1 - \hat{\mathbf{n}}_1 \cdot \mathbf{h}(t) \cdot \hat{\mathbf{n}}_1\big].
\end{aligned} \tag{5.36}$$

Next $\hat{\mathbf{i}}$ is set parallel to arm L_2. The relationships between propagation vectors $(\hat{\mathbf{i}}, \hat{\mathbf{j}}, \hat{\mathbf{k}})$ and the unit vectors $\hat{\mathbf{n}}_i$ along the arms are

$$\begin{aligned}
\hat{\mathbf{i}} &= -\hat{\mathbf{n}}_1 \cos(\theta_3), \qquad & \hat{\mathbf{j}} &= \hat{\mathbf{n}}_1 \sin(\theta_3), \\
\hat{\mathbf{i}} &= \hat{\mathbf{n}}_2, & \hat{\mathbf{j}} &= 0, \\
\hat{\mathbf{i}} &= -\hat{\mathbf{n}}_3 \cos(\theta_1), & \hat{\mathbf{j}} &= -\hat{\mathbf{n}}_3 \sin(\theta_1).
\end{aligned} \tag{5.37}$$

The angles θ_1 and θ_3 are at the spacecraft 1 and 3, respectively and for an equilateral arrangement they will be 60°. However, with unequal arms these will be determined by using the cosine formula giving

$$\cos(\theta_1) = \frac{D_2^2 + D_3^2 - D_1^2}{2D_2D_3}, \qquad \cos(\theta_3) = \frac{D_1^2 + D_2^2 - D_3^2}{2D_1D_2}. \tag{5.38}$$

The expressions for the terms $\hat{\mathbf{n}}_i \cdot \mathbf{h}(t) \cdot \hat{\mathbf{n}}_i$ in Ψ_i are

$$\begin{aligned}\hat{\mathbf{n}}_1 \cdot \mathbf{h}(t) \cdot \hat{\mathbf{n}}_1 &= \begin{pmatrix} -\hat{\mathbf{n}}_1 \cos(\theta_3) & \hat{\mathbf{n}}_1 \sin(\theta_3) & 0 \end{pmatrix} \begin{pmatrix} h_+(t) & 0 & 0 \\ 0 & -h_+(t) & 0 \\ 0 & 0 & 0 \end{pmatrix} \begin{pmatrix} -\hat{\mathbf{n}}_1 \cos(\theta_3) \\ \hat{\mathbf{n}}_1 \sin(\theta_3) \\ 0 \end{pmatrix} \\ &= \hat{n}_1^2 h_+(t) \cos^2(\theta_3) - \hat{n}_1^2 h_+(t) \sin^2(\theta_3 \\ &= h_+(t) \big[\cos^2(\theta_3) - \sin^2(\theta_3\big] \\ &= h_+(t) \cos(2\theta_3), \end{aligned} \tag{5.39}$$

$$\begin{aligned}\hat{\mathbf{n}}_2 \cdot \mathbf{h}(t) \cdot \hat{\mathbf{n}}_2 &= \begin{pmatrix} \hat{\mathbf{n}}_2 & 0 & 0 \end{pmatrix} \begin{pmatrix} h_+(t) & 0 & 0 \\ 0 & -h_+(t) & 0 \\ 0 & 0 & 0 \end{pmatrix} \begin{pmatrix} \hat{\mathbf{n}}_2 \\ 0 \\ 0 \end{pmatrix} \\ &= h_+(t), \end{aligned} \tag{5.40}$$

$$\begin{aligned}\hat{\mathbf{n}}_3 \cdot \vec{h}(t) \cdot \hat{\mathbf{n}}_3 &= \begin{pmatrix} -\hat{\mathbf{n}}_3 \cos(\theta_1) & -\hat{\mathbf{n}}_3 \sin(\theta_1) & 0 \end{pmatrix} \begin{pmatrix} h_+(t) & 0 & 0 \\ 0 & -h_+(t) & 0 \\ 0 & 0 & 0 \end{pmatrix} \begin{pmatrix} -\hat{\mathbf{n}}_3 \cos(\theta_1) \\ -\hat{\mathbf{n}}_3 \sin(\theta_1) \\ 0 \end{pmatrix} \\ &= h_+(t) \big[\cos^2(\theta_1) - \sin^2(\theta_1\big] \\ &= h_+(t) \cos(2\theta_1). \end{aligned} \tag{5.41}$$

The final responses are obtained by inserting these into Equation 5.36 giving

$$\begin{aligned} h_1(t) &= \frac{1}{2}\big[\hat{\mathbf{n}}_3 \cdot \mathbf{h}(t - D_3) \cdot \hat{\mathbf{n}}_3 - \hat{\mathbf{n}}_3 \cdot \mathbf{h}(t) \cdot \hat{\mathbf{n}}_3\big] \\ &= \frac{\cos(2\theta_1)}{2}\big[h_+(t - D_3) - h_+(t)\big], \end{aligned} \tag{5.42}$$

$$\begin{aligned} h_{1'}(t) &= \frac{1}{2}\big[\hat{\mathbf{n}}_2 \cdot \mathbf{h}(t - D_2) \cdot \hat{\mathbf{n}}_2 - \hat{\mathbf{n}}_2 \cdot \mathbf{h}(t) \cdot \hat{\mathbf{n}}_2\big] \\ &= \frac{1}{2}\big[h_+(t - D_2) - h_+(t)\big], \end{aligned} \tag{5.43}$$

$$\begin{aligned} h_2(t) &= \frac{1}{2}\big[\hat{\mathbf{n}}_1 \cdot \mathbf{h}(t - D_1) \cdot \hat{\mathbf{n}}_1 - \hat{\mathbf{n}}_1 \cdot \mathbf{h}(t) \cdot \hat{n}_1\big] \\ &= \frac{\cos(2\theta_3)}{2}\big[h_+(t - D_1) - h_+(t)\big], \end{aligned} \tag{5.44}$$

$$\begin{aligned} h_{2'}(t) &= \frac{1}{2}\big[\hat{\mathbf{n}}_3 \cdot \mathbf{h}(t - D_3) \cdot \hat{\mathbf{n}}_3 - \hat{\mathbf{n}}_3 \cdot \mathbf{h}(t) \cdot \hat{\mathbf{n}}_3\big] \\ &= \frac{\cos(2\theta_1)}{2}\big[h_+(t - D_3) - h_+(t)\big], \end{aligned} \tag{5.45}$$

$$
\begin{aligned}
h_3(t) &= \frac{1}{2}\big[\hat{\mathbf{n}}_2 \cdot \mathbf{h}(t - D_2) \cdot \hat{v}_2 - \hat{\mathbf{n}}_2 \cdot \mathbf{h}(t) \cdot \hat{\mathbf{n}}_2\big] \\
&= \frac{1}{2}\big[h_+(t - D_2) - h_+(t)\big], \qquad (5.46) \\
h_{3'}(t) &= \frac{1}{2}\big[\hat{\mathbf{n}}_1 \cdot \mathbf{h}(t - D_1) \cdot \hat{\mathbf{n}}_1 - \hat{\mathbf{n}}_1 \cdot \mathbf{h}(t) \cdot \hat{\mathbf{n}}_1\big] \\
&= \frac{\cos(\theta_3)}{2}\big[h_+(t - D_1) - h_+(t)\big]. \qquad (5.47)
\end{aligned}
$$

The signal waveforms

A zero phase cosine waveform is assumed for the gravitational wave signal which is

$$h_+(t) = Hcos(2\pi f_0 t), \qquad (5.48)$$

where H is the peak amplitude and f_0 is the frequency. The final responses using this waveform are

$$
\begin{aligned}
h_1(t) &= \frac{H\cos(2\theta_1)}{2}\big[\cos\big(2\pi f_0(t - D_3)\big) - \cos(2\pi f_0 t)\big], \\
h_{1'}(t) &= \frac{H}{2}\big[\cos\big(2\pi f_0(t - D_2)\big) - \cos(2\pi f_0 t)\big], \\
h_2(t) &= \frac{H\cos(2\theta_3)}{2}\big[\cos\big(2\pi f_0(t - D_1)\big) - \cos(2\pi f_0 t)\big], \\
h_{2'}(t) &= \frac{H\cos(2\theta_1)}{2}\big[\cos\big(2\pi f_0(t - D_3)\big) - \cos\big(2\pi f_0 t\big)\big], \\
h_3(t) &= \frac{H}{2}\big[\cos\big(2\pi f_0(t - D_2)\big) - \cos\big(2\pi f_0 t\big)\big], \\
h_{3'}(t) &= \frac{H\cos(2\theta_3)}{2}\big[\cos\big(2\pi f_0(t - D_1)\big) - \cos(2\pi f_0 t)\big]. \qquad (5.49)
\end{aligned}
$$

5.2.2 The likelihood function in the frequency domain

The complex data means that the frequency domain likelihood kernel will contain a complex conjugate which is

$$\mathcal{L}(a|\{\mathbf{d}_i\}, M) = \exp\Big[-\frac{1}{2}\,(\mathbf{s} - \mathbf{h})^{*T}\, C^{-1}\,(\mathbf{s} - \mathbf{h})\Big]. \qquad (5.50)$$

where '*' indicate the complex conjugate. In MATLAB the transpose automatically includes the conjugate.

5.2.2.1 The signal spectra

The gravitational wave was modeled in the time series as a monochromatic cosine signal with initial zero phase. The Fourier transform of a cosine function [63] can be written

as

$$\mathcal{F}\big[\cos(2\pi f_0 t)\big] = \frac{1}{2}\Big[\delta(f - f_0) + \delta(f + f_0)\Big], \tag{5.51}$$

with the time shifted version being given by

$$\mathcal{F}\big[\cos\big(2\pi f_0(t - D_i)\big)\big] = \frac{1}{2}\Big[e^{-2\pi f_0 D_i}\delta(f - f_0) + e^{2\pi f 0 D_i}\delta(f + f_0)\Big], \tag{5.52}$$

which gives delta responses with amplitudes split in half at $\pm f_0$.

The raw data time series for the signals from Section 5.2.1 are

$$h_i(t) = \frac{G_i}{2}\big[\cos(2\pi f_0(t - D_k) - \cos(2\pi f_0 t)\big], \tag{5.53}$$

where G_i represents the gains in arm i. The corresponding spectra are

$$\begin{aligned}\widetilde{h}_i(f) &= \frac{G_i}{2}\Big\{\frac{1}{2}\big[e^{2\pi i f_0 D_i}\delta(f + f_0) + e^{-2\pi i f_0 D_k}\delta(f - f_0)\big] - \frac{1}{2}\big[\delta(f + f_0) + \delta(f - f_0)\big]\Big\} \\ &= \frac{G_i}{4}\big[\delta(f + f_0)(e^{2\pi i f_0 D_k} - 1) + \delta(f - f_0)(e^{-2\pi i f_0 D_k} - 1)\big],\end{aligned} \tag{5.54}$$

and for the single sided spectrum this becomes

$$\widetilde{h}_i(f) = \frac{G_i}{2}\big[\delta(f - f_0)(e^{-2\pi i f_0 D_k} - 1)\big]. \tag{5.55}$$

The terms $\delta(f \pm f_0)$ are complex and for a cosine signal with zero phase this will be $1 + 0i$. The signal spectra for all the optical benches are

$$\begin{aligned}
\widetilde{h}_1(f) &= \frac{H\cos(2\theta_1)}{2}\delta(f - f_0)(e^{-2\pi i f_0 D_3} - 1), & \widetilde{h}_{1'}(f) &= \frac{H}{2}\delta(f - f_0)(e^{-2\pi i f_0 D_2} - 1), \\
\widetilde{h}_2(f) &= \frac{H\cos(2\theta_3)}{2}\delta(f - f_0)(e^{-2\pi i f_0 D_1} - 1), & \widetilde{h}_{2'}(f) &= \frac{H\cos(2\theta_1)}{2}\delta(f - f_0)(e^{-2\pi i f_0 D_3} - 1), \\
\widetilde{h}_3(f) &= \frac{H}{2}\delta(f - f_0)(e^{-2\pi i f_0 D_2} - 1), & \widetilde{h}_{3'}(f) &= \frac{H\cos(2\theta_3)}{2}\delta(f - f_0)(e^{-2\pi i f_0 D_1} - 1).
\end{aligned} \tag{5.56}$$

For the toy model we are assuming no modulation of its amplitude, frequency or phase therefore, the location of the values in the spectra will be exactly at the frequency of the signal. This means that for our model the amplitude search in the frequency domain can be done just at the frequency of the signal. We also chose the frequency of the signal to match exactly one of the bins in the spectra to avoid leakage.

Table 5.1: Values used for the amplitude search.

Parameter	Value
Range of times	0 - 1047 s
Sampling rate (Hz)	1
Offsets (D_1,D_2,D_3)(s)	15, 16, 17
Laser noise means	0
Laser noise variances	10000
Shot noise means	0
Shot noise variances	1
Signal amplitude	5
Signal frequency	$4.9 \times 10^{-3} Hz$
Template range for the amplitude	3-7
Number of templates	1000

5.2.3 Raw data results

The values for the parameters used in the model, data and search are given in Table 5.1. A search was done only for the signal's amplitude therefore all the values of the other parameters were fixed. A section of the covariance matrix is given in Figure 5.4 and the real and imaginary blocks for the power spectral density matrix are given in Figure 5.3. The relative likelihoods for the signal amplitude for both domains are given in Figure 5.2. The frequency domain results include values for both the full spectra and just at the signal frequency in order to show that the block eigendecomposition produced the same results as the full matrix decomposition. The results for all three cases showed same relative likelihood for the signal's amplitude with the most likely value being 5.034 which is within a range of about 0.7% of the actual value.

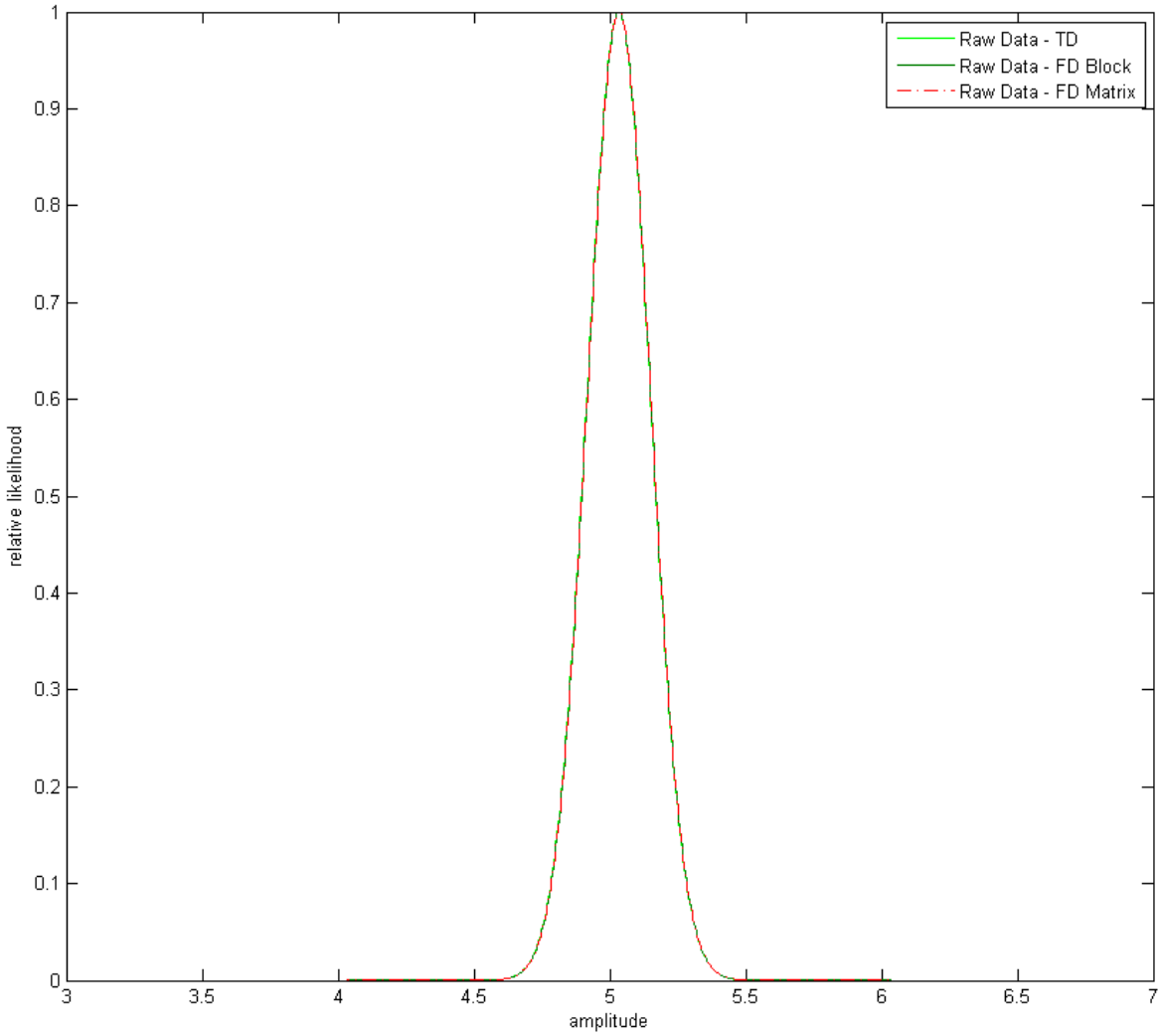

Figure 5.2: The relative likelihoods for the signal amplitude obtained from the raw data time series and spectra. All the values of the other signal parameters were kept fixed during the estimation. For the spectra, results were obtained for the full spectra and for the single frequency. The maximum likelihood values all occur at 5.034.

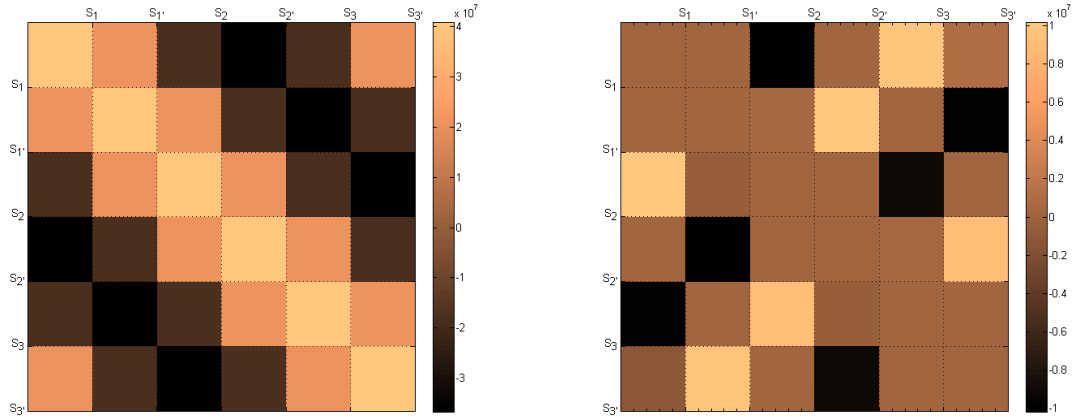

(a) (b)

Figure 5.3: Samples of the power spectral density matrix block at the signal's frequency showing the (a) real and (b) imaginary values. The offsets are 15s, 16s and 17s with noise variances of $\sigma_p^2 = 10000$ and $\sigma_n^2 = 1$.

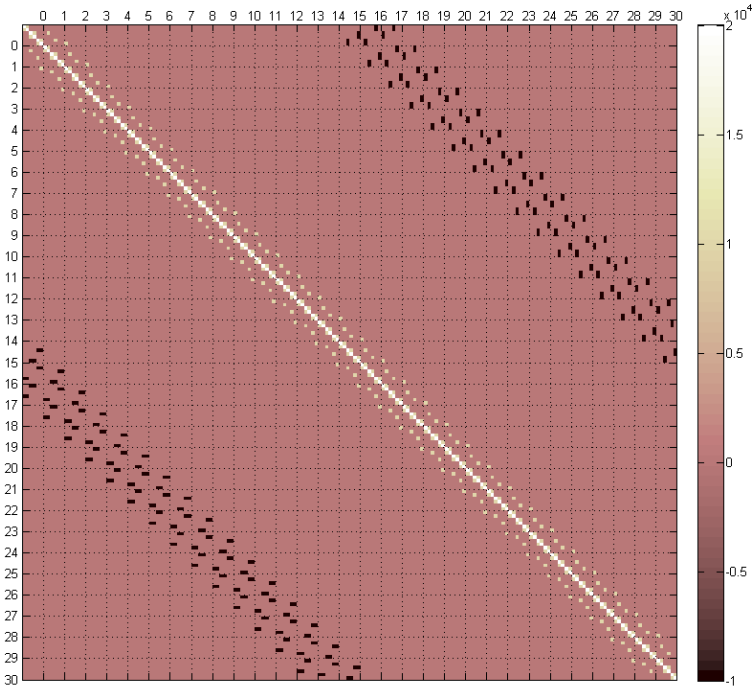

Figure 5.4: A section of the covariance matrix for offsets of $D = \{15, 16, 17\}$ with laser and photodetector noise variances of $\sigma_p^2 = 10000$ and $\sigma_n^2 = 1$, respectively.

5.3 Bayesian inference using the time delay interferometry observables

The current approach to doing LISA data analysis is through the time delay interferometry observables. In this section the results of the analysis using the optimal AET observables are presented. Since these observables were generated in the frequency domain the results are only for that domain. However, in order to compare the results with those obtained for the principal components the AET data were generated from the raw data used in the previous section. The signal amplitude search required the templates of the signal in the AET data spectra therefore these are included in this section.

5.3.1 Simulating the AET time series

The time series for the A, E, T observables in terms of the Sagnacs are

$$\begin{aligned} A(t) &= \frac{1}{\sqrt{2}}[\gamma(t) - \alpha(t)], \\ E(t) &= \frac{1}{\sqrt{6}}[\alpha(t) - 2\beta(t) + \gamma(t)], \\ T(t) &= \frac{1}{\sqrt{3}}[\alpha(t) + \beta(t) + \gamma(t)], \end{aligned} \tag{5.57}$$

where the $\alpha(t)$, $\beta(t)$ and $\gamma(t)$ are given by

$$\begin{aligned} \alpha(t) &= s_{1'}(t) + s_{2'}(t - D_1 - D_2) + s_{3'}(t - D_2), \\ &\quad - s_1(t) - s_2(t - D_3) - s_3(t - D_1 - D_3), \\ \beta(t) &= s_{1'}(t - D_3) + s_{2'}(t) + s_{3'}(t - D_2 - D_3), \\ &\quad - s_1(t - D_2 - D_1) - s_2(t) - s_3(t - D_1), \\ \gamma(t) &= s_{1'}(t - D_3 - D_1) + s_{2'}(t - D_1) + s_{3'}(t) \\ &\quad - s_1(t - D_2) - s_2(t - D_3 - D_2) - s_3(t). \end{aligned} \tag{5.58}$$

The assumption is that the laser phase noises have been canceled, therefore, each phase reading $s_i(t)$ is just a combination of the photodetector noise $n_i(t)$ and gravitational wave signal $h_i(t)$ which is

$$s_i(t) = n_i(t) + h_i(t). \tag{5.59}$$

The raw data used to generate the AET time series therefore, only included the photodetector noises and the signal. The readings s_i are shifted according to the offsets in the Sagnacs given in Equation 5.58.

5.3.2 The AET signal spectra

The signal contributions to the AET data spectra are

$$\begin{aligned}
\widetilde{A}(f) = &\frac{H}{\sqrt{2}}\,\delta(f-f_0)\Big[1-e^{2\pi i f_0 D_2}-e^{2\pi i f_0 (D_1+D_3)}-e^{2\pi i f_0 (D_1+D_2+D_3)}\Big]\\
&-\frac{H\cos(2\theta_1)}{2\sqrt{2}}\,\delta(f-f_0)\Big[1+e^{2\pi i f_0 D_1}-e^{2\pi i f_0 D_2}-e^{2\pi i f_0 D_3}-e^{2\pi i f_0 (D_1+D_2)}\\
&\qquad -e^{2\pi i f_0 (D_1+D_3)}+e^{2\pi i f_0 (D_2+D_3)}+e^{2\pi i f_0 (D_1+D_2+D_3)}\Big]\\
&-\frac{H\cos(2\theta_3)}{2\sqrt{2}}\,\delta(f-f_0)\Big[1-e^{2\pi i f_0 D_1}-e^{2\pi i f_0 D_2}+e^{2\pi i f_0 D_3}+e^{2\pi i f_0 (D_1+D_2)}\\
&\qquad -e^{2\pi i f_0 (D_1+D_3)}-e^{2\pi i f_0 (D_2+D_3)}+e^{2\pi i f_0 (D_1+D_2+D_3)}\Big],\\
\widetilde{E}(f) = &-\frac{H}{\sqrt{6}}\,\delta(f-f_0)\Big[e^{2\pi i f_0 D_1}-e^{2\pi i f_0 D_2}-e^{2\pi i f_0 (D_1+D_2)}+e^{2\pi i f_0 (D_2+D_3)}\Big]\\
&+\frac{H\cos(2\theta_1)}{2\sqrt{6}}\,\delta(f-f_0)\Big[3-e^{2\pi i f_0 D_1}+e^{2\pi i f_0 D_2}-3e^{2\pi i f_0 D_3}-3e^{2\pi i f_0 (D_1+D_2)}\\
&\qquad +e^{2\pi i f_0 (D_1+D_3)}-e^{2\pi i f_0 (D_2+D_3)}+3e^{2\pi i f_0 (D_1+D_2+D_3)}\Big]\\
&+\frac{H\cos(2\theta_3)}{2\sqrt{6}}\,\delta(f-f_0)\Big[3e^{2\pi i f_0 D_1}-e^{2\pi i f_0 D_2}+e^{2\pi i f_0 D_3}+e^{2\pi i f_0 (D_1+D_2)}\\
&\qquad -e^{2\pi i f_0 (D_1+D_3)}+3e^{2\pi i f_0 (D_2+D_3)}-3e^{2\pi i f_0 (D_1+D_2+D_3)}\Big],\\
\widetilde{T}(f) = &-\frac{H}{2\sqrt{3}}\,\delta(f-f_0)\Big[e^{2\pi i f_0 D_1}-e^{2\pi i f_0 D_3}-e^{2\pi i f_0 (D_1+D_2)}+e^{2\pi i f_0 (D_2+D_3)}\Big]\\
&-\frac{H\cos(2\theta_1)}{2\sqrt{3}}\,\delta(f-f_0)\Big[e^{2\pi i f_0 D_1}-e^{2\pi i f_0 D_2}-e^{2\pi i f_0 (D_1+D_3)}+e^{2\pi i f_0 (D_2+D_3)}\Big]\\
&-\frac{H\cos(2\theta_3)}{2\sqrt{3}}\,\delta(f-f_0)\Big[e^{2\pi i f_0 D_2}+e^{2\pi i f_0 D_3}-e^{2\pi i f_0 (D_1+D_2)}+e^{2\pi i f_0 (D_1+D_3)}\Big],
\end{aligned} \tag{5.60}$$

which are used for the templates in the amplitude search.

5.3.3 AET results

The relative likelihood for the signal amplitude is given in Figure 5.5 and the real and imaginary blocks of the power spectral density matrix used in the analysis are given in Figure 5.6. From the plot the most likely value for the signal amplitude is 5.05 which

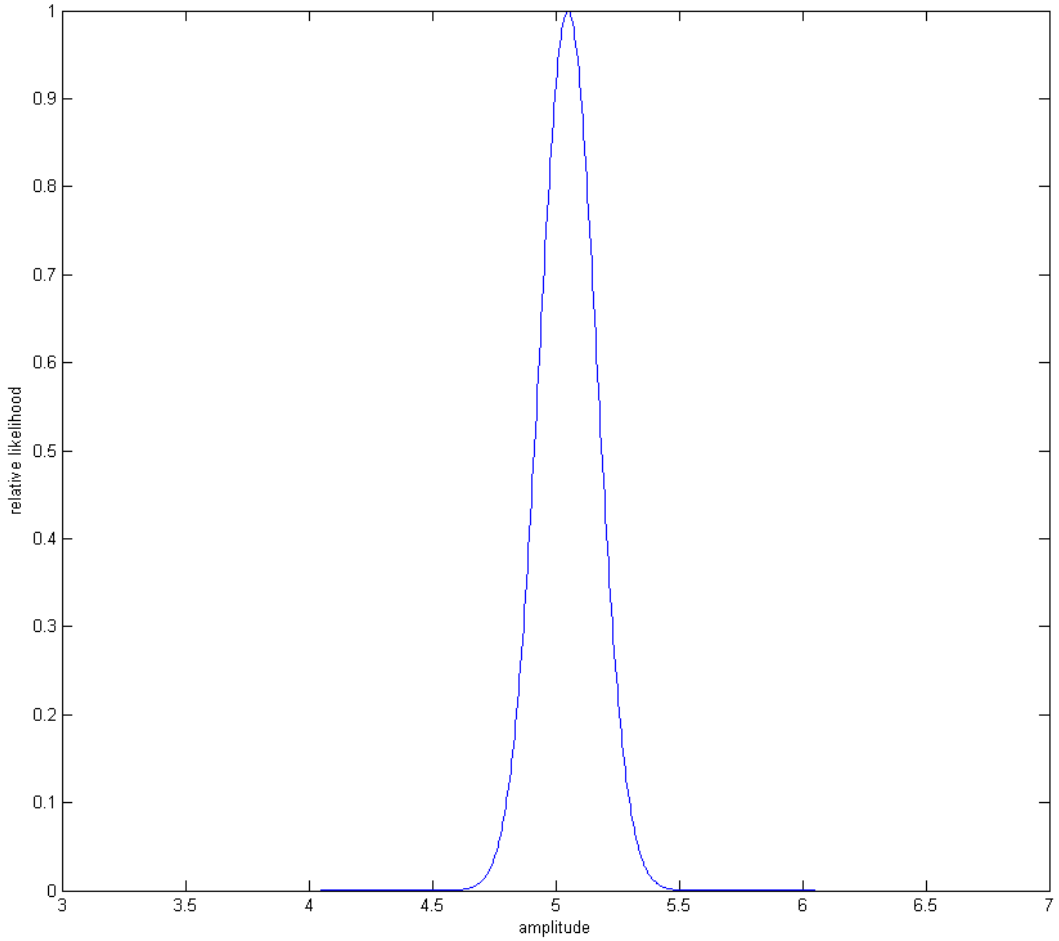

Figure 5.5: The relative likelihood for the signal amplitude for the optimal time delay interferometry observable AET where the maximum likelihood value is at 5.05.

is within a 1% range of the actual value.

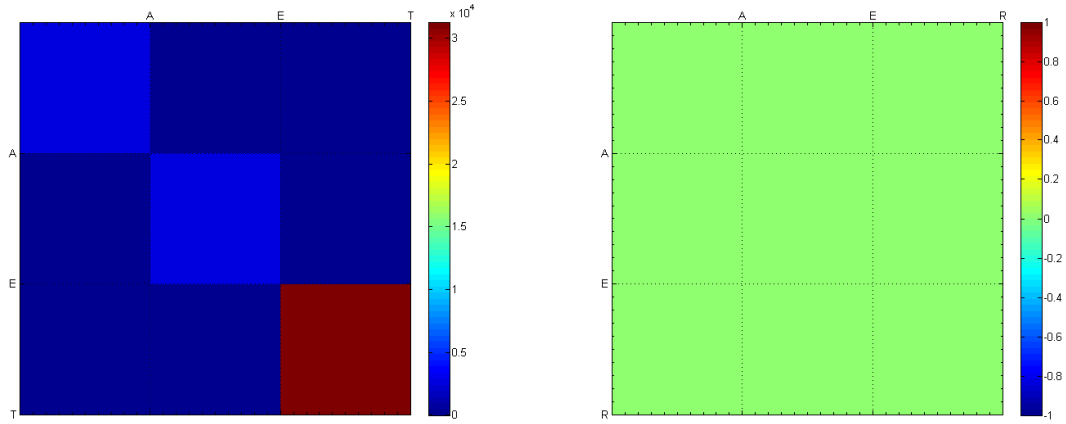

(a) (b)

Figure 5.6: Sample block of the power spectral density matrix at the signal's frequency showing the (a) real and and (b) imaginary values.

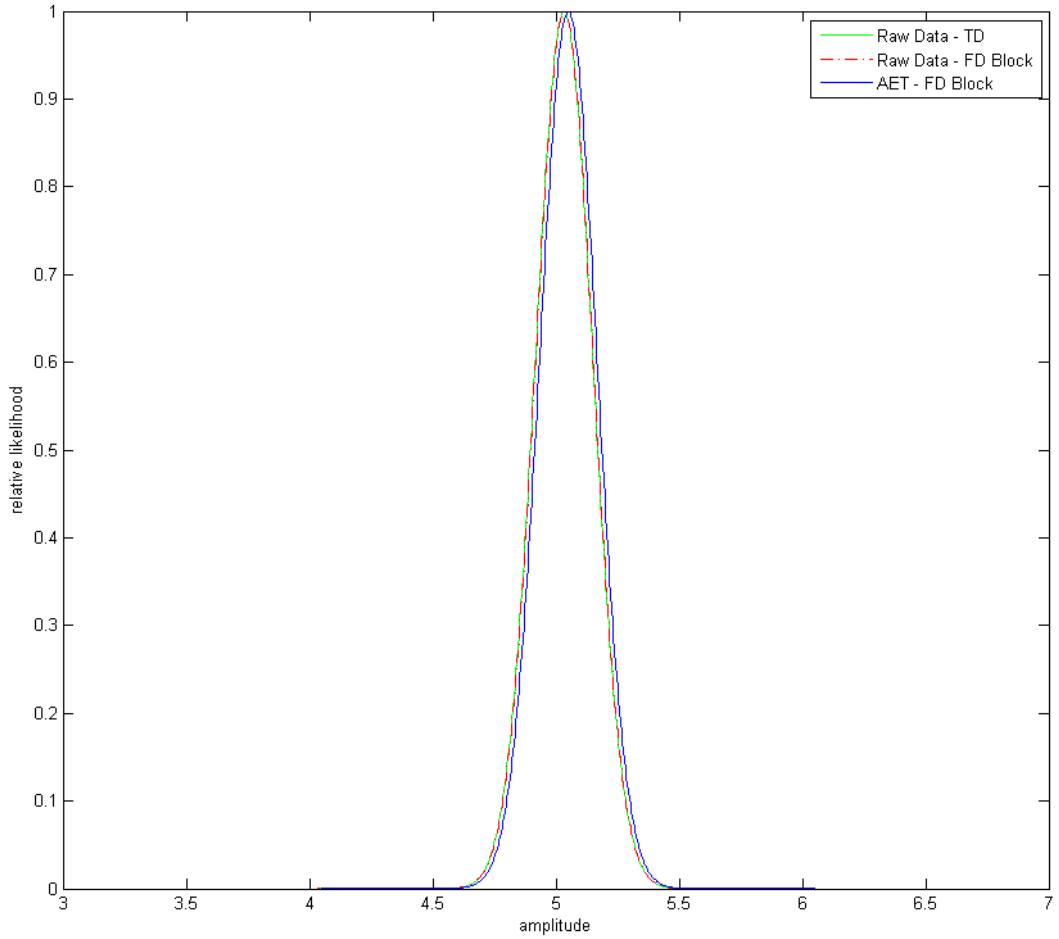

Figure 5.7: The relative likelihoods for the amplitude of the signal obtained from the raw data time series and spectra using principal components and from the *AET* spectra. The maximum likelihoods for the signal amplitudes occur at 5.034, 5.034 for the raw data and 5.05 for *AET*.

5.4 Summary

The relative likelihood plots for the signal amplitude obtained using the raw data and the optimal time delay interferometry data for both domains are given in Figure 5.7 where they have the same precision with estimates of the signal amplitudes of 5.034 for the raw data and 5.05 for the *AET* observables.

Chapter 6

Principal components for more realistic LISA data

In the previous chapters the principal component approach was illustrated using a toy model of LISA in terms of both its configuration and data. The antenna was assumed to be stationary and rigid with unequal arm lengths. The instrumental noises used in the data were restricted to the primary and the limiting sources which are the laser phase and the photodetector (shot) noises respectively, both of which were assumed to be white, Gaussian and stationary with known means and variances. All noise means were set to zero with the variances of each type having the same values of σ_p^2 and σ_n^2, respectively chosen to provide a significant separation between the different types to reflect the situation in the antenna. All the photodetector noises were assumed to be independent and the lasers were phase-locked on each spacecraft resulting in only three laser phase noises. Based on these assumptions, the eigendecomposition of the noise covariance and power spectral density matrices produced two distinct groups of eigenvalues with one set having contributions from both types of noises and the other only photodetector noises. The group of interest is the latter which, because of the equality of the noise variances, led to multiply degenerate values.

In this chapter we investigate how the principal component approach adapts to more complex models of LISA data and the focus will be on the noise covariance and power spectral density matrices as they are the sources of the eigenvalues. The values and types of the eigenvalues will depend on the matrix structure which is determined by the variance and covariances of the noises, the phase-locking of the lasers and the arm lengths therefore a summary of the results of Chapter 3 which outlined their effects on the matrices is given. The final outcome is to see what aspects of real LISA data will prevent the laser noise free eigenvalues from being generated without which the principal components method will not be useful.

6.1 Time domain

Recall that the readings of each optical bench tracking the relative spacecraft motion (long arm reading) is a combination of the laser phase ($p_i(t)$) and the photodetector ($n_i(t)$) noises associated with that bench plus the laser phase noise ($p_j(t - D_k)$) from the optical bench at the other end of the arm. The time series of phase shifts recorded by each bench can be written as

$$s_i(t) = p_j(t - D_k) - p_i(t) + n_i(t), \tag{6.1}$$

where i, j represent the optical benches, k the arms and D_k is the time offset or the light travel time in the arm between the two optical benches. In the toy model, LISA was modeled as a stationary array with static arms that could have equal or unequal lengths which gave a maximum of three values which is indicated by the subscript $k = \{1, 2, 3\}$.

6.1.1 Matrix definitions

Before proceeding a few terms that will be used in this section to describe the matrices will be explained. The main diagonal in a square matrix is the central diagonal that splits the matrix into halves giving upper and lower triangular sections. Super-diagonals and sub-diagonals are those parallel to the main running above and below it, respectively. In a symmetric matrix the values in the upper triangle are a reflection of those in lower triangle about the main diagonal. A Toeplitz matrix is one in which all the values are constant along each diagonal with each diagonal having different values in general. In a symmetric Toeplitz matrix the sub-diagonals are a reflection of the super-diagonals across the main diagonal. The entries of a matrix may also be in the form of blocks where the element appear as smaller matrices within the matrix with the previously mentioned types also having block equivalents. In the toy model of LISA used in the previous chapters the noise covariance matrix is a symmetric block Toeplitz where the diagonals contain the same block repeated along the diagonal.

Table 6.1: Raw data phase readings showing the contributions for the laser phase p_i and photodetector (n_i) noises. The expressions are given for the different types of laser noise phase-locking with unequal ($D_i = L_i/c$) and equal ($D = L/c$) arm lengths.

phase-locking	Phase	Noise contributions in the readings	
		Equal arms D	Unequal arms(D_i)
None	$s_1(t)$	$p_{2'}(t-D) - p_1(t) + n_1(t)$	$p_{2'}(t-D_3) - p_1(t) + n_1(t)$
	$s_{1'}(t)$	$p_3(t-D) - p_{1'}(t) + n_{1'}(t)$	$p_3(t-D_2) - p_{1'}(t) + n_{1'}(t)$
	$s_2(t)$	$p_{3'}(t-D) - p_2(t) + n_2(t)$	$p_{3'}(t-D_1) - p_2(t) + n_2(t)$
	$s_{2'}(t)$	$p_1(t-D) - p_{2'}(t) + n_{2'}(t)$	$p_1(t-D_3) - p_{2'}(t) + n_{2'}(t)$
	$s_3(t)$	$p_{1'}(t-D) - p_3(t) + n_3(t)$	$p_{1'}(t-D_2) - p_3(t) + n_3(t)$
	$s_{3'}(t)$	$p_2(t-D) - p_{3'}(t) + n_{3'}(t)$	$p_2(t-D_1) - p_{3'}(t) + n_{3'}(t)$
Spacecraft	$s_1(t)$	$p_2(t-D) - p_1(t) + n_1(t)$	$p_2(t-D_3) - p_1(t) + n_1(t)$
	$s_{1'}(t)$	$p_3(t-D) - p_1(t) + n_{1'}(t)$	$p_3(t-D_2) - p_1(t) + n_{1'}(t)$
	$s_2(t)$	$p_3(t-D) - p_2(t) + n_2(t)$	$p_3(t-D_1) - p_2(t) + n_2(t)$
	$s_{2'}(t)$	$p_1(t-D) - p_2(t) + n_{2'}(t)$	$p_1(t-D_3) - p_2(t) + n_{2'}(t)$
	$s_3(t)$	$p_1(t-D) - p_3(t) + n_3(t)$	$p_1(t-D_2) - p_3(t) + n_3(t)$
	$s_{3'}(t)$	$p_2(t-D) - p_3(t) + n_{3'}(t)$	$p_2(t-D_1) - p_3(t) + n_{3'}(t)$
All	$s_1(t)$	$p(t-D) - p(t) + n_1(t)$	$p(t-D_3) - p(t) + n_1(t)$
	$s_{1'}(t)$	$p(t-D) - p(t) + n_{1'}(t)$	$p(t-D_2) - p(t) + n_{1'}(t)$
	$s_2(t)$	$p(t-D) - p(t) + n_2(t)$	$p(t-D_1) - p(t) + n_2(t)$
	$s_{2'}(t)$	$p(t-D) - p(t) + n_{2'}(t)$	$p(t-D_3) - p(t) + n_{2'}(t)$
	$s_3(t)$	$p(t-D) - p(t) + n_3(t)$	$p(t-D_2) - p(t) + n_3(t)$
	$s_{3'}(t)$	$p(t-D) - p(t) + n_{3'}(t)$	$p(t-D_1) - p(t) + n_{3'}(t)$

6.1.2 The effects of the laser phase-locking on the covariance matrix

Recall that LISA has six optical benches which are indicated with the subscripts $i, j = \{1, 1', 2, 2', 3, 3'\}$. Each optical bench has its own laser allowing for several options in terms of whether they are linked by phase-locking or left to operate independently. The phase-locking options that are considered are (i) none where all the lasers are acting independently, (ii) spacecraft locked where the two lasers on each spacecraft are locked to each other and (iii) all locked where all the lasers are acting as a single laser. The labeling of the laser noises reflects the phase-locking options. For the independent lasers the labels reflect the optical bench number ($i, j = \{1, 1', 2, 2', 3, 3'\}$). The primed notation is dropped for the spacecraft locked lasers giving $i, j = \{1, 2, 3\}$ which indicate the spacecraft number. When they are all locked the numbers are not used.

The equations for the raw data from all the optical benches are given in Table 6.1 for the different phase-locking options showing the differences with equal and unequal arm lengths. Although the covariances are not given the existence of correlations can be easily be determined. Recall that correlations between two optical benches will only occur if the same noise appear in their readings indicating that the noise type and times must match. For the lasers this depends on the phase-locking and, because of the

structure of the readings, also the time offsets. In this section the focus is on the effects of phase-locking only and the arm lengths will be assumed to be equal.

6.1.2.1 No laser phase-locking

From the equations for this mode of operation in Table 6.1 it can be seen that the only non-zero entries in the covariance matrix will be from the variances, which are the auto-covariances at time t, and the cross-covariances between the raw data from the two optical benches at the end of each arm as these are the only readings that have the same laser phase noises. Recall that auto-covariance expresses the correlations within the same raw data while the cross-covariances are between different data. For example, using the raw data from the optical benches at the end of arm 3 which are $s_1(t)$ and $s_{2'}(t)$, with equal arm lengths D the equations are

$$\begin{aligned} s_1(t) &= p_{2'}(t-D) - p_1(t) + n_1(t), \\ s_{2'}(t) &= p_1(t-D) - p_{2'}(t) + n_{2'}(t), \end{aligned} \tag{6.2}$$

where the same two laser phase noises p_1 and $p_{2'}$ occur in each but with different times. The only auto-covariance within these readings is at time t. For $s_1(t)$ the auto-covariance is

$$\mathrm{cov}[s_1(t_a), s_1(t_b)] = \langle p_{2'}(t_a - D)\, p_{2'}(t_b - D)\rangle + \langle p_1(t_b)\, p_1(t_b)\rangle + \langle n_1(t_b)\, n_1(t_b)\rangle, \tag{6.3}$$

which will only produce non-zero values at time $t_a = t_b = t$, that is,

$$\begin{aligned} \mathrm{cov}[s_1(t), s_1(t)] &= \langle p_{2'}^2(t-D)\rangle + \langle p_1^2(t)\rangle + \langle n_1^2(t)\rangle \\ &= \mathrm{var}[s_1(t)]. \end{aligned} \tag{6.4}$$

These are the main diagonal entries on the covariance matrix. The cross-covariance between the two readings is

$$\mathrm{cov}[s_1(t_a), s_{2'}(t_b)] = -\langle p_{2'}(t_a - D)\, p_{2'}(t_b)\rangle - \langle p_1(t_a)\, p_1(t_b - D)\rangle, \tag{6.5}$$

giving non-zero values when $t_a - t_b = \pm D$ which are the locations of the sub-diagonal and super-diagonal entries. Only one term will contribute at a particular time. For example, for times $t_b = t_a - D$ and $t_a = t_b - D$ the covariances are respectively,

$$\begin{aligned} \mathrm{cov}[s_1(t_a), s_{2'}(t_a - D)] &= -\langle p_{2'}^2(t_a - D)\rangle, \\ \mathrm{cov}[s_1(t_b - D), s_{2'}(t_b)] &= -\langle p_1^2(t_b - D)\rangle, \end{aligned} \tag{6.6}$$

where the noise will also be from different lasers and will only give the same result if they have the same variances. For no phase-locking, the equal arm lengths will produce three diagonals in the covariance matrix including the main diagonal.

6.1.2.2 Lasers phase-locked on each spacecraft

Locking the lasers on each spacecraft to each other introduces correlations between the readings of the optical benches along the two arms that are monitored by that spacecraft. Also, since each arm is monitored by two spacecraft, this also causes correlations with the optical benches on the other spacecraft. So that the spacecraft locking causes mutual correlations between all the optical benches. With spacecraft phase-locking there will only be three independent lasers and this will be reflected in the notation where primed notation $p_{i'}$ will be dropped. The spacecraft phase-locking does not change the auto-covariance nor the cross-covariance between the readings for the optical benches at the end of each arm.

Unlike the optical benches at the end of each arm which have two common noises, the other cross-covariances for the other optical benches will only be due to one common noise between them. This will produce correlations at times consisting of different combinations of t and $t - D$ producing three points of correlations. The correlations at time t will be from the optical benches on the same spacecraft for example, the cross-covariance between for s_1 and $s_{1'}$ on spacecraft 1 is

$$\mathrm{cov}[s_1(t), s_{1'}(t)] = \langle p^2(t) \rangle, \tag{6.7}$$

which occur along the main diagonal. The other two will occur between the readings of the optical bench one spacecraft with the two readings along the arm opposite that spacecraft. For example, for s_1 on spacecraft 1 the arm opposite to spacecraft 1 is arm 1 with optical benches s_2 and $s_{3'}$ and the cross-covariances are

$$\begin{aligned} \mathrm{cov}[s_1(t_a), s_2(t_b)] &= -\langle p_2(t_a - D)\, p_2(t_b) \rangle, \\ \mathrm{cov}[s_1(t_a), s_{3'}(t_b)] &= \langle p_2(t_a - D)\, p_2(t_b - D) \rangle. \end{aligned} \tag{6.8}$$

In the first equation covariances will occur at $t_b - t_a = D$ which will be along the diagonals at $\pm D$. In the second, because of the equal arm lengths, the only possible time for the correlations is for $t_a = t_b = t$ which will also produce values along the main diagonal. The total number of diagonals is three which is the same as for the

independent lasers. However, the increase in the number of correlations will increase the density of the blocks along each diagonal.

6.1.2.3 All lasers phase-locked

Extending the locking to all lasers so that they operate as a single laser means that they will all have the same laser phase noise p as shown in Table 6.1. This results in correlations not only between the readings of all the optical benches but also within each reading. With all laser phase-locked the readings can be written as

$$s_i(t) = p(t - D) - p(t) + n_i(t), \tag{6.9}$$

where the only difference in all the readings will be the photodetector noises n_i. The auto-covariances are

$$\begin{aligned}\mathrm{cov}[s_i(t_a), s_i(t_b)] = \langle p(t_a - D)\, p(t_b - D)\rangle + \langle p(t_a)\, p(t_b)\rangle + \langle n_i(t_a)\, n_i(t_b)\rangle \\ - \langle p(t_a - D)\, p(t_b)\rangle - \langle p(t_a)\, p(t_b - D)\rangle,\end{aligned} \tag{6.10}$$

which now has two extra terms relating to the correlations between the noises within each reading. With equal times t the auto-covariance is

$$\mathrm{var}[s_i(t)] = \langle p^2(t - D)\rangle + \langle p^2(t)\rangle + \langle n_i^2(t)\rangle, \tag{6.11}$$

which occurs along the main diagonal and has the same structure as the other two phase-locking options. When the times are not equal $t_a \neq t_b$ the covariances are

$$\mathrm{cov}[s_i(t_a), s_i(t_b)] = -\langle p(t_a - D)\, p(t_b)\rangle - \langle p(t_a)\, p(t_b - D)\rangle, \tag{6.12}$$

with contributions only from the two other terms. These are similar to the terms in the cross-covariances of Equation 6.5 having non-zero values occurring at $t_a - t_b = \pm D$ which are the sub-diagonals and super-diagonals. The cross-covariances will have similar expressions with the difference being that they will not contain photodetector noises as they are all independent. For example, for two optical bench readings given by

$$\begin{aligned}s_i(t) &= p(t - D) - p(t) + n_i(t), \\ s_j(t) &= p(t - D) - p(t) + n_j(t),\end{aligned} \tag{6.13}$$

their cross-covariances will be

$$\begin{aligned}\mathrm{cov}[s_i(t_a), s_j(t_b)] = \langle p(t_a - D)\, p(t_b - D)\rangle + \langle p(t_a)\, p(t_b)\rangle \\ - \langle p(t_a - D)\, p(t_b)\rangle - \langle p(t_a)\, p(t_b - D)\rangle. \end{aligned} \tag{6.14}$$

For $t_a = t_b = t$ and $t_a \neq t_b$ the covariances are

$$\begin{aligned}\mathrm{cov}[s_i(t), s_j(t)] &= \langle p^2(t - D)\rangle + \langle p^2(t)\rangle, \\ \mathrm{cov}[s_i(t_a), s_j(t_b)] &= -\langle p(t_a - D)\, p(t_b)\rangle - \langle p(t_a)\, p(t_b - D)\rangle, \end{aligned} \tag{6.15}$$

where covariances will occur at t (main diagonal) and $t_a - t_b = \pm D$ (two other diagonals) giving the same three diagonals and in the other cases. The difference in this case is that the blocks will all be full because all the readings are correlated.

6.1.2.4 Summary of the effects of laser phase-locking

The phase-locking affects the matrix by increasing the number of correlations between the readings from the different optical benches. This appears as an increase in the density of the blocks occurring in the diagonals in the matrix. It determines what is correlated and not where the correlations occur in the matrix in that it defines what occurs in the blocks at the points of correlations.

6.1.3 The effects of the arm lengths on the covariance matrix

Although the previous section was focused on the effects of the phase-locking on the covariance matrix from it we were able to see that the correlations away from the main diagonal were located at positions related to the arm lengths which for equal arm lengths occurred at $\pm D$. In this section we show the effects of unequal arm lengths and, because LISA is a moving detector with its structure disturbed by other objects, the effects of motion on the arms will also be considered.

6.1.3.1 Static unequal arm lengths

Recall that with unequal arm lengths the optical bench readings can be written as

$$s_i(t) = p_j(t - D_k) - p_i(t) + n_i(t), \tag{6.16}$$

and with static values D_k will have three different offsets of D_1, D_2 and D_3. Starting with the basic LISA model with no phase-locking of the lasers, recall that the only non-zero values in the matrix are the variances (auto-covariances at same time t) and the cross-covariances between the readings of the optical benches along each arm. The general equation for the variances which are sums of the variances of the different noises can be written as

$$\mathrm{var}[s_i(t)] = \langle p_j^2(t - D_k)\rangle + \langle p_i^2(t)\rangle + \langle n_i^2(t)\rangle. \tag{6.17}$$

These are the values occurring on the main diagonal and the inequality of the arm lengths has not changed their value nor their location. The cross-covariances however, will be affected by the different lengths as these are associated with the correlations between laser phase noises with times t and $t - D_i$. Using the general equations for the optical benches at the end of each arm which can be written as

$$\begin{aligned} s_i(t) &= p_j(t - D_k) - p_i(t) + n_i(t), \\ s_j(t) &= p_i(t - D_k) - p_j(t) + n_j(t), \end{aligned} \tag{6.18}$$

and the cross-covariance will be

$$\mathrm{cov}[s_i(t_a), s_j(t_b)] = -\langle p_j(t_a - D_k)\, p_j(t_b)\rangle - \langle p_i^2(t_a)\, p_i(t_b - D_k)\rangle. \tag{6.19}$$

The locations of the correlations will depend on D_k and will produce three sub-diagonals and three super-diagonals if the arm lengths are all different.

With spacecraft phase-locking the main diagonal will be affected because of the cross-covariances between laser phase noises with times shifted by different offsets $t - D_i$ and $t - D_j$. For example, for s_1 and $s_{3'}$ with equal arm lengths the covariance is

$$\mathrm{cov}[s_1(t_a), s_{3'}(t_b)] = \langle p_2(t_a - D)\, p_2(t_b - D)\rangle, \tag{6.20}$$

producing values when the times are equal and will occur along the main diagonal. With unequal arm lengths this becomes

$$\mathrm{cov}[s_1(t_a), s_{3'}(t_b)] = \langle p_2(t_a - D_3)\, p_2(t_b - D_1)\rangle, \tag{6.21}$$

where the correlations will occur at times that are differences of the offsets $t_a - t_b = \pm(D_3 - D_1)$ shifting them away from the main diagonal. There will be two other differences of $(D_1 - D_2)$ and $(D_2 - D_3)$ producing a maximum of three new diagonals all located between the main diagonal and those at the offset $\pm D_i$ with the smallest

Table 6.2: Raw data phase measurements showing the contributions for the laser phase p_i and photodetector (n_i) noises for directionally dependent arm lengths $D_{i'} \neq D_i$. These are given for the different types of laser noise phase-locking.

Phase-locking	Optical bench phase shift	Noise contributions in the readings
None	$s_1(t)$	$p_{2'}(t-D_3) - p_1(t) + n_1(t)$
	$s_{1'}(t)$	$p_3(t-D_{2'}) - p_{1'}(t) + n_{1'}(t)$
	$s_2(t)$	$p_{3'}(t-D_1) - p_2(t) + n_2(t)$
	$s_{2'}(t)$	$p_1(t-D_{3'}) - p_{2'}(t) + n_{2'}(t)$
	$s_3(t)$	$p_{1'}(t-D_2) - p_3(t) + n_3(t)$
	$s_{3'}(t)$	$p_2(t-D_{1'}) - p_{3'}(t) + n_{3'}(t)$
Spacecraft	$s_1(t)$	$p_2(t-D_3) - p_1(t) + n_1(t)$
	$s_{1'}(t)$	$p_3(t-D_{2'}) - p_1(t) + n_{1'}(t)$
	$s_2(t)$	$p_3(t-D_1) - p_2(t) + n_2(t)$
	$s_{2'}(t)$	$p_1(t-D_{3'}) - p_2(t) + n_{2'}(t)$
	$s_3(t)$	$p_1(t-D_2) - p_3(t) + n_3(t)$
	$s_{3'}(t)$	$p_2(t-D_{1'}) - p_3(t) + n_{3'}(t)$
All	$s_1(t)$	$p(t-D_3) - p(t) + n_1(t)$
	$s_{1'}(t)$	$p(t-D_{2'}) - p(t) + n_{1'}(t)$
	$s_2(t)$	$p(t-D_1) - p(t) + n_2(t)$
	$s_{2'}(t)$	$p(t-D_{3'}) - p(t) + n_{2'}(t)$
	$s_3(t)$	$p(t-D_2) - p(t) + n_3(t)$
	$s_{3'}(t)$	$p(t-D_{1'}) - p(t) + n_{3'}(t)$

value. The actual number of diagonals depends on the values of the offsets.

When the lasers are all phase-locked the number of diagonals that the main diagonal splits into will not increase for the same set of arm lengths. This is because there are still only the three options for the differences between the offsets. The difference in the matrix between this and the spacecraft locking will be in the density of the blocks of these shifted diagonals.

6.1.3.2 Directionally dependent static arm lengths

LISA will be orbiting the Sun with its guiding centre located on the ecliptic. Each of its spacecraft are in their own orbit and the relative motion between them causes an apparent rotation of the plane of the antenna in a clockwise direction with a period of one year. Simulating this motion by assuming a rotating rigid array the effect leads to the light travel times in each arm being dependent on the direction of measurement [20]. From Cornish and Hellings [20], because of the rotation a beam transmitted from a spacecraft will have to lead or aimed ahead the receiving spacecraft. If the actual arm length has a travel time of $\mathcal{D}_i$ and $D_{i'}$ and D_i are the measured times in the clockwise and counter-clockwise directions then the rotation will result in the $D_{i'} < \mathcal{D}_i$ and $D_i > \mathcal{D}_i$.

The raw data showing the directional dependence are given in Table 6.2. With the assumption of fixed values, the directional dependence has increased the number of

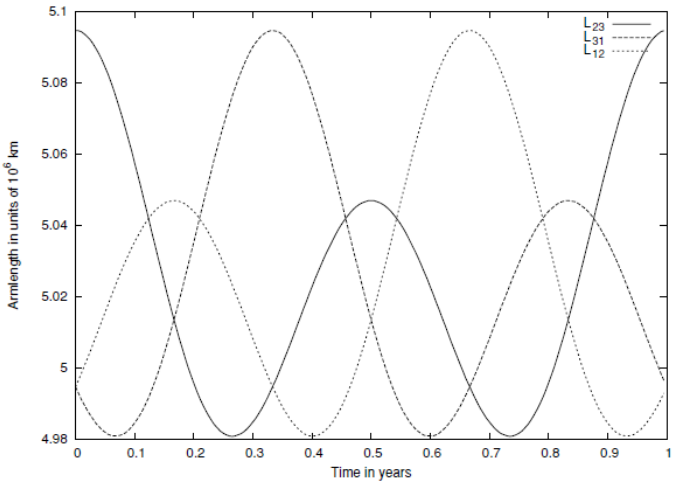

Figure 6.1: The changes in the arm lengths as modeled by Dhurandhar et. al. [23].

offsets in the readings to six since each arm now has two offsets associated with it. The effects are similar to those of the static unequal arms of the previous section but will reflect the increase in the number of offsets. There will be six sub-diagonals and six super-diagonals for all phase-locking options.

For the main diagonal, like the equal arms case, only the phase-locking of the lasers will produce a different number of diagonals. With spacecraft phase-locking although there are six offsets the actual number of differences are still limited to three because they are restricted by the offset times shared by the same laser noises as the correlations occur between times of $t-D_i$ and $t-D_j$. As shown in Table 6.2 the differences restricted to $D_3 - D_{1'}$, $D_{2'} - D_1$ and $D_{3'} - D_2$. However, when all the lasers are phase-locked the differences will include all the offsets. As in the unequal arms case, the actual number of diagonals in both cases will dependent on the values of the offsets.

6.1.3.3 Time varying arm lengths

Apart from the rotational effects, the relative motion between the spacecraft coupled with tidal forces cause continuous changes in the arm lengths that oscillate about a nominal value reflecting orbital period [39, 36]. This produces a breathing or flexing effect [39, 23] with changes in the arm lengths of 1% or approximately 50×10^6m [36]. Figure 6.1 is an example of the changes as modeled by Dhrurandhar et. al. [23].

In the optical bench readings this will produce time varying offsets which will be expressed as functions of time $D_i(t)$. All the other properties related to the arm lengths discussed previously were modeled as static resulting in the diagonal patterns in the

covariance matrix. This is one of the properties that will break the Toeplitz structure of the covariance matrices.

The auto-covariance with the time varying offsets can be written as

$$\mathrm{var}[s_i(t)] = \langle p_{j'}^2\big(t - D_k(t)\big)\rangle + \langle p_i^2(t)\rangle + \langle n_i(t)\rangle, \tag{6.22}$$

which will not be affected by the time varying arm lengths. For the readings at the end of each arm the cross-covariance with the time varying offsets can be written as

$$\mathrm{cov}[s_i(t_a), s_j(t_b)] = -\big\langle p_j\big(t_a - D_k(t)\big)\; p_j(t_b)\big\rangle - \big\langle p_i^2(t_a)\; p_j\big(t_b - D_k(t)\big)\big\rangle, \tag{6.23}$$

with the correlations occurring at $t_a - t_b = \pm D_k(t)$ which is now time dependent. To show the effects near the main diagonal readings s_1 and $s_{3'}$ will be used and the cross-covariance with time varying offsets is

$$\mathrm{cov}[s_1(t_a), s_{3'}(t_b)] = \big\langle p_2\big(t_a - D_3(t)\big)\; p_2\big(t_b - D_1(t)\big)\big\rangle, \tag{6.24}$$

giving correlations at $t_a - t_b = \pm\big(D_3(t) - D_1(t)\big)$ which is also time dependent.

6.1.3.4 Summary of the effects of the arm lengths

The lengths of the arms determine where the correlations occur in the covariance matrix. With static values the matrix has a Toeplitz structure with diagonals occurring away from the main at locations that depend on the values of the arm lengths and on whether there are dependencies in the direction of the measurements of the arm lengths. With time varying arm lengths the diagonals are no longer guaranteed as the location of the correlations will reflect the temporal variations in the arm lengths which destroys the Toeplitz structure.

6.1.4 The effects of the noise variances on the covariance matrix

The variances of the noises determine the values of the covariances in the matrix. When the noises are stationary, that is, their variances do not change with time, the values at times t and $(t - D_i)$ will be the same and the covariance matrix will be Toeplitz. In the simple toy model each noise type was assumed to have the same variances of σ_p^2 and σ_n^2. Here this assumption will be relaxed allowing the noises in each optical

bench to have different values. We also look at the effects of temporal changes in the variances (non-stationarity) and the reduction of the separations between the values for the variances of the two noise types.

6.1.4.1 Unequal noise variances

As done in the previous sections examples will be illustrated for the auto-covariance which determines the values along the main diagonal and one cross-covariance for the sub/super-diagonals. The auto-covariance with independent lasers can be written as

$$\mathrm{var}[s_i(t)] = \langle p_{j'}^2(t - D_k)\rangle + \langle p_i^2(t)\rangle + \langle n_i(t)\rangle, \tag{6.25}$$

where there are contributions from two different laser phase noises and a photodetector noise. For stationary noises with equal variances for each type of noise of σ_p^2 and σ_n^2 Equation 6.25 becomes

$$\mathrm{var}[s_i(t)] = 2\sigma_p^2 + \sigma_n^2. \tag{6.26}$$

With unequal variances, which will be indicated by σ_{pi}^2 and σ_{ni}^2, the auto-covariance using Equation 6.25 is

$$\mathrm{var}[s_i(t)] = \sigma_{pj}^2 + \sigma_{pi}^2 + \sigma_{ni}^2, \tag{6.27}$$

where the difference will be a change in the total variance that will reflect the different noise contributions. This will also be true for the cross-covariances, for example, from the general equation optical benches at the end of an arm is

$$\mathrm{cov}[s_i(t_a), s_j(t_b)] = -\langle p_{j'}(t_a - D_k)\; p_{j'}(t_b)\rangle - \langle p_i(t_a)\; p_i(t_b - D_k)\rangle, \tag{6.28}$$

giving values of $-\sigma_{pi}^2$ or $-\sigma_{pj}^2$ depending on the times of the correlations.

6.1.4.2 Time varying variances

This would be reflected in the changes of the variances with time and, as with the time-varying arm lengths, would break the Toeplitz structure of the Matrix. However, the breaking will be due to different values along all the diagonals. For example, from Equation 6.25 the auto-covariance is

$$\mathrm{var}[s_i(t)] = \big\langle p_{j'}^2\big(t - D_k\big)\big\rangle + \langle p_i^2(t)\rangle + \langle n_i(t)\rangle, \tag{6.29}$$

where there will be no change in the structure of the equation. The temporal variations will be show up as different values for the different times t. Assuming that the variances are the same for each noise type, that is, σ_p^2 and σ_n^2 then the time varying values will be

$$\text{var}[s_i(t)] = \sigma_p^2(t - D_k) + \sigma_p^2(t) + \sigma_n^2(t), \tag{6.30}$$

where $\sigma_p^2(t - D_k)$, $\sigma_p^2(t)$ and $\sigma_n^2(t)$ are the variances for the noises at those times.

6.1.4.3 Separation between the laser phase noise and photodetector noise variances

This was one of the concerns of Romano and Woan [54] in terms of the effects on the splitting of the eigenvalues into the two different groups. In the current design the laser phase noise is expected to be about 10^7 times greater than the photodetector noises giving large separations between the two noise types. In the covariance matrices these are reflected in the values where the laser noise variances overwhelm the photodetector noises which appear only in the elements along the main diagonal. For example, for the independent lasers for variances of $\sigma_p^2 = 1000$ and $\sigma_n^2 = 1$ the values along the diagonal are $2\sigma_p^2 + \sigma_n^2 = 2001$ with the other diagonals being $-\sigma_p^2 = -1000$. As the laser variance approaches the photodetector variances the contributions to the variances are more evenly spread. For example, for the same photodetector noise variances with laser noise variance of $\sigma_p^2 = 2$, the values are now $2\sigma_p^2 + \sigma_n^2 = 5$ and $-\sigma_p^2 = -2$.

However, the reason for the time delay interferometry observables is the size of the laser phase noises, therefore if these are reduced to the level of the secondary noises by improvements in the laser frequency stability then there is no longer any need for these observables. With that said this investigation will investigate the separations up to the limit that they become close to the secondary noises but will be just to determine if they affected by the size of the separations.

6.1.4.4 Summary of the effects of the noise variances

The noise variance determine the values of the covariances in the matrix. They do not affect the location of the correlations. For stationary values and static arm lengths the matrix is Toeplitz but this will be broken by non-stationarity.

6.1.5 Summary

The purpose of this section was to illustrate how the properties of LISA affect its noise covariance matrix and hence determined how these will change the eigenvalues when adapting our approach to a more realistic model of LISA. The actual values of the elements in the matrix are determined by the variances of the different noises. The structure or layout of the matrix is determined by the phase-locking of the lasers and the arm lengths with the former determining the number of correlations and hence the density of the matrix while the latter determines their location. Static values of the arm lengths and variances result in Toeplitz structures which disappears when either has time dependent values.

6.1.6 Results

After determining the effects of each of the properties of the LISA on its noise covariance matrix the next step would be to algebraically generate the eigenvalues from the different matrices to show how they are affected by the different properties. This would be the preferred method as they would show the contributions from each noise source to the eigenvalues. However, as seen in Chapter 4 even for small matrices the computation times for the algebraic solutions are very long. Instead, the effects will be determined using actual values using numeric solutions which are the results presented in this section. The matrices with Toeplitz structures are illustrated with tables of the non-zero values of their first rows.

6.1.6.1 The effects of laser phase-locking and static arm lengths

Initially to illustrate only the effects of phase-locking the arm lengths all had the same value with light travel time of $D = 16$. Also, the variances of each noise type had the same values of $\sigma_p^2 = 1000$ and $\sigma_n^2 = 1$ for the laser phase and photodetector noises, respectively. The covariance matrices for the three phase-locking option of none, spacecraft locked and all locked for times of $t = \{0, 1, \ldots, 23\}$ are given in Figure 6.2. For these the arm lengths are the same and they all have a main diagonal and two others separated from the main by the offset value D. The blocks in the diagonals show the increase in their density with the increase in the number of phase-locked lasers. The

matrix for no phase-locking in Figure 6.2a also differs from the others by having blocks in the main diagonal having only a main diagonal.

The eigenvalues for these covariance matrices are given in columns two to seven of Table 6.3 where the noticeable results are:

- only the phase-locked lasers produced the required laser noise free eigenvalues,
- clear separations exist between the eigenvalues with and without laser noise,
- the number of laser noise free eigenvalues increased with the number of phase-locked lasers.

This seems to indicate that phase-locking of the lasers, which determines the amount of correlations between the optical bench readings, is an important factor in obtaining the laser noise free eigenvalues.

For spacecraft phase-locked lasers the number of eigenvalues is 40 and for all phase-locked lasers it is 120. The separation between the eigenvalues with and without laser phase noises also increased with the increase in phase-locking from 1000 for spacecraft phase-locking to 2000 when they were all phase-locked. The lack of laser noise free eigenvalues for the independent lasers in relation to the structure of the matrix might be due to the blocks along the main diagonal being simple diagonals.

Results for unequal static arm lengths

Next, the restriction on the arm lengths was relaxed by allowing them to have different values with corresponding offsets of $D_i = \{15, 16, 17\}$ to see how the structure of the matrix in terms of the location of the correlations affects the distribution and nature of the eigenvalues. The covariance matrices for these values are given in Figure 6.3 where the expected increase in the number of diagonals in the matrices occurs. The common feature for the three phase-locking options is the splitting of the sub-diagonal and super-diagonals that occurred at the offset of 16 for the equal arm case into three diagonals each reflecting the number of different arm lengths now occurring at offsets from the main diagonal of 15, 16, and 17. The closeness of these values makes the diagonals appear as a bands but this will depend on the sampling rate. The effect of the phase-locking is to introduce other diagonals close to the main diagonal reflecting

the correlations between different offset times e.g. $t_1 - D_i$ and $t_2 - D_j$ giving values at $t_1 - t_2 \pm D_i - D_j$.

The eigenvalues for these matrices are given in Table 6.3 in columns 8 to 13 with results that are similar to those for equal arms. Only the phase-locked lasers produced the laser noise free eigenvalues with an increase in their number with the number of locked lasers. The separation between the eigenvalues with and without laser noises is not as clear as with equal arms. The smallest eigenvalue is 1 and the assumption is that this is associated with the photodetector noises that have variances of $\sigma_n^2 = 1$. Some of the other values especially for spacecraft phase-locking are small compared to the laser phase noise variances and may also only contain photodetector noises, for example, values of 10, 44 and 69. Based on the smallest eigenvalues only, the number of laser noise free eigenvalues for the spacecraft and all locked lasers are 28 and 104, respectively. These are less than the corresponding values for the equal arms indicating a decrease in their number with the increase in the number of different arm lengths.

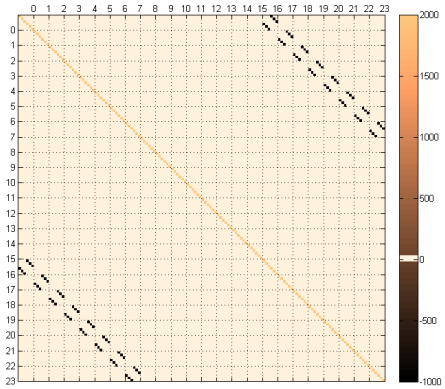

(a)

$C_{0,0}$

$$\begin{vmatrix} 2001 & 0 & 0 & 0 & 0 & 0 \\ 0 & 2001 & 0 & 0 & 0 & 0 \\ 0 & 0 & 2001 & 0 & 0 & 0 \\ 0 & 0 & 0 & 2001 & 0 & 0 \\ 0 & 0 & 0 & 0 & 2001 & 0 \\ 0 & 0 & 0 & 0 & 0 & 2001 \end{vmatrix}$$

$C_{0,16}$

$$\begin{vmatrix} 0 & 0 & 0 & -1000 & 0 & 0 \\ 0 & 0 & 0 & 0 & -1000 & 0 \\ 0 & 0 & 0 & 0 & 0 & -1000 \\ -1000 & 0 & 0 & 0 & 0 & 0 \\ 0 & -1000 & 0 & 0 & 0 & 0 \\ 0 & 0 & -1000 & 0 & 0 & 0 \end{vmatrix}$$

(b)

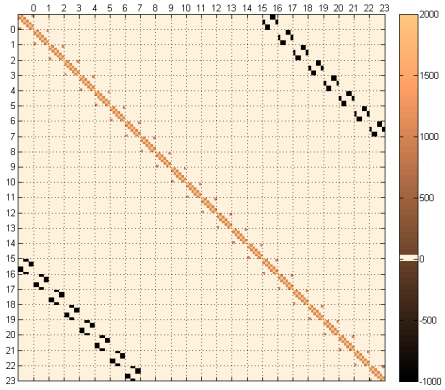

(c)

$C_{0,0}$

$$\begin{vmatrix} 2001 & 1000 & 0 & 0 & 0 & 1000 \\ 1000 & 2001 & 1000 & 0 & 0 & 0 \\ 0 & 1000 & 2001 & 1000 & 0 & 0 \\ 0 & 0 & 1000 & 2001 & 1000 & 0 \\ 0 & 0 & 0 & 1000 & 2001 & 1000 \\ 1000 & 0 & 0 & 0 & 1000 & 2001 \end{vmatrix}$$

$C_{0,16}$

$$\begin{vmatrix} 0 & 0 & 0 & -1000 & -1000 & 0 \\ 0 & 0 & 0 & -1000 & -1000 & 0 \\ -1000 & 0 & 0 & 0 & 0 & -1000 \\ -1000 & 0 & 0 & 0 & 0 & -1000 \\ 0 & -1000 & -1000 & 0 & 0 & 0 \\ 0 & -1000 & -1000 & 0 & 0 & 0 \end{vmatrix}$$

(d)

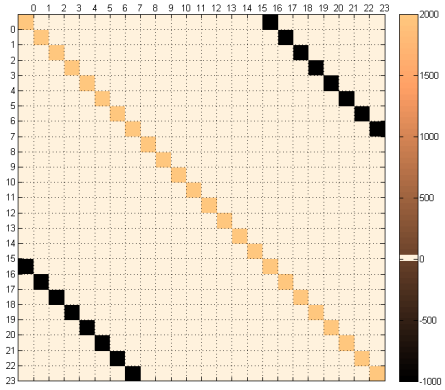

(e)

$C_{0,0}$

$$\begin{vmatrix} 2001 & 2000 & 2000 & 2000 & 2000 & 2000 \\ 2000 & 2001 & 2000 & 2000 & 2000 & 2000 \\ 2000 & 2000 & 2001 & 2000 & 2000 & 2000 \\ 2000 & 2000 & 2000 & 2001 & 2000 & 2000 \\ 2000 & 2000 & 2000 & 2000 & 2001 & 2000 \\ 2000 & 2000 & 2000 & 2000 & 2000 & 2001 \end{vmatrix}$$

$C_{0,16}$

$$\begin{vmatrix} -1000 & -1000 & -1000 & -1000 & -1000 & -1000 \\ -1000 & -1000 & -1000 & -1000 & -1000 & -1000 \\ -1000 & -1000 & -1000 & -1000 & -1000 & -1000 \\ -1000 & -1000 & -1000 & -1000 & -1000 & -1000 \\ -1000 & -1000 & -1000 & -1000 & -1000 & -1000 \\ -1000 & -1000 & -1000 & -1000 & -1000 & -1000 \end{vmatrix}$$

(f)

Figure 6.2: Sample covariance matrices for different laser phase-locking options with lasers that are (a) independent, (b) spacecraft locked and (c) all locked. The arm lengths are all assumed to equal with light travel times of $D = 16$ and the laser phase and photodetector noise variances are $\sigma_p^2 = 1000$ and $\sigma_n^2 = 1$, respectively. The values on the right are for the non-zero blocks of the first rows of the matrices which are the same along the diagonals containing them.

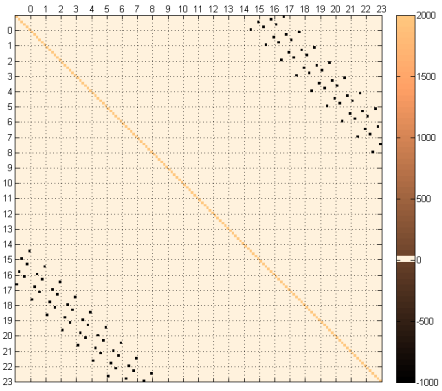

(a)

$R_{0,0}$

2001	0	0	0	0	0	0	0	0	0	0	0
0	2001	0	0	0	0	0	0	0	0	-1000	0
0	0	2001	0	0	0	0	0	0	0	0	0
0	0	0	2001	0	0	0	0	0	0	0	0
0	0	0	0	2001	0	0	-1000	0	0	0	0
0	0	0	0	0	2001	0	0	0	0	0	0

$R_{0,16}$

$R_{0,15}$

0	0	0	0	0	0	0	0	0	-1000	0	0
0	0	0	0	0	0	0	0	0	0	0	0
0	0	0	0	0	-1000	0	0	0	0	0	0
0	0	0	0	0	0	-1000	0	0	0	0	0
0	0	0	0	0	0	0	0	0	0	0	0
0	0	-1000	0	0	0	0	0	0	0	0	0

$R_{0,17}$

(b)

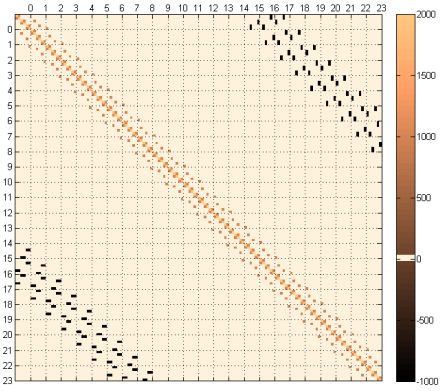

(c)

$R_{0,0}$

2001	1000	0	0	0	0	0	0	0	0	0	0
1000	2001	0	0	0	0	0	0	0	0	0	0
0	0	2001	1000	0	0	0	0	0	0	0	-1000
0	0	1000	2001	0	0	0	0	0	0	0	-1000
0	0	0	0	2001	1000	0	0	-1000	0	0	0
0	0	0	0	1000	2001	0	0	-1000	0	0	0

$R_{0,15}$

$R_{0,1}$

0	0	0	0	0	0	0	0	0	0	-1000	0
0	0	0	0	0	0	0	0	0	0	-1000	0
0	1000	0	0	0	0	0	0	0	0	0	0
0	0	0	0	0	0	0	0	0	0	0	0
0	0	0	1000	0	0	0	-1000	0	0	0	0
0	0	0	0	0	0	0	-1000	0	0	0	0

$R_{0,16}$

$R_{0,2}$

0	0	0	0	0	0	0	0	0	-1000	0	0
0	0	0	0	0	0	0	0	0	-1000	0	0
0	0	0	0	0	0	-1000	0	0	0	0	0
0	0	0	0	0	0	-1000	0	0	0	0	0
0	0	0	0	0	0	0	0	0	0	0	0
1000	0	0	0	0	0	0	0	0	0	0	0

$R_{0,17}$

(d)

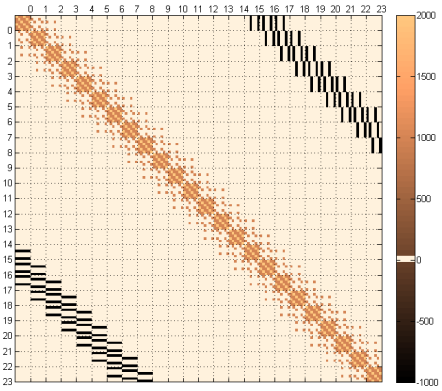

(e)

$R_{0,0}$

2001	1000	1000	2000	1000	1000	0	0	-1000	0	0	-1000
1000	2001	1000	1000	2000	1000	0	0	-1000	0	0	-1000
1000	1000	2001	1000	1000	2000	0	0	-1000	0	0	-1000
2000	1000	1000	2001	1000	1000	0	0	-1000	0	0	-1000
1000	2000	1000	1000	2001	1000	0	0	-1000	0	0	-1000
1000	1000	2000	1000	1000	2001	0	0	-1000	0	0	-1000

$R_{0,15}$

$R_{0,1}$

0	0	0	0	0	0	0	-1000	0	0	-1000	0
1000	0	0	1000	0	0	0	-1000	0	0	-1000	0
0	1000	0	0	1000	0	0	-1000	0	0	-1000	0
0	0	0	0	0	0	0	-1000	0	0	-1000	0
1000	0	0	1000	0	0	0	-1000	0	0	-1000	0
0	1000	0	0	1000	0	0	-1000	0	0	-1000	0

$R_{0,16}$

$R_{0,2}$

0	0	0	0	0	0	-1000	0	0	-1000	0	0
0	0	0	0	0	0	-1000	0	0	-1000	0	0
1000	0	0	1000	0	0	-1000	0	0	-1000	0	0
0	0	0	0	0	0	-1000	0	0	-1000	0	0
0	0	0	0	0	0	-1000	0	0	-1000	0	0
1000	0	0	1000	0	0	-1000	0	0	-1000	0	0

$R_{0,17}$

(f)

Figure 6.3: Sample covariance matrix for unequal offsets $D = \{15, 16, 17\}$ with lasers that are (a) not locked, (b) locked on each spacecraft. The laser phase and photodetector noise variances of $\sigma_p^2 = 1000$ and $\sigma_n^2 = 1$, respectively. The non-zero blocks of the first rows of the matrices are shown on the right.

Table 6.3: Time domain eigenvalues for the different laser noise phase-locking options of none, spacecraft locked and all locked with values for equal and unequal arm lengths with light travel times of $D = 16$ and $D_i = \{15, 16, 17\}$, respectively. The laser phase noise and photodetector noise variances are $\sigma_p^2 = 1000$ and $\sigma_n^2 = 1$ and time values are $t = \{0, \ldots, 23\}$.

phase-locking	Eigenvalues											
	Equal arms						Unequal arms					
None	1001	1001	1001	1001	1001	1001	1001	1001	1001	1001	1001	1001
	1001	1001	1001	1001	1001	1001	1001	1001	1001	1001	1001	1001
	1001	1001	1001	1001	1001	1001	1001	1001	1001	1001	1001	1001
	1001	1001	1001	1001	1001	1001	1001	1001	1001	1001	1001	1001
	1001	1001	1001	1001	1001	1001	1001	1001	1001	1001	1001	1001
	1001	1001	1001	1001	1001	1001	1001	1001	1001	1001	1001	1001
	1001	1001	1001	1001	1001	1001	1001	1001	1001	1001	1001	1001
	1001	1001	1001	1001	1001	1001	1001	1001	1001	1001	1001	1001
	2001	2001	2001	2001	2001	2001	2001	2001	2001	2001	2001	2001
	2001	2001	2001	2001	2001	2001	2001	2001	2001	2001	2001	2001
	2001	2001	2001	2001	2001	2001	2001	2001	2001	2001	2001	2001
	2001	2001	2001	2001	2001	2001	2001	2001	2001	2001	2001	2001
	2001	2001	2001	2001	2001	2001	2001	2001	2001	2001	2001	2001
	2001	2001	2001	2001	2001	2001	2001	2001	2001	2001	2001	2001
	2001	2001	2001	2001	2001	2001	2001	2001	2001	2001	2001	2001
	2001	2001	2001	2001	2001	2001	2001	2001	2001	2001	2001	2001
	3001	3001	3001	3001	3001	3001	3001	3001	3001	3001	3001	3001
	3001	3001	3001	3001	3001	3001	3001	3001	3001	3001	3001	3001
	3001	3001	3001	3001	3001	3001	3001	3001	3001	3001	3001	3001
	3001	3001	3001	3001	3001	3001	3001	3001	3001	3001	3001	3001
	3001	3001	3001	3001	3001	3001	3001	3001	3001	3001	3001	3001
	3001	3001	3001	3001	3001	3001	3001	3001	3001	3001	3001	3001
	3001	3001	3001	3001	3001	3001	3001	3001	3001	3001	3001	3001
Spacecraft	1	1	1	1	1	1	1	1	1	1	1	1
	1	1	1	1	1	1	1	1	1	1	1	1
	1	1	1	1	1	1	1	1	1	1	1	1
	1	1	1	1	1	1	1	1	1	1	1	1
	1	1	1	1	1	1	1	1	1	1	10	44
	1	1	1	1	1	1	69	89	139	224	261	315
	1	1	1	1	1001	1001	444	454	470	479	639	692
	1001	1001	1001	1001	1001	1001	7 06	731	752	947	960	1001
	1001	1001	1001	1001	1001	1001	1001	1001	1001	1001	1001	1001
	1001	1001	1269	1269	1269	1269	1001	1001	1001	1001	1001	1001
	1269	1269	1269	1269	1269	1269	1001	1123	1146	1221	1236	1269
	1269	1269	1269	1269	1269	1269	1269	1269	1269	1329	1376	1391
	2001	2001	2001	2001	2001	2001	1649	1711	2001	2001	2001	2001
	2001	2001	2001	2001	2001	2001	2001	2001	2001	2001	2001	2001
	2001	2001	2001	2001	2001	2001	2001	2001	2001	2001	2001	2001
	2001	2001	2001	2001	2001	2001	2001	2001	2001	2001	2001	2001
	3001	3001	3001	3001	3001	3001	3001	3001	3001	3001	3001	3001
	3001	3001	3001	3001	3001	3001	3001	3001	3001	3001	3001	3001
	3001	3001	3001	3001	4001	4001	3224	3231	3278	3437	3592	3906
	4001	4001	4001	4001	4001	4001	4001	4001	4001	4001	4001	4140
	4733	4733	4733	4733	4733	4733	4423	4466	4688	4733	4733	4733
	4733	4733	4733	4733	4733	4733	4733	4823	4881	4906	5044	5072
	4733	4733	4733	4733	6001	6001	5111	5256	5289	5374	5436	5475
	6001	6001	6001	6001	6001	6001	5551	5575	5717	5719	5921	5925
All	1	1	1	1	1	1	1	1	1	1	1	1
	1	1	1	1	1	1	1	1	1	1	1	1
	1	1	1	1	1	1	1	1	1	1	1	1
	1	1	1	1	1	1	1	1	1	1	1	1
	1	1	1	1	1	1	1	1	1	1	1	1
	1	1	1	1	1	1	1	1	1	1	1	1
	1	1	1	1	1	1	1	1	1	1	1	1
	1	1	1	1	1	1	1	1	1	1	1	1
	1	1	1	1	1	1	1	1	1	1	1	1
	1	1	1	1	1	1	1	1	1	1	1	1
	1	1	1	1	1	1	1	1	1	1	1	1
	1	1	1	1	1	1	1	1	1	1	1	1
	1	1	1	1	1	1	1	1	1	1	1	1
	1	1	1	1	1	1	1	1	1	1	1	1
	1	1	1	1	1	1	1	1	1	1	1	1
	1	1	1	1	1	1	1	1	1	1	1	1
	1	1	1	1	1	1	1	1	318	345	1165	1292
	1	1	1	1	1	1	1910	2583	2938	3769	4202	4430
	1	1	1	1	1	1	4530	4849	5204	5282	5659	5694
	6001	6001	6001	6001	6001	6001	6001	6001	6001	6001	6001	6001
	6001	6001	12001	12001	12001	12001	6001	6417	6505	7375	7636	8135
	12001	12001	12001	12001	18001	18001	9133	10096	10888	11599	12048	12398
	18001	18001	18001	18001	18001	18001	12711	12989	14030	15456	16768	17677

Table 6.4: Time domain eigenvalues for directionally dependent arm lengths with offsets of $D = \{15, 14, 17, 16, 19, 18\}$ and variances of $\sigma_p^2 = 1000$ and $\sigma_n^2 = 1$.

phase-locking	Eigenvalues																	
None	1001	1001	1001	1001	1001	1001	1001	1001	1001	1001	1001	1001	1001	1001	1001	1001	1001	1001
	1001	1001	1001	1001	1001	1001	1001	1001	1001	1001	1001	1001	1001	1001	1001	1001	1001	1001
	1001	1001	1001	1001	1001	1001	1001	1001	1001	2001	2001	2001	2001	2001	2001	2001	2001	2001
	2001	2001	2001	2001	2001	2001	2001	2001	2001	2001	2001	2001	2001	2001	2001	2001	2001	2001
	2001	2001	2001	2001	2001	2001	2001	2001	2001	2001	2001	2001	2001	2001	2001	2001	2001	2001
	2001	2001	2001	2001	2001	2001	2001	2001	2001	3001	3001	3001	3001	3001	3001	3001	3001	3001
	3001	3001	3001	3001	3001	3001	3001	3001	3001	3001	3001	3001	3001	3001	3001	3001	3001	3001
	3001	3001	3001	3001	3001	3001	3001	3001	3001	3001	3001	3001	3001	3001	3001	3001	3001	3001
Spacecraft	1	1	1	1	1	1	1	1	1	1	1	1	1	1	1	1	1	1
	1	1	34	36	65	68	94	131	148	183	190	205	226	269	280	298	355	369
	371	377	393	407	428	444	567	597	636	672	685	729	790	849	859	911	924	967
	991	1001	1009	1075	1127	1191	1224	1256	1307	1335	1378	1432	1467	1512	1516	1595	1647	1737
	1773	1785	1848	1853	2001	2001	2001	2001	2001	2001	2001	2001	2001	2001	2001	2001	2001	2001
	2001	2001	2001	2170	2189	2269	2566	2570	2874	2899	2940	3061	3106	3144	3174	3220	3244	3302
	3321	3324	3440	3586	3589	3775	3810	3813	3845	3951	3952	4064	4157	4213	4224	4371	4592	4665
	4761	4850	4909	4991	5000	5043	5179	5199	5243	5338	5392	5438	5464	5539	5579	5680	5693	5774
All	1	1	1	1	1	1	1	1	1	1	1	1	1	1	1	1	1	1
	1	1	1	1	1	1	1	1	1	1	1	1	1	1	1	1	1	1
	1	1	1	1	1	1	1	1	1	1	1	1	1	1	1	1	1	1
	1	1	1	1	1	1	1	1	1	1	1	1	1	1	1	1	1	1
	1	1	1	1	1	1	1	1	1	1	1	1	1	1	1	1	1	1
	1	1	1	1	1	1	1	1	1	1	1	1	852	1135	1383	2049	2899	3669
	4284	4555	4901	4985	5123	5150	5298	5388	5453	5649	5680	5789	6001	6001	6001	6001	6001	6282
	6391	6449	6696	6739	6886	7103	7663	8311	9095	9961	10796	11340	12061	12171	12253	12535	14299	16764

Directionally dependent arm lengths

The rotation produces a dependence of the lengths of the arms on the direction of motion. This effect is modeled by giving each arm two static values to represent the different light travel times in the different directions. The values used are $D_i = \{15, 14, 17, 16, 19, 18\}$ where they occur in order of $\{1, 1', 2, 2', 3, 3'\}$ for the numbers associated with each arm. The static assumption means that this just increases the number of arm lengths. The covariance matrices for this effect are given in Figures 6.4 and 6.5 where there are increases in the numbers of the diagonals due to the increase in the number of offsets D_i. The actual number of diagonals that are produced close to the main diagonal will depend on the values with the matrix for the all locked lasers showing a large increase in the number of diagonals.

The effects on the eigenvalues is expected to reflect the two previous examples since, as mentioned before, this is essentially just increasing the number of diagonals in the matrices. The number of laser noise free eigenvalues for independent, spacecraft locked and all locked lasers are 0, 20 and 102, respectively showing a decrease in the last two. The separation between values reflects the situation for the three unequal arms where the next value above the photodetector noise variance is 34 which is much smaller than the laser phase noise variances of 1000.

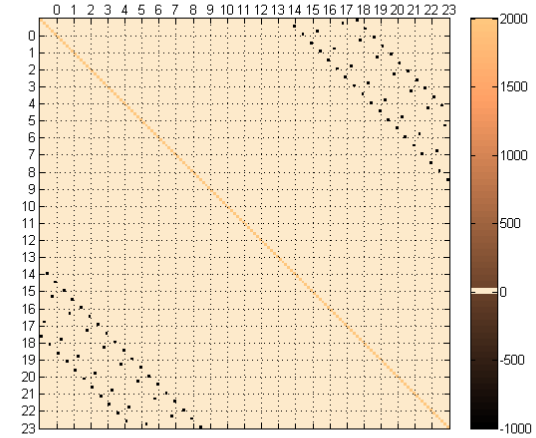

(a)

$C_{0,0}$

2001	0	0	0	0	0
0	2001	0	0	0	0
0	0	2001	0	0	0
0	0	0	2001	0	0
0	0	0	0	2001	0
0	0	0	0	0	2001

$C_{0,14}$

0	0	0	0	0	0
0	0	0	0	0	0
0	0	0	0	0	-1000
0	0	0	0	0	0
0	0	0	0	0	0
0	0	0	0	0	0

$C_{0,15}$

0	0	0	0	0	0
0	0	0	0	0	0
0	0	0	0	0	0
0	0	0	0	0	0
0	0	0	0	0	0
0	0	-1000	0	0	0

$C_{0,16}$

0	0	0	0	0	0
0	0	0	0	0	0
0	0	0	0	0	0
0	0	0	0	0	0
0	-1000	0	0	0	0
0	0	0	0	0	0

$C_{0,17}$

0	0	0	0	0	0
0	0	0	0	0	0
0	0	0	0	0	0
0	0	0	0	0	0
0	0	0	0	0	0
0	0	0	0	0	0

$C_{0,18}$

0	0	0	-1000	0	0
0	0	0	0	0	0
0	0	0	0	0	0
0	0	0	0	0	0
0	0	0	0	0	0
0	0	0	0	0	0

$C_{0,19}$

0	0	0	0	0	0
0	0	0	0	0	0
0	0	0	0	0	0
0	0	0	-1000	0	0
0	0	0	0	0	0
0	0	0	0	0	0

(b)

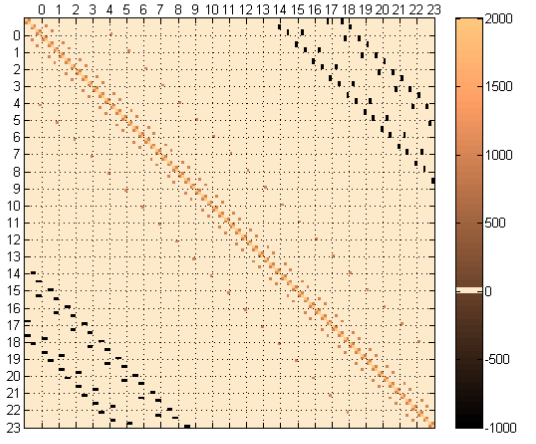

(c)

$C_{0,0}$

2001	1000	0	0	0	0
1000	2001	0	0	0	0
0	0	2001	1000	0	0
0	0	1000	2001	0	0
0	0	0	0	2001	1000
0	0	0	0	1000	2001

$C_{0,14}$

0	0	0	0	0	0
0	0	0	0	0	0
0	1000	0	0	0	0
0	0	0	0	0	0
0	0	0	1000	0	0
0	0	0	0	0	0

$C_{0,15}$

0	0	0	0	0	0
0	0	0	0	0	0
0	0	0	0	0	0
0	0	0	0	0	0
0	0	0	0	0	0
1000	0	0	0	0	0

$C_{0,16}$

0	0	0	0	0	0
0	0	0	0	0	0
0	0	0	0	0	-1000
0	0	0	0	0	-1000
0	0	0	0	0	0
0	0	0	0	0	0

$C_{0,17}$

0	0	0	0	0	0
0	0	0	0	0	0
0	0	0	0	0	0
0	0	0	0	0	0
0	0	0	-1000	0	0
0	0	0	-1000	0	0

$C_{0,18}$

0	0	0	0	-1000	0
0	0	0	0	-1000	0
0	0	0	0	0	0
0	0	0	0	0	0
0	0	0	0	0	0
0	0	0	0	0	0

$C_{0,19}$

0	0	0	0	-1000	0
0	0	0	0	-1000	0
0	0	0	0	0	0
0	0	0	0	0	0
0	0	0	0	0	0
0	0	0	0	0	0

$C_{0,16}$

0	0	0	0	0	0
0	0	0	0	0	0
0	0	0	0	0	0
0	0	0	0	0	0
0	0	-1000	0	0	0
0	0	-1000	0	0	0

$C_{0,17}$

0	0	0	0	0	0
0	0	0	0	0	0
0	0	0	0	0	0
0	0	0	0	0	0
0	0	0	0	0	0
0	0	0	0	0	0

$C_{0,18}$

0	0	0	0	0	0
0	0	0	0	0	0
0	0	0	0	0	0
0	0	0	0	0	0
0	0	0	0	0	0
0	0	0	0	0	0

$C_{0,19}$

0	0	0	0	0	0
0	0	0	0	0	0
0	0	0	0	0	0
0	0	0	0	0	0
0	0	0	0	0	0
0	0	0	0	0	0

(d)

Figure 6.4: Sample covariance matrices for directionally dependent arm lengths with corresponding light travel times of $D_i = \{15, 14, 17, 16, 19, 18\}$ for lasers that are (a) independent and (b) spacecraft locked. The laser phase noise and photodetector noise variances are $\sigma_p^2 = 1000$ and $\sigma_n^2 = 1$, respectively. The values on the right are the non-zero blocks of the first row of each matrix.

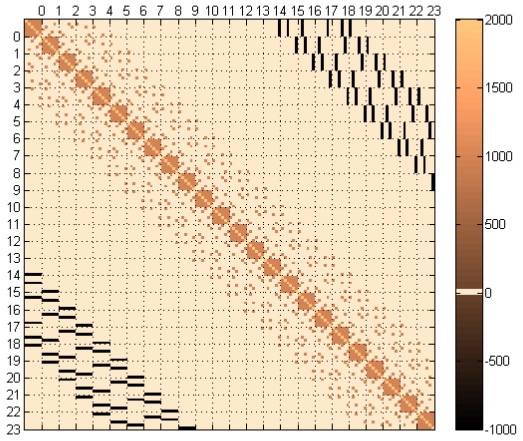

(a)

$C_{0,0}$

2001	1000	1000	1000	1000	1000	0	0	0	0	0	-1000
1000	2001	1000	1000	1000	1000	0	0	0	0	0	-1000
1000	1000	2001	1000	1000	1000	0	0	0	0	0	-1000
1000	1000	1000	2001	1000	1000	0	0	0	0	0	-1000
1000	1000	1000	1000	2001	1000	0	0	0	0	0	-1000
1000	1000	1000	1000	1000	2001	0	0	0	0	0	-1000

$C_{0,1}$

0	0	0	0	0	0	0	0	-1000	0	0	0
0	0	0	0	1000	0	0	0	-1000	0	0	0
0	1000	0	0	0	0	0	0	-1000	0	0	0
1000	0	0	0	0	0	0	0	-1000	0	0	0
0	0	0	1000	0	0	0	0	-1000	0	0	0
0	0	1000	0	0	0	0	0	-1000	0	0	0

$C_{0,2}$

0	0	0	0	0	0	0	-1000	0	0	0	0
0	0	0	1000	0	0	0	-1000	0	0	0	0
0	0	0	0	1000	0	0	-1000	0	0	0	0
0	0	0	0	0	0	0	-1000	0	0	0	0
1000	0	0	0	0	0	0	-1000	0	0	0	0
0	1000	0	0	0	0	0	-1000	0	0	0	0

$C_{0,3}$

0	0	0	0	0	0	0	0	0	0	-1000	0
1000	0	0	0	0	0	0	0	0	0	-1000	0
0	0	0	1000	0	0	0	0	0	0	-1000	0
0	0	0	0	0	0	0	0	0	0	-1000	0
0	0	0	0	0	0	0	0	0	0	-1000	0
0	0	0	0	1000	0	0	0	0	0	-1000	0

$C_{0,4}$

0	0	0	0	0	0	0	0	0	-1000	0	0
0	0	0	0	0	0	0	0	0	-1000	0	0
1000	0	0	0	0	0	0	0	0	-1000	0	0
0	0	0	0	0	0	0	0	0	-1000	0	0
0	0	0	0	0	0	0	0	0	-1000	0	0
0	0	0	1000	0	0	0	0	0	-1000	0	0

$C_{0,5}$

0	0	0	0	0	0	-1000	0	0	0	0	0
0	0	0	0	0	0	-1000	0	0	0	0	0
0	0	0	0	0	0	-1000	0	0	0	0	0
0	0	0	0	0	0	-1000	0	0	0	0	0
0	0	0	0	0	0	-1000	0	0	0	0	0
1000	0	0	0	0	0	-1000	0	0	0	0	0

$C_{0,14}$

0	0	0	0	0	0	0	0	0	0	0	-1000
0	0	0	0	0	0	0	0	0	0	0	-1000
0	0	0	0	0	0	0	0	0	0	0	-1000
0	0	0	0	0	0	0	0	0	0	0	-1000
0	0	0	0	0	0	0	0	0	0	0	-1000
0	0	0	0	0	0	0	0	0	0	0	-1000

$C_{0,15}$

0	0	0	0	0	0	0	0	-1000	0	0	0
0	0	0	0	1000	0	0	0	-1000	0	0	0
0	1000	0	0	0	0	0	0	-1000	0	0	0
1000	0	0	0	0	0	0	0	-1000	0	0	0
0	0	0	1000	0	0	0	0	-1000	0	0	0
0	0	1000	0	0	0	0	0	-1000	0	0	0

$C_{0,16}$

0	0	0	0	0	0	0	-1000	0	0	0	0
0	0	0	1000	0	0	0	-1000	0	0	0	0
0	0	0	0	1000	0	0	-1000	0	0	0	0
0	0	0	0	0	0	0	-1000	0	0	0	0
1000	0	0	0	0	0	0	-1000	0	0	0	0
0	1000	0	0	0	0	0	-1000	0	0	0	0

$C_{0,17}$

0	0	0	0	0	0	0	0	0	0	-1000	0
1000	0	0	0	0	0	0	0	0	0	-1000	0
0	0	0	1000	0	0	0	0	0	0	-1000	0
0	0	0	0	0	0	0	0	0	0	-1000	0
0	0	0	0	0	0	0	0	0	0	-1000	0
0	0	0	0	1000	0	0	0	0	0	-1000	0

$C_{0,18}$

0	0	0	0	0	0	0	0	0	-1000	0	0
0	0	0	0	0	0	0	0	0	-1000	0	0
1000	0	0	0	0	0	0	0	0	-1000	0	0
0	0	0	0	0	0	0	0	0	-1000	0	0
0	0	0	0	0	0	0	0	0	-1000	0	0
0	0	0	1000	0	0	0	0	0	-1000	0	0

$C_{0,19}$

0	0	0	0	0	0	-1000	0	0	0	0	0
0	0	0	0	0	0	-1000	0	0	0	0	0
0	0	0	0	0	0	-1000	0	0	0	0	0
0	0	0	0	0	0	-1000	0	0	0	0	0
0	0	0	0	0	0	-1000	0	0	0	0	0
1000	0	0	0	0	0	-1000	0	0	0	0	0

(b)

Figure 6.5: Sample covariance matrix for directionally dependent arm lengths $D = \{15, 16, 17\}$ for lasers that are all phase-locked. The laser phase and photodetector noise variances of $\sigma_p^2 = 1000$ and $\sigma_n^2 = 1$, respectively. The non-zero block values are given on the right.

Table 6.5: Time domain eigenvalues for time varying arm lengths with laser noise and photodetector noise variances of $\sigma_p^2 = 1000$ and $\sigma_n^2 = 1$. The values are for a section of the larger matrix corresponding to times of $t = \{0, ..., 23\}$.

Phase-locking	Eigenvalues																	
None	587	587	587	587	1001	1001	1001	1001	1001	1001	1001	1001	1001	1001	1001	1001	1001	1001
	1001	1001	1001	1001	1001	1001	1001	1001	1001	1001	1001	1001	1001	1001	1001	1001	1001	1001
	1001	1001	1001	1001	1001	1001	1001	1001	1001	1001	1001	1001	1001	1001	1001	1001	1001	1001
	1001	1001	1001	1001	2001	2001	2001	2001	2001	2001	2001	2001	2001	2001	2001	2001	2001	2001
	2001	2001	2001	2001	2001	2001	2001	2001	2001	2001	2001	2001	2001	2001	2001	2001	2001	2001
	2001	2001	2001	2001	3001	3001	3001	3001	3001	3001	3001	3001	3001	3001	3001	3001	3001	3001
	3001	3001	3001	3001	3001	3001	3001	3001	3001	3001	3001	3001	3001	3001	3001	3001	3001	3001
	3001	3001	3001	3001	3001	3001	3001	3001	3415	3415	3415	3415	4001	4001	4001	4001	5001	5001
Spacecraft	1	1	1	1	1	1	1	1	1	1	1	1	1	1	1	1	1	1
	30	44	55	67	89	102	132	147	180	189	190	229	243	255	281	329	372	377
	391	419	434	471	481	512	530	540	585	595	650	684	720	738	771	788	836	867
	944	1001	1001	1032	1086	1107	1164	1192	1293	1332	1345	1368	1379	1450	1491	1520	1553	1581
	1602	1630	1648	1775	1792	1831	1843	1897	1927	1980	2001	2001	2001	2001	2001	2001	2001	2001
	2001	2001	2214	2360	2440	2455	2611	2720	2753	2806	2909	3051	3094	3113	3140	3184	3242	3280
	3321	3374	3440	3522	3577	3645	3801	3835	3908	4113	4158	4233	4248	4298	4336	4351	4513	4657
	4732	4898	4976	4995	5085	5086	5170	5186	5280	5327	5369	5398	5441	5531	5564	5684	6266	6341
All	1	1	1	1	1	1	1	1	1	1	1	1	1	1	1	1	1	1
	1	1	1	1	1	1	1	1	1	1	1	1	1	1	1	1	1	1
	1	1	1	1	1	1	1	1	1	1	1	1	1	1	1	1	1	1
	1	1	1	1	1	1	1	1	1	1	1	1	1	1	1	1	1	1
	1	1	1	1	1	1	1	1	1	1	1	1	1	1	1	1	1	1
	1	1	1	1	1	1	1	1	1	1	1	1	1112	1227	1383	1737	1770	1881
	2239	2498	2668	2950	3084	3491	3768	3867	4222	4577	4674	4890	5237	5385	5484	5766	5983	6341
	7055	7260	7698	8403	9073	9535	9699	10068	10805	11372	12021	12772	12927	13007	14300	14687	15081	16043

6.1.6.2 The effects of time varying arm lengths

LISA will have time varying arm lengths with changes of about 1% or 50×10^6m which is be approximately 0.17s. For arm lengths of 5×10^9m the light travels times will be about 16.67 ± 0.17s over a period of one year. In order to illustrate this in a small matrix the separations between the arm lengths and their period of change are exaggerated. Only three arm lengths are used with 4 s separations between them with sinusoidal variations based on those in Figure 6.6a. The covariance matrices for the three phase-locking options are shown in Figures 6.9 where the locations of the correlations are seen to mimic the temporal variations in the arm lengths. The eigenvalues in Table 6.5 are for a smaller matrix with the times that match those in the previous sections in order to compare the eigenvalues. As expected only the phase-locked lasers produced the required laser noise free eigenvalues with the numbers for the spacecraft locked and all locked lasers being 18 and 102, respectively. These were close to the values of the directionally dependent arm lengths with similar separations values.

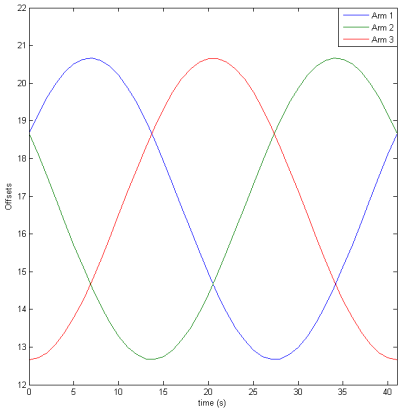

(a)

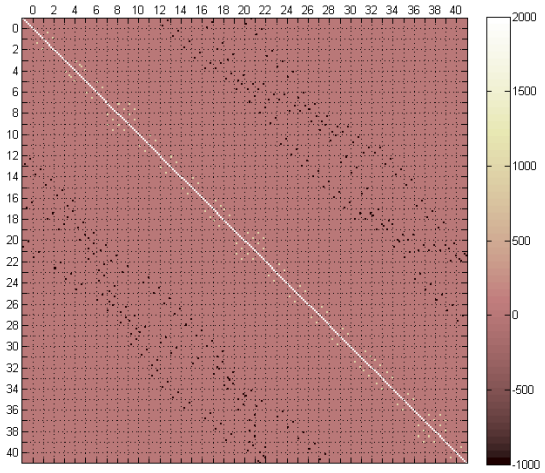

(b)

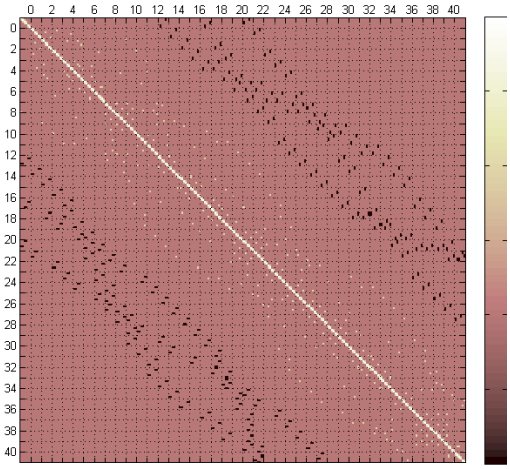

(c)

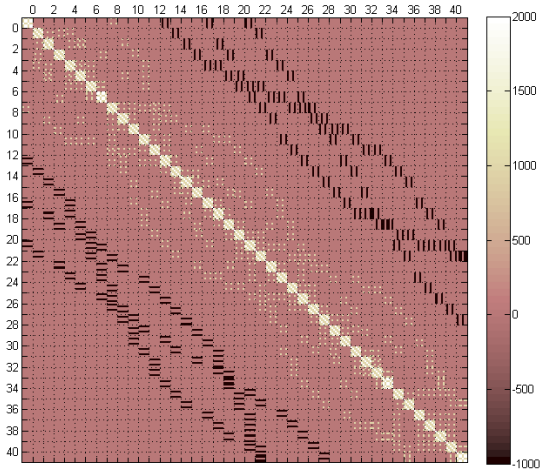

(d)

Figure 6.6: Sample covariance matrices for time varying arm lengths. Three different arm lengths were used initially separated by 4s and allowed to vary according to the patterns shown in (a) which was based on information from Larson [39].

6.1.6.3 The effects of the noise variances

In the previous sections the variances of the two noise types were equal with values of ${\sigma^2}_p = 1000$ and $\sigma_n^2 = 1$ which provided a large separation between them. In this section these restrictions will be removed allowing the lasers and photodetectors to have different variances and also reducing their separation. Each change will be done separately for different phase-locking options.

Different noise variances

In the first set the photodetector noises have the same variances of $\sigma_n^2 = 1$ and the laser phase noise variances are given different values which depend on the phase-locking. The only two phase-locking options that can be used in this case are none and spacecraft locked for which the values for will be $\sigma_{pi}^2 = \{900, 1200, 1500, 1800, 2100, 24000\}$ and $\sigma_{pi}^2 = \{900, 1500, 2100\}$ respectively. The arm length used in this case will be unequal with light travel times of $D_i = \{15, 16, 17\}$ and the times are $t = \{0, \ldots, 23\}$. The covariance matrices for the two phase-locking options are given in Figure 6.7 along with the values for the non-zero blocks of the first row that are included in the figure.

In the second set the laser phase noises had the same variances of $\sigma_p^2 = 1000$ while the photodetector noises variances were $\sigma_{ni}^2 = \{1, 2, 3, 4, 5, 6\}$. Although the photodetector noises only affect the diagonal and are not affected by the phase-locking the three options were done to show how the values are reflected in the eigenvalues. The times and offsets are the same as in the previous section. The covariance matrices are given in Figure 6.8 also with the values of the non-zero blocks of the first row.

The eigenvalues for both cases are given in Table 6.6 with those for the different phase noises in columns 2 to 7 and those for photodetector noises in columns 8 to 13. In both cases the independent lasers did not produce any laser noise free eigenvalues. For the different laser noise variances with spacecraft locked lasers the number of eigenvalues is 29 which is just one more than that obtained for the corresponding unequal arms case.

The noticeable result is that of the different photodetector noises where the eigenvalues reflect the values of the photodetector noise variances. This was one of the issues mentioned by Romano and Woan. Although the degeneracy no longer exists because of the different values it is the splitting of the values into those with and without laser phase noises that is important and this was obtained. However, not all the photodetec-

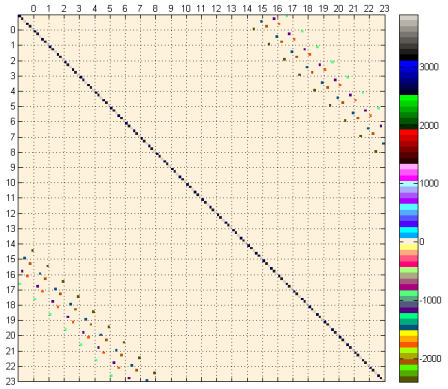

(a)

$R_{0,0}$

$$\begin{bmatrix} 2701 & 0 & 0 & 0 & 0 & 0 \\ 0 & 3301 & 0 & 0 & 0 & 0 \\ 0 & 0 & 3901 & 0 & 0 & 0 \\ 0 & 0 & 0 & 2701 & 0 & 0 \\ 0 & 0 & 0 & 0 & 3301 & 0 \\ 0 & 0 & 0 & 0 & 0 & 3901 \end{bmatrix}$$

$R_{0,16}$

$$\begin{bmatrix} 0 & 0 & 0 & 0 & 0 & 0 \\ 0 & 0 & 0 & 0 & -1200 & 0 \\ 0 & 0 & 0 & 0 & 0 & 0 \\ 0 & 0 & 0 & 0 & 0 & 0 \\ 0 & -2100 & 0 & 0 & 0 & 0 \\ 0 & 0 & 0 & 0 & 0 & 0 \end{bmatrix}$$

$R_{0,15}$

$$\begin{bmatrix} 0 & 0 & 0 & 0 & 0 & 0 \\ 0 & 0 & 0 & 0 & 0 & 0 \\ 0 & 0 & 0 & 0 & 0 & -1500 \\ 0 & 0 & 0 & 0 & 0 & 0 \\ 0 & 0 & 0 & 0 & 0 & 0 \\ 0 & 0 & -2400 & 0 & 0 & 0 \end{bmatrix}$$

$R_{0,17}$

$$\begin{bmatrix} 0 & 0 & 0 & -900 & 0 & 0 \\ 0 & 0 & 0 & 0 & 0 & 0 \\ 0 & 0 & 0 & 0 & 0 & 0 \\ -1800 & 0 & 0 & 0 & 0 & 0 \\ 0 & 0 & 0 & 0 & 0 & 0 \\ 0 & 0 & 0 & 0 & 0 & 0 \end{bmatrix}$$

(b)

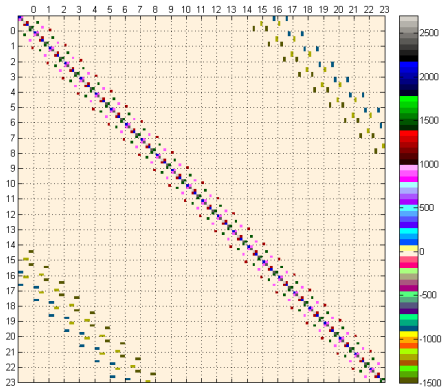

(c)

$R_{0,0}$

$$\begin{bmatrix} 2101 & 900 & 0 & 0 & 0 & 0 \\ 900 & 2401 & 0 & 0 & 0 & 0 \\ 0 & 0 & 2701 & 1200 & 0 & 0 \\ 0 & 0 & 1200 & 2101 & 0 & 0 \\ 0 & 0 & 0 & 0 & 2401 & 1500 \\ 0 & 0 & 0 & 0 & 1500 & 2701 \end{bmatrix}$$

$R_{0,15}$

$$\begin{bmatrix} 0 & 0 & 0 & 0 & 0 & 0 \\ 0 & 0 & 0 & 0 & 0 & 0 \\ 0 & 0 & 0 & 0 & 0 & -1200 \\ 0 & 0 & 0 & 0 & 0 & -1200 \\ 0 & 0 & -1500 & 0 & 0 & 0 \\ 0 & 0 & -1500 & 0 & 0 & 0 \end{bmatrix}$$

$R_{0,1}$

$$\begin{bmatrix} 0 & 0 & 0 & 0 & 0 & 0 \\ 0 & 0 & 0 & 0 & 0 & 0 \\ 0 & 1500 & 0 & 0 & 0 & 0 \\ 0 & 0 & 0 & 0 & 0 & 0 \\ 0 & 0 & 0 & 900 & 0 & 0 \\ 0 & 0 & 0 & 0 & 0 & 0 \end{bmatrix}$$

$R_{0,16}$

$$\begin{bmatrix} 0 & 0 & 0 & 0 & -900 & 0 \\ 0 & 0 & 0 & 0 & -900 & 0 \\ 0 & 0 & 0 & 0 & 0 & 0 \\ 0 & 0 & 0 & 0 & 0 & 0 \\ 0 & -1500 & 0 & 0 & 0 & 0 \\ 0 & -1500 & 0 & 0 & 0 & 0 \end{bmatrix}$$

$R_{0,2}$

$$\begin{bmatrix} 0 & 0 & 0 & 0 & 0 & 0 \\ 0 & 0 & 0 & 0 & 0 & 0 \\ 0 & 0 & 0 & 0 & 0 & 0 \\ 0 & 0 & 0 & 0 & 0 & 0 \\ 0 & 0 & 0 & 0 & 0 & 0 \\ 1200 & 0 & 0 & 0 & 0 & 0 \end{bmatrix}$$

$R_{0,17}$

$$\begin{bmatrix} 0 & 0 & 0 & -900 & 0 & 0 \\ 0 & 0 & 0 & -900 & 0 & 0 \\ -1200 & 0 & 0 & 0 & 0 & 0 \\ -1200 & 0 & 0 & 0 & 0 & 0 \\ 0 & 0 & 0 & 0 & 0 & 0 \\ 0 & 0 & 0 & 0 & 0 & 0 \end{bmatrix}$$

(d)

Figure 6.7: Sample covariance matrices for different laser phase noise variances of (a) $\sigma_p^2 = \{900, 1200, 1500, 1800, 2100, 2400\}$ for independent lasers and (b) $\sigma_p^2 = \{900, 900, 1200, 1200, 1500, 1500\}$ for the spacecraft locked lasers. The phototdetector noise variances are $\sigma_n^2 = 1$ and the offsets are $D = \{15, 16, 17\}$. The values for the non-zero blocks are given on the right.

tor noise variances were represented in the eigenvalues for the spacecraft locked lasers which may just be due to the size of the matrix. The number of eigenvalues obtained for the spacecraft and all locked lasers are 29 and 104 which are similar to those of the corresponding unequal arms.

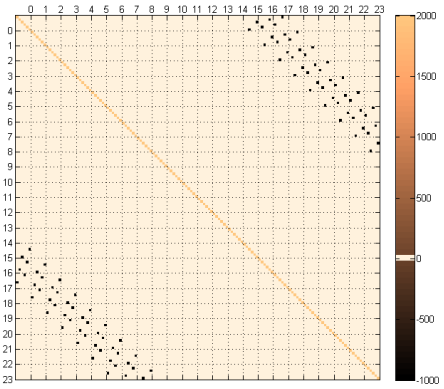

(a)

$R_{0,0}$

2001	0	0	0	0	0
0	2002	0	0	0	0
0	0	2003	0	0	0
0	0	0	2004	0	0
0	0	0	0	2005	0
0	0	0	0	0	2006

$R_{0,16}$

0	0	0	0	0	0
0	0	0	0	-1000	0
0	0	0	0	0	0
0	0	0	0	0	0
0	-1000	0	0	0	0
0	0	0	0	0	0

$R_{0,15}$

0	0	0	0	0	0
0	0	0	0	0	0
0	0	0	0	0	-1000
0	0	0	0	0	0
0	0	0	0	0	0
0	0	-1000	0	0	0

$R_{0,17}$

0	0	0	-1000	0	0
0	0	0	0	0	0
0	0	0	0	0	0
-1000	0	0	0	0	0
0	0	0	0	0	0
0	0	0	0	0	0

(b)

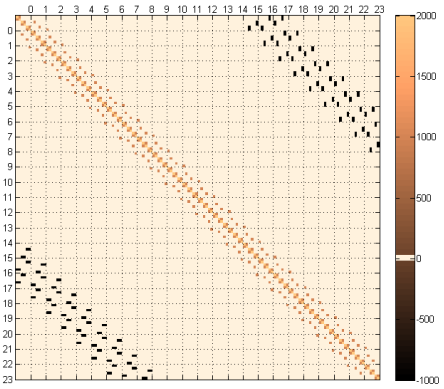

(c)

$R_{0,0}$

2001	1000	0	0	0	0
1000	2002	0	0	0	0
0	0	2003	1000	0	0
0	0	1000	2004	0	0
0	0	0	0	2005	1000
0	0	0	0	1000	2006

$R_{0,15}$

0	0	0	0	0	0
0	0	0	0	0	0
0	0	0	0	0	-1000
0	0	0	0	0	-1000
0	0	-1000	0	0	0
0	0	-1000	0	0	0

$R_{0,1}$

0	0	0	0	0	0
0	0	0	0	0	0
0	1000	0	0	0	0
0	0	0	0	0	0
0	0	0	1000	0	0
0	0	0	0	0	0

$R_{0,16}$

0	0	0	0	-1000	0
0	0	0	0	-1000	0
0	0	0	0	0	0
0	0	0	0	0	0
0	-1000	0	0	0	0
0	-1000	0	0	0	0

$R_{0,2}$

0	0	0	0	0	0
0	0	0	0	0	0
0	0	0	0	0	0
0	0	0	0	0	0
0	0	0	0	0	0
1000	0	0	0	0	0

$R_{0,17}$

0	0	0	-1000	0	0
0	0	0	-1000	0	0
0	0	0	0	0	0
0	0	0	0	0	0
0	0	0	0	0	0
0	0	0	0	0	0

(d)

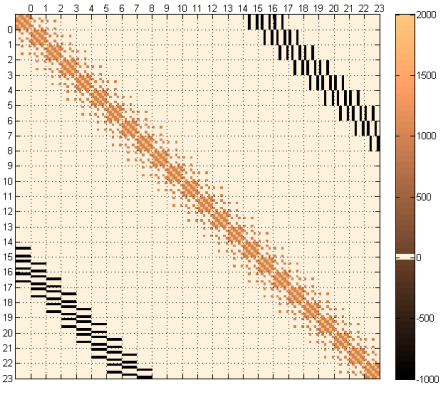

(e)

$R_{0,0}$

2001	1000	1000	2000	1000	1000
1000	2002	1000	1000	2000	1000
1000	1000	2003	1000	1000	2000
2000	1000	1000	2004	1000	1000
1000	2000	1000	1000	2005	1000
1000	1000	2000	1000	1000	2006

$R_{0,15}$

0	0	-1000	0	0	-1000
0	0	-1000	0	0	-1000
0	0	-1000	0	0	-1000
0	0	-1000	0	0	-1000
0	0	-1000	0	0	-1000
0	0	-1000	0	0	-1000

$R_{0,1}$

0	0	0	0	0	0
1000	0	0	1000	0	0
0	1000	0	0	1000	0
0	0	0	0	0	0
1000	0	0	1000	0	0
0	1000	0	0	1000	0

$R_{0,16}$

0	-1000	0	0	-1000	0
0	-1000	0	0	-1000	0
0	-1000	0	0	-1000	0
0	-1000	0	0	-1000	0
0	-1000	0	0	-1000	0
0	-1000	0	0	-1000	0

$R_{0,2}$

0	0	0	0	0	0
0	0	0	0	0	0
1000	0	0	1000	0	0
0	0	0	0	0	0
0	0	0	0	0	0
1000	0	0	1000	0	0

$R_{0,17}$

-1000	0	0	-1000	0	0
-1000	0	0	-1000	0	0
-1000	0	0	-1000	0	0
-1000	0	0	-1000	0	0
-1000	0	0	-1000	0	0
-1000	0	0	-1000	0	0

(f)

Figure 6.8: Sample covariance matrix for different photodetector variances of $\sigma_n^2 = \{1, 2, 3, 4, 5, 6\}$ with laser noise variances of $\sigma_p^2 = 1000$ for no phase-locking with offsets of $D = \{15, 16, 17\}$. The values for the non-zero blocks are given on the right.

Table 6.6: The eigenvalues for different laser phase noise and photodetector noise variances. In columns 2-7 the laser phase noises are $\sigma_p^2 = \{900, 1200, 1500, 1800, 2100, 2400\}$ for independent lasers and $\sigma_p^2 = \{900, 1500, 2100\}$ for spacecraft locked lasers. In both cases the photodetector noise variances are kept constant with values of $\sigma_n^2 = 1$. In columns 8-13 the photodetector noises are $\sigma_n^2 = \{1, 2, 3, 4, 5, 6\}$ and the laser phase noises variances are kept constant with values of $\sigma_p^2 = 1000$.

phase-lock	Eigenvalues											
	Different laser phase noise variances						Different photodetector variances					
None	901	901	901	901	901	901	1002	1002	1002	1002	1002	1002
	901	1201	1201	1201	1201	1201	1002	1002	1002	1002	1002	1002
	1201	1201	1201	1501	1501	1501	1002	1002	1003	1003	1003	1003
	1501	1501	1501	1501	1501	1501	1003	1003	1003	1003	1003	1003
	1801	1801	1801	1801	1801	1801	1003	1003	1003	1003	1003	1003
	1801	2101	2101	2101	2101	2101	1004	1004	1004	1004	1004	1004
	2101	2101	2101	2401	2401	2401	1004	1004	1004	1004	1004	1004
	2401	2401	2401	2401	2401	2401	1004	1004	1004	1004	1004	1004
	2701	2701	2701	2701	2701	2701	2001	2001	2001	2001	2001	2001
	2701	2701	2701	2701	2701	2701	2001	2001	2001	2001	2002	2002
	2701	2701	2701	2701	2701	2701	2002	2002	2002	2002	2002	2002
	2701	2701	3301	3301	3301	3301	2003	2003	2003	2003	2003	2003
	3301	3301	3301	3301	3301	3301	2004	2004	2004	2004	2004	2004
	3301	3301	3301	3301	3301	3301	2004	2004	2004	2004	2005	2005
	3601	3601	3601	3601	3601	3601	2005	2005	2005	2005	2005	2005
	3601	3901	3901	3901	3901	3901	2006	2006	2006	2006	2006	2006
	3901	3901	3901	3901	3901	3901	3003	3003	3003	3003	3003	3003
	3901	4501	4501	4501	4501	4501	3003	3003	3003	3003	3003	3003
	4501	4501	4501	4501	4501	4501	3003	3003	3004	3004	3004	3004
	4501	4501	4501	4501	5401	5401	3004	3004	3004	3004	3004	3004
	5401	5401	5401	5401	5401	5401	3004	3004	3004	3004	3004	3004
	5401	5401	5401	5401	5401	5401	3005	3005	3005	3005	3005	3005
	5401	5401	5401	6301	6301	6301	3005	3005	3005	3005	3005	3005
	6301	6301	6301	6301	6301	6301	3005	3005	3005	3005	3005	3005
Spacecraft	1	1	1	1	1	1	2	2	2	3	3	3
	1	1	1	1	1	1	3	3	3	3	3	3
	1	1	1	1	1	1	3	3	3	3	3	3
	1	1	1	1	1	1	3	3	3	3	4	4
	1	1	1	1	1	51	4	5	5	5	5	47
	78	101	162	250	301	358.5	71	91	142	226	264	318
	498	525	546	560	668	765.6	447	456	473	482	642	694
	787	802	830	993	993	993.4	708	733	754	949	963	1002
	993	993	1002	1010	1032	1034.5	1003	1003	1003	1003	1003	1004
	1147	1183	1263	1329	1341	1342.9	1004	1004	1004	1004	1004	1004
	1343	1343	1343	1343	1357	1386.1	1004	1125	1148	1223	1239	1271
	1451	1455	1560	1593	1655	1698.2	1271	1271	1271	1332	1378	1394
	1783	1895	1922	1987	2100	2108.7	1651	1713	2002	2002	2002	2002
	2255	2287	2328	2359	2370	2401.0	2003	2003	2003	2003	2003	2003
	2401	2401	2401	2422	2529	2582.2	2004	2004	2004	2004	2004	2004
	2679	2737	2817	2838	2937	2938.6	2004	2004	2005	2005	2005	2005
	3081	3081	3081	3081	3081	3137.3	3003	3003	3003	3003	3003	3003
	3151	3543	3588	3674	4121	4120.6	3003	3004	3004	3004	3004	3004
	4121	4121	4121	4359	4470	4532.2	3225	3232	3282	3439	3596	3908
	4810	4867	4867	4867	4867	4866.6	4004	4004	4004	4004	4004	4143
	4896	4908	5076	5085	5195	5208.2	4426	4468	4690	4736	4736	4736
	5575	5649	6031	6350	6361	6363.8	4736	4825	4883	4909	5047	5075
	6401	6404	6422	6429	7286	7292.2	5114	5258	5292	5376	5438	5478
	7311	7313	7344	7354	7455	7456.8	5553	5578	5719	5722	5923	5928
All							1	1	1	1	1	1
							1	1	2	2	2	2
							2	2	2	2	2	2
							2	2	2	2	2	2
							2	2	2	2	2	2
							2	2	2	3	3	3
							3	3	3	3	3	3
							3	3	3	3	3	3
							3	3	3	3	3	3
							3	3	4	4	4	4
							4	4	4	4	4	4
							4	4	4	4	4	4
							5	5	5	5	5	5
							5	5	5	5	5	5
							5	5	5	5	5	5
							5	5	5	5	5	6
							6	6	6	6	6	6
							6	6	321	348	1168	1294
							1912	2586	2941	3771	4205	4433
							4532	4851	5207	5285	5661	5697
							6004	6004	6004	6004	6004	6004
							6004	6419	6507	7377	7638	8138
							9136	10099	10890	11602	12051	12401
							12714	12992	14032	15459	16770	17679

Table 6.7: Time domain eigenvalues for variable laser phase and photodetector variances. The offsets are $D = \{15, 16, 17\}$ and the lasers are locked on each spacecraft.

Eigenvalues													
0.8	0.8	0.8	0..8	0.8	0.8	0.8	0.8	0.8	0.9	0.9	0.9	0.9	0.9
0.9	0.9	0.9	0.9	0.9	0.9	0.9	0..9	0.9	0.9	0.9	0..9	0.9	0.9
0.9	0.9	0.9	0..9	1.0	1.0	1.0	1.0	1.0	1.0	1.0	1.0	1.0	1.0
1.0	1.0	1.0	1.0	1.0	1.0	1.0	1.0	1.0	1.0	1.0	1.0	1.0	1.0
1.0	1.1	1.1	1.1	1.1	1.1	1.1	1.1	1.1	1.1	1.1	1.1	1.1	1.1
1.2	1.2	1.2	1.2	1.2	1.2	1.2	1.2	984	99.4	110.9	118.0	305.8	340.8
387.1	401.5	407.8	416.3	432.4	489.3	511.3	524.0	560.1	563.5	631.9	637.4	672.8	696.2
700.8	721.0	743.5	779.7	803.6	815.0	869.8	892.2	943.8	948.3	1.008.6	1009.3	1047.0	1068.2
1072.1	1087.1	1093.8	1103.5	1191.3	1197.2	1203.7	1215.4	1250.1	1263.0	1273.1	1283.9	1287.3	1297.5
1304.3	1324.7	1336.4	1339.2	1349.9	1378.5	1389.2	1394.2	1434.5	1458.8	1477.3	1483.4	1509.7	1517.8
1528.0	1548.6	1558.6	1560.3	1571.7	1577.0	1582.2	1582.9	1601.4	1609.6	1611.1	1618.0	1627.3	1635.5
1640.8	1651.8	1827.4	1828.8	1832.0	1836.5	1841.0	1846.6	1848.8	1852.7	1859.9	1862.4	1864.7	1878.1
1880.0	1887.2	1899.3	1907.6	2345.2	2547.2	2958.1	2975.5	2978.1	2981.8	3026.9	3103.6	3172.0	3306.0
3390.6	3439.6	3508.3	3553.5	3626.5	3638.1	3677.5	3705.3	3716.9	3726.5	3827.3	3927.5	3964.3	3973.2
3983.4	4013.2	4139.1	4164.2	4188.8	4190.7	4260.7	4275.5	5008.9	5022.7	5043.5	5057.3	5107.3	5125.2
5164.1	5188.7	5200.2	5234.6	5272.7	5335.6	5361.0	5440.8	5459.4	5472.1	5500.0	5515.6	5520.1	5523.2
5635.0	5643.6	5706.2	5720.0	5735.6	5738.2	5760.3	5778.9	5785.7	5827.6	5901.8	5922.2	5970.9	5975.6
6038.3	6079.6	6246.8	6253.0	6277.3	6367.2	6430.2	6453.6	6496.3	6510.2	6705.5	6716.1	6874.6	6878.6

Variable laser phase and photodetector noise variances

To model non-stationarity in the noises the values of their variances were varied sinusoidally about their mean values of $\sigma_p^2 = 1000$ and $\sigma_n^2 = 1$ as illustrated in Figure 6.9a. The covariance matrix was only generated for the spacecraft phase-locked lasers which is given in Figure 6.9b where the temporal changes of the variances result in changes in the values along the diagonals. The eigenvalues for this matrix are given in Table 6.7 and the number of laser noise free values is 78. The larger matrix was used here to illustrate the variations along the diagonals. For a similar sized matrix as those in the other sections the number of eigenvalues is 29. The large separation in the variances allowed the two groups to be easily determined and their values reflected the changing values of the variances.

Small separations between the laser and photodetector noise variances

For this section only the covariance matrices for spacecraft locked lasers and unequal arm lengths with times of $D = \{15, 16, 17\}$ will be used. Three sets of values were investigated for equal and unequal variances with integer and real values which are (i) $\sigma_p^2 = 9$ and $\sigma_n^2 = 1$, (ii) $\sigma_p^2 = 2$ and $\sigma_n^2 = 1$ and (iii)$\sigma_{pi}^2 = \{2.3, 2.4, 2.5, 2.6, 2.7, 2.8\}$ and $\sigma_{ni}^2 = \{0.8, 0.9, 1.0, 1.1, 1.2, 1.3\}$. In the last set the smallest laser noise variance differs from the largest photodetector noise by 1. Only the matrix for the the first set is presented which is in Figure 6.10 to illustrate the differences between the values when the separation between the two types of noises are small. The values of the non-zero blocks are also included.

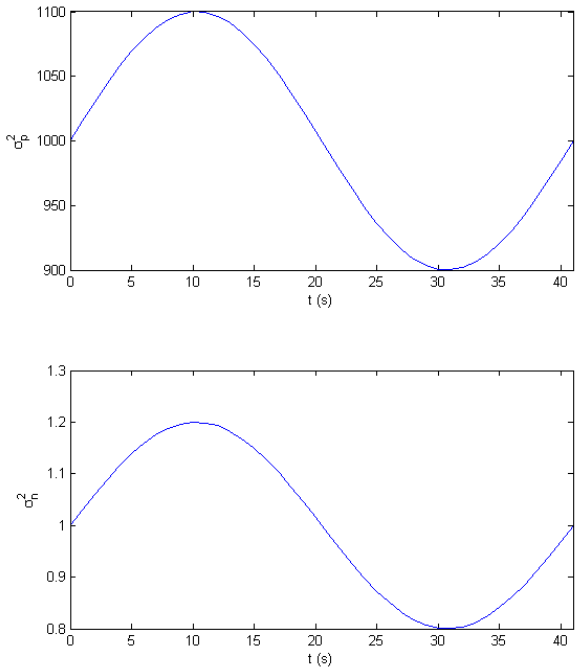

(a)

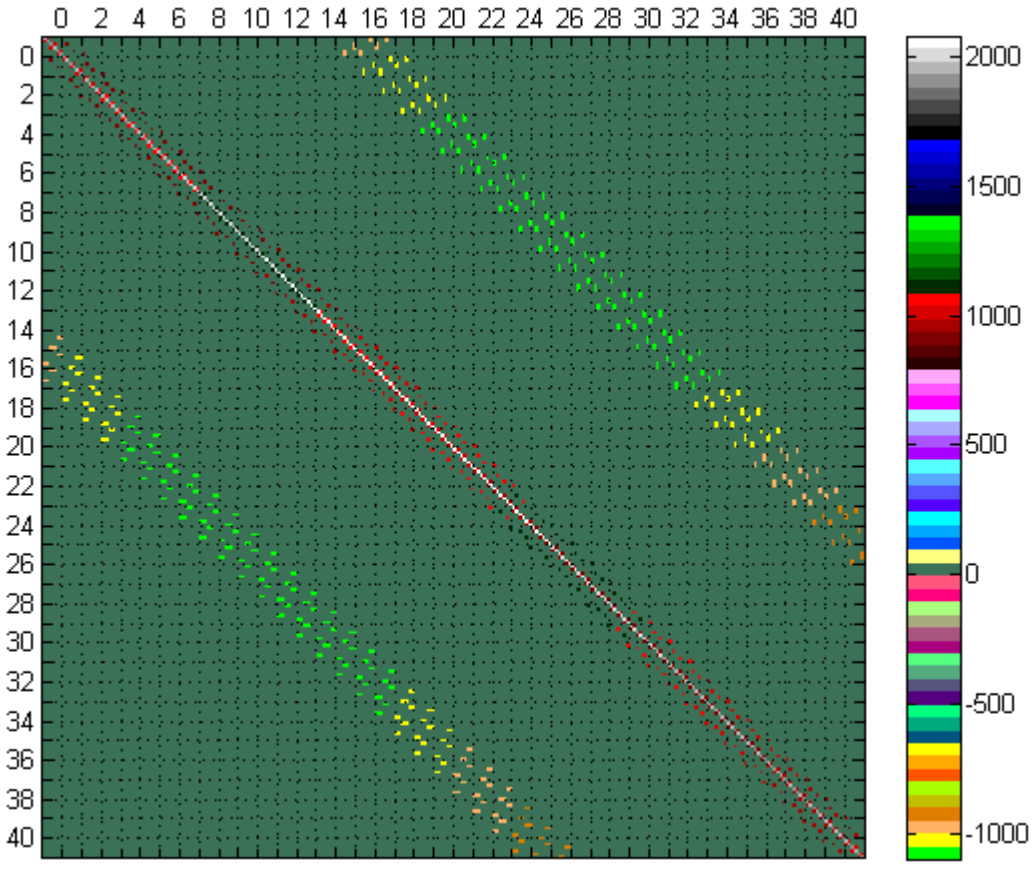

(b)

Figure 6.9: Sample covariance matrix (b) for time varying laser phase and photodetector noise variances with the values varying according to the patterns shown in (a).

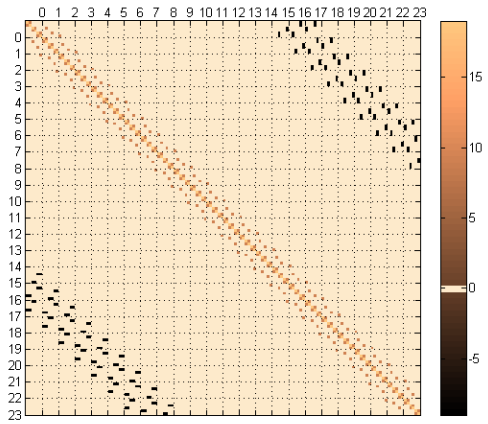

$R_{0,0}$

$$\begin{array}{|cccccc|cccccc|}
19 & 9 & 0 & 0 & 0 & 0 & 0 & 0 & 0 & 0 & 0 & 0 \\
9 & 19 & 0 & 0 & 0 & 0 & 0 & 0 & 0 & 0 & 0 & 0 \\
0 & 0 & 19 & 9 & 0 & 0 & 0 & 0 & 0 & 0 & 0 & -9 \\
0 & 0 & 9 & 19 & 0 & 0 & 0 & 0 & 0 & 0 & 0 & -9 \\
0 & 0 & 0 & 0 & 19 & 9 & 0 & 0 & -9 & 0 & 0 & 0 \\
0 & 0 & 0 & 0 & 9 & 19 & 0 & 0 & -9 & 0 & 0 & 0 \\
\hline
\end{array}$$

$R_{0,15}$

$R_{0,1}$

$$\begin{array}{|cccccc|cccccc|}
0 & 0 & 0 & 0 & 0 & 0 & 0 & 0 & 0 & 0 & -9 & 0 \\
0 & 0 & 0 & 0 & 0 & 0 & 0 & 0 & 0 & 0 & -9 & 0 \\
0 & 9 & 0 & 0 & 0 & 0 & 0 & 0 & 0 & 0 & 0 & 0 \\
0 & 0 & 0 & 0 & 0 & 0 & 0 & 0 & 0 & 0 & 0 & 0 \\
0 & 0 & 0 & 9 & 0 & 0 & 0 & -9 & 0 & 0 & 0 & 0 \\
0 & 0 & 0 & 0 & 0 & 0 & 0 & -9 & 0 & 0 & 0 & 0 \\
\hline
\end{array}$$

$R_{0,16}$

$R_{0,2}$

$$\begin{array}{|cccccc|cccccc|}
0 & 0 & 0 & 0 & 0 & 0 & 0 & 0 & 0 & -9 & 0 & 0 \\
0 & 0 & 0 & 0 & 0 & 0 & 0 & 0 & 0 & -9 & 0 & 0 \\
0 & 0 & 0 & 0 & 0 & 0 & -9 & 0 & 0 & 0 & 0 & 0 \\
0 & 0 & 0 & 0 & 0 & 0 & -9 & 0 & 0 & 0 & 0 & 0 \\
0 & 0 & 0 & 0 & 0 & 0 & 0 & 0 & 0 & 0 & 0 & 0 \\
9 & 0 & 0 & 0 & 0 & 0 & 0 & 0 & 0 & 0 & 0 & 0 \\
\hline
\end{array}$$

$R_{0,17}$

(a) (b)

Figure 6.10: Sample covariance matrix for smaller separations between the laser phase noise and photodetector noises variances. The values for the variances are $\sigma_p^2 = 9$ and $\sigma_n^2 = 1$ with spacecraft locked lasers and offsets of $D = \{15, 16, 17\}$. The values on the right are non-zero blocks of the first row.

The eigenvalues are given in Table 6.8 where in all three sets they do still split into the two groups relating to those with and without laser phase noises. The splitting is judged from the actual values where those that match the phototdetector noises variance are assumed be from them. Values closer to the laser phase noise variances are assumed to be related to combinations of these noises and the phototdetector noises. Note that in all three sets there are values between the two which are much closer to the phtotodetector noises which may just contain this type but are not included in the laser noise free group. As the values get closer to it becomes more difficult to distinguish between the two sets of values.

In the first set with the noise variances for each noise type being equal with values $\sigma_p^2 = 9$ and $\sigma_n^2 = 1$ and the number of eigenvalues equal to the 1 is 30. The values close to the laser noise are 8 and 10 which could be $\sigma_p^2 \pm \sigma_n^2$. The range of values between the photodetector noise values and these are 2 to 7. In the second set where the values are still integers with the laser noise variance reduced to $\sigma_p^2 = 2$ resulting in a separation from the photodetector noises of only 1, the splitting still occurred with the number of values associated with the only photodetector noises increasing to 34. The next set of eigenvalues are equal to 2 where now it is impossible to tell what this is associated with

Table 6.8: Time domain eigenvalues for smaller separations between the variances of the two noise types. The offsets are $\{D = 15, 16, 17\}$ and the lasers are locked on each spacecraft.

Eigenvalues																		
Variances ($\sigma_p^2 = 9$, $\sigma_n^2 = 1$)																		
1	1	1	1	1	1	1	1	1	1	1	1	1	1	1	1	1	1	
1	1	1	1	1	1	1	1	1	1	1	1	2	2	2	3	3	4	
5	5	5	5	7	7	7	8	8	10	10	10	10	10	10	10	10	10	
10	10	10	10	10	10	10	11	11	12	12	12	12	12	12	13	13	14	
16	16	19	19	19	19	19	19	19	19	19	19	19	19	19	19	19	19	
19	19	19	19	19	19	28	28	28	28	28	28	28	28	28	28	28	28	
30	30	30	32	33	36	37	37	37	37	37	38	41	41	43	44	44	44	
44	44	45	45	46	47	47	48	49	49	50	50	51	51	52	52	54	54	
Variances ($\sigma_p^2 = 2$, $\sigma_n^2 = 1$)																		
1	1	1	1	1	1	1	1	1	1	1	1	1	1	1	1	1	1	
1	1	1	1	1	1	1	1	1	1	1	1	1	1	1	1	2	2	
2	2	2	2	2	2	2	2	3	3	3	3	3	3	3	3	3	3	
3	3	3	3	3	3	3	3	3	3	3	4	4	4	4	4	4	4	
4	4	5	5	5	5	5	5	5	5	5	5	5	5	5	5	5	5	
5	5	5	5	5	5	7	7	7	7	7	7	7	7	7	7	7	7	
7	7	8	8	8	9	9	9	9	9	9	9	10	10	10	10	10	10	
10	11	11	11	11	11	11	12	12	12	12	12	12	12	12	12	13	13	
Variances ($\sigma_p^2 = 1.5$, $\sigma_n^2 = 1.0$)																		
1.0	1.0	1.0	1.0	1.0	1.0	1.0	1.0	1.0	1.0	1.0	1.0	1.0	1.0	1.0	1.0	1.0	1.0	
1.0	1.0	1.0	1.0	1.0	1.0	1.0	1.0	1.0	1.0	1.0	1.1	1.1	1.1	1.2	1.3	1.4	1.5	
1.7	1.7	1.7	1.7	2.0	2.0	2.1	2.1	2.1	2.4	2.4	2.5	2.5	2.5	2.5	2.5	2.5	2.5	
2.5	2.5	2.5	2.5	2.5	2.5	2.5	2.7	2.7	2.8	2.9	2.9	2.9	2.9	2.9	3.0	3.1	3.1	
3.5	3.6	4.0	4.0	4.0	4.0	4.0	4.0	4.0	4.0	4.0	4.0	4.0	4.0	4.0	4.0	4.0	4.0	
4.0	4.0	4.0	4.0	4.0	4.0	5.5	5.5	5.5	5.5	5.5	5.5	5.5	5.5	5.5	5.5	5.5	5.5	
5.8	5.9	6.0	6.2	6.4	6.9	7.0	7.0	7.0	7.0	7.0	7.2	7.6	7.7	8.0	8.1	8.1	8.1	
8.1	8.2	8.3	8.4	8.6	8.6	8.7	8.9	8.9	9.1	9.2	9.2	9.3	9.4	9.6	9.6	9.9	9.9	
Variances ($\sigma_p^2 = 1.5$, $\sigma_{ni}^2 = \{0.8, 0.9, 1.0, 1.1, 1.2, 1.3\}$)																		
0.9	0.9	0.9	0.9	1.0	1.0	1.0	1.0	1.0	1.0	1.0	1.0	1.0	1.0	1.0	1.0	1.0	1.0	
1.0	1.0	1.0	1.0	1.1	1.1	1.1	1.1	1.1	1.1	1.2	1.2	1.2	1.2	1.3	1.4	1.5	1.5	
1.7	1.8	1.8	1.8	2.0	2.1	2.1	2.1	2.2	2.3	2.4	2.5	2.5	2.5	2.5	2.5	2.5	2.6	
2.6	2.6	2.6	2.6	2.6	2.6	2.6	2.7	2.7	2.8	2.9	3.0	3.0	3.0	3.0	3.0	3.1	3.2	
3.5	3.6	3.9	3.9	3.9	4.0	4.0	4.0	4.0	4.0	4.1	4.1	4.1	4.1	4.1	4.1	4.1	4.1	
4.1	4.1	4.2	4.2	4.2	4.2	5.5	5.5	5.5	5.5	5.5	5.5	5.5	5.6	5.6	5.6	5.6	5.6	
5.8	5.8	6.0	6.1	6.6	6.9	7.1	7.1	7.1	7.1	7.1	7.3	7.8	7.8	8.1	8.1	8.1	8.1	
8.1	8.3	8.4	8.4	8.7	8.7	8.7	8.9	9.0	9.1	9.2	9.3	9.4	9.4	9.6	9.6	9.9	9.9	
Variances ($\sigma_{pi}^2 = \{1.5, 1.6, 1.7\}$, $\sigma_{ni}^2 = \{0.8, 0.9, 1.0, 1.1, 1.2, 1.3\}$)																		
0.9	0.9	0.9	0.9	1.0	1.0	1.0	1.0	1.0	1.0	1.0	1.0	1.0	1.0	1.0	1.0	1.0	1.0	
1.0	1.0	1.0	1.0	1.1	1.1	1.1	1.1	1.1	1.1	1.2	1.2	1.2	1.2	1.3	1.4	1.5	1.6	
1.8	1.8	1.8	1.9	2.1	2.1	2.2	2.2	2.2	2.5	2.5	2.6	2.6	2.6	2.6	2.6	2.6	2.6	
2.7	2.7	2.7	2.7	2.7	2.7	2.7	2.8	2.9	3.0	3.0	3.1	3.1	3.1	3.1	3.2	3.2	3.3	
3.6	3.7	4.0	4.0	4.1	4.1	4.1	4.1	4.2	4.2	4.2	4.2	4.3	4.3	4.3	4.3	4.4	4.4	
4.4	4.4	4.5	4.5	4.5	4.5	5.6	5.6	5.6	5.6	5.6	5.6	5.7	6.0	6.0	6.1	6.1	6.1	
6.1	6.1	6.3	6.6	7.0	7.1	7.5	7.5	7.5	7.5	7.5	7.7	8.3	8.3	8.4	8.4	8.5	8.5	
8.5	8.6	9.0	9.1	9.1	9.3	9.4	9.5	9.5	9.6	10.0	10.0	10.1	10.1	10.3	10.3	10.6	10.6	

as this is also the value of the laser noise. Even the third set where the values are no longer integers and were also all given different values there are still values that reflect the value of the photodetector noise variances. In this case the number of these values is 32.

6.2 Frequency domain

In this section we investigate the effects of laser phase-locking, arm lengths and the noise variances on the power spectral density matrix. LISA's raw data data are time series so that a frequency domain analysis involves the Fourier transform therefore, understanding what occurs with the data is needed. This is especially important when the noise properties are time dependent, for example, in the case of non-stationary.

6.2.1 The power spectral density matrix

For the toy model the power spectral density matrices will only contain non-zero values in the blocks along the main diagonal since there are no correlations between different frequencies. The effects of the different properties will be confined to these blocks. The size of each block is 6×6 with the auto-power spectral densities occurring on the main diagonal and the cross-power spectral densities elsewhere. Recall that the raw data time series can be written as

$$s_i(t) = p_{j'}(t - D_k) - p_i(t) + n_i(t), \tag{6.31}$$

and its spectrum is

$$\widetilde{s}_i(f) = \widetilde{p}_{j'}(f)\, e^{-2\pi i f D_k} - \widetilde{p}_i(f) + \widetilde{n}_i(f), \tag{6.32}$$

where the time offset D_k becomes a phase shift and $\widetilde{s}_i(f)$ represents the Fourier transform of $s_i(t)$ given by

$$\widetilde{s}_i(f) = \int_{-\infty}^{\infty} s_i(t)\, e^{-2\pi i f t} dt. \tag{6.33}$$

For no phase-locking with unequal arm lengths the auto-power spectra can be written as

$$\begin{aligned} \widetilde{S}_{ii}(f) &= \left\langle \left[\widetilde{p}_{j'}(f)\, e^{-2\pi i f D_k} - \widetilde{p}_i(f) + \widetilde{n}_i(f)\right] \times \left[\widetilde{p}_{j'}(f)\, e^{2\pi i f D} - \widetilde{p}_i(f) + \widetilde{n}_i(f)\right] \right\rangle \\ &= \langle \widetilde{p}^2_{j'}(f) \rangle + \langle \widetilde{p}^2_i(f) \rangle + \langle \widetilde{n}^2_i(f) \rangle. \end{aligned} \tag{6.34}$$

Independent

	s_1	$s_{1'}$	s_2	$s_{2'}$	s_3	$s_{3'}$
s_1	$\sigma^2_{p2'}$ $+\sigma^2_{p1}+\sigma^2_{n1}$	0	0	$-\sigma^2_{p1}\, e^{2\pi i f D_3}$ $-\sigma^2_{p2'}\, e^{-2\pi i f D_3}$	0	0
$s_{1'}$	0	σ^2_{p3} $+\sigma^2_{p1'}+\sigma^2_{n1'}$	0	0	$-\sigma^2_{p1'}\, e^{2\pi i f D_2}$ $-\sigma^2_{p3}\, e^{-2\pi i f D_2}$	0
s_2	0	0	$\sigma^2_{p3'}$ $+\sigma^2_{p2}+\sigma^2_{n2}$	0	0	$-\sigma^2_{p2}\, e^{2\pi i f D_1}$ $-\sigma^2_{p3'}\, e^{-2\pi i f D_1}$
$s_{2'}$	$-\sigma^2_{p1}\, e^{-2\pi i f D_3}$ $-\sigma^2_{p2'}\, e^{2\pi i f D_3}$	0	0	σ^2_{p1} $+\sigma^2_{p2'}+\sigma^2_{n2'}$	0	0
s_3	0	$-\sigma^2_{p1'}\, e^{-2\pi i f D_2}$ $-\sigma^2_{p3}\, e^{2\pi i f D_2}$	0	0	$\sigma^2_{p1'}$ $+\sigma^2_{p3}+\sigma^2_{n3}$	0
$s_{3'}$	0	0	$-\sigma^2_{p2}\, e^{-2\pi i f D_1}$ $-\sigma^2_{p3'}\, e^{2\pi i f D_1}$	0	0	σ^2_{p2} $+\sigma^2_{p3'}+\sigma^2_{n1}$

Spacecraft phase-locked

	s_1	$s_{1'}$	s_2	$s_{2'}$	s_3	$s_{3'}$
s_1	σ^2_{p2} $+\sigma^2_{p1}+\sigma^2_{n1}$	σ^2_{p1}	$-\sigma^2_{p2}\, e^{-2\pi i f D_3}$	$-\sigma^2_{p1}\, e^{2\pi i f D_3}$ $-\sigma^2_{p2}\, e^{-2\pi i f D_3}$	$-\sigma^2_{p1}\, e^{2\pi i f D_2}$	$\sigma^2_{p2}\, e^{2\pi i f (D_1-D_3)}$
$s_{1'}$	σ^2_{p1}	σ^2_{p3} $+\sigma^2_{p1}+\sigma^2_{n1'}$	$\sigma^2_{p3}\, e^{2\pi i f (D_1-D_2)}$	$-\sigma^2_{p1}\, e^{2\pi i f D_3}$	$-\sigma^2_{p1}\, e^{2\pi i f D_2}$ $-\sigma^2_{p3}\, e^{-2\pi i f D_2}$	$-\sigma^2_{p3}\, e^{-2\pi i f D_2}$
s_2	$-\sigma^2_{p2}\, e^{2\pi i f D_3}$	$\sigma^2_{p3}\, e^{-2\pi i f (D_1-D_2)}$	σ^2_{p3} $+\sigma^2_{p2}+\sigma^2_{n2}$	σ^2_{p2}	$-\sigma^2_{p3}\, e^{-2\pi i f D_1}$	$-\sigma^2_{p2}\, e^{2\pi i f D_1}$ $-\sigma^2_{p3}\, e^{-2\pi i f D_1}$
$s_{2'}$	$-\sigma^2_{p1}\, e^{-2\pi i f D_3}$ $-\sigma^2_{p2}\, e^{2\pi i f D_3}$	$-\sigma^2_{p1}\, e^{-2\pi i f D_3}$	σ^2_{p2}	σ^2_{p1} $+\sigma^2_{p2}+\sigma^2_{n2'}$	$\sigma^2_{p1}\, e^{2\pi i f (D_2-D_3)}$	$-\sigma^2_{p2}\, e^{2\pi i f D_1}$
s_3	$-\sigma^2_{p1}\, e^{-2\pi i f D_2}$	$-\sigma^2_{p1}\, e^{-2\pi i f D_2}$ $-\sigma^2_{p3}\, e^{2\pi i f D_2}$	$-\sigma^2_{p3}\, e^{2\pi i f D_1}$	$\sigma^2_{p1}\, e^{-2\pi i f (D_2-D_3)}$	σ^2_{p1} $+\sigma^2_{p3}+\sigma^2_{n3}$	σ^2_{p3}
$s_{3'}$	$\sigma^2_{p2}\, e^{-2\pi i f (D_1-D_3)}$	$-\sigma^2_{p3}\, e^{2\pi i f D_2}$	$-\sigma^2_{p2}\, e^{-2\pi i f D_1}$ $-\sigma^2_{p3}\, e^{2\pi i f D_1}$	$-\sigma^2_{p2}\, e^{-2\pi i f D_1}$	σ^2_{p3}	σ^2_{p2} $+\sigma^2_{p3}+\sigma^2_{n1}$

Figure 6.11: The raw data power spectral densities showing the contributions for the all blocks in the matrix for the independent and spacecraft locked lasers. The arm lengths used are static and unequal with no directional dependence.

An example of the cross-power spectral density using the readings from the optical benches at the end of arm k is

$$\begin{aligned}\widetilde{S}_{ij}(f) &= \left\langle \left[\widetilde{p}_j(f)\, e^{-2\pi i f D_k} - \widetilde{p}_i(f) + \widetilde{n}_i(f)\right] \times \left[\widetilde{p}_i(f)\, e^{2\pi i f D_k} - \widetilde{p}_j(f) + \widetilde{n}_j(f)\right]\right\rangle \\ &= -\langle \widetilde{p}^2_j(f)\rangle\, e^{-2\pi i f D_k} - \langle \widetilde{p}^2_i(f)\rangle\, e^{2\pi i f D_k}. \end{aligned} \tag{6.35}$$

6.2.1.1 The effects of laser phase-locking

The contributions for all the elements in each block are given in terms of σ^2_{pi} and σ^2_{ni} in Figure 6.11 for independent and spacecraft locked lasers with unequal static arm lengths with no directional dependencies. The values for all locked lasers are not given because of space limitations. The general format of the auto-power when all the lasers are phase-locked can be written as

$$S_{ii}(f) = \sigma^2_p \left[2 - e^{-2\pi i f D_k} - e^{2\pi i f D_k}\right] + \sigma^2_{ni}. \tag{6.36}$$

The cross-power densities for the readings along each arm is similar to the auto-power densities but without the photodetector noises which is

$$S_{ij}(f) = \sigma_p^2\big[2 - e^{-2\pi i f D_k} - e^{2\pi i f D_k}\big], \tag{6.37}$$

where D_k is the offset in the arm. Comparing this to the block representing the independent lasers in Figure 6.11, these will replace the values in the two diagonals away from the main. For all the others, the cross-power can be expressed as

$$S_{ij} = \sigma_p^2\big[e^{-2\pi i f (D_k - D_i)} - e^{-2\pi i f D_k} - e^{2\pi i f D_i} + 1\big], \tag{6.38}$$

where D_k and D_j are the offsets in the arms adjacent to optical benches i and j respectively. Again, using the block for the independent lasers, these will replace the zero values. So all the elements in the block for all locked lasers will be occupied. From this it can be seen that the effects of the arm lengths D_i are not the same as in the time domain. Here they are just phase shifts in the values and do not affect the location of the values.

Since the arm lengths do not have the same effects as in the time domain in discussing the phase-locking the unequal arms will be used instead. As seen in Figure 6.11 the effect of phase-locking is to increase the number of correlations which increases the density of the blocks. Without phase-locking only the optical benches at the ends of the arms are correlated resulting in only three diagonals in each block. With phase-locking all the optical benches are correlated resulting in the blocks being full. This is the same as in the time domain.

6.2.1.2 The effects of static arm lengths

The arm lengths occur as phase shifts in the spectra and so they affect the values in the blocks. With equal arm lengths the values that will show major changes from the unequal arms are those that include differences of offsets which only occur with phase-locking. For example, for space-craft locked lasers the cross-power spectral density for s_1 and $s_{3'}$ is $\sigma_{p2}^2\ e^{2\pi i f (D_1 - D_3)}$ which becomes σ_{p2}^2 with equal arm lengths. The same is true for all locked lasers where the cross-power in Equation 6.38 which is

$$S_{ij} = \sigma_p^2\big[e^{-2\pi i f (D_k - D_i)} - e^{-2\pi i f D_k} - e^{2\pi i f D_i} + 1\big], \tag{6.39}$$

which becomes

$$S_{ij} = \sigma_p^2\big[2 - e^{-2\pi i f D} - e^{2\pi i f D}\big]. \tag{6.40}$$

The effects of directionally dependent arm lengths

The directional dependence of the arm lengths will mean that the equations will contain offsets reflecting the directional differences indicated by D_k and $D_{k'}$. The only set that will show changes in the structure of the equations is the cross-power between the optical benches at the ends of each arm when the lasers are all locked. The equation for these is given by Equation 6.37 which is

$$S_{ij} = \sigma_p^2\big[2 - e^{-2\pi i f D_k} - e^{2\pi i f D_k}\big]. \tag{6.41}$$

With directional dependence this becomes

$$S_{ij}(f) = \sigma_p^2\big[e^{-2\pi i f (D_k - D_{k'})} - e^{-2\pi i f D_k} - e^{2\pi i f D_{k'}} + 1\big]. \tag{6.42}$$

6.2.1.3 The effects of the noise variances

As in the time domain the values of the variances determine values of the power and not the location of the correlations. The differences in their values will be reflected in the values in the blocks.

6.2.1.4 Time varying arm lengths and non-stationarity

Recall that the Fourier transform of a time series with an offset is given by

$$\mathcal{F}[s_i(t - D)] = \int_{-\infty}^{\infty} s_i(t - D) e^{-2\pi i f t} dt. \tag{6.43}$$

Letting $u = t - D$ will give $t = u - D$ and $dt = du$ which when substituted into Equation 6.43 gives

$$\begin{aligned} \mathcal{F}[s_i(u)] &= \int_{-\infty}^{\infty} s_i(u) e^{-2\pi i f (u - D)} du \\ &= \int_{-\infty}^{\infty} s_i(u)\ e^{-2\pi i f u}\ e^{-2\pi i f D} du. \end{aligned} \tag{6.44}$$

When D is constant the exponential term $e^{-2\pi i f D}$ will also be constant for each value of f and can be taken out of the integral giving

$$\mathcal{F}[s_i(u)] = e^{-2\pi i f D} \int_{-\infty}^{\infty} s_i(u)\ e^{-2\pi i f u} du \tag{6.45}$$

where the term in the integral is the Fourier transform of $s_i(u)$, therefore

$$\mathcal{F}[s_i(u)] = e^{-2\pi i f D}\ \widetilde{s}_i(f). \tag{6.46}$$

For time dependent offsets $D(t)$ Equation 6.43 becomes

$$\mathcal{F}[s_i(t - D(t))] = \int_{-\infty}^{\infty} s_i(t - D(t)) e^{-2\pi i f t} dt. \tag{6.47}$$

With $u = t - D(t)$ then $t = u - D(t)$ and $dt = du$ giving

$$\begin{aligned} \mathcal{F}[s_i(u)] &= \int_{-\infty}^{\infty} s_i(u) e^{-2\pi i f (u - D(t))} du \\ &= \int_{-\infty}^{\infty} s_i(u) e^{-2\pi i f u}\ e^{-2\pi i f D(t))} du. \end{aligned} \tag{6.48}$$

where the exponential term with the time offset is no longer a constant value and therefore cannot be taken out of the integral. In computing the power spectral densities it is easier to combine it with the non-stationarity.

In dealing with non-stationarity it is easier to view the power spectral densities through the Wiener-Khinchin theorem [47] where it is the Fourier transform of the auto-covariance function $C_{xx}(\tau)$ which for the continuous case van be written as

$$\begin{aligned} S_{xx}(f) &= \mathcal{F}[C_{xx}(\tau)] \\ &= \int_{\tau=\infty}^{\infty} C_{xx}(\tau)\ e^{-2\pi i f \tau} d\tau \end{aligned} \tag{6.49}$$

where τ is the lag and each contribution to a frequency bin is the sum of all the lag values. This can be extended to cross-power spectral densities $S_{xy}(f)$ and cross-covariances $C_{xy}(\tau)$ to give

$$\begin{aligned} S_{xy}(f) &= \mathcal{F}[C_{xy}(\tau)] \\ &= \int_{\tau=\infty}^{\infty} C_{xy}(\tau)\ e^{-2\pi i f \tau} d\tau. \end{aligned} \tag{6.50}$$

The covariance function will include the time dependent arm lengths and variances and since each frequency value is the sum of all the lag values the variations will not be visible in the spectra. They will be averages of all the time values.

6.2.1.5 Summary

With the toy model there are no correlation between frequencies and the power spectral density matrix is a block diagonal. The phase-locking has the same effects as in the time domain and increases the density of the blocks. The arm lengths do not define

Independent

	s_1	$s_{1'}$	s_2	$s_{2'}$	s_3	$s_{3'}$
s_1	$\sigma_{p2'}^2+\sigma_{p1}^2+\sigma_{n1}^2$	0	0	$-\sigma_{p1}^2-\sigma_{p2'}^2$	0	0
$s_{1'}$	0	$\sigma_{p3}^2+\sigma_{p1'}^2+\sigma_{n1'}^2$	0	0	$-\sigma_{p1'}^2-\sigma_{p3}^2$	0
s_2	0	0	$\sigma_{p3'}^2+\sigma_{p2}^2+\sigma_{n2}^2$	0	0	$-\sigma_{p2}^2-\sigma_{p3'}^2$
$s_{2'}$	$-\sigma_{p1}^2-\sigma_{p2'}^2$	0	0	$\sigma_{p1}^2+\sigma_{p2'}^2+\sigma_{n2'}^2$	0	0
s_3	0	$-\sigma_{p1'}^2-\sigma_{p3}^2$	0	0	$\sigma_{p1'}^2+\sigma_{p3}^2+\sigma_{n3}^2$	0
$s_{3'}$	0	0	$-\sigma_{p2}^2-\sigma_{p3'}^2$	0	0	$\sigma_{p2}^2+\sigma_{p3'}^2+\sigma_{n1}^2$

Spacecraft phase-locked

	s_1	$s_{1'}$	s_2	$s_{2'}$	s_3	$s_{3'}$
s_1	$\sigma_{p2}^2+\sigma_{p1}^2+\sigma_{n1}^2$	σ_{p1}^2	$-\sigma_{p2}^2$	$-\sigma_{p1}^2-\sigma_{p2}^2$	$-\sigma_{p1}^2$	σ_{p2}^2
$s_{1'}$	σ_{p1}^2	$\sigma_{p3}^2+\sigma_{p1}^2+\sigma_{n1'}^2$	σ_{p3}^2	$-\sigma_{p1}^2$	$-\sigma_{p1}^2-\sigma_{p3}^2$	$-\sigma_{p3}^2$
s_2	$-\sigma_{p2}^2$	σ_{p3}^2	$\sigma_{p3}^2+\sigma_{p2}^2+\sigma_{n2}^2$	σ_{p2}^2	$-\sigma_{p3}^2$	$-\sigma_{p2}^2-\sigma_{p3}^2$
$s_{2'}$	$-\sigma_{p1}^2-\sigma_{p2}^2$	$-\sigma_{p1}^2$	σ_{p2}^2	$\sigma_{p1}^2+\sigma_{p2}^2+\sigma_{n2'}^2$	σ_{p1}^2	$-\sigma_{p2}^2$
s_3	$-\sigma_{p1}^2$	$-\sigma_{p1}^2-\sigma_{p3}^2$	$-\sigma_{p3}^2$	σ_{p1}^2	$\sigma_{p1}^2+\sigma_{p3}^2+\sigma_{n3}^2$	σ_{p3}^2
$s_{3'}$	σ_{p2}^2	$-\sigma_{p3}^2$	$-\sigma_{p2}^2-\sigma_{p3}^2$	$-\sigma_{p2}^2$	σ_{p3}^2	$\sigma_{p2}^2+\sigma_{p3}^2+\sigma_{n1}^2$

All phase-locked

	s_1	$s_{1'}$	s_2	$s_{2'}$	s_3	$s_{3'}$
s_1	σ_{n1}^2	0	0	0	0	0
$s_{1'}$	0	$\sigma_{n1'}^2$	0	0	0	0
s_2	0	0	σ_{n2}^2	0	0	0
$s_{2'}$	0	0	0	$\sigma_{n2'}^2$	0	0
s_3	0	0	0	0	σ_{n3}^2	0
$s_{3'}$	0	0	0	0	0	σ_{n1}^2

Figure 6.12: Raw data power spectral densities for the first block when the frequency is equal to zero showing the contributions for the all blocks in the matrix for all three phase-locking options. Values for some of the blocks are given on the right.

the structure of the matrix as in the time domain as they appear as phase shifts which determines the values in the blocks and not the locations of the correlations in the blocks. Also, the variances determine the values of the power.

6.2.2 Results

Although in the power spectral density matrices the blocks have small sizes of 6×6 which should be possible to solve algebraically the exponential terms occurring in the some of the power spectral densities increases the complexity of the matrix and the increases the computation times. This means that solutions are obtained as was done in the time domain.

An interesting feature in the matrices is the structure of the zero frequency block for the different phase-locking options. These are given in Figure 6.12 where all the exponential terms disappear and their values are all real. The most striking being the block for all locked lasers where all the laser phase noises cancel leaving only the main diagonal which contains only photodetector noises. For example, for zero frequency

Equations 6.36 and 6.37 with for the equal arm lengths become

$$\begin{aligned} S_{ii}(f) &= \sigma_p^2\big[2 - e^0 - e^0\big] + \sigma_{ni}^2 = \sigma_{ni}^2, \\ S_{ij}(f) &= \sigma_p^2\big[2 - e^0 - e^0\big] \qquad\quad = 0, \end{aligned} \tag{6.51}$$

leading to cancellaion of the laser phase noises.

6.2.2.1 The effects of laser phase-locking

In Figure 6.13 the absolute values of the power spectral density matrices for the three phase-locking options are given. The arm lengths are all equal with values of $D = 16.3$ and the noise variances are $\sigma_p^2 = 1000$ and $\sigma_n^2 = 1$ for the laser phase and photdetector noises, respectively. The matrices show the expected differences between the densities of the blocks for the independent and phase-locked lasers. The cancellation of the laser phase noises is seen in the first block ($f = 0$) for all locked lasers. For all the other blocks the values away from the main diagonal are all the same differing from the main diagonal by 1.

The eigenvalues for these matrices are given in Table 6.9 in columns 3 to 8 where they are grouped by blocks with the block numbers given in column 2. As in the time domain the values that are assumed to be due to only photodetector nosies are those that are equal to their values. The results mostly reflect those of the time domain for the corresponding covariance matrices with the phase-locked lasers providing the splitting of the eigenvalues into groups with and without laser noises. However, for the independent lasers the first block differs from the rest of the blocks in that it also produced the two groups of values. Also, the tenth block contains three values of 9 which are close to the photodetector noises and could also be free from laser noise. For the case where all the lasers are locked, the first block which contains only the photodetector noises has eigenvalues that are equal to their values with no further decomposition occurring.

As in the time domain, the number of eigenvalues increased with the number of lasers that are phase-locked. Ignoring the first blocks, the number of laser phase noise free values are 3 and 5 for spacecraft locked and all locked lasers, respectively. Also, note the large separations between the two sets of values with the only exceptions being the tenth blocks of the phase-locked options.

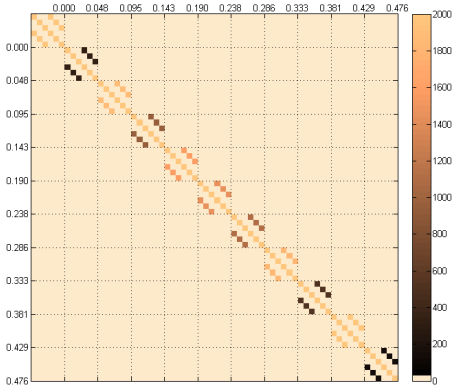

(a)

$S_{0,0}$

2001	0	0	2000	0	0
0	2001	0	0	2000	0
0	0	2001	0	0	2000
2000	0	0	2001	0	0
0	2000	0	0	2001	0
0	0	2000	0	0	2001

$S_{2,2}$

2001	0	0	1893	0	0
0	2001	0	0	1893	0
0	0	2001	0	0	1893
1893	0	0	2001	0	0
0	1893	0	0	2001	0
0	0	1893	0	0	2001

$S_{1,1}$

2001	0	0	328	0	0
0	2001	0	0	328	0
0	0	2001	0	0	328
328	0	0	2001	0	0
0	328	0	0	2001	0
0	0	328	0	0	2001

$S_{3,3}$

2001	0	0	948	0	0
0	2001	0	0	948	0
0	0	2001	0	0	948
948	0	0	2001	0	0
0	948	0	0	2001	0
0	0	948	0	0	2001

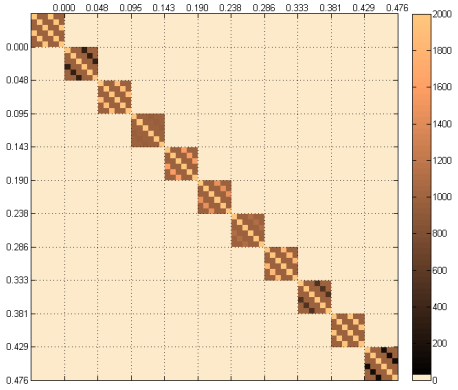

(c)

$S_{0,0}$

2001	1000	1000	2000	1000	1000
1000	2001	1000	1000	2000	1000
1000	1000	2001	1000	1000	2000
2000	1000	1000	2001	1000	1000
1000	2000	1000	1000	2001	1000
1000	1000	2000	1000	1000	2001

$S_{2,2}$

2001	1000	1000	1893	1000	1000
1000	2001	1000	1000	1893	1000
1000	1000	2001	1000	1000	1893
1893	1000	1000	2001	1000	1000
1000	1893	1000	1000	2001	1000
1000	1000	1893	1000	1000	2001

$S_{1,1}$

2001	1000	1000	328	1000	1000
1000	2001	1000	1000	328	1000
1000	1000	2001	1000	1000	328
328	1000	1000	2001	1000	1000
1000	328	1000	1000	2001	1000
1000	1000	328	1000	1000	2001

$S_{3,3}$

2001	1000	1000	948	1000	1000
1000	2001	1000	1000	948	1000
1000	1000	2001	1000	1000	948
948	1000	1000	2001	1000	1000
1000	948	1000	1000	2001	1000
1000	1000	948	1000	1000	2001

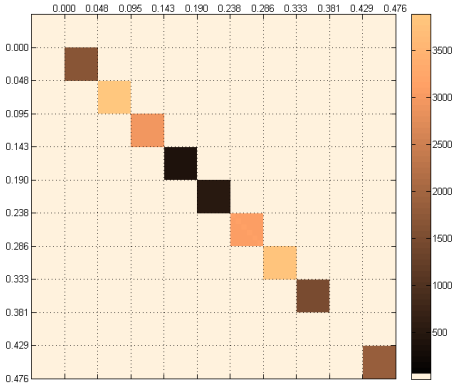

(e)

$S_{0,0}$

1	0	0	0	0	0
0	1	0	0	0	0
0	0	1	0	0	0
0	0	0	1	0	0
0	0	0	0	1	0
0	0	0	0	0	1

$S_{8,8}$

1498	1497	1497	1497	1497	1497
1497	1498	1497	1497	1497	1497
1497	1497	1498	1497	1497	1497
1497	1497	1497	1498	1497	1497
1497	1497	1497	1497	1498	1497
1497	1497	1497	1497	1497	1498

$S_{1,1}$

1673	1672	1672	1672	1672	1672
1672	1673	1672	1672	1672	1672
1672	1672	1673	1672	1672	1672
1672	1672	1672	1673	1672	1672
1672	1672	1672	1672	1673	1672
1672	1672	1672	1672	1672	1673

$S_{9,9}$

9	8	8	8	8	8
8	9	8	8	8	8
8	8	9	8	8	8
8	8	8	9	8	8
8	8	8	8	9	8
8	8	8	8	8	9

$S_{2,2}$

3894	3893	3893	3893	3893	3893
3893	3894	3893	3893	3893	3893
3893	3893	3894	3893	3893	3893
3893	3893	3893	3894	3893	3893
3893	3893	3893	3893	3894	3893
3893	3893	3893	3893	3893	3894

$S_{10,10}$

1852	1851	1851	1851	1851	1851
1851	1852	1851	1851	1851	1851
1851	1851	1852	1851	1851	1851
1851	1851	1851	1852	1851	1851
1851	1851	1851	1851	1852	1851
1851	1851	1851	1851	1851	1852

(f)

Figure 6.13: Sample power spectral density matrices for phase-locking options of (a) none, (c) spacecraft locked and (e) all locked with equal arm lengths of $D = 16.3$. The laser phase and photodetector noise variances are $\sigma_p^2 = 1000$ and $\sigma_n^2 = 1$, respectively. Values for some of the blocks are given on the right.

Table 6.9: Frequency domain eigenvalues for the different phase-locking options with equal of $D = 16.3$ and unequal arm lengths of $D = \{15.3, 16.3, 17.3\}$. The laser phase and photodetector noise variances $\sigma_p^2 = 1000$ and $\sigma_n^2 = 1$, respectively.

Phase-locking	Block	Eigenvalues											
		Equal arms						Unequal arms					
None	1	1	1	1	4001	4001	4001	1	1	1	4001	4001	4001
	2	1673	1673	1673	2329	2329	2329	1106	1673	1733	2270	2329	2896
	3	108	108	108	3894	3894	3894	73	108	0801	3201	3894	3929
	4	1053	1053	1053	2949	2949	2949	33	1053	1215	2787	2949	3969
	5	419	419	419	3583	3583	3583	284	419	1440	2562	3583	3718
	6	535	535	535	3467	3467	3467	535	535	0754	3248	3467	3467
	7	899	899	899	3103	3103	3103	129	619	0899	3103	3383	3874
	8	174	174	174	3828	3828	3828	174	383	1792	2210	3619	3828
	9	1498	1498	1498	2504	2504	2504	316	1053	1498	2504	2949	3686
	10	9	9	9	3993	3993	3993	9	129	0284	3718	3874	3993
	11	1852	1852	1852	2150	2150	2150	1556	1852	1852	2151	2151	2446
Spacecraft	1	1	1	1	1	6001	6001	1	1	1	1	6001	6001
	2	1	1	1	3346	4329	4329	1	1	1	3104	3836	5063
	3	1	1	1	2108	2108	7786	1	1	1	1833	2802	7368
	4	1	1	1	3053	3053	5896	1	1	1	1445	4581	5977
	5	1	1	1	837	5583	5583	1	1	1	1929	3442	6632
	6	1	1	1	1069	5467	5467	1	1	1	2459	2754	6790
	7	1	1	1	2899	2899	6205	1	1	1	1072	5021	5909
	8	1	1	1	2174	2174	7655	1	1	1	1662	3794	6548
	9	1	1	1	2995	4504	4504	1	1	1	2247	3580	6176
	10	1	1	1	17	5993	5993	1	1	1	0278	5703	6022
	11	1	1	1	3702	4150	4150	1	1	1	3556	3917	4530
All	1	1	1	1	1	1	1	1	1	1	1	1	1
	2	1	1	1	1	1	10035	1	1	1	1	1	10093
	3	1	1	1	1	1	23357	1	1	1	1	1	22041
	4	1	1	1	1	1	17687	1	1	1	1	1	16260
	5	1	1	1	1	1	2508	1	1	1	1	1	6525
	6	1	1	1	1	1	3204	1	1	1	1	1	8631
	7	1	1	1	1	1	18612	1	1	1	1	1	13224
	8	1	1	1	1	1	22964	1	1	1	1	1	12001
	9	1	1	1	1	1	8982	1	1	1	1	1	12470
	10	1	1	1	1	1	49	1	1	1	1	1	15196
	11	1	1	1	1	1	11104	1	1	1	1	1	12293

6.2.2.2 The effects of different static arm lengths

This section will also include the directional dependence of the arm lengths as they are modeled using static values giving six different arm lengths. The absolute values of the power spectral density matrices for arm lengths of $D_i = \{15.3, 16.3, 17.3\}$ are given in Figure 6.14 where the matrix with the most changes is the one for all locked lasers. The matrices for the directional values $D_i = \{15.3, 14.3, 17.3, 16.3, 19.3, 18.3\}$ are given in Figure 6.15.

The eigenvalues for the $D_i = \{15.3, 16.3, 17.3\}$ are given in columns 9 to 14 of Table 6.9 where they show the same pattern as for equal arm lengths. Ignoring the first block of the independent lasers, the splitting of the values into the two groups is linked to the phase-locked lasers with large separations between their values. The numbers of laser noise free eigenvalues are the same as for equal arms with 3 and 5 for spacecraft and all locked lasers, respectively. For the independent lasers, as for equal arm lengths, the

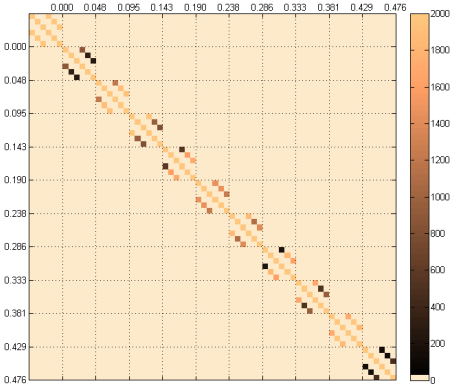

(a)

$S_{0,0}$

2001	0	0	2000	0	0
0	2001	0	0	2000	0
0	0	2001	0	0	2000
2000	0	0	2001	0	0
0	2000	0	0	2001	0
0	0	2000	0	0	2001

$S_{2,2}$

2001	0	0	1200	0	0
0	2001	0	0	1893	0
0	0	2001	0	0	1928
1200	0	0	2001	0	0
0	1893	0	0	2001	0
0	0	1928	0	0	2001

$S_{1,1}$

2001	0	0	895	0	0
0	2001	0	0	328	0
0	0	2001	0	0	268
895	0	0	2001	0	0
0	328	0	0	2001	0
0	0	268	0	0	2001

$S_{3,3}$

2001	0	0	1968	0	0
0	2001	0	0	948	0
0	0	2001	0	0	786
1968	0	0	2001	0	0
0	948	0	0	2001	0
0	0	786	0	0	2001

(b)

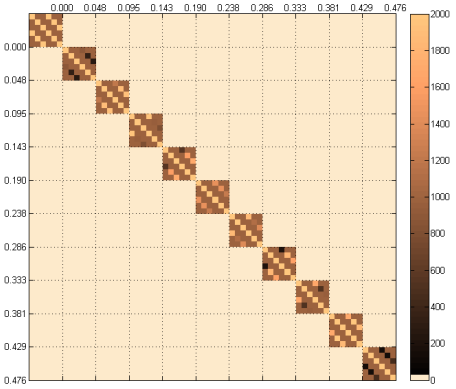

(c)

$S_{0,0}$

2001	1000	1000	2000	1000	1000
1000	2001	1000	1000	2000	1000
1000	1000	2001	1000	1000	2000
2000	1000	1000	2001	1000	1000
1000	2000	1000	1000	2001	1000
1000	1000	2000	1000	1000	2001

$S_{2,2}$

2001	1000	1000	1200	1000	1000
1000	2001	1000	1000	1893	1000
1000	1000	2001	1000	1000	1928
1200	1000	1000	2001	1000	1000
1000	1893	1000	1000	2001	1000
1000	1000	1928	1000	1000	2001

$S_{1,1}$

2001	1000	1000	895	1000	1000
1000	2001	1000	1000	328	1000
1000	1000	2001	1000	1000	268
895	1000	1000	2001	1000	1000
1000	328	1000	1000	2001	1000
1000	1000	268	1000	1000	2001

$S_{3,3}$

2001	1000	1000	1968	1000	1000
1000	2001	1000	1000	948	1000
1000	1000	2001	1000	1000	786
1968	1000	1000	2001	1000	1000
1000	948	1000	1000	2001	1000
1000	1000	786	1000	1000	2001

(d)

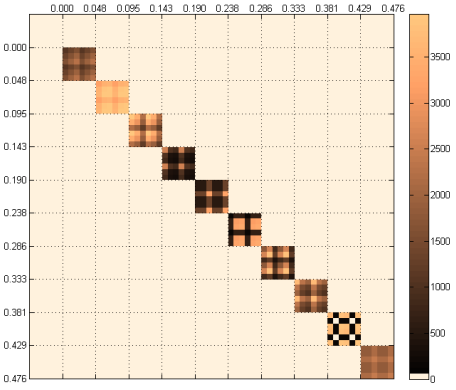

(e)

$S_{0,0}$

1	0	0	0	0	0
0	1	0	0	0	0
0	0	1	0	0	0
0	0	0	1	0	0
0	0	0	0	1	0
0	0	0	0	0	1

$S_{8,8}$

3686	2349	1969	3685	2349	1969
2349	1498	1255	2349	1497	1255
1969	1255	1053	1969	1255	1052
3685	2349	1969	3686	2349	1969
2349	1497	1255	2349	1498	1255
1969	1255	1052	1969	1255	1053

$S_{1,1}$

1106	1360	1584	1105	1360	1584
1360	1673	1948	1360	1672	1948
1584	1948	2269	1584	1948	2268
1105	1360	1584	1106	1360	1584
1360	1672	1948	1360	1673	1948
1584	1948	2268	1584	1948	2269

$S_{9,9}$

3718	173	3794	3717	173	3794
173	9	177	173	8	177
3794	177	3873	3794	177	3872
3717	173	3794	3718	173	3794
173	8	177	173	9	177
3794	177	3872	3794	177	3873

$S_{2,2}$

3201	3529	3545	3200	3529	3545
3529	3894	3910	3529	3893	3910
3545	3910	3929	3545	3910	3928
3200	3529	3545	3201	3529	3545
3529	3893	3910	3529	3894	3910
3545	3910	3928	3545	3910	3929

$S_{10,10}$

1852	1851	2127	1851	1851	2127
1851	1852	2127	1851	1851	2127
2127	2127	2446	2127	2127	2445
1851	1851	2127	1852	1851	2127
1851	1851	2127	1851	1852	2127
2127	2127	2445	2127	2127	2446

(f)

Figure 6.14: Sample power spectral density matrices for unequal arm lengths of $D = \{15.3, 16.3, 17.3\}$ for phase-locking options of (a) none, (c) spacecraft locked and (e) all locked. The laser noise and photodetector noise variances are $\sigma_p^2 = 1000$ and $\sigma_n^2 = 1$, respectively.

Table 6.10: Frequency domain eigenvalues for directionally dependent arm lengths with values of $D = \{15.3, 14.3, 17.3, 16.3, 19.3, 18.3\}$ for lasers that are (a) independent, (c) spacecraft locked and (e) all locked. The laser phase and photodetector noise variances are $\sigma_p^2 = 1000$ and $\sigma_n^2 = 1$, respectively.

Phase-locking	Block	Eigenvalues					
None	1	1	1	1	4001	4001	4001
	2	419	1383	1440	2562	2619	3583
	3	316	383	1498	2504	3619	3686
	4	383	495	1215	2787	3507	3619
	5	254	1160	1383	2619	2842	3748
	6	1	23	23	3979	3979	4001
	7	619	1383	1733	2269	2619	3383
	8	174	383	1792	2210	3619	3828
	9	383	708	950	3052	3294	3619
	10	129	899	1383	2619	3103	3873
	11	1	90	90	3912	3912	4001
Spacecraft	1	1	1	1	1	6001	6001
	2	1	1	1	2393	3682	5928
	3	1	1	1	1473	4306	6224
	4	1	1	1	1581	4157	6265
	5	1	1	1	1919	4099	5985
	6	1	1	1	1091	3118	7795
	7	1	1	1	2382	4178	5442
	8	1	1	1	1662	3793	6548
	9	1	1	1	2221	3154	6629
	10	1	1	1	1600	4319	6084
	11	1	1	1	793	3711	7499
All	1	1	1	1	1	1	1
	2	1	1	1	1	1	8759
	3	1	1	1	1	1	17353
	4	1	1	1	1	1	13619
	5	1	1	1	1	1	12477
	6	1	1	1	1	1	14868
	7	1	1	1	1	1	12619
	8	1	1	1	1	1	12001
	9	1	1	1	1	1	13360
	10	1	1	1	1	1	11383
	11	1	1	1	1	1	11131

first block differs from the rest producing the two groups of eigenvalues. Also, the tenth block the low value of 9 still appears but only once.

The eigenvalues for the directionally dependent arm lengths are given in Table 6.10. Again the results are similar to those of the previous case with the space-craft locked lasers being the ones that, in general, produced the two groups of eigenvalues with large separations between their values. The numbers of the laser noise free values are the same being 3 and 5 for spacecraft and all locked laser, respectively. For the independent the first block is still the exception for that option but now there are other 1's occurring in blocks 6 and 11. Also, in these two blocks there are values of 23 and 90 which again could be associated with photodetectors noises.

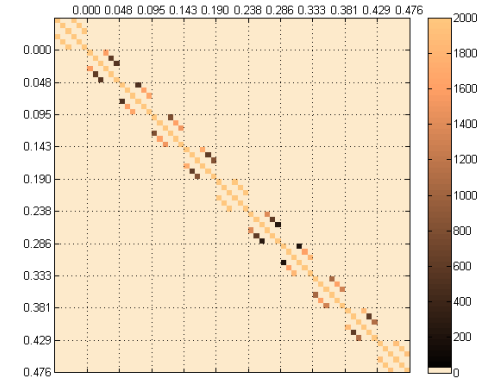

(a)

$S_{0,0}$

2001	0	0	2000	0	0
0	2001	0	0	2000	0
0	0	2001	0	0	2000
2000	0	0	2001	0	0
0	2000	0	0	2001	0
0	0	2000	0	0	2001

$S_{2,2}$

2001	0	0	1872	0	0
0	2001	0	0	618	0
0	0	2001	0	0	1102
1872	0	0	2001	0	0
0	618	0	0	2001	0
0	0	1102	0	0	2001

$S_{1,1}$

2001	0	0	1582	0	0
0	2001	0	0	618	0
0	0	2001	0	0	561
1582	0	0	2001	0	0
0	618	0	0	2001	0
0	0	561	0	0	2001

$S_{3,3}$

2001	0	0	1911	0	0
0	2001	0	0	2000	0
0	0	2001	0	0	1911
1911	0	0	2001	0	0
0	2000	0	0	2001	0
0	0	1911	0	0	2001

(b)

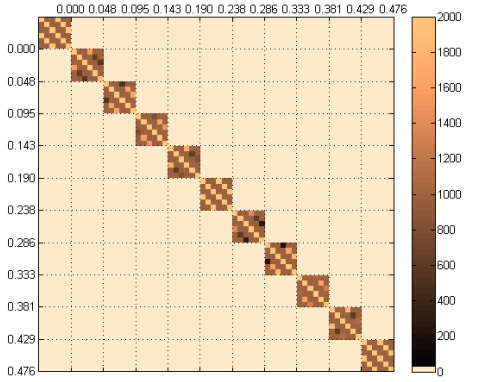

(c)

$S_{0,0}$

2001	1000	1000	2000	1000	1000
1000	2001	1000	1000	2000	1000
1000	1000	2001	1000	1000	2000
2000	1000	1000	2001	1000	1000
1000	2000	1000	1000	2001	1000
1000	1000	2000	1000	1000	2001

$S_{2,2}$

2001	1000	1000	1582	1000	1000
1000	2001	1000	1000	618	1000
1000	1000	2001	1000	1000	561
1582	1000	1000	2001	1000	1000
1000	618	1000	1000	2001	1000
1000	1000	561	1000	1000	2001

$S_{1,1}$

2001	1000	1000	1872	1000	1000
1000	2001	1000	1000	618	1000
1000	1000	2001	1000	1000	1102
1872	1000	1000	2001	1000	1000
1000	618	1000	1000	2001	1000
1000	1000	1102	1000	1000	2001

$S_{3,3}$

2001	1000	1000	1911	1000	1000
1000	2001	1000	1000	2000	1000
1000	1000	2001	1000	1000	1911
1911	1000	1000	2001	1000	1000
1000	2000	1000	1000	2001	1000
1000	1000	1911	1000	1000	2001

(d)

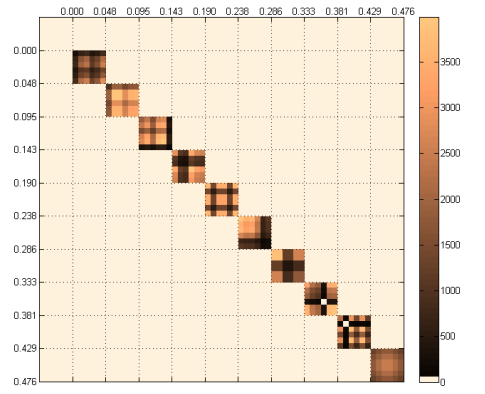

(e)

$S_{0,0}$

1	0	0	0	0	0
0	1	0	0	0	0
0	0	1	0	0	0
0	0	0	1	0	0
0	0	0	0	1	0
0	0	0	0	0	1

$S_{9,9}$

3201	2188	1835	321	3434	3529
2188	1498	1255	219	2349	2414
1835	1255	1053	184	1969	2024
321	219	184	33	344	354
3434	2349	1969	344	3686	3788
3529	2414	2024	354	3788	3894

$S_{1,1}$

254	651	758	396	529	848
651	1673	1948	1017	1360	2180
758	1948	2269	1184	1584	2539
396	1017	1184	619	826	1325
529	1360	1584	826	1106	1772
848	2180	2539	1325	1772	2842

$S_{10,10}$

2269	135	2964	1427	2904	1184
135	9	177	85	173	71
2964	177	3873	1865	3794	1547
1427	85	1865	899	1827	745
2904	173	3794	1827	3718	1515
1184	71	1547	745	1515	619

$S_{1,1}$

950	1922	1930	1408	1742	1767
1922	3894	3910	2852	3529	3580
1930	3910	3929	2865	3545	3597
1408	2852	2865	2091	2586	2623
1742	3529	3545	2586	3201	3246
1767	3580	3597	2623	3246	3294

$S_{10,10}$

1270	1533	1762	1762	1533	1269
1533	1852	2127	2127	1851	1533
1762	2127	2446	2445	2127	1762
1762	2127	2445	2446	2127	1762
1533	1851	2127	2127	1852	1533
1269	1533	1762	1762	1533	1270

(f)

Figure 6.15: Sample power spectral density matrices for directionally dependent arm lengths with values of $D = \{15.3, 14.3, 17.3, 16.3, 19.3, 18.3\}$. The laser phase and photodetector noise variances are $\sigma_p^2 = 1000$ and $\sigma_n^2 = 1$, respectively.

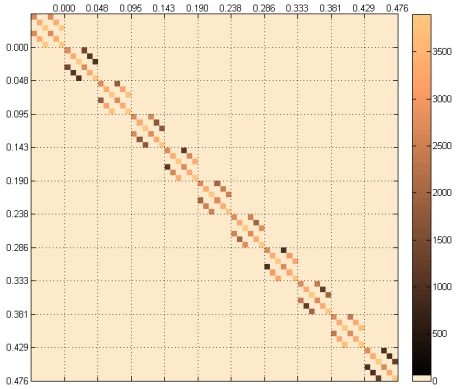

(a)

$S_{0,0}$

2701	0	0	2700	0	0
0	3301	0	0	3300	0
0	0	3901	0	0	3900
2700	0	0	2701	0	0
0	3300	0	0	3301	0
0	0	3900	0	0	3901

$S_{2,2}$

2701	0	0	1772	0	0
0	3301	0	0	3136	0
0	0	3901	0	0	3767
1772	0	0	2701	0	0
0	3136	0	0	3301	0
0	0	3767	0	0	3901

$S_{1,1}$

2701	0	0	1451	0	0
0	3301	0	0	1039	0
0	0	3901	0	0	1034
1451	0	0	2701	0	0
0	1039	0	0	3301	0
0	0	1034	0	0	3901

$S_{3,3}$

2701	0	0	2661	0	0
0	3301	0	0	1753	0
0	0	3901	0	0	1742
2661	0	0	2701	0	0
0	1753	0	0	3301	0
0	0	1742	0	0	3901

(b)

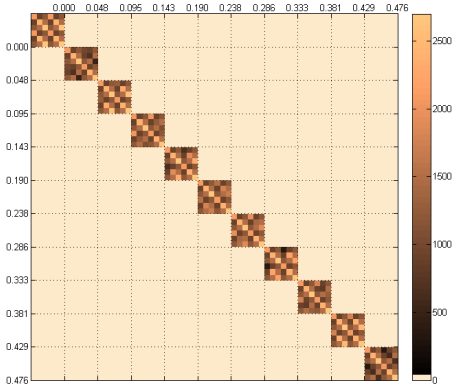

(c)

$S_{0,0}$

2101	900	1200	2100	900	1200
900	2401	1500	900	2400	1500
1200	1500	2701	1200	1500	2700
2100	900	1200	2101	900	1200
900	2400	1500	900	2401	1500
1200	1500	2700	1200	1500	2701

$S_{2,2}$

2101	900	1200	1282	900	1200
900	2401	1500	900	2279	1500
1200	1500	2701	1200	1500	2604
1282	900	1200	2101	900	1200
900	2279	1500	900	2401	1500
1200	1500	2604	1200	1500	2701

$S_{1,1}$

2101	900	1200	977	900	1200
900	2401	1500	900	711	1500
1200	1500	2701	1200	1500	469
977	900	1200	2101	900	1200
900	711	1500	900	2401	1500
1200	1500	469	1200	1500	2701

$S_{3,3}$

2101	900	1200	2067	900	1200
900	2401	1500	900	1254	1500
1200	1500	2701	1200	1500	1096
2067	900	1200	2101	900	1200
900	1254	1500	900	2401	1500
1200	1500	1096	1200	1500	2701

(d)

Figure 6.16: Sample power spectral density matrices for different laser noise variances of $\sigma_p^2 = \{900, 1200, 1500, 1800, 2100, 2400\}$ for independent lasers and $\sigma_p^2 = \{900, 1500, 2100\}$ for spacecraft locked lasers. The photodetector noise variances is $\sigma_n^2 = 1$ and the arm lengths are $D = \{15.3, 16.3, 17.3\}$.

6.2.2.3 The effects of the noise variances

In this section the results for the effects of different values for the noise variances and of small separations between the two noise types are given. For the case of different variances this was done for each noise type separately. The variances used for the laser phase noises were $\sigma_{pi}^2 = \{900, 1200, 1500, 1800, 2100, 24000\}$ for no phase-locking and $\sigma_{pi}^2 = \{900, 1500, 21000\}$ for spacecraft locked lasers with $\sigma_n^2 = 1$. For different photodetector noises the values used were $\sigma_{ni}^2 = \{1, 2, 3, 4, 5, 6\}$ with the laser phase noise variance with the same values of $\sigma_p^2 = 1000$. The offsets used were $D_i = \{15.3, 16.3, 17.3\}$.

Table 6.11: Frequency domain eigenvalues for different laser phase and photodetector noise variances. In columns 2-7 the laser phase noises are $\sigma_p^2 = \{900, 1200, 1500, 1800, 2100, 2400\}$ for independent lasers and $\sigma_p^2 = \{900, 1500, 2100\}$ for spacecraft locked lasers. In both cases the photodetector noise variances are kept constant with values of $\sigma_n^2 = 1$. In columns 8-13 the photodetector noises are $\sigma_n^2 = \{1, 2, 3, 4, 5, 6\}$ and laser phase noise variances are kept constant with values of $\sigma_p^2 = 1000$.

Phase-locking	Block	Eigenvalues											
		Different laser variances						Different photodetector variances					
None	1	1	1	1	5401	6601	7801	2	3	4	4003	4004	4005
	2	1250	2262	2867	4152	4341	4935	1108	1676	1736	2273	2331	2897
	3	134	165	929	4473	6437	7668	77	111	803	3202	3896	3932
	4	40	1548	2159	5054	5363	5643	35	1056	1218	2791	2951	3970
	5	521	633	1552	3850	5969	7281	288	421	1442	2563	3586	3721
	6	629	806	1370	4773	5796	6432	536	537	758	3251	3469	3470
	7	154	1129	1334	5249	5268	6674	130	622	902	3105	3387	3875
	8	264	702	1763	3640	6338	7100	176	386	1793	2212	3623	3831
	9	375	1890	2098	4504	5027	5912	317	1057	1500	2507	2952	3688
	10	13	236	338	5064	6589	7566	12	132	286	3719	3877	3995
	11	1781	2370	2667	3621	4232	5135	1559	1853	1854	2152	2153	2450
Spacecraft	1	1	1	1	1	6162	8240	2	3	4	5	6003	6004
	2	1	1	1	3085	5050	6268	2	3	5	3107	3839	5065
	3	1	1	1	2232	2992	9179	3	3	5	1835	2804	7371
	4	1	1	1	1554	6228	6622	2	4	4	1448	4584	5979
	5	1	1	1	2346	3590	8467	2	4	5	1931	3445	6635
	6	1	1	1	2451	3670	8283	2	3	5	2462	2756	6792
	7	1	1	1	1198	5850	7355	2	4	4	1075	5024	5912
	8	1	1	1	1969	4052	8383	3	3	5	1664	3796	6550
	9	1	1	1	2328	4667	7408	2	3	5	2250	3582	6178
	10	1	1	1	320	5933	8150	2	4	5	280	5705	6025
	11	1	1	1	3577	4561	6266	2	4	5	3559	3919	4533
All	1							1	2	3	4	5	6
	2							1	2	4	4	6	10096
	3							1	2	4	5	6	22044
	4							1	3	3	5	6	16262
	5							2	3	3	5	6	6526
	6							1	2	4	5	5	8634
	7							1	2	4	4	6	13227
	8							1	3	3	4	6	12003
	9							2	2	3	5	6	12472
	10							2	2	4	5	5	15198
	11							1	2	4	5	6	12296

The effects of different noise variances

The matrices for the different laser phase noises for the two phase-locking cases are given in Figure 6.16 and those for the different photodetector noises are in Figure 6.17. The eigenvalues for the matrices are given in Table 6.11. For both sets, the results are the same as in the previous sections where the independent lasers did not produce the two groups of values except for the first block. Also, for the spacecraft locked lasers, the number of laser noise free eigenvalues is 3 for all blocks except the first with large separations between their values and those with laser phase noises. For the case with different photodetector noise variances the laser noise free eigenvalues reflect the different values but not all are present for each block.

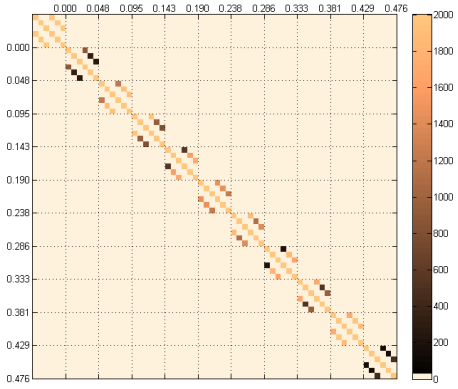

(a)

$S_{0,0}$

2001	0	0	2000	0	0
0	2002	0	0	2000	0
0	0	2003	0	0	2000
2000	0	0	2004	0	0
0	2000	0	0	2005	0
0	0	2000	0	0	2006

$S_{10,10}$

2001	0	0	1717	0	0
0	2002	0	0	1992	0
0	0	2003	0	0	1872
1717	0	0	2004	0	0
0	1992	0	0	2005	0
0	0	1872	0	0	2006

$S_{1,1}$

2001	0	0	895	0	0
0	2002	0	0	328	0
0	0	2003	0	0	268
895	0	0	2004	0	0
0	328	0	0	2005	0
0	0	268	0	0	2006

$S_{11,11}$

2001	0	0	149	0	0
0	2002	0	0	149	0
0	0	2003	0	0	445
149	0	0	2004	0	0
0	149	0	0	2005	0
0	0	445	0	0	2006

(b)

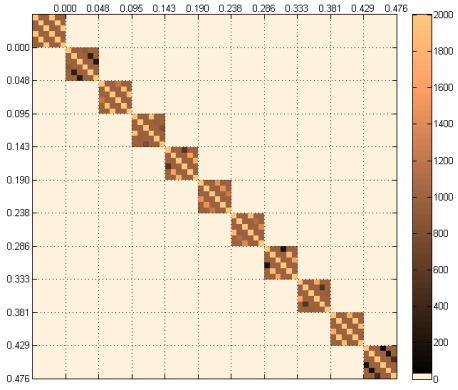

(c)

$S_{0,0}$

2001	1000	1000	2000	1000	1000
1000	2002	1000	1000	2000	1000
1000	1000	2003	1000	1000	2000
2000	1000	1000	2004	1000	1000
1000	2000	1000	1000	2005	1000
1000	1000	2000	1000	1000	2006

$S_{10,10}$

2001	1000	1000	1717	1000	1000
1000	2002	1000	1000	1992	1000
1000	1000	2003	1000	1000	1872
1717	1000	1000	2004	1000	1000
1000	1992	1000	1000	2005	1000
1000	1000	1872	1000	1000	2006

$S_{1,1}$

2001	1000	1000	895	1000	1000
1000	2002	1000	1000	328	1000
1000	1000	2003	1000	1000	268
895	1000	1000	2004	1000	1000
1000	328	1000	1000	2005	1000
1000	1000	268	1000	1000	2006

$S_{11,11}$

2001	1000	1000	149	1000	1000
1000	2002	1000	1000	149	1000
1000	1000	2003	1000	1000	445
149	1000	1000	2004	1000	1000
1000	149	1000	1000	2005	1000
1000	1000	445	1000	1000	2006

(d)

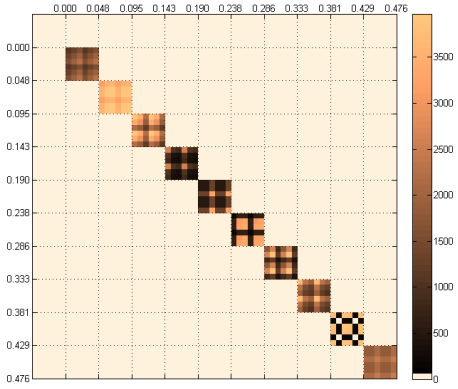

(e)

$S_{0,0}$

1	0	0	0	0	0
0	2	0	0	0	0
0	0	3	0	0	0
0	0	0	4	0	0
0	0	0	0	5	0
0	0	0	0	0	6

$S_{9,9}$

3686	2349	1969	3685	2349	1969
2349	1499	1255	2349	1497	1255
1969	1255	1055	1969	1255	1052
3685	2349	1969	3689	2349	1969
2349	1497	1255	2349	1502	1255
1969	1255	1052	1969	1255	1058

$S_{1,1}$

1106	1360	1584	1105	1360	1584
1360	1674	1948	1360	1672	1948
1584	1948	2271	1584	1948	2268
1105	1360	1584	1109	1360	1584
1360	1672	1948	1360	1677	1948
1584	1948	2268	1584	1948	2274

$S_{10,10}$

3718	173	3794	3717	173	3794
173	10	177	173	8	177
3794	177	3875	3794	177	3872
3717	173	3794	3721	173	3794
173	8	177	173	13	177
3794	177	3872	3794	177	3878

$S_{2,2}$

3201	3529	3545	3200	3529	3545
3529	3895	3910	3529	3893	3910
3545	3910	3931	3545	3910	3928
3200	3529	3545	3204	3529	3545
3529	3893	3910	3529	3898	3910
3545	3910	3928	3545	3910	3934

$S_{11,11}$

1852	1851	2127	1851	1851	2127
1851	1853	2127	1851	1851	2127
2127	2127	2448	2127	2127	2445
1851	1851	2127	1855	1851	2127
1851	1851	2127	1851	1856	2127
2127	2127	2445	2127	2127	2451

(f)

Figure 6.17: Sample power spectral density matrices for different photodetector noise variances of $\sigma_n^2 = \{1, 2, 3, 4, 5, 6\}$ with laser phase noises of $\sigma_p^2 = 1000$ for lasers that are (a) independent, (c) phase-locked on each spacecraft and (e) all locked. The arm lengths used are $D = \{15.3, 16.3, 17.3\}$.

The effects of small separation between the laser phase and photodetector noise variances

As in the time domain the laser phase noise variances were reduced to values that were close to the photodetector noises variances. Five combinations of variances were used which are given in Table 6.12 along with the eigenvalues for 11 blocks. The power spectral density matrix given in Figure 6.18 is the only one presented which corresponds to the first set of variances in the table where the laser phase variances are $\sigma_p^2 = 9$ and the photodetector noises variances are $\sigma_n^2 = 1$. As in the previous cases the assumption here is that the eigenvalues with same values as the photodetector noise variances will be the ones that are assumed to be free from laser phase noise. The other eigenvalues that are not equal to these are ignored especially because of the closeness in two types of variances.

For the first set in Table 6.12 the variances are $\sigma_n^2 = 1$ and $\sigma_p^2 = 9$ where the closeness of the values does not affect the separation into the two groups which are still be easily distinguished because of the reasonable differences between the two sets of eigenvalues. Even when there is only a difference of 1 between the two noise variances which is the second set of values in Table 6.12 the two groups of eigenvalues are still obvious even though there has been a large drop on the differences between their values. The same is true for the other three sets with separations between smallest laser phase noise variance and the largest photodetector noise variances being difference of only 0.5 and 0.2. The Fourier transform sums all the values in the time series and this produces larger separations in their values in the spectra.

6.3 Summary

In this section the aim was to determine how certain properties of LISA relating to its noise covariance and power spectral density matrices affect the nature if the eigenvalues. We were interested in finding out what would prevent the eigenvalues from splitting into the two distinct groups related to those with and without laser phase noises. The properties that were investigated are the phase-locking of the lasers, the arm lengths and the variances of laser phase and photodetector noises. This was done in the time and frequency domains which included summaries of the effects these properties on the

Table 6.12: Frequency domain eigenvalues for small separations between the laser phase and photodetector noise variances with the lasers locked on each spacecraft and with arm lengths of $D = \{15.3, 16.3, 17.3\}$.

Set	Noise Variance	Block	Eigenvalues					
1	$\sigma_n^2 = 1$, $\sigma_p^2 = 9$	1	1	1	1	1	55	55
		2	1	1	1	29	36	47
		3	1	1	1	18	26	67
		4	1	1	1	14	42	55
		5	1	1	1	18	32	61
		6	1	1	1	23	26	62
		7	1	1	1	11	46	54
		8	1	1	1	16	35	60
		9	1	1	1	21	33	57
		10	1	1	1	3	52	55
		11	1	1	1	33	36	42
2	$\sigma_n^2 = 1$, $\sigma_p^2 = 2$	1	1	1	1	1	13	13
		2	1	1	1	7	9	11
		3	1	1	1	5	7	16
		4	1	1	1	4	10	13
		5	1	1	1	5	8	14
		6	1	1	1	6	7	15
		7	1	1	1	3	11	13
		8	1	1	1	4	9	14
		9	1	1	1	5	8	13
		10	1	1	1	2	12	13
		11	1	1	1	8	9	10
3	$\sigma_n^2 = 1.0$, $\sigma_p^2 = 1.5$	1	1.0	1.0	1.0	1.0	10.0	10.0
		2	1.0	1.0	1.0	5.7	6.8	8.6
		3	1.0	1.0	1.0	3.8	5.2	12.1
		4	1.0	1.0	1.0	3.2	7.9	10.0
		5	1.0	1.0	1.0	3.9	6.2	11.0
		6	1.0	1.0	1.0	4.7	5.1	11.2
		7	1.0	1.0	1.0	2.6	8.5	9.9
		8	1.0	1.0	1.0	3.5	6.7	10.8
		9	1.0	1.0	1.0	4.4	6.4	10.3
		10	1.0	1.0	1.0	1.4	9.6	10.0
		11	1.0	1.0	1.0	6.3	6.9	7.8
4	$\sigma_{ni}^2 = \{0.8, 0.9, 1.0, 1.1, 1.2, 1.3\}$, $\sigma_p^2 = 1.5$	1	0.9	1.0	1.1	1.2	10.0	10.1
		2	0.9	1.0	1.2	5.7	6.8	8.6
		3	1.0	1.0	1.2	3.8	5.3	12.1
		4	0.9	1.1	1.1	3.3	8.0	10.0
		5	0.9	1.1	1.2	3.9	6.2	11.0
		6	0.9	1.0	1.2	4.7	5.2	11.2
		7	0.9	1.1	1.1	2.7	8.6	9.9
		8	1.0	1.0	1.2	3.5	6.7	10.9
		9	0.9	1.0	1.2	4.4	6.5	10.3
		10	0.9	1.1	1.2	1.5	9.6	10.1
		11	0.9	1.1	1.2	6.4	6.9	7.9
5	$\sigma_{ni}^2 = \{0.8, 0.9, 1.0, 1.1, 1.2, 1.3\}$, $\sigma_{pi}^2 = \{1.5, 1.6, 1.7\}$	1	0.9	1.0	1.1	1.2	10.2	11.1
		2	0.9	1.0	1.2	5.8	7.5	9.0
		3	1.0	1.0	1.2	4.0	5.4	12.9
		4	0.9	1.1	1.1	3.4	8.8	10.3
		5	0.9	1.1	1.2	4.1	6.4	11.8
		6	0.9	1.0	1.2	4.8	5.6	11.9
		7	0.9	1.1	1.1	2.8	9.3	10.3
		8	1.0	1.0	1.2	3.7	6.9	11.7
		9	0.9	1.0	1.2	4.6	7.0	10.8
		10	0.9	1.1	1.2	1.5	9.9	11.0
		11	0.9	1.1	1.2	6.8	7.0	8.5

respective covariance and power spectral density matrices.

The overall results were that in both domains the property that had the major effect

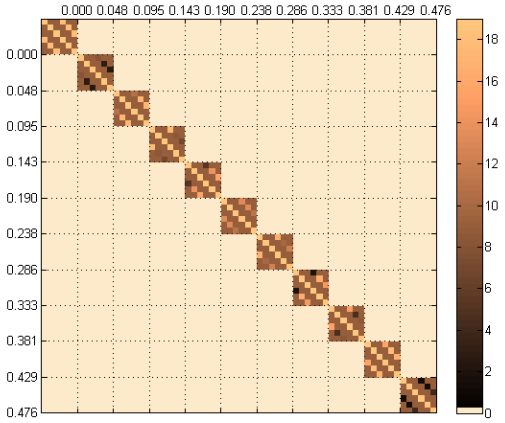

(a)

$S_{0,0}$

19	9	9	18	9	9	19	9	9	15	9	9
9	19	9	9	18	9	9	19	9	9	4	9
9	9	19	9	9	18	9	9	19	9	9	9
18	9	9	19	9	9	15	9	9	19	9	9
9	18	9	9	19	9	9	4	9	9	19	9
9	9	18	9	9	19	9	9	9	9	9	19

$S_{9,9}$

$S_{1,1}$

19	9	9	8	9	9	19	9	9	15	9	9
9	19	9	9	3	9	9	19	9	9	18	9
9	9	19	9	9	2	9	9	19	9	9	17
8	9	9	19	9	9	15	9	9	19	9	9
9	3	9	9	19	9	9	18	9	9	19	9
9	9	2	9	9	19	9	9	17	9	9	19

$S_{10,10}$

$S_{2,2}$

19	9	9	11	9	9	19	9	9	1	9	9
9	19	9	9	17	9	9	19	9	9	1	9
9	9	19	9	9	17	9	9	19	9	9	4
11	9	9	19	9	9	1	9	9	19	9	9
9	17	9	9	19	9	9	1	9	9	19	9
9	9	17	9	9	19	9	9	4	9	9	19

$S_{11,11}$

(b)

Figure 6.18: Sample power spectral density matrix for laser phase and photodetector noise variances of $\sigma_p^2 = 9$ and $\sigma_n^2 = 1$respectively. The arm lengths are $D = \{15.3, 16.3, 17.3\}$ with the lasers phase-locked on each spacecraft. The values shown on the right are for some of the blocks of the matrix.

on the splitting of the eiegenvalues into the two distinct groups was the phase-locking of the lasers. When the lasers were all independent (no phase-locking) no laser phase noise free eigenvalues were obtained. The other properties were mostly tested with the three phase-locking options and the results did not change for the independent lasers, that is, the other properties did not override this result. For the noise variances, having different and real values just led to the eigenvalues reflecting these values which was also true for time varying variances. When the laser phase and photodetector noise variances had values that were close the two groups were still produced but being able to distinguish between them depended on how close their values were. In general it easier to do this in the frequency domain. More detailed summary of the results for each domain are given in the following sections.

6.3.1 Time domain

The structure of time domain covariance matrix in terms of the locations of its values is determined by the type of laser phase-locking and by the arm lengths. The phase-locking determines the number of correlations that occur between the optical benches therefore, defined the density of the blocks while the arm lengths determine the location

Table 6.13: Summary of the laser noise free eigenvalues in the time domain for the matrices with time values of $t = \{0, ..., 23\}$.

Property	Option	Number of eigenvalues		
		None	Spacecraft	All
Arm lengths	Equal	0	40	120
	Unequal	0	28	104
	Directional	0	20	102
	Time varying	0	18	102
Variances	Unequal laser	0	29	-
	Unequal photodetector	0	29	104
	Variable (both)	-	29	-

of the blocks within the matrix. The values of the entries are determined by the noise variances.

It was discovered that the property prevented the splitting of the eigenvalues into the two groups was the absence laser phase-locking, that is the covariance matrices for independent lasers did not produce any laser noise free eigenvalues. The behaviour/nature of the arm lengths and noise variance did not override this result. A summary of the eigenvalues for the different options investigated is given in Table 6.13. With phase-locking the number of these values increased with the number of locked lasers but they decreased with the increase in the number of different values for the arm lengths.

6.3.2 Frequency domain

In the toy model there are no correlations between the different frequencies and the power spectral density matrices are all block diagonals. As in the time domain the laser phase-locking determines the number of correlations between the optical benches readings which is reflected in the structure of the individual blocks. It is also the property that determines the location of the correlations within each block. The arm lengths appear as phase shifts in the power spectra therefore contribute in the blocks along with the noise variances. The contributions to each frequency in the spectra is the sum of the time domain values therefore, the time varying arm lengths and variances do not have the same effects on the power spectral density matrix as they do in the covariance matrix.

In general the results reflect those of the time domain in terms of what prevents the splitting in to the two groups of eigenvalues but with a few quirks. The property that prevented the splitting in to the two groups is the absence of phase-locking. However,

Table 6.14: Summary of the eigenvalues in the frequency domain for the different options.

Case	Block Number	Number of eigenvalues None	Spacecraft	All
Generally	1	3	4	6
	2 - 11	0	3	5
For directionally dependent arms	1	3	4	6
	2-5,7-10	0	3	5
	6, 11	1	3	5

note that the first blocks of the matrices where the frequency is zero have slightly different properties than the other blocks. So the absence of laser noise free eigenvalues for the power spectral density matrices with independent lasers excludes the first block. As in the time domain the nature of the variances did not override the results for independent lasers nor did change the number of eigenvalues. The arm lengths mostly followed this pattern however, with the directionally dependent values there were a few laser noise free eigenvalues appearing in two of the blocks for the non zero frequencies. Also the number of laser noise free eigenvalues seem to be defined by the phase-locking where they were greater for all locked lasers. A summary of the eigenvalues is given in Table 6.14 where they are all grouped since the numbers did not change for the different properties with the exception of the directionally dependent arm lengths which is shown separately.

Chapter 7

Conclusions

Space-based laser interferometer gravitational detectors will allow observations below 1 Hz which is out of the range of ground-based systems due to limitations caused by gravity gradient noises and restrictions on the physical arm lengths. LISA was the original NASA-ESA design for a space-based detector consisting of three satellites that maintain a nearly equilateral triangle formation with sides of 5×10^9 m as they orbit the Sun in a location that is about 20° behind the Earth. The time varying unequal arm lengths coupled with the significant travel times between the spacecraft prevents the cancellation of the overwhelming laser phase noises by the methods used in ground-based interferometers. This was resolved with the time delay interferometry observables which are linear combinations of the raw data with appropriate time offsets that result in their cancellation. The conventional way of doing LISA analysis is through these observables which have to be generated before any weak signal extraction can be performed. However, another way of obtaining the sensitivity for the data was presented by Romano and Woan that allowed it to be accomplished during signal extraction which was achieved by performing a principal component analysis of the raw data. They illustrated how this provided two distinct groups of eigenvalues that were distinguished by the absence of laser phase noises in one set, the target group, which could be used to factorise the likelihood function used in the Bayesian inference. Their investigations were done in the time domain using a small covariance matrix with integer values for times, arm lengths and noise variances.

In this thesis we implemented the principal component approach using a toy model of LISA based on a static rigid array with unequal integer arm lengths and with data consisting of a simple sinusoidal signal, laser phase noises and photodetector noises. The analysis was done in the time and frequency domains and, for comparing of the results, we also performed the analysis using the conventional approach with the frequency domain optimal AET observables. The principal components are obtained from the noise (data) covariance and power spectral matrices therefore, in testing how this

method handled real LISA data we focused on the properties of LISA that affect them including the laser phase-locking, arm lengths and noise variances. We were interested in how the method adapted to time varying arms as this proved to be the breaking point of some of the traditional time delay interferometry observables. We were also interested in what could prevent the occurrence of the laser noise free eigenvalues as this is necessary for the success of this method. Romano and Woan found that it was possible to use the eigenvectors of the principal components to generate one of the time delay interferometry observables suggesting a connection between them therefore this was also investigated.

For testing the connection between the principal components and the TDIs we used a small covariance matrix in order to obtain exact solutions using algebraic methods. From this we were able to generate the four Sagnac observables for different times from the time domain eigenvectors and also the AET observables from the frequency domain eigenvectors which indicates that this method is just another way of obtaining the time delay interferometry observables. The difference is that the observables generated in this manner are tied to the length of the data and are not general expressions like the traditional observables, for example, Sagnac $\alpha(7)$ and $\alpha(8)$ were generated from different sets of eigenvectors. Also, multiple eigenvalues that are free from laser phase noises are produced with this method which means that it allows the simultaneous generation of many time delay interferometry observables.

The property that prevented the generation of the eigenvalues that were free from laser phase noises was the absence of phase-locking. This was also true for the frequency domain but with some exceptions with the zero bin. For the separation between the values of the variances of the two noises this was reduced to 0.2 and this did not prevent the two distinct groups but it was more difficult to distinguish between them. However, the reason for the time delay interferometry observables is the size of the laser phase noises which result in the weak signals being overwhelmed, therefore, if the values are reduced to the levels of the secondary noises which are close to the signals this is no longer an issue and their cancellation would no longer be required. In terms of the time varying arm lengths, this did not affect this method in the same way that it does the traditional time delay interferometry observables. In this method the variations will appear in the covariance matrix and from our toy model investigations this did not

prevent the occurrence of the eigenvalues with no laser phase noises.

For the signal detection we performed an amplitude search for a simple sinusoidal gravitational wave and obtained the same accuracy and precision as that acquired using the conventional approach with the time delay interferometry observables. The suggestion by Romano and Woan was to factorise the likelihood with analysis done only on the laser noise free data however, we found that this was not required as the size of the laser phase noises meant that the inverse reduced their contribution in the transformed data. The signal extraction process uses templates of the signals which depend on the structure of the data used and for real LISA data the minimum number of terms in the geometric observables is 16. The principal component approach uses the raw data that contain only two copies of the signal in the raw data. The laser phase noise free data, the time delay interferometry observables, are obtained by transforming the raw data using the eigenvectors.

The overall results are that (i) the principal components approach is another way of producing the time delay interferometry observables which are obtained from the eigendecomposition of the covariance matrix, (ii) analysis using these principal components produced the same results as the conventional time delay interferometry observables and (iii) this approach adapts readily to real LISA data especially in dealing with time varying arms. The advantage of this method is that it simplifies LISA data analysis by incorporating the laser noise cancellation in the statistical inference achieving the same results as the conventional approach. Future work could include a real test of the method by applying it to the more realistic data of the Mock LISA Data Challenges.

This method depends on capturing the variances and covariances in the data which defines the principal components therefore, the covariance matrix must match what is occurring in the data. In our investigation these were generated algebraically based on assumptions made about the noise characteristics and behaviour. One of those assumptions was Gaussian distributed noises which are completely defined by the covariance matrix therefore, this could be a problem for distributions for which this does not occur. Determining the noise characteristics and behaviour is also a problem with the traditional time delay interferometry observables. However, for these observables there are some that will have low responses to gravitational waves, zero signal observables, that would provide information about the noises. One other option is to include a search on

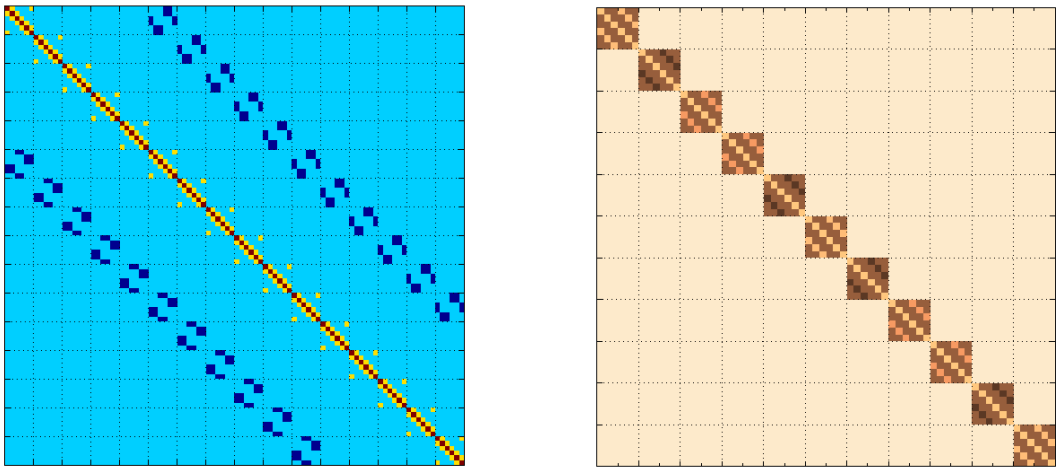

(a) (b)

Figure 7.1: Samples of the raw data covariance and power spectral density (absolute) matrices for spacecraft phase-locked lasers and equal arm lengths.

the noise characteristics in the inference. Another major problem, which is also shared with the conventional approach, is the matrix inversion. The PCA has the advantage of diagonalising the covariance matrix which is trivial to invert but the problem is transferred to the eigendecomposition. However, for the algebraic solution the characteristic equation only requires the determinant of the covariance matrix while the inversion also uses the matrix of cofactors. In the time domain the computation times for the eigendecomposition of the matrix using algebraic solutions scales very badly with the size of the matrix, for example, it took approximately 9 h to obtain results for a 90×90 matrix which just covers a time span of 15 s. Computation times using numeric solutions scaled better with time but overall they were still slow, for example, it took 7 m to compute a 18000×18000 (50 m) square matrix which is extremely small for the size of LISA data.

7.1 Future work

Potential for future work is on the eigendecomposition of these large matrices which is essential for the principal components and would also be useful for the matrix inversion for the conventional approach. The covariance matrix has non-zero contributions that are restricted to narrow bands near the main diagonal which will not change in width with the increase in the size of the matrix. The bandwidth will change slightly with the temporal changes but will not go beyond the maximum that reflects the 1% change

due to flexing. Samples of the matrices in the time and frequency domains in Figure 7.1 are for static stationary array with the laser phase-locked on each spacecraft and equal arm lengths. While for full matrices computing the determinant is non-trivial, the sparseness of LISA's covariance matrix could lead to simplification of the computation. The determinant is in the characteristic equation used for algebraic solutions which is

$$\left|\mathbf{C} - \lambda I\right| = 0, \tag{7.1}$$

where $\mathbf{C}$ is the covariance matrix and I is the unit matrix. The traditional way to compute the determinant is to use one row or column of the matrix. Using the first with elements given by c_{1j} the equation for computing the determinant from Petersen and Pederson [48] is

$$\det(\mathbf{C}) = \sum_{j=1}^{n} (-1)^{j+1} c_{1j} \det\left([\mathbf{C}]_{1j}\right) \tag{7.2}$$

where $[\mathbf{C}]_{1j}$ is a smaller matrix obtained from $\mathbf{C}$ by deleting the row 1 and column j. For LISA most of the elements in the row are zero with a possible maximum of $D_i - D_j$ band near the main diagonal and the D_i. There will also be zeros within the band as shown in Figure 7.1a and the quantity will depend on the lengths of the arms, phase-locking and sampling rate. In that example there are only five non-zero values. Also, because the determinant is a sum of the values computed for each element in the first row as given in Equation 7.2, there is the opportunity for parallel computation with the values for each element c_{1j} computed separately and then summed.

Other possibilities are from transforming the matrix into forms that have trivial solutions for the determinant such as diagonal and triangular matrices or have closed form solutions such as tridiagonal matrices. A block diagonal structure was obtained in the frequency domain for our toy examples as shown in Figure 7.1b where eigendecomposition it allowed the decomposition to be performed on individual blocks. This structure was obtained because of the assumption of the lack of correlations between frequencies. In theory the small size (6×6) should allow algebraic solutions with reasonable times but this depended on the values in the blocks which includes exponential terms. Despite this the partitioning allows parallel computation which can also be used for numeric methods. The diagonal structure of the matrix will be lost if there are correlations between the frequencies and the problems will be similar to those of the time domain.

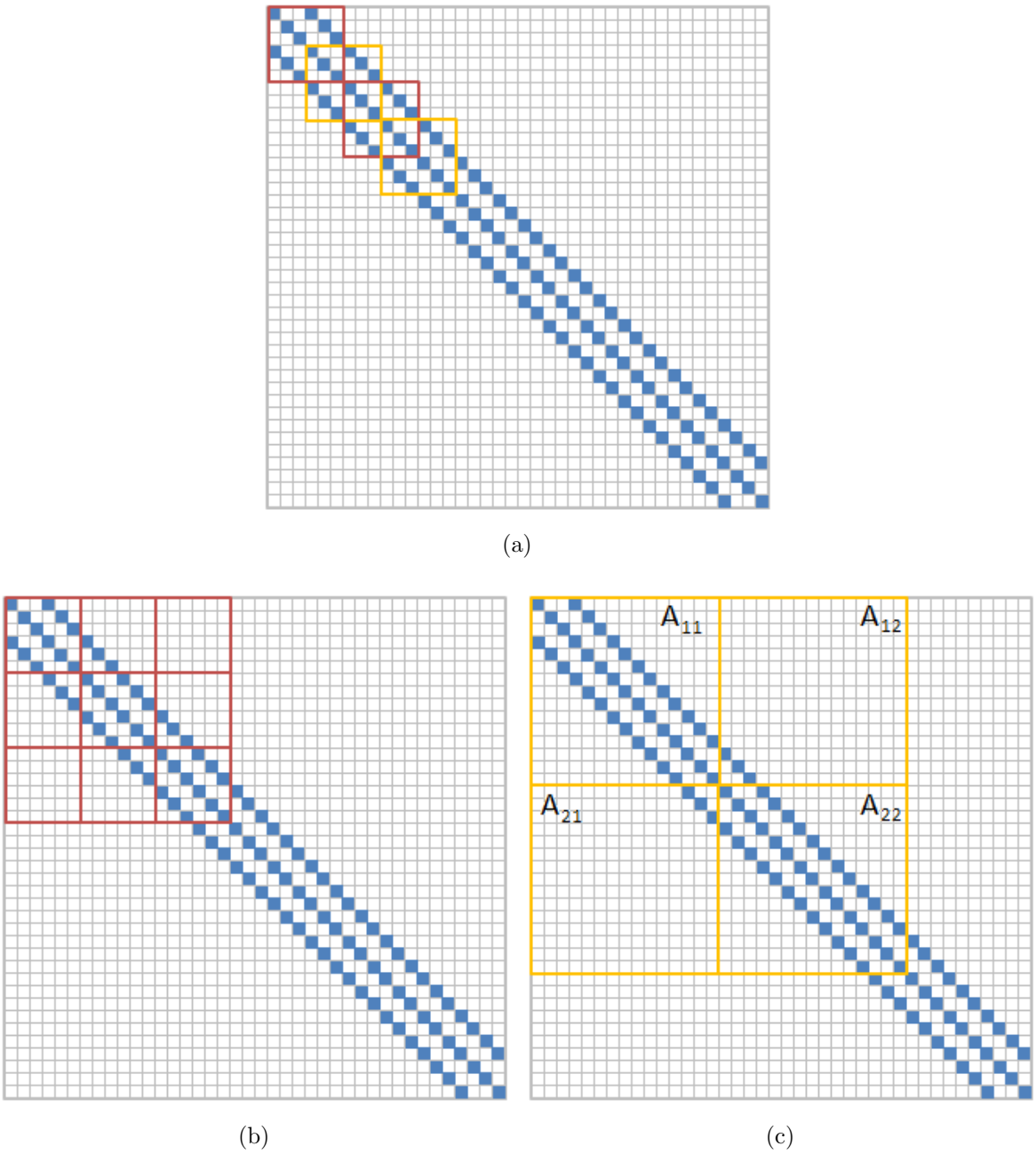

(a)

(b)

(c)

Figure 7.2: Matrix partitioning possibilities for the covariance matrix. The small blocks represent the 6×6 blocks for the optical benches and the larger red and yellow blocks are the partitions. This would represent the case for equal arm lengths and all lasers phase-locked with the separations between the diagonals reduced for illustration.

Other ways of obtaining the diagonal and tridiagonal structure is by partitioning the matrix into blocks. Unfortunately, there is no way to partition the covariance matrix to obtain independent blocks. This is illustrated in Figure 7.2b which would represent the case of equal arm lengths and all lasers phase-locked. The separation between the diagonals have been reduced for illustrative purposes. In this figure the small blocks in the matrices represent the 6×6 blocks of the covariance matrices with the blue ones

indicating non-zero values and the coloured squares are used to show the partitioning. The only possibility for diagonal solution is with overlapping blocks Figure 7.2a. This could be investigated to determine if there is a solution that will account for the shared blocks. In this illustration the small size of the partition made the overlap large but with large blocks the contribution from each block will be reduced.

For the tridiagonal case which are illustrated in Figures 7.2b and 7.2c giving three types of blocks including those centred on the main diagonal, those next to the main diagonal, and the others which will all be zero. A simple example is for a matrix consisting of the four blocks in Figure 7.2c where the determinant is given by Petersen and Pederson [48] as

$$\det\left(\begin{bmatrix}\mathbf{A}_{11} & \mathbf{A}_{12}\\ \mathbf{A}_{21} & \mathbf{A}_{22}\end{bmatrix}\right) = \det\big(\mathbf{A}_{22}\big)\cdot\det\big(\mathbf{C}_1\big) = \det\big(\mathbf{A}_{11}\big)\cdot\det\big(\mathbf{C}_2\big), \tag{7.3}$$

where

$$\begin{aligned}\mathbf{C}_1 &= \mathbf{A}_{11} - \mathbf{A}_{12}\mathbf{A}_{22}^{-1}\mathbf{A}_{21},\\ \mathbf{C}_2 &= \mathbf{A}_{22} - \mathbf{A}_{21}\mathbf{A}_{11}^{-1}\mathbf{A}_{12},\end{aligned} \tag{7.4}$$

with possibility of checking how this expanded to the larger matrix. There are methods that take advantage the symmetric structure and give closed form solutions such as that given for symmetric banded Topelitz matrices by Trench [74] with solutions related to the bandwidth and both the matrix size. Also, there are solutions for general block tridiagonal matrices [56] but require nonsingular blocks which can be avoided by partitioning the matrix allow for this. These cases will only work for some simplification of LISA such as fixed arm lengths, however, they may still be useful depending on how much the breathing of the arms affect the matrix structure which will depend on the phase-locking and sampling rate.

Bibliography

[1] Abbott, B. P., et al. GW150914: The Advanced LIGO Detectors in the Era of First Discoveries. *Phys. Rev. Letters 116*, 131103 (2016).

[2] Abbott, B. P., et al. GW151226: Observation of Gravitational Waves from a 22-Solar-Mass Binary Black Hole Coalescence. *Phys. Rev. Letters 116*, 241103 (2016).

[3] Abbott, B. P., et al. Observation of Gravitational Waves from a Binary Black Hole. *Phys. Rev. Letters 116*, 061102 (2016).

[4] Adams, M. R., and Cornish, N. J. Discriminating between a stochastic gravitational wave background and instrumental noise . *Phys. Rev. D 82*, 022002 (2010).

[5] Andrae, R. Error estimation in astronomy . *arXiv:1009.2755v3* (October 2010). DOI:10.1016/S0003-4916(02)00025-8.

[6] Armstrong, J. W., Estabrook, F. B., and Tinto, M. Time-delay Interferometry for Space-based Gravitational Wave Searches. *Ap. J. 527* (1999), 814.

[7] Armstrong, J. W., Estabrook, F. B., and Tinto, M. Time delay Interferometry. *Class. Quantum Grav. 20* (2003), S283.

[8] Arnaud, K. A., et al. An Overview of the Mock LISA Data Challenges. *AIP Conf. Proc. 873* (2006), 619.

[9] Babak, S., et al. The Mock LISA Data Challenges: from Challenge 1B to Challenge 3 . *Class. Quantum Grav. 25*, 184026 (2008).

[10] Bender, P., et al. LISA: Laser Interferometer Space Antenna for the detection and observation of gravitational waves. LISA: Pre-Phase A Report MPQ 233, NASA, July 1998.

[11] Bender, P., et al. LISA: A cornerstone mission for the observation of gravitational waves. System and Technology Study Report ESA-SCI(2000)11, ESA, 2000.

[12] Berry, C. P. L., and Gair, J. R. Observing the Galaxy's massive black hole with gravitational wave bursts. *MNRAS 429* (2013).

[13] Blair, D. G., Ju, L., Zhao, C., and Howell, E. J. Gravitational Waves. In *Advanced Gravitational Wave Detectors*. Cambridge Books Online, 2015.

[14] Bohm, D. *The Special Theory of Relativity*. Routledge, 1996.

[15] Box, G. P., and Tiao, G. C. *Bayesian Inference in Statistical Analysis*. Addison-Wesley Publishing Co., 1973.

[16] Bretthorst, G. L. Bayesian Spectrum Analysis and Parameter Estimation. In *Lecture Notes in Statistics*, vol. 48. Springer, 1988.

[17] Cheng, T.-P. *Relativity, Gravitation and Cosmology*. Oxford Scholarship Online, February 2010.

[18] Cornish, N. J. Gravitational Wave Confusion Noise. *arXiv:gr-qc/030402v1* (April 2003).

[19] Cornish, N. J., and Crowder, J. LISA data analysis using Monte Carlo methods. *Phys. Rev. D 72*, 043005 (2005).

[20] Cornish, N. J., and Hellings, R. W. The effects of orbital motion on LISA time delay interferometry. *Class. Quantum Grav. 20* (2003), 4851.

[21] Cramer, B., Stebbins, R. T., and Prince, T. A. Tech. rep.

[22] Crowder, J., and Cornish, N. J. LISA Source Confusion. *Phys. Rev. D 70*, 082004 (2004).

[23] Dhurandhar, S. V., Nayak, K. R., Koshti, S., and Vinet, J.-Y. Fundamentals of the LISA stable flight formation. *Class. Quantum Grav. 22*.

[24] Dhurandhar, S. V., Nayak, K. R., and Vinet, J.-Y. Algebraic approach to time-delay data analysis for LISA. *Phys. Rev. D 65*, 102002 (May 2002).

[25] Dwyer, S., Sigg, D., and Ballmer, S. W. Gravitational wave detector with cosmological reach. *Phys. Rev. D 91*, 082001 (2015).

[26] Eastabrook, F. B., Tinto, M., and Armstrong, J. W. Time-delay analysis of LISA gravitational wave data: Elimination of spacecraft motion effects. *Phys. Rev. D 62*, 042002 (2000).

[27] Einstein, A. *Relativity: The Special and General Theory.* Methuen & Co. Ltd., 1920.

[28] esa.int. European Space Agency: LISA Pathfinder Completes First Operations Phase, 2016. http://sci.esa.int/lisa-pathfinder/58006-lisa-pathfinder-completes-first-operations-phase/.

[29] Faulks, H., et al. LISA: Study of the Laser Interferometer Space Antenna. LISA-Final Technical report LI-RP-DS-009, NASA, April 2000.

[30] Gair, J. R., Vallisneri, M., Larson, S. L., and Baker, J. G. Testing General Relativity with Low-Frequency, Space-Based Gravitational-Wave Detectors. *Living Rev. Relativity 16*, 7 (2013).

[31] Giampieri, G., Hellings, R. W., Tinto, M., and Faller, J. E. Algorithms for unequal-arm michelson interferometers. *Optics Comm. 699* (1996).

[32] gsfc.nasa.gov. Mock LISA Data Challenge, 2016. http://astrogravs.gsfc.nasa.gov/ docs/mldc/, Accessed: April 2016.

[33] Held, L., and Bové, D. S. Bayesian Inference. In *Applied Statistical Inference.* Springer-Verlag, 2014.

[34] Hsu, H. *Schaum's Outline of Probability, Random Variables, and Random Processes.* McGraw-Hill, 2011.

[35] Hulse, R. A., and Taylor, J. H. Discovery of a Pulsar in a Binary. *Astrophys. J. 195* (January 1975).

[36] Jennrich, O. LISA technology and instrumentation. *Class. Quantum Grav. 26*, 153001.

[37] jolliffe, I. T. *Principal Component Analysis.* Springer, 2002.

[38] Lance, A. L., Seal, W. D., and Labaar, F. Phase Noise and AM Noise Measurements in the Frequency Domain. *Infrared and Millimeter Waves 11*, 239 (1984).

[39] Larson, S. L. LISA: A Modern Astrophysical Observatory. In *Gravity in the Quantum World and the Cosmos*, no. SLAC-R-819, T023.

[40] ligo.org. Introduction to LIGO and Gravitational Waves: Sources of Gravitational Waves. Accessed: 28 November 2015.

[41] lisapatherfinder.org. LISA Pathfinder: Fact Sheet, 2016. http://sci.esa.int/lisa-pathfinder/47363-fact-sheet/, Accessed: 19 April 2016.

[42] Nayak, K. R., Dhurandhar, S. V., and Vinet, J.-Y. Improving the sensitivity of LISA. *Class. Quantum Grav. 20*.

[43] Nayak, K. R., and Vinet, J.-Y. Algebraic approach to time-delay data analysis for orbiting LISA. *Phys. Rev. D 70*, 102003 (November 2004).

[44] Nayak, K. R., and Vinet, J.-Y. Algebraic approach to time-delay data analysis: orbiting case. *Class. Quantum Grav. 22*, 10 (April 2005).

[45] O'Hagan, A., and Luce, B. R. *A Primer on Bayesian Statistics in Health Economics and Operations Research*. MEDTAP International, Incorporated, 2003. Online version.

[46] Otto, M., Heinzel, G., and Danzmann, K. TDI and clock noise removal for the split interferometry configuration of LISA. *Class. Quantum Grav. 29*, 205003.

[47] Papoulis, A., and Pillai, S. U. Two Random Variables. In *Probability, Random Variables and Stochastic Processes*. McGraw-Hill.

[48] Petersen, K. B., and Pederson, M. S. The Matrix Cookbook, January 2012. Http://matrixcookbook.com.

[49] Phinney, E. S. eLISA: Astrophysics and cosmology in the millihertz regime. *arXiv:1201.3621v1*.

[50] Pitkin, M., Reid, S., Rowan, S., and Hough, J. Gravitational Wave Detection by Interferometry: (Ground and Space). *Living Rev. Relativity 14*, 5 (2011).

[51] Prince, T. A., Tinto, M., and Larson, S. L. LISA Optimal Sensitivity. *Phys. Rev. D 66*, 122002 (2002).

[52] Riles, K. Gravitational Waves: Sources, Detectors and Searches. *arXiv:1209.0667v3* (February 2013).

[53] Riley, K. F., Hobson, M. P., and Bence, S. J. *Mathematical Methods for Physics and Engineering*. Cambridge University Press, 2006.

[54] Romano, J. D., and Woan, G. A Principal Component Analysis for LISA - the TDI Connection. *Phys. Rev. D 73*, 102001 (May 2006).

[55] Ryder, L. *Introduction to General Relativity*. Cambridge University Press, 2009.

[56] Sandryhaila, A., and Moura, J. M. F. Eigendecomposition of Block Tridiagonal Matrices. *arXiv:1306.0217v1*.

[57] Sathyaprakash, B. S., and Schutz, B. F. Physics, Astrophysics and Cosmology with Gravitational Waves. *Living Rev. Relativity 12*, 2 (2009).

[58] Saulson, P. R. Terrestrial gravitational noise on a gravitational wave antenna. *Phys. Rev. D 30*, 4 (1984).

[59] Shaddock, D. A. Operating LISA as a Sagnac interferometer. *Phys. Rev. D. 69* (2004), 022001.

[60] Shaddock, D. A., Tinto, M., Eastabrook, F. B., and Armstrong, J. W. Data combinations accounting for LISA spacecraft motion. *Phys. Rev. D 68*, 061303 (2003).

[61] Shlens, J. A Tutorial on Principal Component Analysis. *arXiv:gr-qc/030402v1* (April 2014).

[62] Speigel, M. R., Schiller, J., and Srinivasan, R. A. *Schaum's Outline of Probability and Statistics*. McGraw-Hill, 2011.

[63] Stoecklin, M. P. Tables of common transform pairs.

[64] Taylor, J. H., and Weisberg, J. M. A new test of genral relativity: gravitational radiation and the binary pulsar PSR 1913+16. *Astrophys. J. 253* (February 1982).

[65] Thorne, K. Gravitational Waves. *arXiv:9506086v1* (Jul 1995).

[66] Tinto, M., and Armstrong, J. W. Unequal-arms Michelson Interferometers. *PTTI 30* (1998), 173.

[67] Tinto, M., and Artmstrong, J. W. Cancellation of Laser Noise in an Unequal-arm Interferometer Detector of Gravitational Radiation. *Phys. Rev. D 59*, 102003 (1999).

[68] Tinto, M., and Dhurandhar, S. V. Time delay interferometry. *Living Rev. Relativity 8*, 4 (2005). http://www.livingreviews.org/lrr-2005-4.

[69] Tinto, M., Eastabrook, F. B., and Armstrong, J. W. Time-delay for LISA. *Phys. Rev. D 65*, 082003 (2002).

[70] Tinto, M., Eastabrook, F. B., and Armstrong, J. W. Time delay interferometry with moving spacecraft arrays. *Phys. Rev. D 69*, 082001 (2004).

[71] Tinto, M., and Larson, S. L. LISA time-delay interferometry zero-signal solution: Geometrical properties. *Phys. Rev. D. 70*, 062002 (2004).

[72] Tinto, M., and Larson, S. L. The LISA zero-signal solution. *Class. Quantum Grav. 22* (2005), S531.

[73] Trench, W. F. Banded symmetric Toeplitz matrices: where linear algebra borrows from difference equations.

[74] Trench, W. F. On the eigenvalue problem for Toeplitz band matrices. *Linear Algebra and its Applications 64* (January 1985).

[75] Umstätter, R., et al. Bayesian modeling of source confusion in LISA data. *Phys. Rev. D 72*, 02001 (July 2005).

[76] Umstätter, R., et al. LISA source confusion: identification and characterization of signals. *Class. Quantum Grav. 22*, 18 (August 2005), S901.

[77] Vallisneri, M. Geometric time delay interferometry. *Phys. Rev. D 72*, 042003 (2005).

[78] Wang, Y., Heinzel, G., and Danzmann, K. First stage of LISA data processing: Clock synchronization and arm-length determination via hybrid-extended Kalman filter. *Phys. Rev. D 90*, 064016 (September 2014).

[79] Weinberg, D. Astronomy 810: Statistics Notes.

[80] Weisberg, J. M., Nice, D. J., and Taylor, J. H. Timing measurements of the relativistic binary pulsar PSR 1913+16. *Astrophys. J. 722* (October 2010).